Doctoral Dissertation
Doctoral Program in Energy Engineering (34th Cycle)

Versatile, direct nanocasting strategy to N-rich ordered mesoporous carbons for selective post-combustion CO_2 capture and energy storage

By

Elisa Maruccia
******

Supervisors:
Prof. Claudio Gerbaldi, Supervisor
Prof. Candido Fabrizio Pirri, Co-Supervisor

Doctoral Examination Committee:
Prof. Francesca Bonino, Referee, University of Turin
Prof. Christian Durante, Referee, University of Padua

Politecnico di Torino
2022

Declaration

I hereby declare that, the contents and organization of this dissertation constitute my own original work and does not compromise in any way the rights of third parties, including those relating to the security of personal data.

Elisa Maruccia

2022

To my family

Acknowledgment

In any case, while it is all very well to talk of 'turning points', one can surely only recognise such moments in retrospect. Naturally, when one looks back to such instances today, they may indeed take the appearance of being crucial, precious moments in one's life; but of course, at the time, this was not the impression one had.

- Kazuo Ishiguro, The Remains of the Day

In the end, I would like to thank every people that took part in my life during these years, also the ones that are not present now while I am crossing the finishing line. I would like to thank them as well because sometimes discontinuity is an important teacher.

My last but deep gratitude goes to my family, my dad, my mum, and my sister. They walked along with me during these three years with a caring presence and support. The ambitious goals are meaningful if you can share them with someone. They have always been a model for the honestly conquered results and my motivation for always learning and improving. To them, I dedicate this thesis.

Preface

During the last century, the extraordinary progress of technology created the illusion of a fair distribution of wealth, but, on the other hand, the overexploitation of natural resources for reaching top-quality standards of living, may result in their forthcoming depletion. Presently, the exacerbation of the energy crisis, due to the repercussion of COVID-19 pandemic, is threatening European countries with fuel and food shortage. The high vulnerability of economics to the fluctuation of the cost and supply of fuels is directly related to the still prevalent energetic dependence of human and industrial activities from exhaustible and geographically limited resources. The other side of the coin of fossil fuel exploitation is global warming. Indeed, the alarming increase of surface temperature, caused by uncontrolled greenhouse gases (GHG) emissions from the combustion of fossil fuels, is radically altering global natural ecosystems and endangering life on Planet Earth.

In this scenario, the development of innovative technologies based on renewable and equally distributed resources and efficient systems for GHG sequestration are amongst the most effective strategies available for coping the energetic and climate crises. Most of GHG emissions derive either from the transportation or manufacture and electricity production sectors. Carbon dioxide (CO_2) is the most abundant GHG and the major contributor to global warming. Nowadays, replacing the combustion of fossil fuels through electrification is the most valid strategy for reducing polluting emissions from the transportation sector. Automotive industry relies on the recent progresses in energy storage technologies to limit or even fully replace the production of internal combustion engines in the near future. Concerning the prevention of GHG emissions from large-scale plants, Carbon Capture and Storage (CCS) technologies presently rely on CO_2 sequestration from exhausted gases, so as to avoid its direct release in the atmosphere.

In such a scenario, this Ph.D. dissertation aims to tackle the above detailed issues by providing effective, sustainable strategies for the development of innovative, highly performing, selective CO_2 sorbent materials, namely nitrogen-containing ordered mesoporous carbon (OMC) by the nanocasting procedure

The outcome of the work contains eight main chapters, comprising the introductory section and concluding remarks. An overview of currently available strategies for tackling the climate crisis is presented in the introductory section (Chapters 1-4). In details, Chapter 1 introduces key concepts and general guidelines for Climate Change mitigation. Chapter 2 illustrates CCS technologies, by examining the main available strategies and their Technological Readiness Level. Chapter 3 concerns physical adsorbents, and particularly examines some crucial features affecting CO_2 capture. Chapter 4 deals with OMCs, starting from a brief history of templated synthesis, and focusing afterwards on the nanocasting procedure and CO_2 capture performances by literature works.

The experimental section mainly describes the development and comprehensive characterization of N-rich ordered mesoporous carbons (NOMCs) with different texture and surface chemistry as selective CO_2 sorbents (Chapters 5-6). In details, Chapter 5 investigates the role of porosity and nitrogen incorporation in CO_2 capture and selectivity by OMCs, while Chapter 6 tackles CO_2 selective separation and NOMC-sorbents reusability from moist flue gases. Finally, as a proof-of-concept of their possible application in other energy-related fields, NOMCs were also exploited as promising anode active materials in Li- and Na-ion batteries; results are discussed in Chapter 7. The Appendix (1-3) Section includes details about the methodology of synthesis, physico-chemical, gas adsorption and electrochemical investigation of the materials prepared and under study. The experimental work was carried out both at the Department of Applied Science and Technology, Politecnico di Torino, and at the Center for Sustainable Future Technology, Italian Institute of Technology. A nine-month internship was conducted in the research group of Prof. Freddy Kleitz, at the Department of Inorganic Chemistry and Functional Materials, University of Vienna, to acquire knowledge and expertise in the synthesis and fundamental characterization of functional nanoporous materials with ordered arrangement of the pores suitable for gas storage and electrochemical applications.

In conclusion, the work presented in this Ph.D. dissertation represents a meticulous overview of the most efficient technologies presently available for the mitigation of the energetic and climate crises. Although the target remains certainly challenging and arduous, the achieved experimental results effectively contributed to the comprehension of crucial mechanisms regarding gas adsorption and paved the way for future applications in the energy storage field, thus providing useful tools for directing the future research efforts in GHGs sequestration and, possibly, alkali-ion secondary batteries.

Contents

List of Figures

List of Tables

Chapter 1

1. Background

1.1. Greenhouse gases and global warming

Planet Earth is the comfortable place, which hosts living beings and plant life also thanks to the warming effect played by some of the gases present in the atmosphere, which absorb the thermal energy received from the Sun and re-emit it back to the surface [1]. These gases are called greenhouse gases (GHGs) and the produced warming phenomenon is called the greenhouse effect. The greenhouse effect is responsible for the increase of 21 °C of the Earth's surface temperature in respect of the situation in which only non-absorbing gases were present in the atmosphere [2]. Indeed, the main components of the Earth's atmosphere, *viz.* nitrogen (N_2) and oxygen (O_2), are rigid diatomic molecules, the configuration of which makes them unable to vibrate and absorb the thermal radiation coming from the Sun [3]. Conversely, the so-called GHGs, i.e. carbon dioxide (CO_2), water vapor (H_2O), methane (CH_4), nitrous oxide (N_2O), chlorofluorocarbons (CFCs) and ozone (O_3) are characterized by loosely bonded atoms, which allow vibrations and, consequently, the absorption of the thermal radiation [3]. CO_2 is generated by the respiration processes of all living organisms, the combustion of fossil fuels and the fermentation of sugars [4]. Although the anthropic contribution was crucial in enriching their quantity, CO_2, CH_4 and N_2O were present in the atmosphere even before the pre-industrial times; on the contrary, other GHGs are synthetic, like hydrofluorocarbons (HFCs), perfluorocarbons (PFCs), sulphur hexafluoride (SF_6) and halons [5].

Terrestrial greenhouse effect differentiates from the one occurring in other planets, like Mars and Venus, because of the presence of water and clouds. The water cycle (evaporation, condensation and precipitation) is indeed strongly related to the temperature and air pressure variation and it is indirectly influenced by the non-condensable GHGs concentration, therefore operates like an alarm bell for the health of the Earth's climate [6] Accordingly, although water vapor and clouds together are considered to contribute to the 75 % of the greenhouse effect, the major concern is addressed to the non-condensable gases (CO_2, CH_4, N_2O, CFCs and O_3), since their amount alters the thermal balance and, consequently, the water vapor concentration in the air, which in turn again heavily contributes to the altered warming effect [1]. Moreover, among the non-condensable GHGs some of them are defined as long-lived GHGs, because they remain in the atmosphere for hundreds of years, as in the case of N_2O, or even for centuries to millennia in the case of CO_2 [7]. Conversely, CH_4 and aerosol are named as short-lived climate forcer (SLCF), since they persist in the atmosphere for few days up to decades [7].

Therefore, although the natural greenhouse effect is a necessary and intrinsic component of the Earth's thermal system, the imbalance of the GHGs concentration owing to the anthropogenic contribution, is responsible for the alarming global warming, which is causing the threatening climate change experienced nowadays. According to the most updated estimations of the Intergovernmental Panel on Climate Change (IPCC), the concentration of CO_2, CH_4 and N_2O reached 410 ppm, 1866 ppb and 332 ppb, respectively, in 2019 [8], compared to ca. 280 ppm, 700 ppb and 270 ppb in pre-industrial times [9], and in 2020, 10.2 GtC yr^{-1} (37.4 $GtCO_2$ yr^{-1}) of human-induced CO_2 were released in the atmosphere [10]. The evolution of the total human-induced drivers of the climate change in the period 1970-2010 is shown in Figure 1.1. The 78% of the total GHGs emissions is only due to the anthropogenic CO_2 release from the combustion of fossil fuels and, generally speaking, in industrial processes [11].
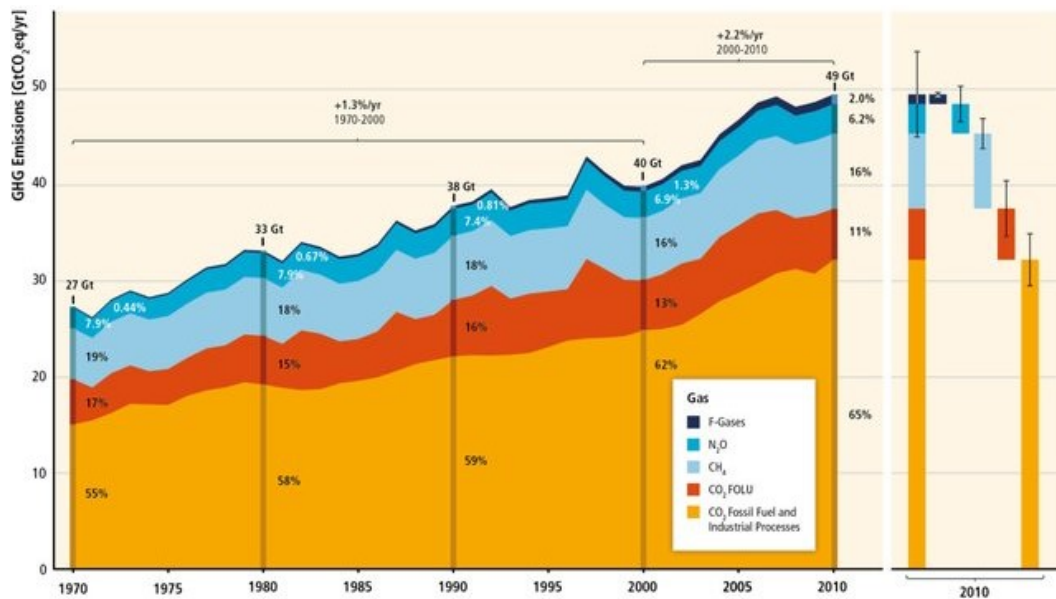
Figure 1.1: Contribution of the total anthropogenic GHG emissions (GtCO$_2$eq y^{-1}) in 1970-2010 by CO$_2$ from the combustion of fossil fuels and industrial processes and forestry and other land use (FOLU), CH$_4$, N$_2$O and fluorinated gases (F-gases) (original caption in [11]). Reprinted with permission from [11].

For the aforementioned reasons, it is ascertained that GHGs play a crucial role in the perturbation of the energy balance of the Earth-atmosphere system, hence they are defined as drivers of the climate change. The Earth's energy budget variation is quantified by means of the radiative forcing (RF), a quantity which expresses the net change of the radiative flux (W m^{-2}) at the tropopause (boundary between troposphere and stratosphere) or the top of the atmosphere, owing to the variation of an external driver of climate change [12]. GHGs absorb the outgoing infrared (thermal) radiation, providing a positive contribution to the radiative forcing and thus causing the surface warming [13]. Figure 1.2 clearly shows that, in 2011, the RF produced by anthropogenic sources compared to the pre-industrial era (the origin of the scale is set at the year 1750, RF = 0 W m^{-2}) is equal to 2.29 W m^{-2} and that CO$_2$ provides the major contribution among the other considered drivers, with a RF equal to 1.68 W m^{-2} [12].

Emitted compound	Resulting atmospheric drivers	Radiative forcing by emissions and drivers	Level of confidence
CO₂	CO₂	1.68 [1.33 to 2.03]	VH
CH₄	CO₂ H₂Oˢᵗʳ O₃ CH₄	0.97 [0.74 to 1.20]	H
Halo-carbons	O₃ CFCs HCFCs	0.18 [0.01 to 0.35]	H
N₂O	N₂O	0.17 [0.13 to 0.21]	VH
CO	CO₂ CH₄ O₃	0.23 [0.16 to 0.30]	M
NMVOC	CO₂ CH₄ O₃	0.10 [0.05 to 0.15]	M
NOₓ	Nitrate CH₄ O₃	-0.15 [-0.34 to 0.03]	M
Aerosols and precursors (Mineral dust, SO₂, NH₃, Organic carbon and Black carbon)	Mineral dust Sulphate Nitrate Organic carbon Black carbon	-0.27 [-0.77 to 0.23]	H
	Cloud adjustments due to aerosols	-0.55 [-1.33 to -0.06]	L
	Albedo change due to land use	-0.15 [-0.25 to -0.05]	M
	Changes in solar irradiance	0.05 [0.00 to 0.10]	M
Total anthropogenic RF relative to 1750	2011	2.29 [1.13 to 3.33]	H
	1980	1.25 [0.64 to 1.86]	H
	1950	0.57 [0.29 to 0.85]	M

Radiative forcing relative to 1750 (W m⁻²)

Figure 1.2: Radiative forcing owing to different natural and anthropogenic contributors in 2011 compared to the pre-industrial times (around the year 1750) (original caption in [12]). Reprinted with permission from [12].

1.2.   Climate actions and future scenarios

In this scenario, the implementation of new regulations in force became fundamental and indeed strictly necessary to arrest and, possibly, reverse this alarming trend and drive the urgent climate actions. The United Nations Conference on Environment and Development (UNCED) held in 1992 in Rio de Janeiro joined an International Treaty, the United Nations Framework Convention on Climate Change (UNFCCC) as a shared commitment for cooperation against climate change. In December 1997, during the third Conference of the Parties (COP) of UNFCCC, the Kyoto Protocol was adopted and entered into force on 16th February 2005 with the aim of committing the participant Countries to the reduction of the emissions of GHGs as a first action against climate change [14]. More recently, new

and more defined guidelines were settled during COP 21, which took place in Paris in 2015. Precisely, in this circumstance, another important international treaty, the so-called Paris Agreement, was adopted by 196 Parties, according to which the involved Countries committed to keep the average increase in the global temperature "well below" 2 °C, preferentially below 1.5 °C, above pre-industrial levels [15]. The targets of the Paris Agreement were renewed in 2021 during COP26 in Glasgow, which was originally planned for 2020, but then postponed because of COVID-19 pandemic. COP26 added new requirements to the Paris Agreement, such as the substantial reduction of the emissions by 2030, aiming to reach net zero emissions by the middle of the current century [16].

Simultaneously, the commitment to the climate change mitigation did not remain limited to the technicians and legislators' tables, but it expanded throughout the society, leading to a wide public participation, especially among young people. In this respect, the "Fridays for Future" movement, which started with a climate strike in August 2018 by the 15-years old Swedish activist Greta Thunberg, played a crucial role in conveying worldwide the message of the urgency of taking drastic measures against the climate crisis. Starting from the summer of 2018, several climate strikes took place to push the Governments toward a concrete realization of the targets established in the Paris Agreement. The so-called "Greta Thunberg effect" is a real social phenomenon, which proved to be effective in mobilizing people from all over the World towards collective actions, not anymore restricted to the youth aged population [17].

Now, it is interesting to make some consideration about the effectiveness on the long-term (2081−2100) of the established targets in the mitigation of the climate crisis. In this respect, the Sixth Assessment Report, drawn up by IPCC in 2021 [8], illustrated five supposed different scenarios on the basis of the evolution of the emissions of the main human-induced drivers of the climate change. These scenarios (see Figure 1.3) are named as SSPx-y, where "SSPx" is the acronym for "Shared Socio-economic Pathway" and "y" indicates approximatively the respective level of RF. The contributions to the global surface temperature increase in the period 2081−2100 were predicted for the different scenarios: i) the optimistic prediction of very low GHGs emissions and CO_2 emissions approaching the net zero goal around or after 2050, followed by net negative CO_2 emissions (SSP1_1.9 and SSP1_2.6); ii) the intermediate GHGs emissions (SSP2-4.5) and CO_2 emission stabilizing around the current levels until 2050; and, finally, iii) very high GHGs emissions (SSP3-7.0 and SSP5-8.5) and CO_2 emission that roughly double from current levels by 2100 and 2050, respectively. The information that can be extrapolated from this model is that if drastic and decisive measures are not taken

immediately as in the SSP1-1.9 or SSP1-2.6 scenarios, the Paris Agreement target of keeping the average increase in the global temperature "well below" 2 °C compared to pre-industrial times will not be realized. From the illustrative graphs in Figure 1.3, it is also possible to observe that the major contribution to the temperature increase is given by CO_2, in respect to the other non-CO_2 GHGs.
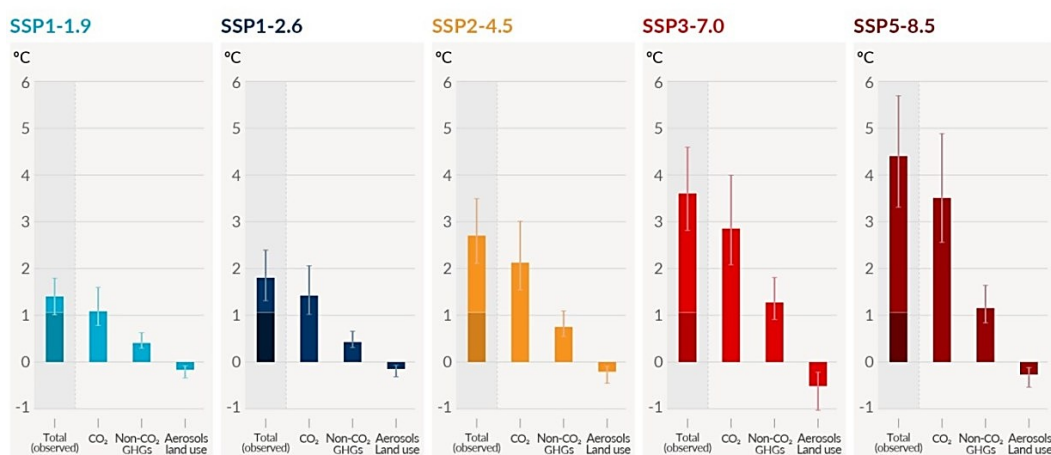
Figure 1.3: Prediction of the contribution to the global surface temperature increase from five scenarios corresponding to different emissions levels of the anthropogenic key drivers of climate change, relative to the 2081-2100 period in respect to 1850-1900. The darker shade illustrates the heating up to date [8].

The realization of the ambitious target of the net zero emissions by 2050 requires the integration of the most innovative technologies. For the sake of completeness, it is recommended the reading of the work by Borasio et al. [18], which provides an interesting example of a possible scenario for the deep decarbonization of the Italian energy system, which will be enabled by - quoting the authors' own words - "a high interpenetration of intermittent renewables, storage and sector coupling technologies". The proposed nearly-zero carbon emission configuration of the Italian energy system shown in Figure 1.4, allows to reach an overall emission of 9.5 $MtCO_2$ y^{-1}, which corresponds to the 97 % reduction in comparison to the level of 1990 [18].
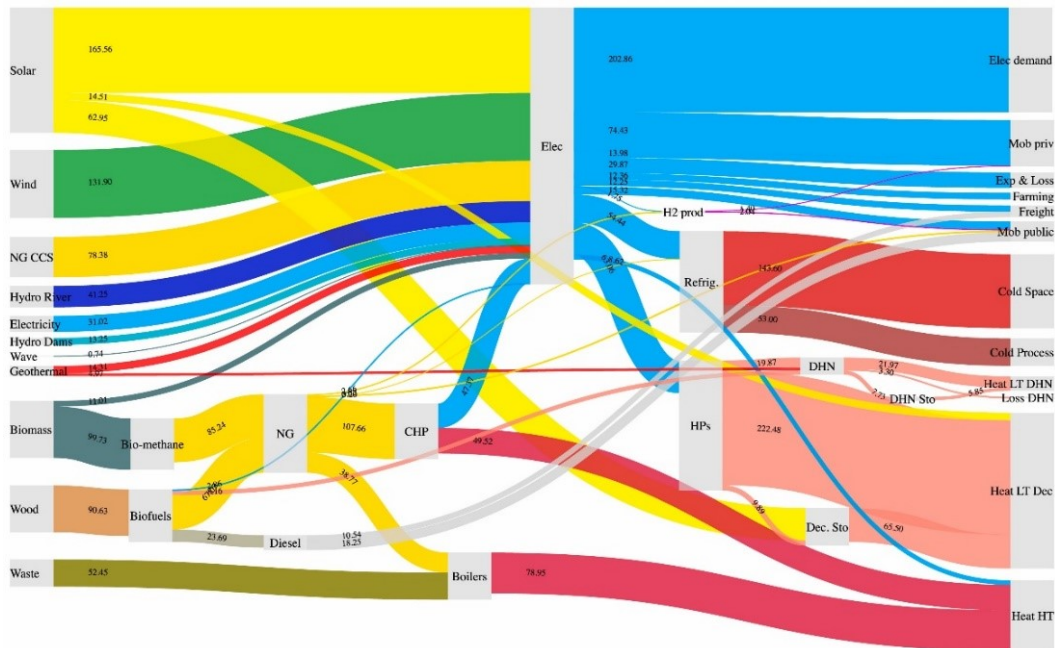
Figure 1.4: Main energy flows for the modelled deep decarbonization scenario of the Italian energy system in the year 2050. Abbreviations: natural gas (NG), carbon capture & storage (CCS), combined heat & power (CHP), district heating network (DHN), decentralised (dec.), heat pumps (HPs), electricity (elec.), storage (sto), low temperature (LT), mobility (mob), private (priv), export (Exp.), high temperature (HT), production (prod). Courtesy of [18].

Chapter 2

2. Carbon capture and Storage

2.1.   Carbon capture and storage technologies (CCS) and approaches for CO_2 capture from power plants

As described in Paragraph 1.1 and Paragraph 1.2, among the other drivers of the climate change, CO_2 is the most abundant GHGs, counting for the 78 % of the total emissions [19], and provides the major contribution to the RF [12], and to the consequent increase in the global surface temperature [8]. Hence, the main efforts are currently devoted towards reducing CO_2 emissions, by developing technologies at low carbon footprint. Indeed, as long as the technologies based on renewable energy sources become fully competitive to meet the energy demand, which is currently satisfied by fossil fuels, carbon capture and storage (CCS) plays a crucial role for mitigating the effects of CO_2 emissions and coping the consequences of the current climate crisis in the near future [20]. CCS technologies are based on the sequestration of CO_2 emitted by large point sources, such as coal-based, natural and synthesis gas processing, and cement plants, avoiding its direct release in the atmosphere [21]. CO_2 capture is sequestered from highly concentrated gas mixtures, before or after combustion, compressed and transported to a safe storage site, where it is safely stored and eventually recycled as a feedstock [22].

CCS occurs through three different possible processes, namely pre-combustion, oxy-combustion and post-combustion as shown in Figure 2.1.

In the following paragraphs, the three processes will be briefly described.
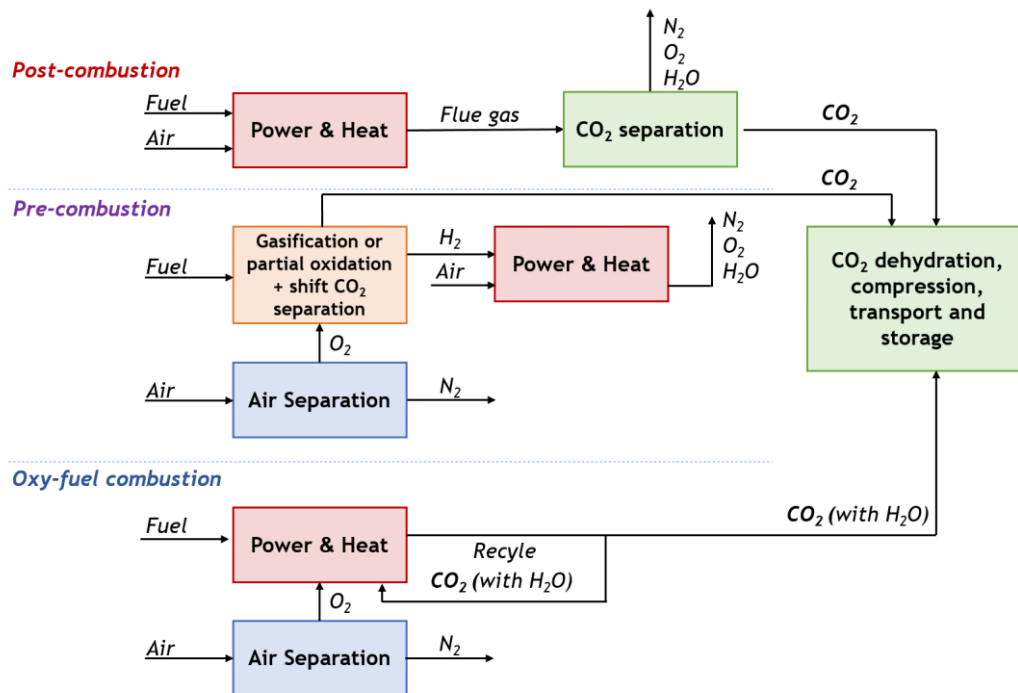
Figure 2.1: Schematic representation of the three main approaches for CO_2 capture from power plants: post-combustion, pre-combustion and oxy-combustion. Reprinted and readapted with permission from [23].

2.1.1. Post-combustion CO_2 capture

Post-combustion CO_2 capture deals with flue gases emitted by burning the fuel under air, so that they contain an excess of N_2. Precisely, the flue gas is approximately composed by 73−77 % of N_2, 15−16 % of CO_2, 5−7 % of H_2O and 3−4% of O_2 in coal-fired power plants [24] and 67−72 % of N_2, 8−10 % of CO_2, 18−20 % of H_2O and 2−3 % of O_2 in natural gas-fired power plants [25]; trace amounts of CO (20 ppm), NO_x (< 800 ppm), and SO_2 (< 500 ppm) are also present [26]. Post-combustion flue gas has a total pressure of 1 atm and its temperature ranges between 40 and 70 °C [26]. The remarkable advantage of this approach is that it can be easily retrofitted in already operative power plants, without modifying the existing configuration/combustion technology, and it is the simplest technology currently available for tackling CO_2 capture [27,28]. However, the main drawback of this technology is the difficulty of the separation of CO_2 at low concentration and low partial pressure (< 0.15 atm) [29], thus the need of treating high volumes of gases and of compressing the captured CO_2 [30].

2.1.2. Pre-combustion CO_2 capture

Pre-combustion technology is typically employed in industrial plants that use H_2 as the energy source. H_2 is produced by the gasification of the fossil fuel in the presence of sub-stoichiometric amounts of O_2, obtained by the separation of oxygen from the air by a cryogenic air separator, and usually some steam [27]. The gasification of the fossil fuel at elevated pressure produces a mixture containing predominantly CO and H_2, named as "synthesis gas". Then, CO reacts with steam to give a water-gas shift reaction, producing CO_2 (25-35%) and H_2 (30-50%) at high pressure (5-40 bar) [31]. In pre-combustion capture, the separation process deals with CO_2 and H_2 at high pressure and temperature, with traces amount of O_2, CO and steam [20,31,32]. High pressure gases are beneficial for capture, increasing the driving force for CO_2 separation and avoiding costs related to compression [26]. However, in pre-combustion capture some challenges have to be faced, for example the high cost of the technology and the complexity of the overall operational process, owing to the necessity of dealing with gasification and water gas shift reactors, scarce technical knowledge for good operability and industrial implementation [26,30].

2.1.3. Oxy-combustion CO_2 capture

Oxy-combustion capture technology is based on the combustion of the fuel in absence of nitrogen, in order to avoid the formation of NO_x compounds [31]. In this way, high-purity CO_2 and condensable water vapor can be easily separated via compression [20]. The volume of the reactor is reduced because the volume of the gas is decreased by the absence of nitrogen, the main component of atmospheric air; however, on the other hand, the combustion in pure oxygen is more complicated than in air [26]. In order to moderate the high-flame temperature due to the combustion in pure O_2, recycled flue gas (60%) is mixed to pure oxygen during combustion [26,33]. The gaseous exhausted product mixture is mainly composed of CO_2 (55-65%) and H_2O (25-35%). If H_2O is successfully removed, nearly pure CO_2 can be capture [31]. The drawback of this technology consists in the high energy demand for the initial separation step of nitrogen and oxygen from air and the current scarce know-how on the commercial scale [30].

2.2. CO_2 separation approaches

The major technological approaches proposed for CO_2 capture and separation include: absorption, adsorption, cryogenic distillation, membranes, gas hydrates

and chemical looping combustion. They are schematically represented and their characteristics overviewed in Figure 2.2.
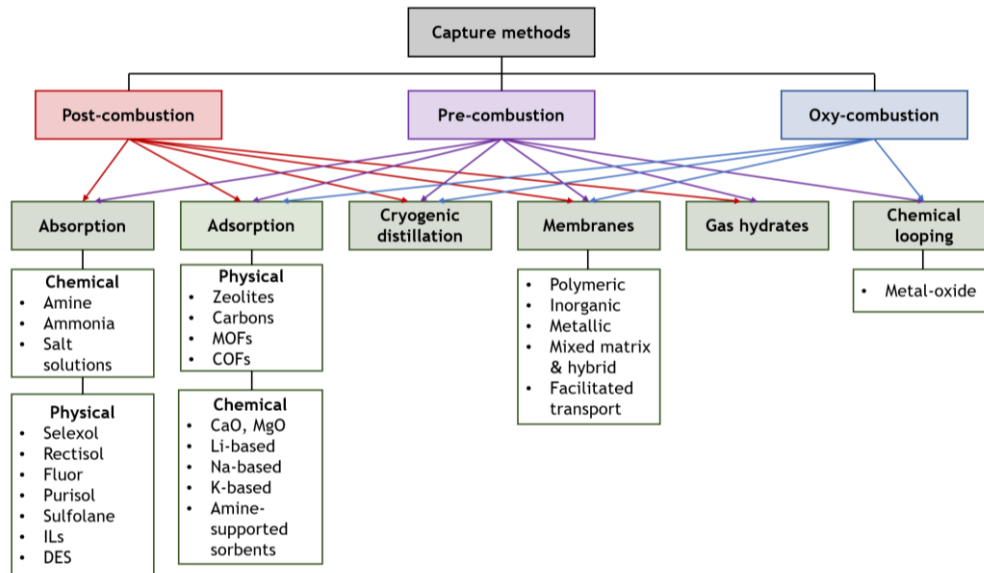
Figure 2.2: Overview of the technological approaches for CO_2 capture and separation. Reprinted and readapted with permission from [26,32].

2.2.1. Absorption

Chemical absorption involves chemical reactions between solvents (e.g., amine solutions, ammonia, salt solutions) and CO_2, with the formation of intermediate products, which are dissolved in the solvent itself [34]. Therefore, after the sorption process, the solvent is heated with low pressure steam in order to allow the release of the absorbed CO_2 and, subsequently, the regenerated solvent is recycled and reused [32]. The selective sorption is guaranteed by the chemical affinity between the solvent and the target solute, in our case CO_2, in respect to the other components of the flues gas (e.g. O_2 or N_2) [35]. Absorption is carried out at low temperature (35–50 °C, the limits are given by the condensation point of the gas and the freezing point of the solvent) and at relatively low CO_2 pressure, proportional to the concentration [35]. The criteria for the choice of a suitable solvent include on the one hand operative requisites, such as a high absorption capacity and rate, while, on the other hand, some intrinsic features, such as good thermal and chemical stability, low vapor pressure, viscosity and molecular weight, as well as scarce corrosion rate [32]. Moreover, the achievement of an optimal balance between a good chemical affinity and a feasible regeneration, in terms of expended energy and averted degradation of the solvent, is also extremely important [35]. For low partial

pressure absorption, the most common commercial alkanolamine used for CO_2 capture are monoethanolamine (MEA), diethanolamine (DEA), triethanolamine (TEA) dyglicolamine (DGA), diisopranolamine (DIPA) and methyldiethanolamine (MDEA) [36]. Ammonia (NH_3) is also a suitable solvent for CO_2 capture, thanks to its low toxicity, high resistance to degradation, mild conditions of regeneration and low cost [37]. Two major approaches based on NH_3 scrubbing are distinguished accordingly to the temperature of the treated exhausted gas. The conventional ammonia process tackles the flue gas at nearly ambient temperature (20−40 °C), whereas the so-called "chilled" or "precipitating" process occurs at lower temperatures (2−10 °C) with the precipitation of ammonium carbonate compounds [34]. NH_3 processes bring about some issues, like the volatility of ammonia and the corrosion/clogging of the pipes consequently to the precipitation of the solid compounds formed after the reaction with the absorbed CO_2 [37]. As for the salt solutions, conventional carbonate/bicarbonates (potassium and sodium), hydroxides (potassium, sodium and calcium) and amino acid salts solution are the most widely used [34]. From the capital cost investment viewpoint, MEA-based processes are more convenient than K_2CO_3–based ones for the treatment of low pressure CO_2 sources, as in the case of flue gases [36]. Precisely, chemical CO_2 absorption by MEA is currently the most mature and, indeed, the only commercialized technology for post-combustion CO_2 capture [32,38]. However, the sizeable energy consumption for high temperature solvent regeneration, the poor selectivity among acid gases, the high price of the materials, the high heat of absorption, the high corrosion of the equipment, the existence of side reactions and amine degradation by high temperature flue gases or the presence of contaminations such as SO_2, NO_2 and O_2, and large equipment size are remarkable limitations of this technology [34,35,38].

Physical absorption is suitable for pre-combustion flue gases, because it is recommended for the CO_2 capture at high partial pressure [32]. The typical physical absorption processes are Selexol[TM], Rectisol[(R)], Purisol, Fluor and Sulfolane processes, which use as physical solvents dimethyl ether of polyethylene glycol, cold methanol, N-methyl-2-pyrrolidone and propylene carbonate and 2,3,4,5-tetrahydrothiophene-1,1-dioxide, respectively [32]. Ionic liquids (ILs) are salts with melting points below 100 °C, which are composed by an organic cation and an inorganic or organic anion [39]. They are attractive solvents for many applications, including CO_2 capture and separation. Conventional ILs are physical absorbents [26] and the solubility of CO_2 is related to their free volume, ILs size, cation and anion [34]. However, the physical solubility of CO_2 in ILs is low [26]; thus, the synthesis of task-specific ionic liquids (TSILs) with basic functional groups, like

amines, was exploited to increase the solubility through a chemical absorption [34]. Hence, they are considered both chemical and physical sorbents. In general, chemical absorption is used if the CO_2 solubility is dependent on the structure of the amino functional group attached to the IL [34,40]; on the contrary, physical absorption is more appropriate if the solubility depends on the free volume, ILs size, cation and anion [34]. The peculiar structure of ILs provides many interesting properties, such as the non-volatility [40], good thermal and chemical stability [38], higher CO_2 solubility and selectivity [40]. In particular, selectivity is a crucial goal in gas separation and gas purification from flue gases, where mixtures including impurities (e.g., SO_2, H_2S, CH_4, CO, N_2, O_2, and H_2) besides CO_2 are involved. CO_2 is more soluble in ILs than other common gases (e.g., N_2, CH_4) [41]; nonetheless, the introduction of functional groups is one possibility to furtherly improve the selectivity. However, the functionalization increases ILs viscosity, which furtherly increases after CO_2 absorption; this is actually an intrinsic limitation of ILs. Adding water [40] or organic solvents [39] in small amounts or combining ILs with other polymer materials forming IL-based membranes could overcome the problem of high viscosity, accelerating the gas mass transfer [39,40] and, at the same time, reducing the costs [39]. Biodegradability and biocompatibility are another important factors to be considered. Davarpanah et al. [39] substituted common non-biodegradable and/or biocompatible cation and anions with ions derived from metabolic molecules (e.g. choline, a proved nontoxic and biocompatible cation) and amino acids (renewable, biodegradable, biocompatible and naturally abundant anions). Other drawbacks of ILs are the high cost and the often time/energy consuming complicated synthesis. Promising alternatives to ILs are the deep eutectic solvents (DESs), which have similar properties, but easier synthesis and lower cost [41].

2.2.2. Adsorption

Adsorption is a heterogeneous process between gas molecules, named as *adsorbates*, which approach the surface of a solid, named as adsorbent, and the solid itself. The gas species are attracted by the electronic environment at the surface of the solid, achieving a more energetically favorable configuration that allows the reduction of the free motion, thus a decrease of the entropy of the system occurs [42]. Therefore, from a thermodynamic point of view, adsorption must be an exothermic process ($\Delta H \leq 0$), in order to balance the entropy variation reduction, while maintaining an advantageous free-energy driving force ($\Delta G \leq 0$) [43]. Adsorption phenomena are distinguished into physisorption, if the adsorbate and the adsorbent interact with weak intermolecular forces, such as electrostatic

interactions or van der Waals forces, or chemisorption if they reversibly reacts forming stronger chemical bonds, such as covalent bonds, and generating a surface compound [30,32,44]. The advantage of physisorption is the lower energy required for regeneration (−25 to −50 kJ mol^{-1}) compared to chemisorption (−60 to −90 kJ mol^{-1}) [21]. However, the penalty for the lower heat of adsorption in physisorption processes is the reduced selectivity [32]. The features of an ideal CO_2 adsorbent include high adsorption capacity, fast adsorption/desorption kinetics, selectivity over the other components of the flue gas, especially N_2 and H_2O, easy and feasible regeneration ability, good mechanical, thermal and chemical stability, tolerance towards contaminants (e.g., SO_2, NO_x, Hg) and moisture, and finally low operational and sorbent costs [21,22,30,38,45,46]. Adsorbents are usually solid porous materials with high surface area, which are classified according to their pore size into [47]:

- *Microporous,* if their pore size is lower than 2 nm;

- *Mesoporous,* if their pore size is within 2−50 nm;

- *Macroporous,* if their pore size is larger than 50 nm.

Typical physisorbents are solid porous materials like zeolites [48], porous carbonaceous materials (activated carbons, carbon molecular sieves, carbon nanotubes, template carbon materials, pyrogenic carbons) [49,50], metal-organic frameworks (MOFs) [24], and covalent-organic frameworks (COFs) [51,52]. Conversely, alkaline metal-based sorbents, such as calcium and magnesium oxides (viz. CaO and MgO), which produce an exothermic reaction with CO_2, forming the corresponding carbonate [53] are among the most typical chemisorbents [54]. Lithium-based sorbents (lithium zirconate Li_2ZrO_3 and lithium silicate Li_4SiO_4), sodium and potassium carbonates (Na_2CO_3, K$_2$CO3) are also common sorbents, which undergo similar reversible reactions with CO_2 during the chemical absorption process [32]. The functionalization of solid supports (polymers, silica materials, zeolites, carbons, carbon nanotubes, MOF [55]) with amines is another common strategy to improve the interaction of the sorbent with the CO_2 molecules, via formation of chemical bonds [44,56]. Physical adsorption benefits from high pressure and low temperatures. On the contrary, solid oxide chemisorbents (e.g., CaO, MgO and Li_4SiO_4) are medium- to high-temperature sorbents [54].

Gas adsorption is strongly related to both temperature and pressure conditions of the capture process. More precisely, the adsorption/desorption cycles are performed with alternate variation of pressure and/or temperature, accordingly to a

series of techniques described in the literature [26,38]. In a pressure swing adsorption (PSA) process, adsorption occurs above atmospheric pressure, while desorption is performed by reducing gas pressure [21,30]. In a vacuum swing adsorption (VSA) process, the adsorption is carried out at atmospheric pressure and near-room temperature, while desorption at reduced pressure [38]. In a temperature swing adsorption (TSA) process, the regeneration step requires heating with hot air or steam in order to promote desorption [26,38]. In an electric swing adsorption (ESA) process, during regeneration, a low-voltage is applied to the sorbent and the heating produced by Joule effect causes CO_2 release [26]. Pressure or vacuum and temperature adsorptions (PTSA or VTSA, respectively) are hybrid processes in which the effects of both temperature and pressure are exploited. The Joule effect in ESA produces a localized direct heating of the adsorbents, which makes the process advantageous as compared to TSA and PSA, thanks to the lower required heating and the higher heating rate [38]. PSA process is also considered more efficient and faster than TSA [26]. However, the compression of substantial volumes of N_2 and CO_2 in the flue gas of a real power plant is another issue to be properly managed for PSA processes [42]. Another important factor in the regeneration step is the carrier gas. For a lab-scale experiment, inert gases, such as N_2, Ar or He, are successfully used for CO_2 release, but the high cost makes their practical application unaffordable in real plants for the treatment of huge gas volumes [55]. Steam is a good alternative because it is cheap, available and simple to be separated from CO_2. However, its use introduces other issues like the degradation of the sorbent or the occupation of adsorption sites by water, accounting for the use of a third gas for the release of water vapor, which directly impacts on cost [55].

2.2.3. Cryogenic distillation

In cryogenic separators, CO_2 is liquefied and obtained with very high purity (> 99.95%) from a mixture of N_2 and CO_2; all the other components (gases and particulate) of the flue gas are previously removed [35]. Drawbacks of this approach include the high energy consumption for the refrigeration and the necessity of additional separation processes to remove NO_x, SO_x, H_2O and O_2 from the flue gas before CO_2 removal [35].

2.2.4. Membranes

Membrane separation processes represent a valid alternative to absorption technologies for pre-combustion (CO_2/H_2 separation) and post-combustion

(CO_2/N_2 separation) flue gas treatment, owing to the lower energy consumption and capital investment cost, as well as their remarkable compactness and compatibility with the installation in remote areas [26,36]. The separation ability of the membranes is exercised according to the physical and/or chemical interactions between the different species in the gaseous mixtures and the membrane support, determining the eventual permeation on the basis of the size (kinetics) or affinity (thermodynamic) properties of the permeate [26]. The main features for a high performing membrane are: high CO_2 permeability and CO_2/N_2 selectivity, good thermal and chemical stabilities, high resistance to plasticization and aging, together with effectiveness of manufacturing cost and the possibility of assembly membrane modules with different sizes and shapes [57]. Selective membranes can be ceramic, polymeric, or mixed-matrix membrane, namely polymeric membranes in which inorganic fillers are dispersed in order to improve the selectivity, permeability and to reduce the plasticization of polymeric membranes [22,58,59]. Another category of membranes for CO_2 separation is represented by facilitated transport membranes. Facilitated transport membranes, besides the "solution-diffusion" transport process as for non-facilitated membranes, combine an active transport mechanism by a reversible reaction with a carrier that then diffuses through the membrane driven by a concentration gradient [58]. The release of the permeate and the regeneration of the carrier both occur at the downstream side, due to the lower partial pressure of the permeate [60]. The interaction with a reactive carrier improves both the permeability and the selectivity of the membrane; however, CO_2 permeance and selectivity are reduced by the increase of the feed pressure, conversely to what happens with non-facilitated membranes [58]. Typical facilitated transport membranes are the supported liquid membranes (SLMs), also known as *immobilized liquid membranes*. They are characterized by the presence of a liquid solvent supported onto the surface or inside the pores of the membranes [61]. In gas membrane contactors, the membranes represent an interface between the gas and the liquid (solvent) which chemical absorb CO_2 [58,62]. In details, CO_2 is carried from the gas phase through microporous and hydrophobic membranes, before being absorbed in the liquid phase [62]. They can operate in "non-wetted" or *wetted* modes, depending if pores are filled with gas or liquid, respectively. The former reduces the resistance to gas diffusion of several orders of magnitude [58]. The main advantages of membrane capture approach are the simplicity and low investment cost, the dimensional compactness and the absence of hazardous solvents, which are normally used in absorption technologies [26]. Despite the encouraging opportunities offered by the membrane separation approach, however, the still challenging compromise between permeability and selectivity, short-life

time, plasticization and fouling, currently prevent their large-scale application [28,36]. In addition, the relatively low CO_2 concentration and pressure of the operative conditions of post-combustion process negatively affect the driving force for an efficient separation [28].

2.2.5. Gas hydrates and chemical looping combustion

Gas hydrates are ice-like inclusion compounds, which present polyhedral cages of hydrogen-bonded water, with whom guest molecules can physically interact by means of van der Waals forces [26]. The formation of CO_2 hydrate, as a solid compound made of molecular CO_2 enclathered in crystalline lattices formed by water molecules, is an interesting method for trapping CO_2 from pre-combustion flue gases.

The chemical looping combustion (CLC) involves two reaction steps which occur consecutively and in a cyclic way exploiting metal oxides as solid-state oxygen carriers to burn fossil fuels [63]. The advantages over conventional combustion system is the production of non-hazardous exhausted gas, made up of only CO_2 and water vapor, free of NO_x, and from which CO_2 can be easily separated by condensation of the water vapor [26,63].

2.3.   Carbon dioxide transportation and storage

Carbon dioxide, after being separated from the flue gas, is carried to the storage place. Transport systems are divided into two main groups: onshore and offshore transport. The main solutions for onshore transport are road, railways and pipelines; for offshore transport, instead, pipelines and ships are common methods [64]. Ships are the most reliable means for offshore transport [65], whereas pipelines are mostly effective for onshore transport, especially in the case of high volume of transferred CO_2 and long distances [66]. CO_2 is transported into ships in the liquid phase below ambient temperature and at high pressure, typically at -2 °C and 20 bar [67]. Similarly, CO_2 is preferentially transferred through pipelines in the dense phase (liquid or supercritical state) in order to optimize the mass/volume ratio [65,66]. Supercritical CO_2 is the preferred state, which, in the case of CO_2, means temperature and pressure above 32.1 °C and 72.9 atm, respectively [68]. Accordingly, operative conditions for CO_2 transport in pipelines require temperatures from 13 to 44 °C and a pressure range of 85–150 bar [66]. The presence of impurities in the transferred CO_2 is critical because it affects the boundaries of the single-phase equilibrium of CO_2 and, in the case of water contaminations (above

50 ppm), it can lead to the formation of carbonic acid, which is corrosive for the pipelines [66].

Geological storage is currently considered the most feasible solution for the safe accumulation of the sequestrated CO_2, thanks to the possibility to contain up to tens of million tons of CO_2 [66]. Saline aquifers, enhanced oil recovery (EOR) in depleted oil and gas reservoirs, and unmineable deep coal seams are the most conventional sites exploited for the geological CO_2 sequestration [69]. The requirements for assessing the suitability of a geological site for CO_2 storage account for adapt porosity features, thickness and permeability of the reservoir rock and a safe and stable geological environment; moreover, the distance from the source of CO_2, the storage capacity, the presence of pathways for potential leakage, and the economic feasibility are also crucial for the application. [66]. Alternatively, CO_2 can be stored as solid hydrates. This is a promising technology, although currently at the early stages. CO_2 is injected into the pores of a sediment and stored as hydrates in depleted hydrate reservoirs, deep marine basins, seafloor CO_2 pellet deposition, partially saturated depleted oil and gas reservoirs, as well as deep saline aquifers [69].

2.4.   Technology Readiness Level (TRL) of carbon capture and storage technologies

The Technology Readiness Level (TRL) is a method to define the level of maturity at a present time of a technology process, method or technique, for its use in an operative plant [70]. TRL is based on a nine-unit scale, where level 1 refers to the basic principle establishment and 9 to the successful use of the full system in projected applications (see Figure 2.3) [71]. The review of Bui et al. [72] reports the classification of different technologies regarding carbon capture, transport, storage and utilization on the basis of their TRL (Figure 2.4) [72]. Focusing on CO_2 capture technologies, the authors [72] attributed TRL9 (commercial level) to the pre-combustion natural gas processing and the post-combustion sequestration using aqueous amine-based chemical absorbents. As previously mentioned, the considerable advantage of post-combustion capture over pre-combustion and oxy-combustion processes is the advantage to be retrofitted in existing conventional coal- or gas-fired power plants [73]. At present, solvent-based CO_2 absorption by traditional aqueous amine solutions (e.g., 30 wt.% MEA in water) is the most mature technology [74,75], indeed it is classified as TRL9 in the mentioned evaluation [72]. However, a techno-economic study estimates at 80% (compression costs included) the additional cost in respect to the usual price of electricity due to

the integration of a 30 wt.% MEA absorption process to a coal-fired plant [76]. Moreover, the production of corrosive and harmful degradation compounds, together with the intensive energy penalty due to amine-based sorbents regeneration, hampers the extensive implementation of amine scrubbing processes also from a safety and environmental point of view [77].
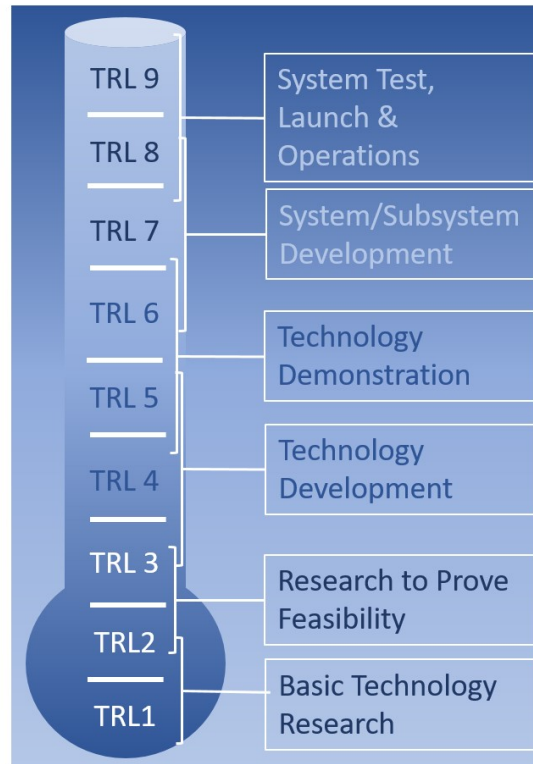
Figure 2.3: Technology Readiness Level (TRL) description. Reprinted and readapted from [71].

Hence, these issues pave the way for the implementation of innovative technologies, which rely on solid adsorbents for CO_2 capture [28,78]. In the referred work dated 2018, post-combustion adsorption was classified as TRL7 (advanced demonstration stage), which means close to the commercialization [72]. The interest on this technology as a promising alternative separation technique is intended to increase, thanks to the advantageous potentiality in reducing the regeneration energy requirement and the easiness of handling dry solid sorbents [21]. As for the CO_2 transport options, ships and pipelines are currently the ones at the commercial level (TRL9). Conversely, regarding carbon storage, the injection of CO_2 for EOR or in saline formation as storage method is classified as TRL9 [72].

Several examples of plants at the commercial, pilot or demonstration levels were mentioned already in 2014, as detailed in the review article by Leung at al. [66]. EOR is also considered as an economically favorable technology, because CO_2 injection facilitates the residual oil and gas extraction from nearly depleted reservoirs and compensate the usual high cost of CCS technologies [66].

Concept	Formulation	Proof of concept (lab tests)	Lab prototype	Lab-scale plant	Pilot plant	Demonstration	Commercial Refinement required	Commercial
TRL1	TRL2	TRL3	TRL4	TRL5	TRL6	TRL7	TRL8	TRL9
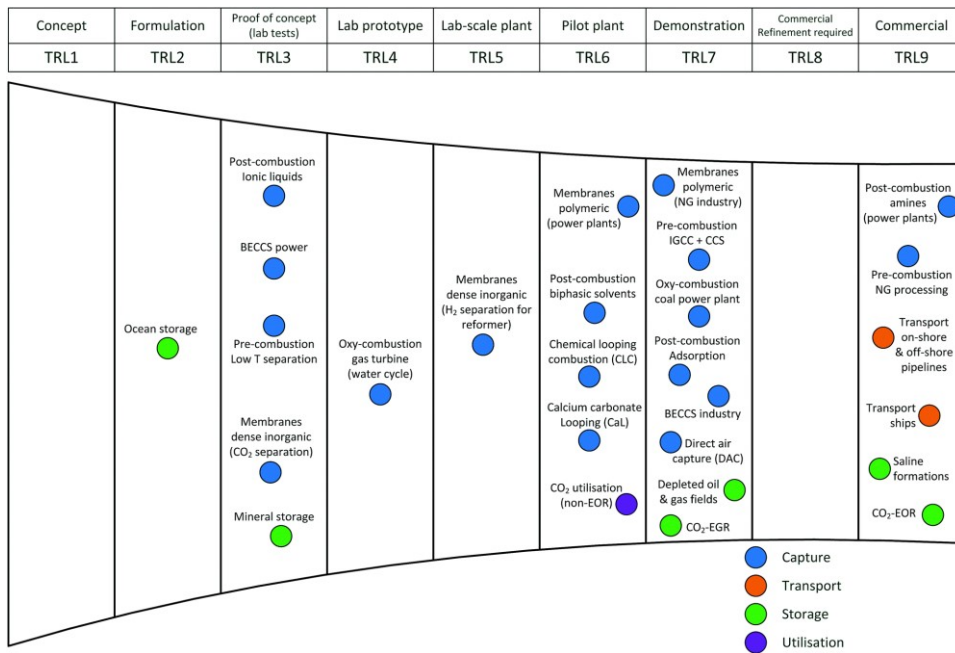
Figure 2.4: Current development progress of carbon capture, storage, transport and utilization technologies on the basis of their of technology readiness level (TRL). Reprinted with permission from [72].

Chapter 3

3. Physical adsorbents for CO$_2$ capture

3.1. Design of ideal physisorbents for CO$_2$ separation from post-combustion flue gas

An adsorption process involves the interaction between gas molecules (adsorbates) attracted by the electronic environment at the surface of a solid (adsorbent), which, driven by the reduction of their free energy, accumulate close to the surface of the solid itself [42]. The adsorption phenomena can be either physical or chemical, depending on the type and binding force of the adsorbent-adsorbate interaction. Physical adsorption is characterized by the occurring of weak intermolecular forces, namely electrostatic interactions or van der Waals forces, whereas chemical adsorption by reversible chemical bonds formation, such as covalent bonds [30,32,44].

Based on the techno-economical evaluation carried out in Paragraph 2.4, hereafter the attention will be focused on physical adsorbents for post-combustion CO$_2$ capture, named as *physisorbents*, with the aim to examine the potentiality and limits of this emerging strategy. The beneficial energy saving for regeneration of sorbents and the coping of safety, environmental and corrosion issues as compared to the traditional amine-based absorption technologies, makes CO$_2$ physisorption by solid sorbents particularly attractive, actually raising the interest towards a real industrial application [79].

The design of an effective adsorbent for CO$_2$ separation from flue gas passes through the following aspects [21,22,30,38,45,46,80,81]:

- ◆ *Adsorption capacity for CO$_2$*

  The equilibrium capacity ($n_{CO2,ads}$) determines the necessary amount of sorbent materials and the volume of the adsorbent vessels, therefore directly affecting the capital cost. It is a common practice referring to the working capacity ($\Delta n_{CO2} = n_{CO2,ads} - n_{CO2,des}$ [82]), which corresponds to the effective

capacity in an adsorption/desorption cycle, rather than to the equilibrium capacity. A reference value of working capacity to be competitive with a MEA-scrubbing process is in the order of 3-4 mmol g^{-1}.

◆ *Selectivity for CO2*
  The selectivity for CO_2 over the other components of the flue gas, mainly N_2 and H_2O, is an important parameter because it influences the efficiency of the process and the purity of the recovered CO_2, which consequently strongly impacts on the transport and storage stages.

◆ *Adsorption/desorption kinetics*
  The adsorption/desorption kinetics controls the working cycle time and the required sorbent amount.

◆ *Regeneration of sorbents*
  The feasibility and affordability of a process are strongly related to the easiness and effectiveness of the regeneration, precisely, low energy consumption for desorption and complete restoration of the initial adsorption capacity. Sorbents regenerability (R (%) = $\Delta n_{CO2}/ \Delta n_{CO2,ads}$ x 100 [82]) is highly related to the isosteric heat of adsorption and the Henry's law constant (see Paragraphs 3.3.1 and 3.3.2), two crucial parameters for evaluating the strength of the CO_2/adsorbent interaction.

◆ *Mechanical, thermal and chemical stabilities*
  Good mechanical, thermal and chemical stabilities guarantee high durability after several working cycles and contrast a frequent sorbent replacement.

◆ *Tolerance towards contaminants*
  Tolerance towards contaminants (e.g., SO_2, NO_x, Hg) and moisture is essential for keeping repetitive working cycles stable.

◆ *Low operational and sorbent costs*
  The energy consumption of an adsorption process originates mainly from the compression of the gas before entering the adsorption column and the final desorption stage. A CO_2 adsorption process is considered economically affordable if the sorbent cost is around 10 $ kg^{-1}.

3.2.   General mechanisms of physical CO_2 adsorption

At low CO_2 partial pressure conditions, that is below 0.2 bar, as for the post-combustion flue gas, the interplay between adsorbent and adsorbate is predominant in respect to the adsorbate-adsorbate interaction, conversely to what occurs for feeds with high CO_2 partial pressure [78]. The proper design of the pore architecture and the control of the chemical surface properties are the most used approaches for fostering a selective CO_2-adsorbent design. Indeed, it is generally agreed that micropores (< 2 nm) and, particularly, ultramicropores (< 0.7 nm) are effective in boosting both CO_2 adsorption capacity and selectivity, because of the enhanced adsorption potential in very small pores as compared to supermicropores (0.7−2 nm) or mesopores (> 2 nm) [78,83–85]. Three main mechanisms were identified at the basis of the selective interaction between adsorbent and adsorbate, namely thermodynamic or equilibrium principle, kinetics effect, and molecular sieving effect. They are commonly exploited to achieve the crucial target of selectivity for CO_2 adsorption over the other bulk components of the flue gas mixture.

3.2.1. Thermodynamic principle

Thermodynamic separation operates through characteristic interactions among the different components of a mixture on the basis of polarizability, permanent dipole moment, quadrupole moment, and magnetic susceptibility [86]. Suitable functionalization, such as the introduction of polar functional groups, polar atoms or extra-framework ions, can strongly increase the adsorption potential of the sorbent, and thus the interaction with the target molecule [49,78]. N_2 is the most abundant component of post-combustion flue gases [24,25], therefore it is extremely necessary studying the CO_2 over N_2 selectivity while assessing a suitability of a sorbent. CO_2 and N_2 are both linear symmetric molecules, with no net dipolar moment; however, the C=O polar bonds of the CO_2 molecule provides a higher dipole moment ($13.4 \ 10^{-40} \ cm^2$), in respect to the N_2 molecule ($4.7 \ 10^{-40} \ cm^2$), which means a stronger interaction with the polar sites at the surface of the adsorbent and, thus, its preferential adsorption [49]. However, in the presence of moisture, CO_2 adsorption capacity and selectivity is severely threaten. Indeed, if the mechanism of adsorption is based only on electrostatic interactions water molecules would be preferentially adsorbed, as they possess a dipole moment, while CO_2 possesses only a quadrupole moment [49].

3.2.2. Kinetics principle

The kinetics of diffusion is another aspect that plays an important role in determining the selectivity. The diffusivity of a gas species inside the voids of a porous sorbent is influenced by its effective kinetic diameter. Conversely to what occurs in the gas phase, CO_2 has a smaller effective kinetic diameter (3.3 Å) in a porous sorbent than the N_2 molecule (3.6 Å) [48]. Therefore, N_2 diffusivity can be strongly reduced as compared to CO_2 when the pore size approaches the N_2 kinetic diameter; as a result, CO_2 reaches the adsorption sites before N_2 and it is preferentially adsorbed [48,86].

3.2.3. Molecular sieving effect

Likewise, the size and the shape of a molecule can also determine the selectivity for a specific component of a mixture accordingly to the "molecular sieving effect" [86]. The components of the mixture with a kinetic diameter smaller than the pore size of the material are allowed to penetrate, thus being adsorbed, the others are excluded [86]. For adsorbents characterized by such pore features, CO_2/N_2 selectivity is therefore possible thanks to the difference in the kinetic diameter between CO_2 and N_2 [49]. Conversely, in the case of wet flue gases, the problem of competitive adsorption between CO_2 and H_2O persists for "molecular sieves", since water molecule kinetic diameter (2.65 Å) is smaller than the one of CO_2 [78].

3.3.   Assessment of adsorbent-adsorbate interaction and selectivity

3.3.1. Isosteric enthalpy of adsorption (ΔH_{ads})

The isosteric enthalpy of adsorption (ΔH_{ads}) is a quantity, which is commonly used to estimate the binding force of the interaction between the adsorbate, CO_2 in this case, and the surface of the solid sorbent. ΔH_{ads} can be calculated by using a calorimetric-volumetric approach, thus directly measuring the heat released during the adsorption with a calorimeter. Another possibility consist in opting to an indirect approach, that is through experimental isotherms obtained at a minimum of two different but close temperatures ($\Delta T \approx 10\text{-}20$ K), or, preferentially, from three isotherms with $\Delta T \approx 10$ K [87]. The indirect approach is the most widely used because of the higher availability in common laboratories of equipment for volumetric gas adsorption measurements rather than calorimetric equipment. Since the heat of adsorption varies with the surface coverage, it is common to refer to the

isosteric heat of adsorption, which is the heat released at the same surface coverage, i.e. at the same gas uptake. The pressure, which corresponds to the same surface coverage at the different measured temperatures, is determined from surface coverage *vs.* pressure plots [88]. Using these values of pressure, it is possible to construct the Arrhenius plot (i.e., $\ln p$ *vs.* $1/T$) from the integrated form of the Clausius-Clapeyron equation [87] (Equation 3.1)

$$\ln \frac{p_2}{p_1} = \frac{\Delta H_{ads}}{R} \left(\frac{1}{T_2} - \frac{1}{T_1}\right) \qquad\qquad \text{(Eq. 3.1)}$$

From the slope of the Arrhenius plot, ΔH_{ads} is derived [88]; R (8.314 J mol^{-1} K^{-1}) is the universal gas constant. A desirable value of the ΔH_{ads} lays in the range 30−50 kJ mol^{-1}, which corresponds to an intermediate value amongst an effective interaction and an easy desorption [49].

3.3.2. Henry's law constant (K_H)

The affinity of CO_2 for the adsorbent surface can also be estimated by the Henry's law constant (K_H). K_H (mmol g^{-1} kPa^{-1}) is calculated from pure CO_2 adsorption isotherms in the limit of zero coverage using the virial isotherm model (Equation 3.2) [89]:

$$p = \frac{n_{ads}}{K_H} exp(C_1 n_{ads} + C_2 n_{ads}^2 + C_3 n_{ads}^3) \qquad\qquad \text{(Eq. 3.2)}$$

where n_{ads} is the quantity of adsorbed species and C_1, C_2 and C_3 are the virial coefficients.

3.3.3. Methods of selectivity determination

The ideal adsorption solution theory (IAST) is the most widely used method for estimating the separation performance of an adsorbent from single-gas adsorption isotherms [78]. In this Paragraph, it is referred to CO_2/N_2 selectivity, due to the typical composition of a post-combustion flue gas. However, this method can be used for calculating the selectivity in respect to other compositions. The basic assumption of the IAST theory is that the adsorbate is an ideal solution in equilibrium with the gas phase; then, CO_2/N_2 selectivity is established from the equilibrium adsorption capacity at a given pressure and temperature from single CO_2 and N_2 adsorption experiments [78]. IAST selectivity therefore (S_{IAST}) is calculated according to Equation 3.3 [90]:

$$S_{IAST} = \frac{x_{CO2}/x_{N2}}{y_{CO2}/y_{N2}} \qquad\qquad\qquad\qquad \text{(Eq. 3.3)}$$

where x_{CO2} and x_{N2} are the molar fraction of adsorbed CO_2 and N_2 respectively, and y_{CO2} and y_{N2} are the molar fractions of CO_2 and N_2 in the gas phase for the chosen composition.

Alternatively, another method for estimating the CO_2/N_2 selectivity from single-component isotherms is the Henry's law selectivity, calculated as the ratio between the CO_2 and N_2 Henry's law constants, $K_H(CO_2)$ and $K_H(N_2)$, respectively, obtained in the low-pressure and low-surface coverage region, according to Equation 3.4 [78]:

$$S_H = \frac{K_H(CO_2)}{K_H(N_2)} \qquad\qquad\qquad\qquad\qquad \text{(Eq. 3.4)}$$

CO_2/N_2 selectivity is also calculated from the ration of the initial slopes (IS) of the single-component CO_2 and N_2 adsorption isotherms (see references [91–95]).

Actually, although the advantageous simplicity of the described models for learning information about the selectivity of sorbents from single-component isotherms, a reliable evaluation of the separation ability passes through gas mixture measurements, because single component measurements rely on equilibrium adsorption results, whereas real separation processes are conducted under kinetic conditions [49,96]. In this regard, lab-scale mixed-gas experiments can be carried out by breakthrough experiments in fix-bed reactors [49,78] or thermogravimetic analysis [97–99]. In a fix-bed reactor, the gas mixture, with a specific composition defined by the respective flow rate, is flown through the column where the adsorbent powders are packed and kept at a controlled temperature [49]. The gas composition at the exit of the reactor is measured by gas chromatography or mass spectrometry and the amount of adsorbed gas of the species i (q_i, cm^3 g^{-1}) can be calculated accordingly to Equation 3.5 [49,78]:

$$q_i = \frac{F_{in,i} \cdot t - V_{dead} - \int_0^t F_{out,i}\, dt}{m} \qquad\qquad \text{(Eq. 3.5)}$$

where t is the adsorption time (min), $F_{in,i}$ the inlet flow rate of the specific gas (cm^3 min^{-1}), $F_{out,i}$ the outlet flow rate of the specific gas (cm^3 min^{-1}), V_{dead} is the dead volume of the adsorption system (cm^3), and m the mass of the adsorbent (m).

Once the amount of adsorbed gases are calculated (q_{CO2} and q_{N2}), the CO_2/N_2 selectivity from a breakthrough experiment can be calculated from Equation 3.6:

$$S_{BT} = \frac{q_{CO2}}{y_{CO2}} \cdot \frac{q_{N2}}{y_{N2}} \qquad\qquad\qquad\qquad \text{(Eq. 3.6)}$$

where y_{CO2} and y_{N2} are the molar fraction of CO_2 and N_2 in the gas phase for the chosen composition.

3.4. Physisorbents for selective CO₂ capture

3.4.1. Zeolites

Described for the first time in 1756 by the Swedish mineralogist Axel F. Cronstedt [100], zeolites are microporous inorganic crystalline materials, the framework of which is built by four-connected TO_4 tetrahedra (T stands for tetrahedrally coordinated Si, Al, or P, etc.), linked to each other by sharing their vertex oxygen atom [101]. Zeolites are usually aluminosilicates of elements form IA and IIA groups (i.e., Na, K, Mg, Ca), composed by four-connected frameworks of $[AlO_4]^{5-}$ and $[SiO_4]^{4-}$ tetrahedra [102]. The difference in the oxidation state between Al(III) and Si(IV) generates a negative charge, which is compensated by an extra-framework cation [48]. Hydrate zeolites are described by the chemical formula in Equation 3.7:

$$M_{2/n}O \cdot Al_2O_3 \cdot ySiO_2 \cdot wH_2O \qquad\qquad \text{(Eq. 3.7)}$$

where M is the extra-framework cation with n valence, y varies between 2 and 200, and w represents the number of moles of water molecules [102].

The tetrahedral blocks are organized in 6-rings, 8-rings, 12-rings or more secondary building units, forming cages or cylinders, which constitute the pore network of the specific zeolite structure [103]. Zeolites are largely exploited for gas adsorption and separation, thanks to their high surface area and interconnected and regular porosity, distributed in the size range within 0.3−1.0 nm, and characterized by pore volumes from 0.10 to 0.35 $cm^3 g^{-1}$ [102]. There is a wide variety of natural or artificial zeolites, and every year new materials are added to the database of zeolite structures by the Structure Commission of the International Zeolite Association (IZA). A useful classification of the different types of zeolites relies on their pore size. Small-pore zeolites (such as Zeolite A, CHA, RHO) are characterized by 8 atoms (8-rings) in tetrahedral coordination and their pore size is in the range of 0.30− 0.45 nm; medium-pore size zeolites (e.g. ZSM-5) are characterized by 10-rings with pore size of 0.45− 0.60 nm; large-pore zeolites (Zeolite X, Y) are composed by 12-rings of 0.60 − 0.80 nm size and extra-large ore zeolites with >12-ring pores (e.g., UTD-1) [102,104,105]. Some examples of zeolite structures are shown in Figure 3.1.
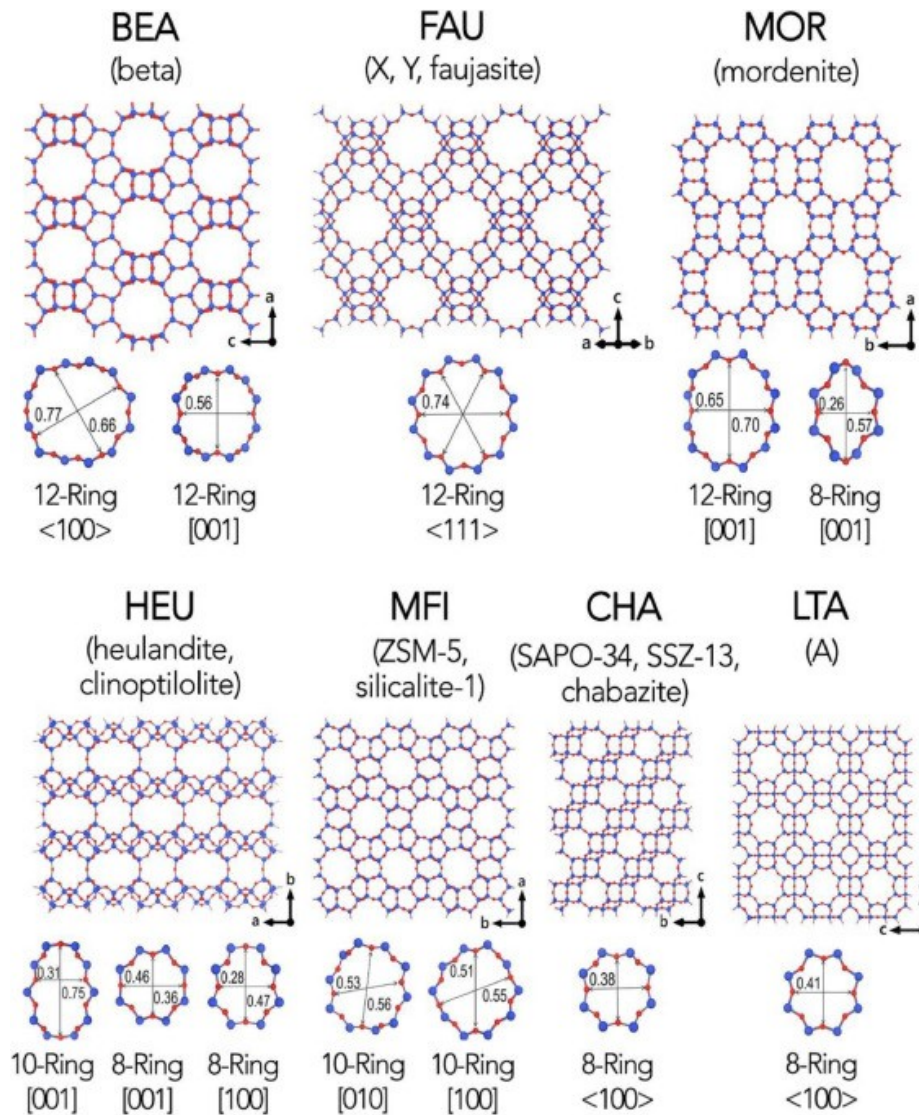
Figure 3.1: Common zeolite frameworks. The different structures are named with the three-letters code assigned by the International Zeolite Association (in bold) and the framework type (in brackets). Reprinted with permission from [106].

The crucial aspect of small-pore zeolites, such as KFI, CHA and LTA is that their pore opening is very close to the kinetic diameters of CO_2, N_2 and CH_4, hence an increased selectivity is supposed to derive from the resultant molecular sieving effect [107]. Other admission mechanisms controlled by external stimuli (such as light, heat or electrical fields) besides the mere steric mechanism, is experienced for a selection of microporous sorbents, essentially of the zeolite and MOF family [108]. Particularly, Shang at al., in their work dated 2012 [109] named for the first time as "molecular trapdoor mechanism" the peculiar ability of gas discrimination

performed by opportunely modified chabazites (CHA) exchanged with cations such as Cs^+ or K^+ that reside at the center of the 8-membered ring pore cavity [109,110]. These extra-framework cations are defined by the authors as "door-keeping", because, according to the temperature conditions, they allow or block the guest molecules to access the internal cavities [111]. This peculiar property is particularly interesting for gas separation, because the components of a mixture that have a higher interaction ability with the door-keeping ion, such as to induce its temporary and reversible deviation from the center of the 8-membered ring cavity, can access and therefore been selectively adsorbed [109]. In the specific case of CO_2 separation, the higher dipole moment in respect to two common competitive gases, such as CH_4 and N_2, makes CO_2 able to interact strongly with the energy potential of the door-keeping cation, lowering the energy barrier for the movement of the ion from its equilibrium position at the center of the 8-membered ring [112]. On the contrary, N_2 and CH_4 are not able to interact with the cation and their admission is allowed only at a temperatures higher than a critical temperature, when the thermal energy is responsible for the deviation of the cation from its position at the center of the 8-membered ring cavity [109]. In another subsequent work, the authors obtained a remarkable high selectivity achieved from a multicomponent equilibrium adsorption experiment in a mixture composed by (50:50, v/v) CO_2/N_2 at 75 °C and 1 bar, within the temperature range typical of post-combustion flue gas (40 − 90 °C) exploiting the molecular trapdoor by a fly-ash derived potassium chabazite with Si/Al = 1.9 [113].

However, despite the enhanced selectivity achieved by small-pore zeolites, their penalty consists in the slow kinetics owing to the reduced diffusivity throughout the narrow porosity; on the contrary, large pore zeolites show higher adsorption capacity and faster kinetics, but poor selectivity [114]. Khoramzadeh *et al.* [115] carried out a thorough comparison of various types of zeolites characterized by different pore size: 13X (NaX), 4A (NaA), 5A (CaA) and beta. The large-pore zeolite 13X showed the highest CO_2 adsorption capacity (4.6 – 5.9 mmol g^{-1} at 1.6 bar in the temperature range 10 − 50 °C) and the highest selectivity in the high pressure regime (1646 predicted by the IAST model at 10 °C and 1 bar), owing to the highest surface area and pore volume in respect to the other examined types of zeolites [115]. The small-pore zeolite 4A showed the highest selectivity at low pressure (602 predicted by IAST at 10 °C and 0.2 bar), because the stronger interaction between adsorbate and adsorbent occurring in small pores is particularly beneficial in the low pressure regime [115]. The zeolite beta studied in the mentioned work was the less selective, independently from the temperature and pressure conditions [115]. To be thorough, the performance of several types of

zeolite sorbents regarding CO_2 capture and CO_2/N_2 selectivity were summarized in Table 3.1. As it can be deduced from the data in Table 3.1, in cation-rich zeolites, such as zeolite X ($1 < Si/Al < 1.5$ [116]), the CO_2 adsorption capacity is remarkably high, benefitting from the enhanced interaction between the charge distribution of CO_2 and the cation-induced internal electrical field gradient [117]. On the other hand, the electrophilic character of CO_2 promotes the interaction with the partial negative charge of the lattice oxygen atoms, which is directly proportional to the Al content [118]. Therefore, the reduced hydrophilic character of cation-poor zeolites (e.g., zeolite Y, $Si/Al > 1.5$ [116]) can provide advantages in CO_2 separation, particularly from wet flue gases [117,119]. For in depth details and comprehensive overview on zeolite adsorbents applied for CO_2 capture, the review articles of Kumar *et al.* [120] and Chatterjee *et al.* are recommended [121].

Table 3.1: Comparison of the performances in terms of CO_2 adsorption capacity and CO_2/N_2 separation of several types of zeolite adsorbents from representative literature reports.

Zeolite types[REF]	CO_2 capacity[a] mmol g^{-1}	CO_2/N_2 selectivity [b]	T_{ads}[c] °C	P_{ads}[d] bar
NaA or 4A (LTA)[115]	2.22	625.4 (CO_2:N_2=0.6:0.4)	30	0.2
CaA or 5A (LTA)[122]	3.72	250[a] (CO_2:N_2=0.15:0.75)	40	0.15
KCHA (CHA)[113]	0.81	688.8[a] (CO_2:N_2=0.5:0.5)	75	1
ZSM-5[123]	2.15	57 (CO_2:N_2=0.15:0.85)	25	1
NaX or 13X (FAU)[115]	4.46	850.8 (CO_2:N_2=0.6:0.4)	30	1
NaX or 13X (FAU)[124]	6.1	/	25	1.01
Zeolite-Y (FAU)[125]	5.40	850.8 (CO_2:N_2=0.15:0.85)	25	1.01
Beta (BEA)[126]	4.1	/	25	1

[a]CO_2 adsorption capacity measured in 100% CO_2 atmosphere, [b]CO_2/N_2 selectivity calculated via IAST model, [c]adsorption temperature; [d]adsorption pressure.

3.4.2. Metal-organic frameworks (MOFs)

Metal-organic frameworks (MOFs) are organic-inorganic hybrid porous crystalline solids composed of inorganic polyatomic metal-containing clusters, (also called secondary building units, SBUs), linked by rigid organic linkers (Figure 3.2) [127–129].
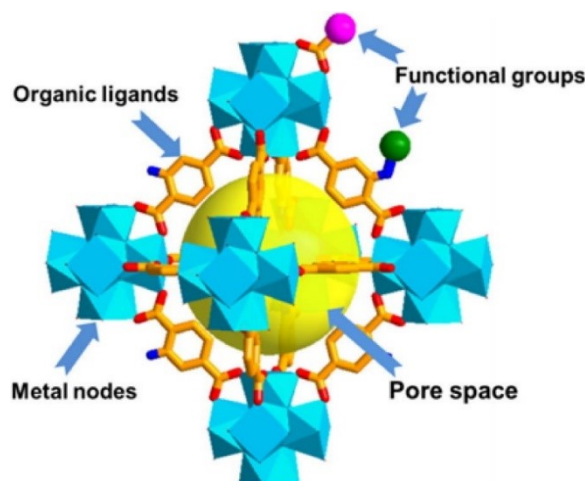
Figure 3.2: Schematic representation of the basic structural unit of MOFs. Reprinted with permission from [129].

MOFs possess some peculiar features, which make them particularly interesting for gas sequestration. First of all, it is worth mentioning the incomparable obtainable high surface typically ranging from 1000 to 10000 $m^2\,g^{-1}$ [129]. Precisely, the limit of MOFs theoretical surface area was established at $\sim$14600 $m^2\,g^{-1}$ [130]). Additionally, the peculiar possibility to tailor MOFs structure by introducing accessible unsaturated metal sites, heteroatoms, covalently linked functionality, and establishing specific interactions with the adsorbate allow to adapt and improve enormously the adsorptive properties of this type of materials [131]. The selectivity for CO_2 adsorption in rigid MOFs occurs on the basis of the typical mechanisms of physisorption, e.g. molecular sieving effect, surface/adsorbate interactions or a combination of them [132]. Another interesting peculiarity of some MOFs is a characteristic flexible structure, related to local movements of the organic ligands, which allows a reversible transformation in their framework as a consequence of an external stimuli, such as temperature, mechanical constrain, guest adsorption, light exposure and so on [133,134]. The so-called *breathing effect* is related to a sizeable variation of the unit cell volume, with the change from closed (c_p) or narrow pores (n_p) to large pores (l_p), owing to the

interaction with guest molecules [132,135]. The so-called *gate opening/closing effect*, that is the opening of closed porosities or even the generation of apertures in non-porous MOFs because of the external stimuli, is governed by the differential guest/host interaction strength, according to which some molecules pass through, whereas some others are blocked [132]. Several literature works report the exploitation of the *breathing effect* in flexible MOFs as an expedient to increase adsorbents' selective CO_2 capture [136–143].

Another original strategy for the size-selective CO_2 capture is described by the work of Yang *et al.* [144], where the embedding of ordered rotary groups into the ultramicropores of the MOF sorbent was carried out for varying the channel size and hence achieving the steric separation of the different components in a gas mixture. Indeed, a CO_2 uptake of 4.56 mmol g^{-1} at 25 °C and 1 bar and IAST selectivity of 355 and 136, for (15:85, v/v) CO_2/N_2 and (50:50, v/v) CO_2/CH_4 mixture, respectively, at 1 bar and 25 °C, were obtained [144].

Metal-organic polyhedra (MOP), as supermolecular building blocks (SBBs), are explored for the construction of metal-organic materials with outstanding performance in gas adsorption [145,146]. Liu *et al.* [147] realized a polyhedron-based metal-organic framework (PMOF), with a high density of both open metal and Lewis basic sites, which show a CO_2 adsorption capacity at 1.01 bar of 185 cm³ g^{-1} (8.2 mmol g^{-1}) and 104 cm³ g^{-1} (4.6 mmol g^{-1}) at 0 °C and 25 °C, respectively. Analogously, using a pure supermolecular-linker approach, Song *et al.* [148] obtained a MOF with considerable IAST selectivity in (15:85, v/v) CO_2/N_2 and (50:50, v/v) CO_2/CH_4 mixtures equal to 581 and 13.5, respectively, combined by a high CO_2 uptake of 5.3 mmol g^{-1} at 25 °C and 1.01 bar. The enhanced adsorption performances are attributed to the improved interaction between the CO_2 molecules and the pore surface, thanks to the presence of open metal sites, amide groups and chloride/monodentate hydroxide [148].

Finally, the works of Wen *et al.* [149] and Li *et al.* [150] are relevant for CO_2 uptake at low pressure (0.15 bar). In particular, in the former work, a CO_2 uptake of 3.56 mmol g^{-1} at 23 °C and IAST selectivity of ~600 and 100 for (15:85, v/v) CO_2/N_2 and (50:50, v/v) CO_2/CH_4 mixtures, respectively, were achieved [149]. The latter reports a CO_2 adsorption capacity of 4.21 mmol g^{-1} and a breakthrough selectivity of 75 at 25 °C in a binary gas mixture of (15:85, v/v) CO_2/N_2 [150]. For the courtesy of the reader, the performances in terms of CO_2 adsorption and CO_2/N_2 separation of the cited examples of MOFs adsorbents are summarized in Table 3.2.

Table 3.2: Comparison of the performances in terms of CO_2 adsorption capacity and CO_2/N_2 separation of several examples of MOF adsorbents from representative literature reports

MOF types[REF]	CO_2 capacity[a] mmol g^{-1}	CO_2/N_2 selectivity	T_{ads}[d] °C	P_{ads}[e] bar
ZU-66[144]	4.56 (100% CO_2)	355[b] (CO_2:N_2=0.15:0.85)	25	1
JLU-Liu46[147]	4.6 (100% CO_2)	42[b] (CO_2:N_2=0.15:0.85)	25	1.01
NJU-Bai52[148]	5.30 (100% CO_2)	581[b] (CO_2:N_2=0.15:0.85)	25	1
UTSA-120[149]	3.56 (100% CO_2)	~600[b] (CO_2:N_2=0.15:0.85)	23	0.15
MIL-101(Cr)[150]	4.21 (100% CO_2)	~75[c] (CO_2:N_2=0.15:0.85)	25	0.15

[a]CO_2 adsorption capacity measured in 100% CO_2 atmosphere, [b]CO_2/N_2 selectivity calculated via IAST model; [c]CO_2/N_2 selectivity calculated via breakthrough experiments; [d]adsorption temperature; [e]adsorption pressure.

Besides the separation ability from CO_2/N_2 or CO_2/CH_4 mixtures, the structural stability under humid conditions and the competitive adsorption between CO_2 and H_2O require to be carefully taken into consideration [151,152]. Therefore, several research works focused on the development of water-tolerant and CO_2/H_2O selective sorbents for CO_2 separation from wet flue gases [151–155]. However, for a more deepen analysis of the synthesis and design procedure of MOF, as adsorbents and their application in gas separation, the readers may refer the following recent and detailed review articles [128,132,156–159].

3.4.3. Covalent-organic frameworks (COFs)

Another type of porous organic frameworks is represented by covalent-organic frameworks (COFs). Synthesized for the first time in 2005 by Yaghi and co-workers [160], COFs are crystalline, extended solids having fully organic structures in which the building units are linked by strong covalent bonds, such as C−C, C−N, C−O, B−O, and C−Si [161]. They possess similar features compared to MOFs as regards gas storage and separation, such as high selectivity, porosity and structural tunability, and low regeneration energy [52,159]. In addition, the purely covalently

bonded and metal-free structures lend COFs a higher chemical resistance (in organic solvents and in acid or basic conditions) and thermal stability than MOFs, which are conversely based on coordinative bonds [162]. Moreover, the low density derived from the light constituting elements (i.e., H, B, C, N and O) represent further potential advantages [52,159].

However, the chemical and hydrolytic stability remain an arduous challenge in COFs. The enhancement of the hydrophobic character via functionalization with long-chain alkyl or fluorine group are some exploited strategies for improving the stability under wet condition [159]. For a more in depth analysis of water adsorption behavior on chemically stable COFs and their role on the CO_2 capture performances, the work of Ge and co-workers is highly recommended [163].

Among the most common COF structures, triazine-based and imine-based COFs are more chemically and hydrolytically stable, thus promising in CO_2 uptake than boron-based COFs [161]. In this regards, it is worth mentioning the work of Zhao et al. [164] where the incorporation of fluorine by means of strongly polar C−F bonds in the covalent triazine-based framework (CTF) enhanced simultaneously CO_2 adsorption, CO_2/N_2 selectivity and water tolerability, by the increase of the electrostatic interaction, ultramicroporosity content and hydrophobicity, respectively. The properly designed and synthesized perfluorinated covalent triazine-based framework improved the adsorption performances in comparison to the basic CTF sample, achieving a CO_2 uptake of 0.92 and 3.21 mmol g^{-1} at 25 °C and under low-pressure (0.1 bar) and atmospheric pressure (1b bar) regimes, respectively, together with a remarkable breakthrough selectivity of 77 in (10:90, v/v) CO_2/N_2 mixtures [164].

3.4.4. Carbonaceous adsorbents

Carbonaceous adsorbents are mainly based on carbon atoms in different that give rise to a numerous kind of materials, such as carbon allotropes (carbon nanotubes - CNTs, graphene and fullerenes), activated carbons (ACs), biomass-derived carbons, pyrogenic carbons, templated carbons, carbon molecular sieves, carbon aerogels, carbon nanofibers, etc. [165]. Among the plentiful variety of solid adsorbents, carbon materials overachieve the other non-carbonaceous sorbents for their extraordinary tunable chemical properties (e.g., bond hybridization and surface chemistry) and structural features (e.g., porosity and morphology) [166]. As for any adsorption process, the low CO_2 selectivity in gas mixtures is a critical aspect to be taken in consideration and the design of the pore architecture and the adjustment of the surface properties are the commonly exploited strategies for promoting a selective CO_2 adsorption in carbon materials [30]. Precisely, a method

for tailoring the surface properties is the incorporation of heteroatoms in the carbon framework via post-modification methods or, preferentially, via the direct carbonization of nitrogen-containing precursors, whereas the porosity can be tuned by template-assisted synthesis or activation treatments [167]. More detailed description of the role of pore structure and surface chemistry on CO_2 adsorption and selectivity on CO_2 capture by carbonaceous adsorbents is detailed in the followings:

- ◆ *Role of pore structure*
  As already discussed in Paragraph 3.2, the interaction energy between non-polar adsorbate molecules and non-functionalized adsorbent surfaces originates from short-range attractive and long range repulsive forces; the attractive interaction energy is considerably enhanced in narrow pores, owing to the reduced distance between neighbouring walls that causes the overlapping of the potential fields [168]. Precisely, pores with diameters < 0.8 nm and < 0.5 nm are known for enhancing CO_2 adsorption at higher (1 bar) and lower (0.1 bar) partial pressures, respectively [169]. On the other hand, it is fair to underline that the adsorption rate in microporous carbons is considerably reduced by high mass-transfer resistance; as it will be described in the following Paragraphs, this issue can be solved by introducing some content of meso- and macroporosity or a hierarchical pore structure for effectively improving gas diffusion and mass transfer [169,170].

- ◆ *Role of surface chemistry*
  The incorporation of heteroatoms (e.g., N, O, S, B, and P) of different electronegativity as compared to the C atoms in the carbon framework is a common method for modifying the electron cloud density around the carbon skeleton, and therefore for tuning the interaction with the CO_2 molecules [168]. The surface of pristine carbon has an intrinsic basic character originated by delocalized electrons in the basal plane of the graphene sheets from the π electrons of the double bonds [170]. Nitrogen is the most typical heteroatom incorporated in the carbon framework for increasing the strength of the interaction with CO_2 molecules, indeed higher adsorption energies and CO_2/N_2 selectivity are usually experienced after N incorporation [167]. N-containing groups can increase the interaction mainly through three types of interactions: acid-base, electrostatic (quadrupole), and hydrogen-bonding [168]. The acid-base interaction occurs between the electron-deficient C atom of the CO_2 molecule (weak Lewis acid) and the intercalated negatively

charged N atoms (Lewis base) [168,171]. The electrostatic (quadrupole) interaction occurs because of the interaction between the electric quadrupole moment of CO_2, that arises from the strong dipolar C=O bonds, and the high electrostatic potential induced by the incorporation of the N-containing species [168,169]. The incorporation of N atoms into the carbon framework enhances the adsorbate-adsorbent interaction also by promoting the hydrogen bonding formation between the electronegative O atom of the CO_2 molecule and hydrogen atoms from CH and NH groups on the carbon surface (N− H···O) [168,169]. Among the N species that are usually incorporated in the carbon framework (such as pyrydinic, pyridonic, pyrrolic, graphitic or quaternary, amine, nitro, and nitroso species, see Figure 3.3), pyridine and pyridone nitrogen contribute more effectively to CO_2 adsorption. Pyridinic N, in particular, is the most crucial one because it strongly interacts with CO_2 by acid-base interactions [170]. The strengthening and stabilization of adsorbed CO_2 at the carbon surface played by the incorporated N species positively affects also CO_2/N_2 selectivity [170]. O-containing functional groups, such as carbonyl- and hydroxyl moieties, also enhance CO_2 adsorption, owing to the electron densities surrounding O atoms of these functional groups [168]. For a more detailed analysis of the role of the different O- and N-functional groups in CO_2 adsorption, the review paper of Petrovic et al. is recommended [171].
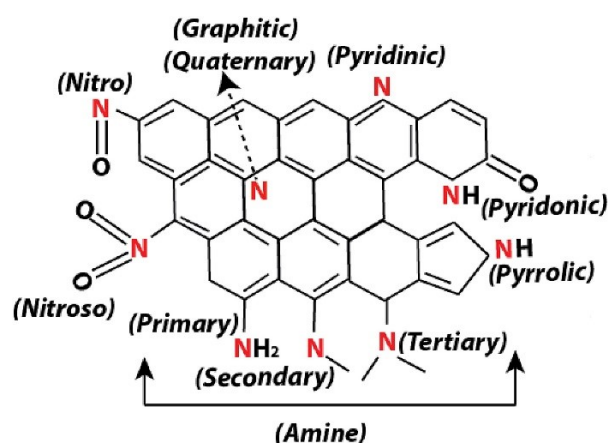
Figure 3.3: Schematic representation of the different types of nitrogen functionalities formed by N atoms incorporation in carbon frameworks. Reprinted with permission from [170].

Hence, the extraordinary easiness of properly tailoring the carbon-based sorbents properties allow to obtain high specific surface area, high porosity,

favorable regenerative conditions, good electronic properties, and, consequently, remarkable gas storage performances [165]. Furthermore, carbonaceous adsorbents are particularly attractive for realistic application thanks to their low-cost, chemical and thermal stability [172,173]. In general, the low-cost is an advantage of carbons as compared to other adsorbents. However, the cost-effectiveness of the whole sorption process is strictly related to the sorbent production process; for instance, the use of biomass as cheap carbon feedstock is a strategy for reducing sorbents cost, along with the choice of simple synthesis procedures. In addition, pristine carbons are intrinsically hydrophobic, so in principle, their capture efficiency is not sensitively influenced by the presence of moisture in the flue gas mixture [172,173].

Nonetheless, as mentioned above, oxygen- and nitrogen-based functional groups increase the polarity of the carbon framework, thus providing some degree of hydrophilicity at the carbon surface [170]. Hence, this aspect cannot be neglected in the case of CO_2 adsorption from moisture-containing flue gases. For instance, it was found that pyridinic and pyridonic N suffer the most drastic reduction in CO_2 uptake in the presence of moisture [170]. Table 3.3 summarizes the CO_2 adsorption capacity and CO_2/N_2 separation of different categories of carbonaceous adsorbents.

Table 3.3: Comparison of the performances in terms of CO_2 adsorption capacity and CO_2/N_2 separation of several examples of carbonaceous adsorbents from representative literature reports

Carbonaceous adsorbent [REF]	CO_2 capacity[a] mmol g^{-1}	CO_2/N_2 selectivity	T_{ads}[e] °C	P_{ads}[f] bar
Activated carbon[174]	3.05 (100% CO_2)	10.59[b] (CO_2:N_2=0.15:0.85)	25	1
Biochar[175]	/ (100% CO_2)	2.8[c] (CO_2:N_2=0.30:0.70)	30	1
Graphene[176]	4.21 (100% CO_2)	107−50[c] (CO_2:N_2=0.15:0.85)	25	1
Carbon nanofibers[177]	3.11 (100% CO_2)	20[d] (CO_2:N_2=0.5:0.5)	25	1
N-doped porous carbon[178]	8.3 (100% CO_2)	67 (CO_2:N_2=0.15:0.85)	0	1

[a]CO_2 adsorption capacity measured in 100% CO_2 atmosphere, [b]CO_2/N_2 selectivity calculated via IAST model; [c]CO_2/N_2 selectivity calculated via breakthrough experiments; [d]CO_2/N_2 selectivity calculated via TGA experiments as (S=n_{CO2}/ n_{N2}); [e]adsorption temperature; [f]adsorption pressure.

3.4.4.1.   Activated carbons (ACs)

In the past decades, commercial activated carbons (ACs) were largely produced from fossil sources, such as coal and petroleum coke; however, fossil fuel depletion and the natural presence of mineral contaminants in coal encouraged the use of biomass as sustainable carbon feedstock [167,173]. Naturally occurring, cheap, renewable and abundant lignocellulose-based biomasses are collected from agricultural or forest residues and transformed into renewable precursors for the realization of value-added products [4,167,173]. Oxygen and nitrogen atoms in biomass can be partly retained in the final carbon; this provides a simple route to incorporate functional groups into the carbon matrix [167]. Other alternative sources, such as plastics (PVC and PET) as well as industrial wastes or polymers, were also considered for the production of ACs [173]. Activated carbons can be obtained with high surface area, well-developed micro- and ultramicroporosity, high content of surface functionalities and chemical polarity, that are beneficial for boosting the CO_2 uptake and enhance the adsorption kinetics [4,179]. These crucial features are obtained from activation processes along with biomass pyrolysis. The activation treatments can be either physical or chemical. Physical activation is simpler and more environmental friendly, but, on the other hand, chemical activation requires low reaction time and lower temperature as compared to the physical activation process [180]. Upon physical activation, the raw material, previously carbonized under inert atmosphere (Ar or N_2), is treated at high temperature by an activating agent, typically CO_2 or steam [22]. CO_2 reacts with carbon via a slow and sluggish reaction, generating mainly micropores, with narrow pore size distribution, whereas steam reacts faster, producing mainly meso- and macropores from the enlargement/coalescence of micropores [181]. The chemical activation relies upon a one-step process, which considers firstly the wet-impregnation or solid-solid mixing of the raw material with the chemical activating agent, and then, the simultaneous carbonization/activation treatment [22]. Typical chemical activating agents for porosity development/adjustment are potassium hydroxide (KOH), zinc chloride ($ZnCl_2$) and phosphoric acid (H_3PO_4). The different chemical activating agents generate different type of porosity. KOH generates gaseous products, which leave micropores in the carbon framework [181]. $ZnCl_2$ generates micropores as well, but if the temperature is furtherly increased, micropores aee converted into mesopores [181]. The chemical activation with H_3PO_4 originates phosphorous-rich functional groups along with extra-porosity [181]. Chemical activation can also be used for adding (or removing) specific surface functional groups, as in the case of high-temperature ammonia (NH_3) treatments, conceived for introducing nitrogenous groups (such as amide,

imide, pyrrolic, pyridinic and lactame groups), while removing acidic oxygen, for giving an enhanced basic character [50].

3.4.4.2.   Pyrogenic carbons (PCs)

Pyrogenic carbon materials usually include charcoal, biochar, agrichar, and carbonized biomass [50]. Similarly to activated carbons, PCs are prepared from agricultural residues, forestry waste, the organic fraction of municipal solid waste, industrial biomass by-products, and animal manures [182]. PCs differ from ACs because they generally lack of an activation process and are prepared at relatively lower temperatures [182]. Usually, biomass is converted into biochar by a pyrolysis treatment, which involves thermal degradation of biomass under inert atmosphere at elevated temperatures under the limited content or complete absence of oxygen [181]. Slow pyrolysis (heating rate < 10 °C min^{-1}) guarantees higher final yield (30−50%, according to the type of biomass used), as compared to fast pyrolysis, which is characterized by higher heating rates (< 300 °C min^{-1}) and very short residence time (seconds) [181]. Besides pyrolysis, PCs can be prepared by other methods, such as microwave-assisted pyrolysis and hydrothermal carbonization (HTC) [50]. HTC is a thermochemical process, where the carbonaceous precursors are treated in a pressurized aqueous solution at lower temperatures in respect to the dry pyrolysis (120−250 °C, with or without the presence of a catalyst [50,180,183]. Hydrochar can be also functionalised by oxygen- and nitrogen-rich functional groups using appropriate precursors [180].

3.4.4.3.   Graphene-based adsorbents

Discovered by Geim and Novoselov in 2004, graphene is an innovative two-dimensional material constituted by single layers of sp^2 hybridized carbon atoms, arranged into a crystalline honeycomb network, the layers of which are connected by relatively weak forces [165,184,185]. The first applications of graphene/graphite in CO$_2$ adsorption are dated 2012, with the purpose to exploit its large active surface area (theoretical value of 2630 m^2 g^{-1}) and the unique possibility to introduce defects in its hexagonal lattice for creating pores with adapt radii for selectively admitting CO$_2$ [184,186,187]. Additionally, the outstanding mechanical properties of graphene, that is the inherent mechanical strength and stiffness, are extremely useful for affording the high packing densities in the adsorption column and guaranteeing a long lifetime after numerous and repetitive TSA/PSA working cycles [187]. Besides, in TSA processes, the remarkable thermal conductivity would accelerate the heat transfer through the adsorbent bed, thus reducing the regeneration cycle time, and lowering the operating costs [187]. Moreover, pristine graphene is chemical inert if compared to many chemicals present in flue gas (O$_2$,

SO_2, NO_X) and highly hydrophobic and relatively stable towards exposure to humid and hot environmental conditions [172,187]. Although the pristine graphene surface is not highly active in CO_2 adsorption, an increased reactivity is shown by graphene-based materials, owing to the presence of oxygen-containing functional groups [179,188]. Indeed, the planar geometry of graphene-based materials (graphene oxide, reduced graphene oxide, carbon nanotubes) is adapt for heteroatoms incorporation (e.g., N, B, Al, S, and so on) or functionalization, for the purpose of enhancing the molecular interaction with CO_2, hence adsorption capacity and selectivity [165,172,186–189]. Precisely, different methods were reported for the synthesis of nitrogen-doped graphene materials, such as post-synthetic ammonia treatment or the direct synthesis from nitrogen-containing precursors [189]. However, graphene as a bulk material has the tendency to form irreversible agglomerates upon usage, and its production process is energy/time consuming; hence these drawbacks hinder is large-scale application [187] .

3.4.4.4.   Carbon nanofibers (CNFs)

Solid sorbent for CO_2 capture are normally used in the form of powder, which may cause some issues such as the chocking of the equipment. Porous carbon fibers, knitted as mats, felt or fabric, can cope this issue, while being more easy to handle in practical applications [190–192]. In addition, their peculiar thread-like structure ensures large specific surface area and wide range of pore size distribution, proving to be beneficial for CO_2 adsorption [193]. Electrospinning followed by carbonization is one of the most reliable and competitive methods for obtaining ultra-fine and continuous nanofibers [192]. The porosity can be furtherly tuned by chemical or physical activation processes [190]. The obtained activated carbon fibers (ACFs) present different micro-structure also accordingly to the polymer precursor, since each polymer has a distinct degradation process [194]. The most common polymer precursors include polyacrylonitrile (PAN), polyvinyl acetate, viscose, aramid Nomex®, pitch-based materials, phenolic resin, petroleum pitch, melamine resin, polyvinyl chloride (PVC), polyvinyl alcohol (PVA), polyaniline (PANI), Kevlar® (poly(phenylene terephtalamide)), cellulose, polyimide, polybenzimidazole, and phenolic resins [192,195]. Basic functional groups, crucial for the CO_2 adsorption and selectivity, can be introduced by using N-containing precursors or after the reaction of NH_3 with the ACFs at high temperatures or by directly activating precursor fibers with NH_3 [190].

3.4.4.5.   Porous polymers

Porous organic polymers (POPs) are suitable as CO_2 adsorbents, owing to their lightweight (they typically consist of light elements such as H, B, C, N, and O),

high specific surface area, and tunable pore structure and chemical properties [196–198]. Moreover, POPs have remarkable physical and chemical stability, thus they can be used under harsh conditions, such as high temperature and pressure, and in the presence of humidity and acidic substances [199]. At present, numerous types of POPs were studied for CO_2 capture, such as microporous organic polymers (MOPs), porous polymer networks (PPNs), hyper cross-linked polymers (HCPs), polymers with porous aromatic frameworks (PAFs), porous melamine–formaldehyde (MF), covalent organic polymers (COPs), polymers with intrinsic microporosity (PIMs), conjugated microporous polymers (CMPs) and polymer with covalent triazine-based frameworks (CTFs) [196–198]. The CO_2 capture capacity and selectivity of HCPs and CMPs can be enhanced by introducing heteroatoms and/or electron-rich groups, such as N, O, Si [196,198]. In the case of CMPs, it is also possible to improve their affinity with CO_2 by tailoring the conjugated linker and chemical functionality [200]. Generally speaking, the introduction of nitrogen moieties or amino units and the incorporation of polar organic functionalities or inorganic ions within POPs network is efficient in enhancing CO_2 capture capacity and selectivity [199,201]. However, it is worth considering that this approach usually significantly reduces POPs specific surface area [201].

Another category of polymer-based adsorbents is represented by porous inorganic polymers, which are flexible structures, generated by the coordination bonds between metal ions and organic linkers [202]. Here, during the adsorption process, the CO_2 molecule interacts with the open metal site, while a change of the polymer pore structure induces a structural distortion [202].

The drawbacks of the polymer-based adsorption technology include the high cost of monomers and synthetic pathways (use of noble metal catalysts), the limited performances under real flue gas condition (low pressure and high temperature), and finally the complexity of the POP-based membrane preparation, due to POPs insolubility [196].

Chapter 4

4. Ordered mesoporous carbons

4.1.   Brief history of templated synthesis

Although purely microporous sorbents are advantageous for their efficiency and selectivity in CO_2 capture, the slow mass-transport through the narrow cavities along with the inaccessibility of very small pores cause hindered diffusion and hamper their widespread industrial application [203,204]. Indeed, while micropores and ultramicropores (< 2 and 0.7 nm, respectively) are crucial for fostering both CO_2 adsorption and selectivity [83–85], the introduction of mesopores, especially if they are organized in the form of an ordered porous network, improves gas diffusion and enhances the CO_2 uptake kinetics [204]. Before the development of templated synthesis, mesopores in carbon materials were created by poorly reproducible and controllable processes, as for activated carbons and carbon aerogels [205]. Howbeit, highly structured and ordered porous architectures can be obtained by using non-reactive elements as templates [206]. Two strategies are available for templated synthesis: exotemplating exploits rigid porous inorganic solids as molds (*hard template*), while in endotempating, porogenic agents (*soft templates*) are directly added to the carbon-based precursor mixture [206,207]. Initially, the *template* concept was related specifically to amphiphilic surfactants and biomacromolecules used as structure directing agents for the soft templated synthesis of mesoporous silicate molecular sieves [208]. More recently, the concept of templated synthesis extended also to the exotemplated synthesis of carbonaceous materials, metals, metal oxides, phosphates, polymers, sulfides, ceramics, etc. [209].

Several types of templates were explored for ordered carbon synthesis; most of them were reviewed by Inagaki et al. [205] and described in Figure 4.1 [210]. In 1982, the pioneering work of Gilbert and coworkers [211] shows the first example of using a solid sacrificial template, namely a silica gel or porous glass, for the synthesis of porous glassy carbon. Five years later, in 1988, the work of Kyotani et al. [212] described the synthesis of two-dimensional oriented carbons inside the

interlamellar voids of a layered clay mineral (precisely montmorillonite), which hence acted as a regularly structured template.
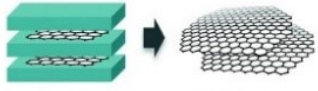
Year	Template	Scheme illustration	Obtained carbon	Dimension	Template-derived ordered structure
1982	Silica gels, Porous glasses		Porous glassy carbons	3D	No
1987	NaCl		Porous carbons	3D	No
1988	Montmorillonite		Thin graphite	2D	No
1995 1998	Anodic Al oxides (AAO)		Carbon nanotubes	1D	No
1997 1998 2000	Zeolites		ZTCs	3D	Yes
1998	Silica opals		Carbon inverse opals	3D	Yes
1999	Mesoporous silicas		Ordered mesoporous carbons	3D	Yes
2004	Micro-phase separated block copolymers		Ordered mesoporous carbons	3D	Yes
2005	Organic micelle		Ordered mesoporous carbons	3D	Yes
2008 2011	Metal-organic frameworks (MOFs)		Disordered porous carbons	3D	No
2011	Ni foam		Macroporous graphene	3D	No
2016	Al_2O_3 nanoparticles		Mesoporous graphene	3D	No
2017	Organic crystals		Ordered carbonaceous frameworks	3D	Yes

Figure 4.1: Time progress of templated carbons synthesis, with a special focus on the parent template type and the obtained carbon structure. Readapted and reprinted from [210].

In 1992, the scientists from the Mobil Oil Corporation reported the synthesis of the first example of mesostructured silica, namely MCM-41 (Mobil Composition

of Matter No. 41), using an amphiphilic alkylammonium ion surfactant as the structure directing agent [213,214]. MCM-41 having a two-dimensional hexagonal structure (*P6mm* space-group symmetry) is only the first member of the so-called M41S family, which includes also MCM-48 [215] (three-dimensional cubic system, *Ia$\bar{3}$d* space-group symmetry) and MCM-50 (lamellar structure without space-group symmetry) mesostructured silica [216]. The remarkable innovation brought by M41S molecular sieves is the extension of the concepts of uniform pore size from an exclusive attribute of a subgroup of microporous materials to the range of mesopores [208].

Another family of widely studied mesostructured silica is the SBA-n (Santa Barbara Amorphous) family. The two most successful members of this family are SBA-15 (two-dimensional hexagonal, *P6mm* space-group symmetry) [217] and SBA-16 (cubic cage-structured, *Im$\bar{3}$m* space-group symmetry), both synthesized from triblock copolymers, such as $EO_{20}PO_{70}EO_{20}$ (Pluronic 123) and $EO_{106}PO_{70}EO_{106}$ (Pluronic F127), respectively [213]. Other members of the SBA-n family are SBA-11 (cubic, *Pm$\bar{3}$m* space-group symmetry), SBA-12 (three dimensional hexagonal, *P6$_3$/mmc* space-group symmetry), and SBA-14 (three dimensional cubic), synthetized from oligomeric nonionic alkyl-ethylene oxide surfactants, such as $C_{16}EO_{10}$, $C_{18}EO_{10}$, and $C_{12}EO_4$, respectively [213]. Noteworthy, in 2003 Kleitz and coworkers [218], announced the synthesis of high-quality mesoporous cubic *Ia$\bar{3}$d* silica, designated as KIT-6 (Korean Advanced Institute of Science and Technology No. 6), with enlarged pore size and wall thickness as compared to MCM-48, using a new synthetic route which involves the use of a proper mixture of Pluronic P123 block copolymer and butanol as *cosolute*, for directing the formation of the porous mesostructure.

In 1998, *nanocasting* was introduced by Göltner for defining the technique used for the preparation of mesoporous organic polymers by the replication of a rigid and interconnected pore system of block copolymer-templated silica [219]. The main steps of the nanocasting process for templated porous carbons preparation are listed below and sketched in Figure 4.2 [220,221]:

- synthesis of the silica hard template (Figure 4.2a);
- impregnation of the template with a suitable precursor solution and its polymerization inside the template porous network (Figure 4.2b);
- carbonization of the carbon/silica composite;
- template removal by dissolution of silica in HF or NaOH solution (Figure 4.2c).
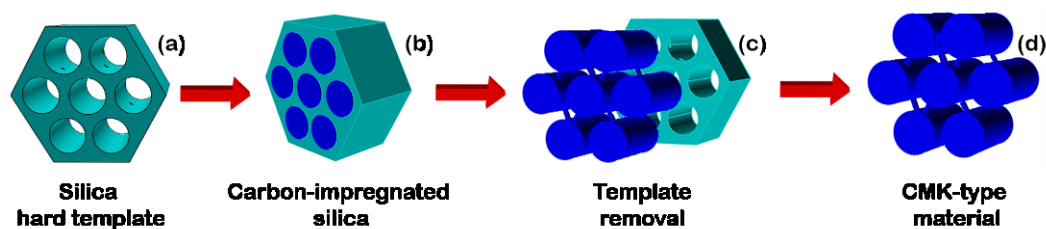
Figure 4.2: Schematic representation of the nanocasting procedure for the synthesis of ordered mesoporous carbons from a silica hard template.

Indeed, silica and aluminosilicates combine geometrical flexibility and relatively facile synthesis, along with a remarkable chemical, thermal and hydrolytic stability that make them particularly suitable as hard templates for nanocasting synthesis. Indeed, differently from non-siliceous materials, they offer the possibility to be removed by dissolution in NaOH or HF based solutions, after the impregnation with the carbon-based mixture, while retaining the formed ordered carbon replica structure [209]. Taking advantages from this peculiar feature, from the second half of 1990s, porous anodic aluminum oxide [222] and zeolite Y [223] were used as *hard templates* by the Japanese research group lead by Prof. Akira Tomita for the synthesis of 1D carbon materials and microporous carbons, respectively. In 1999, Ryoo and coworkers from the Korean Advanced Institute of Science and Technology (KAIST) [224], published the first synthesis of carbon molecular sieves, namely CMK-1 (CMK-n, Carbon Mesostructure by KAIST [225]), using MCM-48 ordered mesoporous silica as *hard template*. The CMK-1 replicas consist of two separated enantiomeric sub-frameworks, which undergo a structural transformation upon the template dissolution, responsible of reduced pore symmetry, as deduced from the low-angle X-ray diffraction pattern inconsistent with the $Ia\bar{3}d$ space group of the original MCM-48 silica template [226]. In 2000, the same research group announced the first synthesis of a carbon molecular sieve, namely CMK-3, which retained the same pore symmetry of the parental SBA-15 ordered silica template [227]. Henceforth, between the end of 1990s and the beginning of 2000s, the synthesis of ordered mesoporous carbons remarkably progressed, owing to the availability of different structures of ordered mesoporous silica. Indeed, compared to the other types of *hard templates*, mesoporous silica structures are easily synthesizable with tunable size of pore diameters, wall thicknesses as well as multiple pore geometries, thus paving the way to the synthesis of a wide variety of templated mesoporous carbon replicas [228]. Among these, it is worth mentioning CMK-8 carbon replicas from the cubic $Ia\bar{3}d$ KIT-6 template. If silica is aged at temperature higher than 70 °C, the template CMK-8

carbon preserves the same pore symmetry of the parent template, owing to the presence of porous bridges between the channel-like enantiomeric systems of the KIT-6 template [218,229]. Conversely, if KIT-6 silica is aged at temperatures within 35−60 °C, the carbon replicas undergo a structural transformation upon the template removal, similarly to CMK-1 [229].

On the other hand, the peculiarity and advantage of endotemplating (also referred to as *soft templating*) concern the reduction of the number of synthesis steps as compared with *hard templating*. Indeed, in the former case, the template removal and the carbonization occur in the same stage, consequently avoiding the use of hazardous chemicals, such as NaOH or HF for the silica based template removal [207,230]. Typical structure directing agents are cationic quaternary ammonium compounds (e.g., hexadecyltrimethyl ammonium bromide, CTAB) or commercial Pluronic triblock copolymers (e.g., P123, F127 or F108) [231]. However, *soft-templating* is not as reproducible as hard templated nanocasting, since the structure directing agents are not rigid like solid templates and the process is highly influenced by the synthesis conditions [207]. Table 4.1 summarizes the

Table 4.1: The most relevant ordered carbonaceous mesostructures obtained as replicas of ordered mesoporous silica hard templates.

Year	CMK-n	Template	Structure	Reference
1999	CMK-1	MCM-48	Cubic $I4_132$	[232]
2001	CMK-2	SBA-1	Cubic $Pm3n$	[233]
2000	CMK-3	SBA-15	2-D hexagonal $P6mm$ (rod type)	[227]
2002	CMK-4	MCM-48	Cubic $Ia\bar{3}d$	[234]
2003	CMK-5	SBA-15	2-D hexagonal $P6mm$ (tube)	[235]
2005	CMK-6	SBA-16	Cubic $Im\bar{3}m$ (full cage-like)	[236]
2005	CMK-7	SBA-16	Cubic $Im\bar{3}m$ (hollow cage-like)	[236]
2003	CMK-8	KIT-6	Cubic $Ia\bar{3}d$ (rod type)	[218]
2003	CMK-9	KIT-6	Cubic $Ia\bar{3}d$ (nanotube-type)	[218]

4.2. Nanocasting

4.2.1. Hard template synthesis

Silica-based mesoporous structures are usually obtained by the cooperative self-assembly of inorganic precursors in solutions and amphiphilic molecules, such as surfactants and block copolymers [216,237,238]. In surfactant templated synthesis, the mesopore diameters can be controlled by varying the surfactant tail length and expanding the micelles with suitable organic additives [232]. Typical inorganic precursors are organosilicate compounds, such as tetramethylorthosilicate (TMOS) or tetraethylorthosilicate (TEOS). These alkoxides, i.e. esters of silicic acid ($Si(OH)_4$), are hydrolyzed at a suitable pH level in water-based solutions, causing the cleavage of the ester bond, thus generating alcohol and a free reactive silanol group that undergoes condensation reactions with other silanol groups [239]. The driving force of the cooperative self-assembly mechanism is the interaction between the surfactants and the inorganic precursors. It occurs either as an electrostatic pathway, based on supermolecular assembly of charged surfactants with charged inorganic precursors, or a neutral pathway, via hydrogen bonding between surfactant and inorganic precursor [240]. As anticipated in Paragraph 4.1, quaternary cationic surfactants ($C_nH_{1n+1}N(CH_3)_3$-Br, n = 8 −22), such as cetyltrimethylammonium bromide ($C_{16}H_{33}N(CH_3)_3$-Br, CTAB), were used as templates for the synthesis of M41S mesoporous silicate molecular sieves under hydrothermal, basic conditions [208]. Moreover, nonionic poly(alkylene oxide) surfactants (e.g., $C_{16}EO_{10}$, $C_{18}EO_{10}$, and $C_{12}EO_4$) and poly(ethylene oxide)-b-poly(propylene oxide)-b-poly(ethylene oxide) (PEO_mPPO_n-PEO_m) block copolymers (e.g., $EO_{20}PO_{70}EO_{20}$ and $EO_{106}PO_{70}EO_{106}$) were used for the synthesis of several members of the SBA-n family. Compared to cationic surfactants, they benefit from lower decomposition temperature and alternative surfactant removal procedures [213]. The cooperative templating mechanism involved in the synthesis of M41S and SBA-n families occurs via different stages [240]:

- micelles formation;
- micelle or aggregates formation, driven by inorganic-organic interactions between small silica oligomers and surfactant;
- condensation of the inorganic precursor at the external surface of the micelles;
- intermicellar condensation, leading to the formation of the ordered mesophase;

 ◆ complete polymerization of the silica source during the hydrothermal
   treatment at high temperature;
 ◆ surfactant removal by solvent extraction or by calcination.

Figure 4.3 shows the different steps involved during the cooperative inorganic-organic self-assembly of 2D hexagonal SBA-15 synthesis [241]. Another possible pathway for mesostructured synthesis in the "true" liquid crystal templating process, which is characterized by the use of a higher concentration of surfactants [208,240].
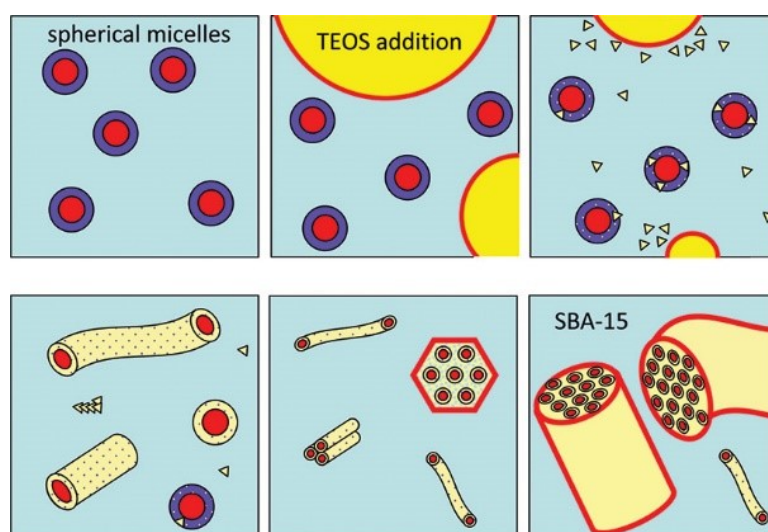
Figure 4.3: Cooperative inorganic-organic self-assembly during 2D hexagonal SBA-15 synthesis: (a) initial formation of a micellar solution; (b) addition of the inorganic silica precursor (TEOS), (c) initial stage of hydrolysis; (d) shape evolution of the micelles; (e) nucleation of the 2D-hexagonal phase; (f) growth and precipitation of the 2D-hexagonal phase. Readapted and reprinted from [241].

Oligomeric and block-copolymer surfactants were widely applied with the intention to extend the range of pore sizes (3−30 nm for SBA-15, in contrast to 2 − 10 nm for MCM-41 materials) and to improve hydrothermal stability by increasing silica wall thickness, up to 3−6 nm, which in the case of alkylammonium surfactants (CTAB) are limited maximum at 1−1.5 nm [242–244]. Additionally, SBA-15 silica appeared to be more suitable than MCM-41 as a hard template, thanks to the presence of disordered microporosity, located inside the pore walls, which confers connectivity between the ordered large pore channels [245]. Indeed, the lack of connectivity between the primary hexagonal mesopores of MCM-41 causes the collapse of the carbon replica upon the template removal, yielding a disordered

microporous structure [220]. On the other hand, the interconnections inside the pore walls of SBA-15 silica are particularly important because, by linking the carbon nanorods, which form inside the cylindrical hexagonally-arranged mesopores, the retention of the original pore symmetry is assured even after template removal [227,246]. The complementary micropores/mesopores originate from the condensation of the silica framework around the hydrated hydrophilic EO-blocks, which surround the non-ionic micelles within the forming pore walls of SBA-15 [242,245]. These connecting pores, located inside the pore walls of the silica, remain preserved also after the high temperature treatments typical of the preparation of ordered mesoporous carbons from nanocasting (up to 880 °C) [245,246]. The work of Galarneau et al. [242] describes the mechanism of formation of secondary pore connectivity between the primary hexagonally arranged mesopores (Figure 4.4). Essentially, when SBA-15 is prepared by 35−60 °C hydrothermal treatment, the hydrated micelles organize keeping each other at ca. 4 nm, which is the minimum distance according to the repulsion force carried out by PEO chains of opposite combs [242]. In this temperature range, no interconnections between micelles are present, but only some ultramicroporosity generated by protruding PEO chains [242]. When the synthesis temperature is higher than 80 °C, PEO chains withdraw on the surface of the micelles and PEO−PEO interaction occurs, generating intermicellar attraction between adjacent micelles; as a result, along with the collapse of the ultramicroporosity, secondary porosity forms inside the silica walls, acting as bridges between adjacent mesopores [242]. Finally, if the solid forms at temperatures higher than 130 °C, ultramicroporosity is not observed because ultramicropores collapse in wider pore bridges [242].

Block copolymers allowed the synthesis of MCM-48-like mesoporous silica, with larger pore size and wall thickness, in respect to the previous one obtained from ionic surfactants. The block copolymer-templated cubic silica gained improved hydrothermal stability from the enlargement of the pore walls, similarly to the case of SBA-15 in respect to MCM-41. The synthesis of large mesopores (4−12 nm) cubic $Ia\bar{3}d$ KIT-6 was obtained adding, at low HCl concentration conditions, n-butanol as a *cosolute* (hydrotropic molecules) to the block copolymer-water system [229]. The addition of butanol is considered to promote the swelling of the hydrophobic volume of the block-copolymer micelles, causing the formation of micellar aggregates with decreased curvature (lamellar mesophase). Subsequently, the condensation in the silicate region, owing to further reaction at 35 °C or during hydrothermal treatment, leads to the folding and regular modulation

of the silica surface, inducing significant changes in micelle curvature, which finally evolves into a highly ordered cubic $Ia\overline{3}d$ [218].
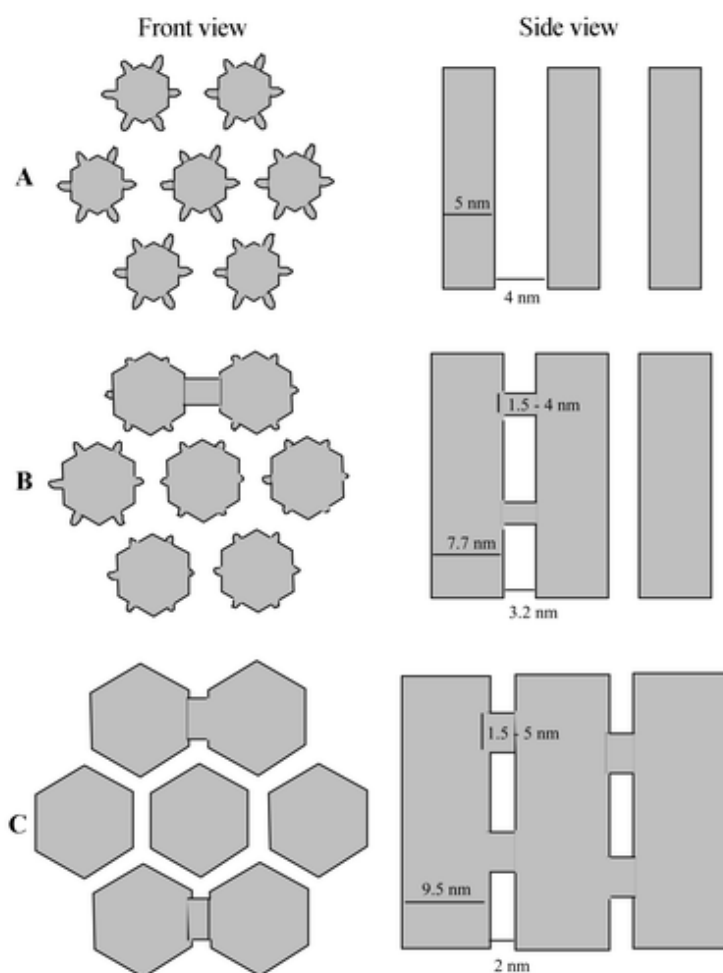
Figure 4.4: Illustration of SBA-15 mesostructure formation, according to the temperature of the thermal treatment: (A) at 35 < T < 60 °C micropores are present, while no connection exists between mesopores, (B) at T ~100 °C micropores are still present but in lower concentration and connections between mesopores formed, and (C) at T > 130 °C micropores are fully transformed in bridge connections between mesopores. Readapted and reprinted from [242].

4.2.2. Carbon source impregnation, pyrolysis and hard template removal

In a typical nanocasting procedure, the ordered mesoporous silica template is degassed simultaneously at moderately high temperature (generally, around 150−

160 °C [99,247]) and under vacuum, in order to remove obstructive adsorbed gases, thus making the pore network accessible for accommodating the carbon precursor solution. Indeed, the carbon source is introduced in the liquid state, in order to properly fill the pore and replicate accurately their architecture. The two most common carbon sources are sucrose, which is infiltrated in its aqueous solution, and furfuryl alcohol that is liquid at room temperature. The amount of precursor solution that is supposed to fill the template porosity is calculated on the basis of the pore volume of the parent silica template. For instance, accordingly to Joo et al. [246], theoretically the amount of sucrose capable of filling a silica template with a pore volume of 1 cm^3 g^{-1} is ca. 1.6 g, being the density of sucrose 1.59 g·cm^{-3}. If sucrose is introduced in the form of an aqueous solution containing sulfuric acid, the maximum amount of sucrose that can be introduced will be reduced to 1.25 g [246]. Accordingly, similar consideration can be taken for the other carbon sources. Other typical carbon sources are phenol resin monomers, acetylene, glucose, xylose, acenaphthene, mesophase pitch, petroleum pitch, etc. [224,225,248]. Impregnation is usually carried out in two steps, where the second one aims to fill the voids and empty space remained after the first thermal treatment; overall, the amount of solution impregnated during the second step is approximately 2/3 of the amount of the first impregnation [227,249]. The carbon sources are converted into carbon by pyrolysis within the porosity of silica, by heating up to 800−1100 °C under controlled atmosphere [224]. An acidic polymerization catalyst is also dissolved in the carbon source solution, sulfuric acid being the most suitable for the pyrolysis of carbohydrates [225] and p-toluensulfonic acid for the pyrolysis of furfuryl alcohol [249]. The carbon/silica composite obtained after pyrolysis is treated once or multiple times in HF or in NaOH ethanol/water solution (this latter being softer, performed at room temperature or heating up to 100 °C) to accomplish a complete silica removal [225,250–252]. Nanocasting is also suitable for obtaining heteroatom-doped ordered mesoporous carbons. One approach is the copolymerization of heteroatom containing-compounds inside the pores of the silica template together with the carbon source or, as a preferred alternative, the direct polymerization of carbon source containing heteroatom(s). Examples of heteroatom-containing precursors are aniline [253–255], melamine [256], glucosamine hydrochloride [99], and pyrrole for N doping [257], triphenylphosphine for F doping [258], boric acid for B doping [259], and ammonium fluoride for F+N codoping [260]. The other approach is the modification of the already prepared OMCs by thermal treatment with a dopant-source (e.g., melamine [261] for N doping, thiourea for S and N codoping [262]), or by post-treatments with ammonia or urea [263,264]. The first approach, also

referred to as direct approach, is more convenient because it reduces the number of synthesis steps and allows a better control of both the chemical composition and the heteroatom distribution [265].

4.3.   Ordered mesoporous carbons and carbon dioxide capture

This thesis work focuses on the synthesis of nitrogen-containing ordered mesoporous carbons obtained by the nanocasting technique and using sustainable and renewable carbon feedstock. In this Paragraph, the performances of the here prepared sorbents are temporary excluded from the discussion, whereas the following chapters will discuss them thoroughly and in details. Briefly, in this Paragraph, some representative literature reports are revised, in order to shed light on the crucial aspects affecting the CO_2 adsorption performances by referring to experimental results. The main details on the adsorbents synthesis and CO_2 characterization are summarized in Table 4.2. Staring from the work of García-Díez et al. [97], a low-value coal tar distillation product was used as carbon source, namely, creosote. The authors applied chemical or physical activation treatments for increasing the volume of micropores [97]. It is worth noticing that the chemical activation treatment conceived for creating additional microporosity, at the same time reduces remarkably the N content [97].

However, the authors evidenced the effectiveness of the contribution of a well-ordered mesostructure in making microporosity more accessible and CO_2 capture performances compatible with highly microporous activated carbon materials [97]. The same beneficial effect of mesoporoity on the adsorption rate as compared to pure microporous materials was also observed by Vorokhta et al. [90]. The evolution of this concept was undertaken by Zhang and coworkers [92], who synthesized single crystal ordered mesoporous carbons, which possess smaller particle sizes, and more interconnected mesoporous channels, thus offering a shorter diffusion pathways and more accessible porosity. Wan et al. [266] used 3-aminophenol as both carbon and nitrogen sources, varying its concentration aiming at regulating the final N content. The authors observed that by increasing the 3-aminophenol content, the amount of incorporated nitrogen increases, but the order of the mesostructured was concurrently damaged. The optimal performance was achieved by an intermediate 3-aminophenol content, thus showing the importance of both nitrogen content and ordered mesostructure.

Table 4.2: Comparison of the performance in terms of CO_2/N_2 separation of OMCs/NOMCs developed in this work with the most significant literature reports.

Materials REF	Synthesis	Precursor	N %	CO$_2$ capacity mmol·g^{-1}	Selectivity CO$_2$:N$_2$	T$_{ads}$[n] °C	P$_{ads}$[o] bar	T$_{act}$[p] °C
NOMC CMK-3 [97]	H.T.[f] + C.A.[g]	Creosote	0.37[a]	~ 0.7 (CO$_2$:N$_2$=20:80)	-	25	1	120
	H.T.[f] + P.A.[h]		2.39[a]	~ 0.6 (CO$_2$:N$_2$=20:80)	-			
OMC CMK-3 [90]	H.T.[f]	Furfuryl alcohol	-	1.7 (100% CO$_2$)	-	20	1	200
					35.2:1 – 38:1[c] (CO$_2$:N$_2$= 15:85)	20-50		
Syngle crystal NOMC [92]	One-pot self-assembly	Resorcinol, HMT[l], urea, ammonia	0.78[b]	2.78 (100% CO$_2$)	29:1 [d]	25	1	200
NOMC [266]	S.T.[i]	resorcinol, 3-aminophenol, L-lysine	2.5[b]	2.50 (100% CO$_2$)	43:1 [c] (CO$_2$:N$_2$= 15:85)	25	1	120
NOMC [263]	S.T.[i]	sucrose, ammonia, TEPA[k]	2.56[a]	1.41 (100% CO$_2$)	m.i. [e] (CO$_2$:N$_2$= 10:90)	35	1	120
NOMC [91]	S.T.[i]	resorcinol, HMT[j] EDA[l]	2.97[a]	2.71 (100% CO$_2$)	28:1 [d]	25	0.95	150
NOMC [267]	S.T.[i]	phloroglucinol formaldehyde resol, PEI[m]	21.58[a]	2.58 (100% CO$_2$)	64:1 [c] (CO$_2$:N$_2$= 10:90)	30	1	180
NOMC [264]	S.T.[i]	Terephthal-aldehyde, m-m-aminophenol, F127, urea	6.53[a]	1.64 (100% CO$_2$)	54.0:1[c] (CO$_2$:N$_2$= 15:85)	25	0.15	150

[a]determined by elemental analysis (wt. %); [b]determined by XPS (at. %); [c] determined by Ideal Adsorption Solution Theory (IAST) method; [d] determined by initial slope (IS) method; [e] m.i. denotes missing information; [f] H.T. is for hard template; [g] C.A. is for chemical activation; [h] P.A. is for physical activation; [i] S.T. is for soft templating; [j] HMT is for hexamethylenetetramine; [k] TEPA is for tetraethylenepentamine; [l] EDA is for ethylenediamine; [m] PEI is for poly(ethyleneimine), [n]adsorption temperature, [o]adsorption pressure, [p] activation temperature before adsorption measurements.

Nevertheless, in most of the literature report nitrogen groups were introduced via post-synthesis modification, by ammonia or urea heat treatment, amine refluxing or similar [92,263,264]. Morover, as a general drawback, the previously cited studies [90–92,264,266] employed toxic carbon sources and/or additional activation steps for the adjustment of microporosity. Conversely, in this thesis work, adsorbents with abundant and tailored porosity were readily prepared by the nanocasting procedure, without requiring any further activation steps, simply by using glucosamine hydrochloride, as concurrent carbon and nitrogen source. This choice of carbon source allows the direct incorporation in a single step of the crucial N functionalities, bypassing time/energy consuming ammonia post-treatments or amine refluxing processes. Glucosamine hydrochloride itself is a non-toxic and potential natural occurring source of carbon, hence it shows highly promising prospects as a suitable raw material for biomass valorization in a circular economy loop.

4.4. Ordered mesoporous carbons as anode materials in secondary batteries

A considerable fraction of the total GHG emissions derives from the transportation sector. Today, the mission of reducing this sizeable contribution to environmental pollution relies on replacing fossil fuel combustion with vehicle electrification. The most attractive technology for driving this revolution is currently represented by Li-ion secondary batteries (abbreviated as LIBs). However, the supply of lithium is starting to deplete and it will soon become not enough to satisfy the growing demand for LIBs in the markets for portable devices and electric vehicles. Hence other systems are currently being examined by researchers. Sodium-ion batteries (NIBs) are presently the most interesting alternative for such a replacement due to the similar chemistry to lithium and the higher abundance and cost-effectiveness of Na-containing precursors [268].

In the plethora of possible active electrode materials for energy storage devices, which are extensively discussed in many review articles [269,270], carbonaceous materials are among the most attractive contender for negative electrode (anode) in Li-ion cells, mainly thanks to their electronic and ionic conductivity, low cost, and abundance [271]. Graphite is the most commonly used anode material in commercial rechargeable lithium batteries, since it can electrochemically intercalate and de-intercalate Li ions in the layered structure made up of graphene planes placed at a mutual distance of 0.3354 nm [271–273]. Its anisotropic structure is responsible for the in plane electronic conduction and the ion intercalation

between the graphene sheets [271]. In addition, graphite allows for maximizing cell voltage owing to the very low average de-/lithiation potential of 0.2 V vs. Li/Li$^+$, which is superior only to the one of metallic lithium [274]. However, the theoretical specific capacity (372 mA h g^{-1}) and the rate performance of graphite are not sufficient for meeting the requirements for high-energy and high-power LIBs [272]. Moreover, graphite is not able to significantly intercalate Na ions because of the narrow interlayer spacing and limited active sites in the highly ordered graphitic domains where the insertion of Na ions is difficult owing to the larger ionic radius than Li-ions (0.102 nm versus 0.076 nm) [268,272,275]. Based on these assumptions, the implementation of commercially available materials for the negative electrode in LIBs or NIBs batteries is a fundamental need.

Porous hard (poorly or non-graphitizing) carbons are characterized by larger interlayer distances, thus ion transport and Li/Na insertion/de-insertion are assisted by the improved accessibility [272]. Specifically, Na storage in amorphous carbon materials can be modeled as an "adsorption-insertion" mechanism, where adsorption occurs in micropores and edge active sites, while insertion takes place in the ordered regions [276]. In this scenario, the peculiar characteristics of OMCs are used for the preparation of negative electrodes in LIBs and NIBs. Indeed, OMCs take advantage of the high surface area and the ordered interconnected porosity to enhance the active interfacial area with the electrolyte and reduce the diffusion length of ions, thus facilitating the charge transfer reactions and ion transport, hence the electrochemical performance [277–279]. In addition, porous materials may easily accommodate volume changes occurring during cycling, thanks to their structural features [280]. Heteroatom inclusion in the pristine carbon framework is a well-known strategy to tailor the electrochemical properties of carbonaceous materials. For instance, N as a heteroatom increases the electronic conductivity of the carbon framework, owing to the stronger electronegativity of N than C, and the hybridization of the N lone pair electrons with the π electrons in carbon [277,278,281]. Accordingly, the insertion of heteroatoms creates defects and enhances the interlayer spacing, thus generating an assisted pathway for ion diffusion and storage [275]. Hence, NOMCs analyzed in this thesis dissertation for the application as selective CO_2 sorbents appear promising also for the application as electrodes in LIBs/NIBs cells. Therefore, Chapter 7 reports some preliminary results from the utilization of these materials for Li and Na storage, according to the same perspective of decarbonizing the most impactful activities of our society.

Chapter 5

5. N-containing CMK-8-type ordered mesoporous carbons investigated as CO_2 adsorbents

5.1.   Introduction

Since their first introduction in 1999, ordered mesoporous carbons (OMCs) were widely investigated and explored for sizeable number of different applications. In this thesis work, the peculiar properties of N-containing ordered mesoporous carbon (NOMC) materials were exploited for the preparation and fine tuning of effective and selective CO_2 adsorbents. Indeed, as introduced in Paragraph 3.4.4, porous carbon materials exhibit suitable properties for satisfying this target, taking advantage of their easily achievable large surface area, tunable porous structure, and surface properties, along with good thermal and chemical stability and resistance to moisture. Their cost-effectiveness is related to the production process; commercial and cheap highly porous carbons are also available and used commercially, particularly those derived from low-cost biomass feedstock.

In this scenario, an original, alternative straightforward synthetic approach was chosen for the preparation of nitrogen-containing ordered mesoporous carbons (namely, NOMCs), using a sustainable, natural occurring and potentially biomass-derived carbon source. Indeed, the adsorbents studied in this work were readily obtained by applying the well-known nanocasting technique and D-glucosamine hydrochloride as concurrent carbon/nitrogen (C/N) source. D-glucosamine is obtained from the hydrolysis of chitin, which is the second most abundant natural polysaccharide. The derived D-glucosamine hydrochloride was here explored, to the best of my knowledge, for the first time as a sustainable source to obtain in a single-step, by the nanocasting approach, N-loaded ordered CMK-8-type mesoporous carbons conceived for greenhouse gas adsorption/separation. Indeed, D-glucosamine satisfies the prerequisite of non-toxic and natural occurring C/N

source, thus meeting sustainability requirements in a circular economy perspective. Moreover, the synthesis procedure was opportunely selected in order to avoid post-synthesis modifications, thus reducing the number of synthesis step. Briefly, the novel NOMC materials were prepared by impregnating D-glucosamine into the pores of the KIT-6 ordered mesoporous silica hard-template, followed by pyrolysis and silica removal steps. Different KIT-6 hard-templates and pyrolysis conditions were applied to induce changes in the porosity and in the amount and type of nitrogen functionalities of the NOMC materials. For the courtesy of the reader, details of the synthesis procedure are available in Appendix A1, whereas the methodology adopted for the physico-chemical characterization and the CO_2 adsorption testing is illustrated in Appendix A2. Indeed, this chapter is mainly focused on the investigation of the effects of microporosity and N-incorporation on CO_2 adsorption and selectivity, which was obtained by a comprehensive set of physico-chemical and adsorption techniques. Precisely, different testing conditions (temperature and gas composition) were considered, and both selectivity and reusability were evaluated, so as to unravel the feasibility of the use of the synthetized materials as efficient, and highly selective CO_2 adsorbents in a circular economy perspective. The experimental results included in this Chapter are included in the work of Maruccia et al. [99]. The full paper (Figures and Tables included) is here reproduced, reprinted and readapted with permission.

5.2.   Experimental section

5.2.1. Materials and methods

The detailed synthesis procedure of CMK-8-type NOMCs materials is described in Appendix A1. Precisely, the starting point is the synthesis of the KIT-6 hard template (as illustrated in Paragraph A1.3) and consequently its impregnation with the carbon source solution for the preparation of the templated CMK-8-type carbons (process described in Paragraph A1.5). The resulting samples are named X_Y(Z), where X is the carbon source (Glucosamine (G) or sucrose (S), respectively), Y the pyrolysis temperature (varying from 600 to 900 °C), and Z the temperature of the hydrothermal treatment of the silica template (i.e., 40 or 100 °C). A summary of the basic information about the prepared CMK-8 samples is listed in Table 5.1.

Table 5.1: List of CMK-8 samples synthesized in this work.

Sample name	Carbon source	Pyrolysis temperature, T_p °C	Hard template
G_600(40)	Glucosamine hydrochloride	600	KIT-6_40
G_750(40)	Glucosamine hydrochloride	750	KIT-6_40
G_900(40)	Glucosamine hydrochloride	900	KIT-6_40
G_600(100)	Glucosamine hydrochloride	600	KIT-6_100
G_750(100)	Glucosamine hydrochloride	750	KIT-6_100
G_900(100)	Glucosamine hydrochloride	900	KIT-6_100
S_900(100)	Sucrose	900	KIT-6_100

The methodology adopted for the physico-chemical characterization of the synthesized materials and the CO_2 adsorption testing is illustrated in Appendix A2, precisely in Paragraphs A2.1 and A2.2, respectively. The schemes in Figure 5.1 illustrate the used technique, with a reference to the relative Paragraph in the Appendix A2 in which they are discussed.
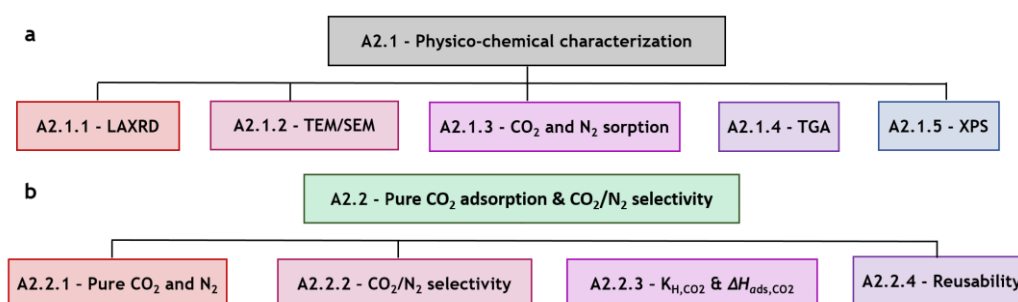
Figure 5.1: Scheme of the investigative methodology: a) physico-chemical characterization and evaluation of the performances in pure CO_2 adsorption and CO_2/N_2 selectivity b) on N-containing CMK-8 carbons.

5.2.2. Structural-morphological characterization

Low-angle X-ray diffraction analysis as a nondestructive method, was widely utilized to attain precise information about the structural attributes of the materials, chiefly the ordered arrangement in the mesoporous structures [226,282,283]. The LAXRD diffraction pattern of KIT-6 silica is characteristic of cubic $Ia\bar{3}d$ symmetry of pores (see Figure 5.2) [218].
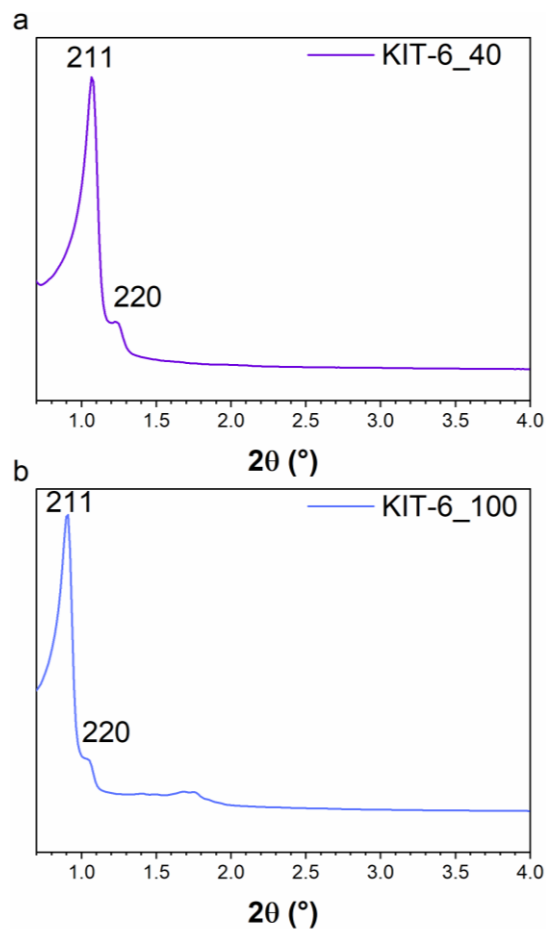
Figure 5.2: LAXRD patterns of KIT-6 hard templates: a) KIT-6_40 and b) KIT-6_100.

The order mesoporous structure of the two families of carbon replicas was confirmed by both LAXRD and HR-TEM characterization techniques. In detail, X_Y(100) samples maintain the same $Ia\bar{3}d$ symmetry of the silica template, as demonstrated by the well-resolved (211) and (220) reflections in LAXRD patterns (see Figure 5.3b,c).
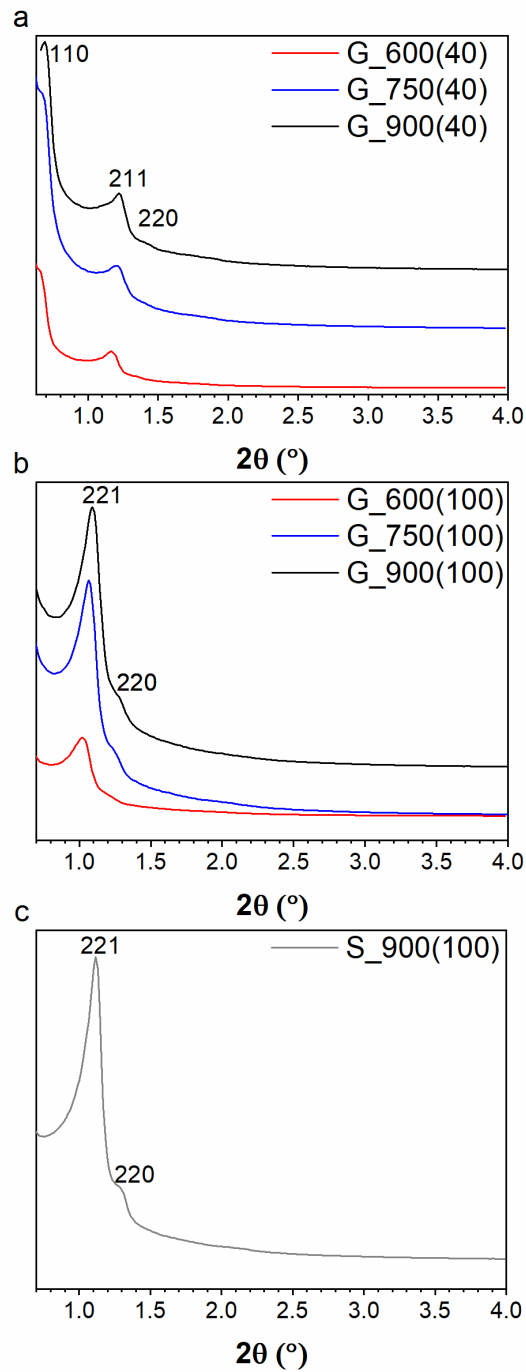
Figure 5.3: LAXRD patterns of CMK-8 samples: a) NOMCs of the G_Y(40) series (G_600(40), G_750(40), G_900(40), red, blue, black lines respectively), b) NOMCs of the G_Y(100) series (G_600(100), G_750(100), G_900(100), red, blue, black lines respectively), c) reference pristine carbon sample, namely S_900(100).

On the contrary, an additional diffraction peak at $2\theta < 1°$ indexed as (110) reflection reveals a change in the symmetry for the G_Y(40) samples from the respective template (Figure 5.3a) [226].

The HR-TEM images in Figure 5.4 show the highly ordered porous structure of both the families of CMK-8 samples. X_Y(100) series of samples are characterized by a dense and interwoven framework (Figure 5.4c,d,e), derived by the replication of both the two interconnected pore systems of KIT-6_100. On the contrary, G_Y(40) series of samples displays disconnected framework systems that can be well distinguished in Figure 5.4a,b. This observation corroborates the hypothesis of independent filling of the template porosity, typical for the replica from KIT-6_40 [284]. In addition, the FESEM images show a highly porous structure (Figure 5.4f); in some areas of the samples, it is even possible to appreciate the ordered disposition of the pores. The lower symmetry of the mesostructure of this family of carbons was explained by the absence of connectivity among the two mesoporous channel systems of KIT-6 when the hydrothermal treatment is performed at a temperature below 70 °C [229]. Their symmetry can be attributed to $I4_1/32$ [234], which is typically observed in CMK-1-type carbons, a carbon family derived from the replication of two pairs of non-interconnected pore systems of MCM-48 silica hard template [285]. The intensity and definition of LAXRD peaks increase as T_p increases, indicating a higher ordering in the mesoporous structure.
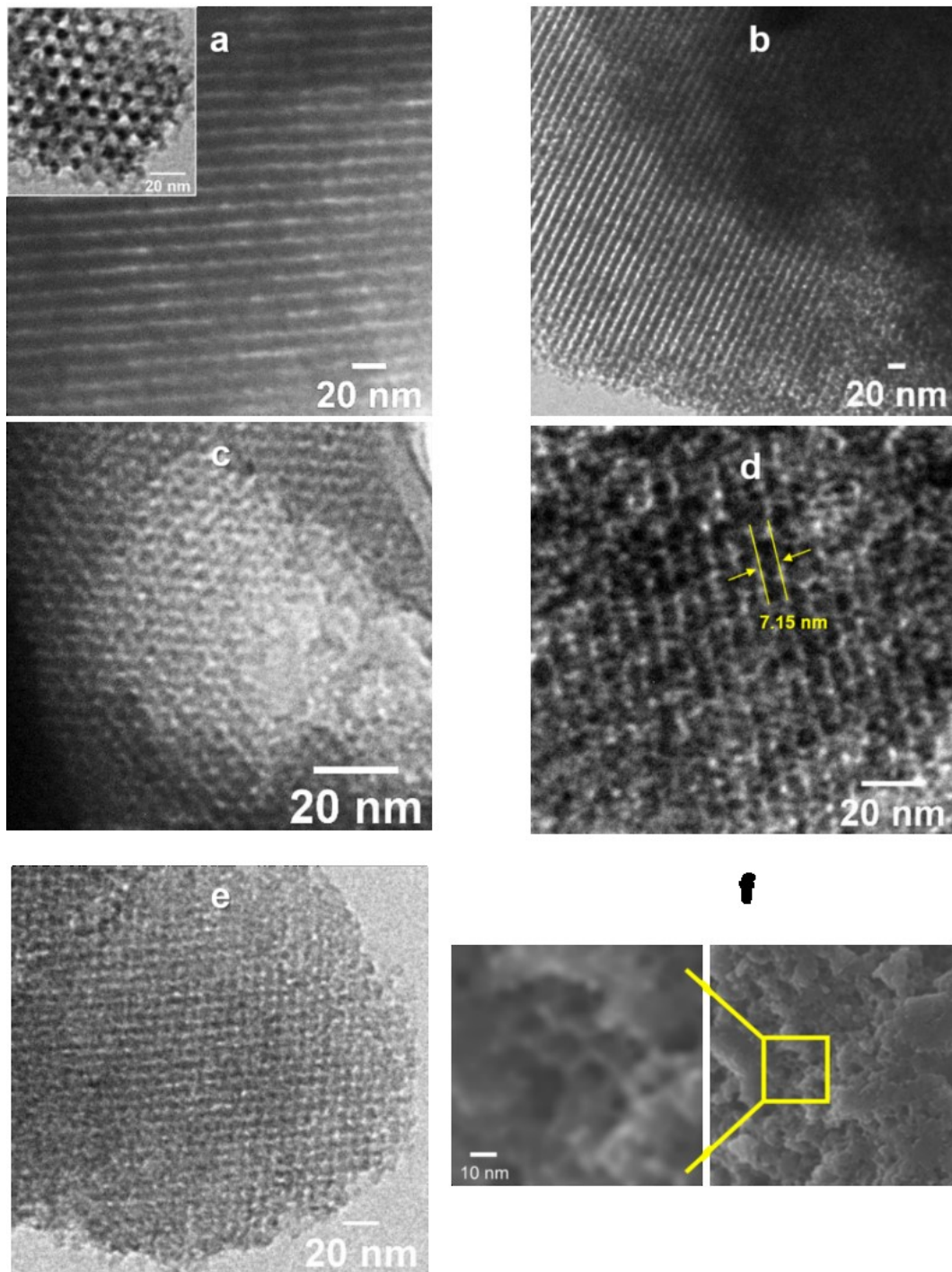
Figure 5.4: HR-TEM micrographs of a) G_600(40) with, in inset, insights into the ordered porous structure, b) G_900(40), c) G_600(100), and d) G_900(100), e) S_900(100), f) FESEM image of G_900(100) with a focus on the ordered porous architecture.

The XRD unit cell size a_{211} was calculated from the (211) reflection using the expression $a_{211} = \sqrt{6} \cdot d_{211}$, where the interplanar spacing d_{211} was calculated using the Bragg's law. The shrinkage of the mesostructure after the high-temperature treatment is observed by the decrease of the interplanar d-spacing and, consequently, of the unit cell size as T_p increases (Table 5.2).

Table 5.2: LAXRD and TEM parameters of all the samples under study.

Samples	d_{110} [a] nm	d_{221} [b] nm	d_{220} [c] nm	$D_{p,TEM}$ [d] nm
KIT-6_40	-	8.3	7.1	-
KIT-6_100	-	9.8	8.4	-
G_600(40)	13.1	7.6	6.7	5.3; 7.2
G_750(40)	12.8	7.4	6.7	-
G_900(40)	12.8	7.3	6.4	5.3; 7.6
G_600(100)	-	8.6	7.4	4.2
G_750(100)	-	8.2	7.2	-
G_900(100)	-	8.1	7.0	4.3
S_900(100)	-	7.9	6.8	4.7

[a] interplanar spacing relative to (110) reflection, [b] interplanar spacing relative to (211) reflection, [c] interplanar spacing relative to (220) reflection, [d] pore size calculated from TEM images.

The porosity features were investigated by N_2 adsorption-desorption measurements at -196 °C. All the samples, including KIT-6-type silica and CMK-8-type carbons show type IVa isotherms (IUPAC classification), which is typical of mesoporous materials like MCM-41 (Figure 5.5and Figure 5.6, respectively). The family of samples G_Y(40) shows two hysteresis loops in the range $0.65 < p/p_0 < 0.85$, which correspond to a bimodal pore size distribution (see Figure 5.6a.b). The family of samples X_Y(100) shows one hysteresis loop in the relative pressure range $0.4 - 0.8$ and a pore size distribution centered at 4.5 nm (Figure 5.6c,d and e,f). Besides the main population of pores, for both the G_Y(40) and G_Y(100) families of samples, an additional population of pores of size around 11 nm is present, probably due to incomplete pore filling [286]. Indeed, this population of larger pores is more evident for the replicas of the silica aged at 40 °C than for the one aged at 100 °C. This evidence can be again explained by the absence of interconnections between the two coupled sets of pores of KIT-6_40, which prevents the complete pore filling by the carbon source solution, or more precisely the filling of only one of the two channel systems, leading to uncoupled sub-frameworks formation [287].
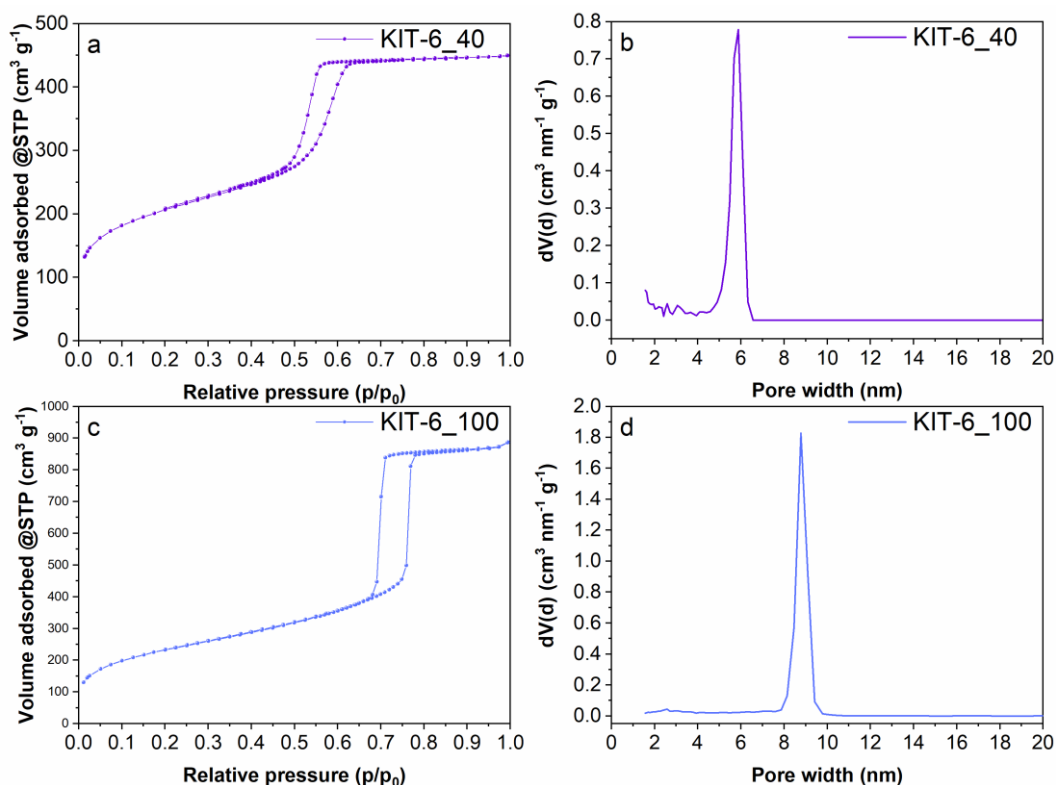
Figure 5.5: N_2 adsorption-desorption isotherms at -196 °C and NLDFT pore size distributions of (a,b) KIT-6 samples aged at 40 °C, and (c,d) KIT-6 samples aged at 100 °C.

The specific surface area was calculated with both BET (S_{BET}) and QSDFT (S_{DFT}) methods. However, in the presence of microporosity, the BET method can be unreliable because it is difficult to distinguish between monolayer-multilayer adsorption and micropore filling [288]. For this reason, S_{DFT} is considered more reliable as QSDFT method takes into account heterogeneity and surface roughness of carbon materials [289]. S_{DFT} increases at higher T_p, while the pore volume is not considerably affected by the temperature of pyrolysis. V_{mp} increases with the increase of T_p due to a more advanced pyrolytic degradation and reorganization of the carbon precursor and the release of small molecules with the increase of the temperature of pyrolysis [290].
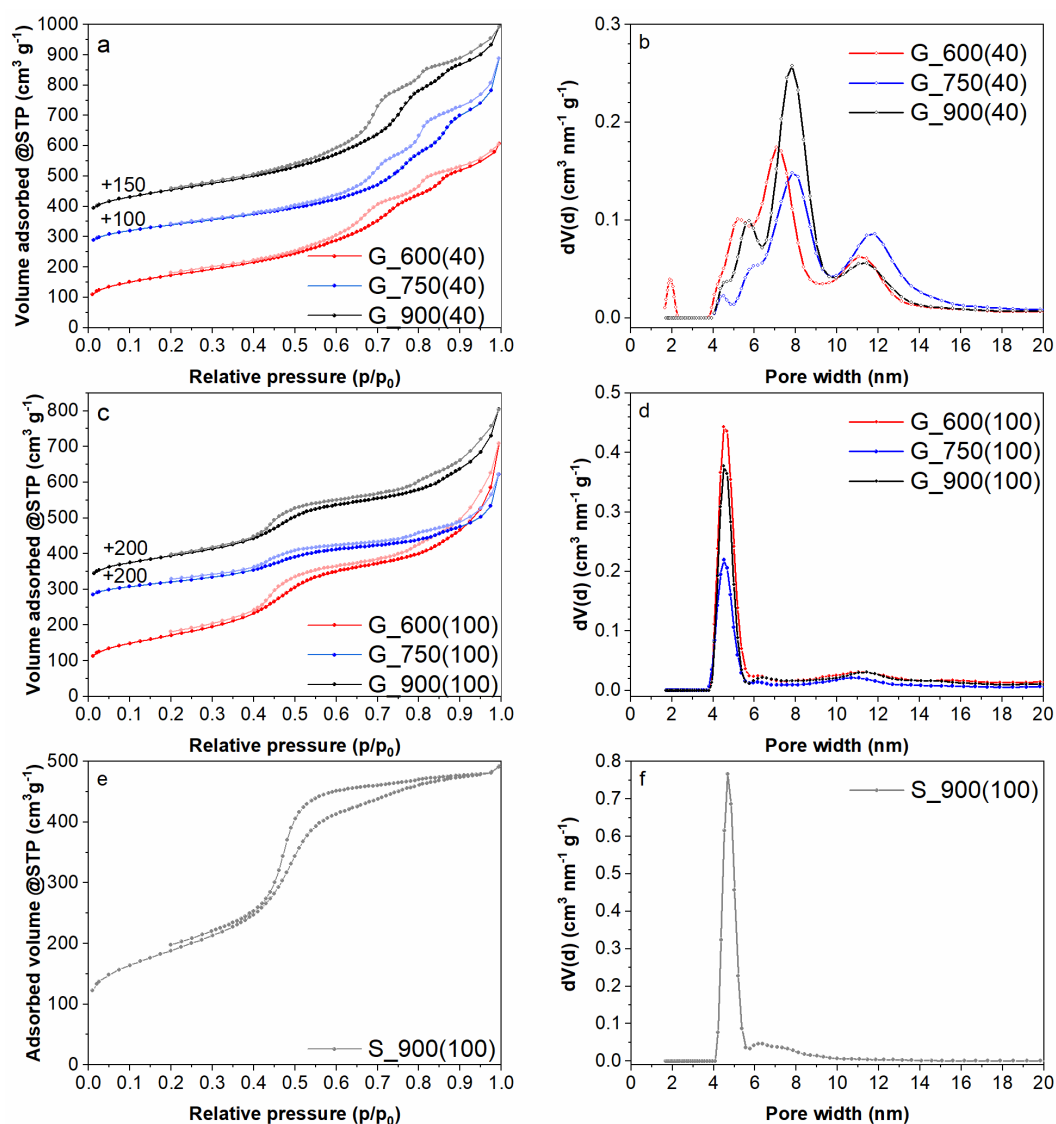
Figure 5.6: N$_2$ adsorption-desorption isotherms at -196 °C and QSDFT pore size distributions of NOMC samples obtained from glucosamine at different temperatures: (a,b) G_600(40), G_750(40), and G_900(40) (red, blue, and black lines, respectively), (c,d) G_600(100), G_750(100), and G_900(100) (red, blue, and black lines, respectively), (e,f) S_900(100) (grey line).

It is also worthy to highlight that the bimodal micropore size distribution (see Figure 5.7b) is composed of pores smaller than 1 nm and the percentage of V_{ump} over V_{mp} is in the range of $63 - 70$ % for all the G-series of samples (56 % for the S-derived sample), determined from the CO$_2$ adsorption-desorption isotherms at 0 °C (see Figure 5.7a). The sample from sucrose has a lower specific surface area, and particularly important for the application, a lower micropore content.
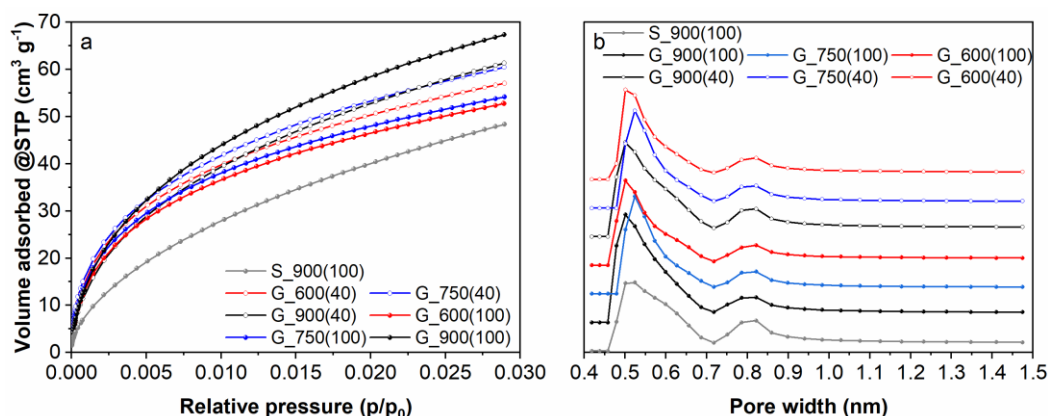
Figure 5.7: CO$_2$ adsorption isotherms at 0 °C (a) and NLDFT micropore size distributions (b) of OMC samples from glucosamine and sucrose: G_600(40), G_750(40), and G_900(40) (red, blue, and black empty dots, respectively) and G_600(100), G_750(100), G_900(100), and S_900(100) (red, blue, black, and gray full dots, respectively).

The textural properties are summarized in Table 5.3. Good agreement is observed between the pore diameters calculated from N$_2$ physisorption and from HR-TEM images (Figure 5.4, Figure 5.6, Table 5.2 and Table 5.3). The wall thickness (*b*) was calculated using a geometrical model ($b = {a_{211}}/{2} - D_{p,DFT}$) [229]. The parameter *b* decreases with the increase of the ageing temperature for silica, which conversely reflects in thicker pore walls in the respective carbon replica. For carbon replicas, *b* decreases as long as T_p increases because of the phenomenon of framework shrinkage [291]. Besides the main population of pores, for both the G_Y(40) and G_Y(100) families of samples, an additional population of pores is present with size around 11 nm, probably due to incomplete pore filling [286]. Indeed, this population of larger pores is more evident for the replicas of the silica aged at 40 °C than for the one aged at 100 °C. This evidence can be again explained by the absence of interconnections between the two coupled sets of pores of KIT-6_40, which prevents the complete pore filling by the carbon source solution, or more precisely the filling of only one of the two channel systems, leading to uncoupled sub-frameworks formation [287].

Table 5.3: Physicochemical properties of the ordered mesoporous materials prepared and under study in this work

Samples	a_{211}[a]	b[b]	S_{BET}	S_{DFT}	$V_{p,DFT}$	D_p[c]	V_{ump}	V_{mp}	D_{mp}[d]
	nm	nm	$m^2\,g^{-1}$		$cm^3\,g^{-1}$	nm	$cm^3\,g^{-1}$		nm
KIT-6_40	20.4	4.3	735	738	0.7	5.9	-	-	-
KIT-6_100	24.0	3.2	841	734	1.3	8.8	-	-	-
G_600(40)	18.6	3.1	619	779	0.9	5.2; 7.1	0.11	0.16	0.5; 0.8
G_750(40)	18.0	2.1	673	1043	0.9	5.8; 8.0	0.12	0.17	0.5; 0.8
G_900(40)	17.8	2.1	727	1062	1.0	5.8; 7.8	0.12	0.19	0.5; 0.8
G_600(100)	21.2	6.1	609	748	0.8	4.5	0.10	0.15	0.5; 0.8
G_750(100)	20.2	5.6	424	639	0.5	4.5	0.10	0.15	0.5; 0.8
G_900(100)	19.8	5.4	693	1069	0.8	4.5	0.13	0.22	0.5; 0.8
S_900(100)	19.4	5.0	673	783	0.8	4.7	0.09	0.16	0.5; 0.8

[a] unit cell size (a_{211}) calculated using the expression $a_{211} = \sqrt{6} \cdot d_{211}$
[b] wall thickness (b) calculated by geometrical model, $b = {a_{211}}/{2} - D_{p,DFT}$ [229]
[c] pore width (D_p) in the mesoporous range, calculated by NLDFT and QSDFT methods for silica and carbons, respectively, applied to N_2 isotherms at -196 °C
[d] pore width (D_{mp}) of carbon samples in the microporous range, calculated by NLDFT method applied to CO_2 isotherms at 0 °C.

5.2.3. Physico-chemical characterization

Thermal degradation analysis on CMK-8 samples (Figure A.2.2) was performed under air flow in the temperature range of 30 – 800 °C (see Appendix A2.1, Paragraph A2.1.4.1 in). No significant weight loss is visible until 550 – 580 °C (see Figure A.2.2), therefore the samples are thermally stable under degassing conditions (up to maximum 500 °C in inert N_2 atmosphere, see Paragraphs A2.2 and A2.3), which is remarkable for an OMC material. The TGA analysis allowed also to assert that silica template removal was successful as shown by the low residue observed after TGA analysis (Figure A.2.2) and the low atomic percentage of Si (< 1 at. %) from XPS survey analysis (Figure A.2.3 and Table 5.4).

Table 5.4: Atomic percentage of Si in the OMCs under study, accordingly to XPS analysis.

Samples	Si at. %
G_600(40)	0.0
G_750(40)	0.6
G_900(40)	0.2
G_600(100)	0.8
G_750(100)	0.6
G_900(100)	0.2
S_900(100)	0.0

However, the XPS analysis was performed mainly to investigate the surface chemical composition and the bonding state. The surface atomic ratio of C, N, and O atoms was determined form XPS survey spectra (Figure A.2.3) and it is listed in Figure 5.8a. The XPS regions of the previous elements were selected for high-resolution (HR) acquisitions to obtain semi-quantitative information based on peak areas and chemical information from the deconvolution into different chemically shifted components. Carbon signal was fitted by using three components (see Figure A.2.4 and Figure A.2.7a in Appendix A2, Paragraph A2.1.5) assigned to C—C sp^2 (284.3 – 284.7 eV), C–O/C–N (285.9 – 286.5 eV), and C=O/C=N (286.5 – 287.6 eV) [292,293]. Oxygen signal (see Figure A.2.5 and Figure A.2.7b in Appendix A2,Paragraph A2.1.5) was fitted by using three components assigned to C=O (~531 eV), C–O (~533 eV), and COOH (~534 eV) [293]. The N-bonding state was studied in relation to the pyrolysis temperature to understand the effect of the thermal treatment on the development of the different N species and their influence on CO_2 adsorption. The N1s signals of NOMCs were fitted by using three components assigned to pyridinic (N-6, 397.7 – 398.9 eV), pyrrolic (N-5, 399.9 – 400.7 eV), and graphitic (N-Q, 401.0 – 401.8 eV) nitrogen-based structures [292] (Figure A.2.6 in Appendix A2, Paragraph A2.1.5) and graphically summarized in Figure 5.8b.
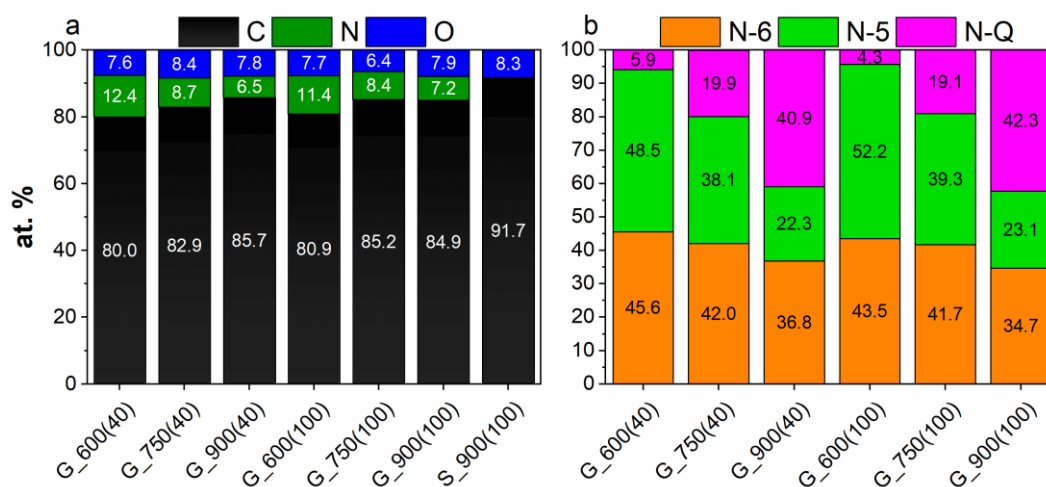
Figure 5.8: a) Surface atomic ratio of C, N, and O as derived from XPS analysis of NOMCs prepared and under study in this work; b) relative ratio of the N-species (N-6, N-5 and N-Q) in G-derived NOMCs, as calculated from the deconvolution of the high resolution XPS signals in the N1s region (full spectra are available in Appendix A2).

Accordingly, the fraction of N-5 decreases slightly when T_p increases from 600 to 750 °C, but it decreases dramatically at 900 °C. N-6 follows the same trend, even if the reduction is less appreciable. In contrast, N-Q is detected in a very low concentration in the sample pyrolyzed at 600 °C, but its relative amount increases with the increment of the pyrolysis temperature. Indeed, N-Q concentration is lower than 20% up to 750 °C, but at 900 °C becomes the most abundant species. The evolution of nitrogen-containing moieties is ascribed to their different thermal stability. Particularly, N-5 is less stable than N-6 and N-Q at a higher temperature, as observed by Stańczyc et al. [294]. The surface atomic percentage of C and O/C and N/C ratio were plotted *vs.* the pyrolysis temperature in Figure 5.9. The surface C relative amount increases with the increment of the pyrolysis temperature as a consequence of the loss of heteroatoms [295]. In the T_p range 600 – 900 °C, the N/C content decreases while O/C remains almost constant, consistently with the findings of Gehring et al. [295].

The XPS survey scan also detected some percentages (ca. 0.3 at.%) of sulphur contaminations deriving from the sulphuric acid used as the polymerization catalyst during the carbonization process of the C or C/N precursor. Several literature reports mention the incorporation of sulphur as heteroatom to enhance CO_2 adsorption in carbonaceous sorbents [296–299]. Precisely, the sulfur-containing functional groups can interact with CO_2 in different ways: i) by acidic interactions

as for the neutral sulfur, ii) by polar interactions as for the oxidized sulfur, iii) by hydrogen bonding as in the case of sulfonic acids [300]. In the sample under study, the content of surface S is approximately constant in all the samples and very low, i.e. from 2 to 5 % of the surface N content. On the basis of these observations, it is reasonably assumed that the contribution of S to the CO_2 uptake is negligible and undiscernible in respect to the contribution due to the N species.
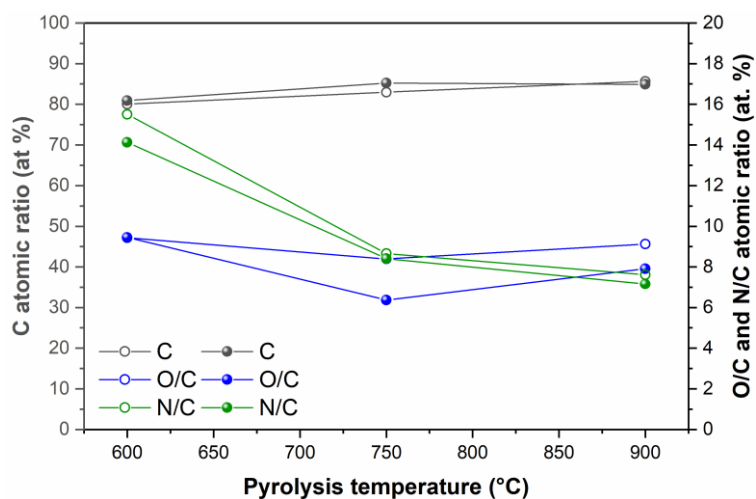
Figure 5.9: Relative ratio of C, N and O from XPS. Empty dots samples from KIT-6_40 (G_600(40), G_750(40), and G_900(40)), full dots samples from KIT-6_100 ((G_600(100), G_750(100), and G_900(100)).

5.2.4. CO_2 adsorption measurements

5.2.4.1. Evaluation of the force of interaction between the CO_2 and the adsorbents' surface

The isosteric enthalpy of adsorption ΔH_{ads} and Henry's constant K_H were calculated from the adsorption isotherms in pure CO_2 to assess the intensity of the interaction between the gas and the adsorbents. ΔH_{ads} decreases as a function of surface coverage (Figure 5.10) because the adsorption occurs initially at the higher energy sites [247,301], and the steeper ΔH_{ads} drop is, the larger the energetic heterogeneity of the adsorption sites.
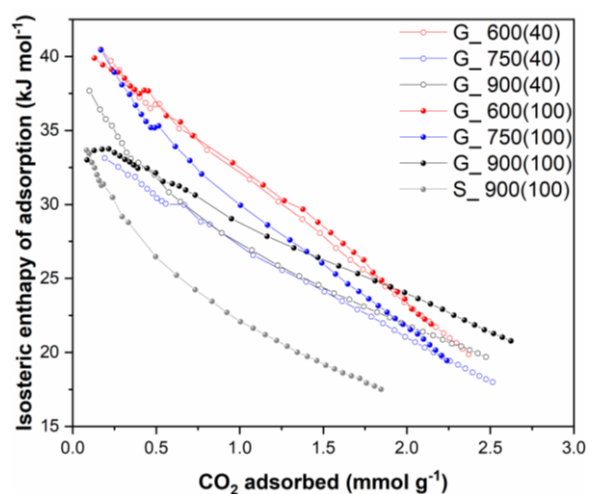
Figure 5.10: Isosteric enthalpy of adsorption vs. amount of CO_2 adsorbed for all the samples under study.

ΔH_{ads} at low coverage lies in the range of $33 - 40$ kJ mol^{-1} for all the samples, which is attributable to a physisorption mechanism (-25 to -50 kJ mol^{-1}) [21].

Henry's constant (K_H) and the virial coefficients C_1 e C_2 were also calculated from the CO_2 isotherms at 0 °C (Figure A.2.16) and listed in Table 5.5. Sample S_900(100), which lacks nitrogen, or the samples pyrolyzed at 900 °C show lower values of K_H compared to those pyrolyzed at $600 - 750$ °C. This is the evidence of the relationship between the nitrogen content and the strength of CO_2-adsorbent interaction. The samples with a higher N content, particularly in the pyridinic form, have a higher K_H, because they can interact strongly with CO_2 [302].

Table 5.5: Henry constants (K_H) and virial coefficients (C_1 and C_2) of NOMCs calculated from CO_2 isotherms at 0 °C.

Samples	K_H mmol g^{-1} kPa^{-1}	C_1 g $mmol^{-1}$	C_2 (g $mmol^{-1}$)^2
G_600(40)	0.639 ± 0.006	1.787 ± 0.009	$- 0.204 \pm 0.002$
G_750(40)	0.582 ± 0.018	1.586 ± 0.028	$- 0.165 \pm 0.006$
G_900(40)	0.288 ± 0.007	1.218 ± 0.023	$- 0.130 \pm 0.005$
G_600(100)	0.500 ± 0.006	1.786 ± 0.013	$- 0.205 \pm 0.003$
G_750(100)	0.559 ± 0.013	1.753 ± 0.023	$- 0.186 \pm 0.006$
G_900(100)	0.318 ± 0.008	1.057 ± 0.022	$- 0.090 \pm 0.005$
S_900(100)	0.124 ± 0.004	1.240 ± 0.040	$- 0.197 \pm 0.012$

5.2.4.2.   Pure CO₂ adsorption

A preliminary study of the sample performances was carried out from the observation of the adsorbed amounts in pure CO_2 at -10, 0 and 10 °C at an absolute pressure up to 1 bar using a volumetric sorption analyzer. The amounts of CO_2 adsorbed by the samples at each temperature are listed in Table 5.6. G_900(100) shows the highest CO_2 adsorption capacity in these conditions associated with the highest micro- and ultra-micropore volumes. Differently, the N-lacking homologous S_900(100) sorbent has the lowest adsorption. This result confirms that the use of glucosamine as a carbon source instead of sucrose enhances the CO_2 uptake in this family of ordered mesoporous materials, through the simultaneous increase of microporosity and nitrogen inclusion. Interestingly, the adsorption loss, observed by increasing the adsorption temperature from -10 to 10 °C, follows the pyrolysis temperature order of $750 < 600 < 900$ °C, and the highest drop is found in the S-derived sample. This observation suggests that the beneficial effect of nitrogen in improving CO_2 adsorption and selectivity gains a crucial role against microporosity at a temperature close to RT [303].

Table 5.6: Pure CO_2 adsorption at -10, 0 and 10 °C in a volumetric sorption analyzer [a] at 100 kPa and at 30 °C in a gravimetric sorption analyzer[b] at 90 kPa.

Sample name	n_{ads}[a] @ −10 °C	n_{ads}[a] @ 0 °C	n_{ads}[a] @ 10 °C	n_{ads}[a] loss ΔT (-10°C,10°C)	n_{ads}[b] @ 30 °C
	mmol g⁻¹			%	mmol g⁻¹
G_600(40)	2.90	2.54	2.37	18.3	1.18
G_750(40)	3.04	2.68	2.54	16.4	1.37
G_900(40)	3.17	2.72	2.50	21.1	1.38
G_600(100)	2.71	2.36	2.18	19.6	1.17
G_750(100)	2.72	2.41	2.23	18.0	1.23
G_900(100)	3.37	3.01	2.64	21.7	1.47
S_900(100)	2.47	2.16	1.88	23.9	0.97

Pure CO_2 sorption analysis using [a] a volumetric sorption analyzer; b a gravimetric sorption analyzer.

Similar results were achieved in pure CO_2 adsorption measurements at 30 °C and up to 90 kPa (0.9 bar) performed with a gravimetric sorption analyzer. The maximum weight increase of 6.5% (1.47 mmol g⁻¹ of adsorbed CO_2) is achieved by sample G_900(100) at 90 kPa (see Figure 5.11 and Table 5.6). In general, the

micropore and, in particular, the ultramicropore volume strongly influence pure CO_2 adsorption in the range of investigated temperatures [304].
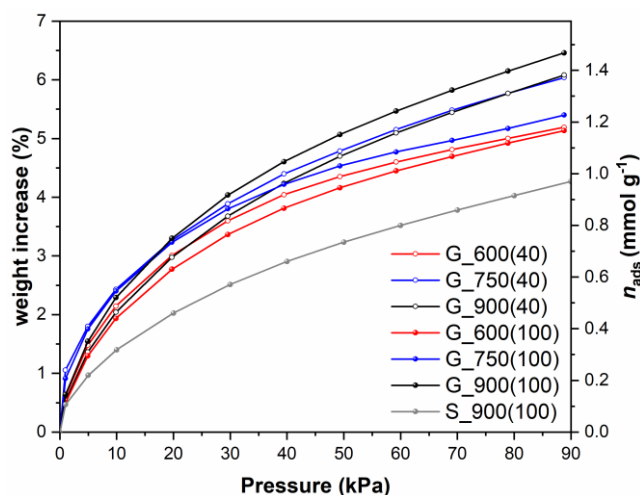
Figure 5.11: Pure CO_2 adsorption at 30 °C up to 90 kPa performed with a gravimetric sorption analyzer.

To investigate the effect of the type and amount of N inclusions, but excluding the contribution of microporosity, the CO_2 adsorbed amount normalized over the micropore volume (CO_2 ads./V_{mp}, mmol cm^{-3}) was correlated with the overall XPS surface N content and each N species for all the G-derived samples, accordingly to the procedure already used by Sánchez-Sánchez et al. [303]. The experimental data were fitted with a linear function (see Figure 5.12), and both the nature and the intensity of the contribution of each species in CO_2 adsorption was estimated from the slope of the trend line. Generally, we can state that the increment of the overall surface nitrogen content on the carbon surface has a beneficial effect, as indicated by the positive slope of the trend line (Figure 5.12a), in agreement with the results of Li et al. [305]. N-6 and N-5 enhance the CO_2 adsorption (Figure 5.12b,c), even if to a different extent. Indeed, from the comparison of the values of the slopes, both N-5 and N-6 positively participate to the CO_2 adsorption, but the highest contribution is due to N-6. N-6 and N-Q interact more easily with CO_2 due to their higher basicity compared with pyrrolic moieties [306]. N-5 promotes the adsorption of CO_2 through hydrogen-bonding-like interactions occurring between the positively charged hydrogen atom bonded to the nitrogen atom of the pyrrolic moiety and the oxygen atom of CO_2 [307], which is a weaker interaction than the Lewis acid-base one occurring in N-6 and N-Q [306]. As reported by Lim et al. [306], CO_2 is adsorbed onto the surface of quaternary nitrogen containing carbon

with an angle of up to 179.93, while the presence of N-5 structures lead to the alignment of CO_2 and N-H on an axis.
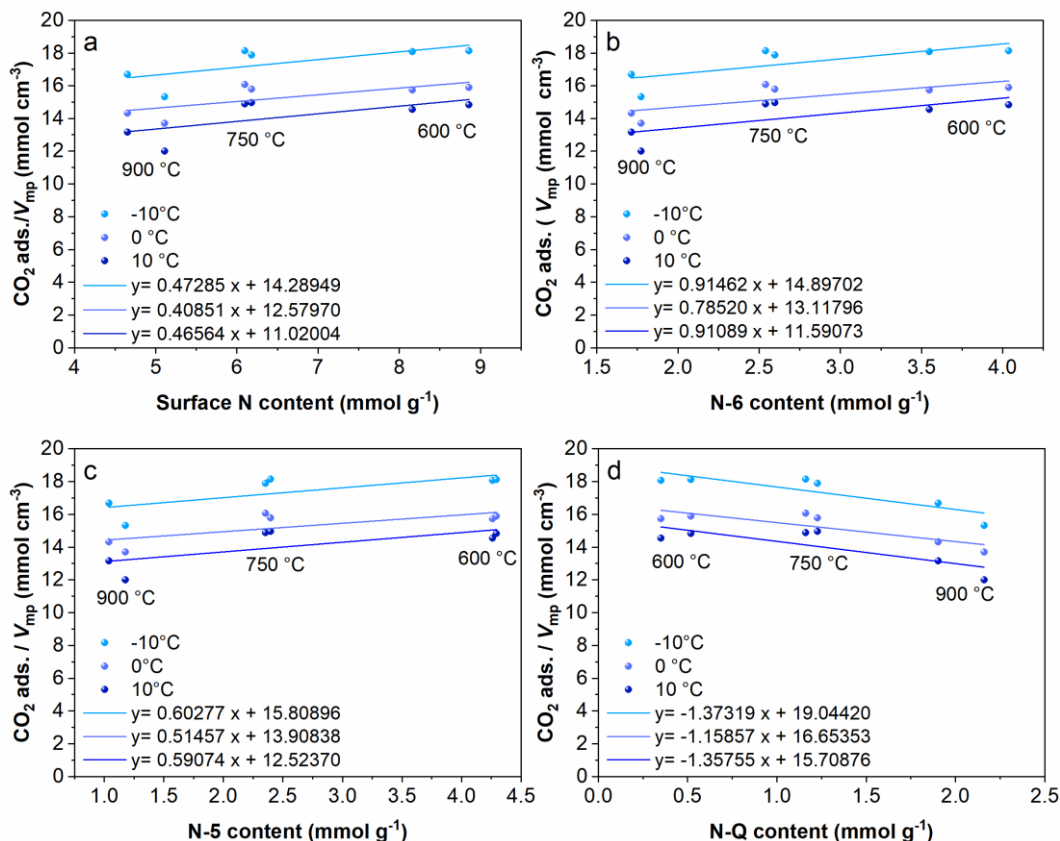
Figure 5.12: Pure CO_2 adsorption at 30 °C up to 90 kPa performed with a gravimetric sorption analyzer.

Accordingly, this last interaction (H-bonding) prevents an efficient π–π stacking between CO_2 and the graphitic carbon orbital system due to geometrical constrains as occurs in the case of N-Q. In principle, also N-Q should increase the affinity for CO_2 when compared with the bare carbon surface [307]. However, in this specific case, CO_2 ads/V_{mp} decreases with the increase of N-Q (Figure 5.12d), which is likely ascribed to the less abundant total concentration (mmol g^{-1}) of N-Q species when compared with N-5 and N-6. Moreover, the increase in N-Q concentration is related to the decrease of N-6 and N-5, which contribute to CO_2 adsorption in a stronger or comparable extent, respectively [306]. Nevertheless, the highest concentration of N-Q coincides with the higher content of micro- and ultra-micropores, which strongly contributes to CO_2 adsorption, particularly at lower temperature. The simultaneous presence of both nitrogen and oxygen atoms could

also positively affect the CO_2 adsorption performances of the material [308]. The interaction mechanism during the CO_2 adsorption is mainly due to the dipolar interactions as in the case of nitrogen-based materials even if the adsorption is mainly due to nitrogen species, as previously reported by Wu et al. [309].

5.2.4.3.   *CO_2/N_2 selectivity*

TGA measurement was performed at 35 °C and 1 bar exposing the samples to a mixture composed of 20 vol.% CO_2 and 80 vol. % of N_2 to evaluate the competitive adsorption of these two gases; results are shown in Figure 5.13a,b. Temperature and gas composition conditions were chosen to be similar to a typical exhaust gas [26]. The conditions scheme used to perform these experiments is shown in Figure A.2.15 in Paragraph A2.2.2.1. The observed sample weight increase is related to CO_2 adsorption (Figure 5.13b and Table 5.7). However, the amount of adsorbed CO_2 in these conditions is lower if compared to the values obtained by the measurements performed under pure CO_2. The generic decrease of CO_2 adsorption is ascribed to the increase of the tested temperature, typically observed for a physisorption process [310], to the lower partial pressure of CO_2 in the gas flow, and to the slight amount of adsorbed nitrogen considered in the initial mass, that will be partially replaced by CO_2 due to the preferential adsorption of CO_2 as compared to N_2. The beneficial effect of nitrogen content in carbon samples is more significant when adsorption occurs at higher temperature and in a mixed CO_2/N_2 gas atmosphere. Indeed, G_600(Z) and G_750(Z) samples here match or outperform G_900(Z) series of samples, which in contrast demonstrated enhanced performance under pure CO_2 adsorption conditions in the temperature range from −10 to 30 °C. The improved selectivity is attributed to the higher surface N content and, particularly, to the superior concentration of pyridinic-N inclusions. Actually, Lim et al. [306] demonstrated that N-6 is particularly effective in selective adsorption, not only for the strong affinity for CO_2, but also for the high adsorption energy difference between CO_2 and N_2. Indeed, higher CO_2 adsorption values, equal to 3.6 and 3.5 % weight increase (0.82 and 0.80 mmol g^{-1}, respectively), are reached by the samples G_600(40) and G_750(40), respectively, which in these conditions outperform G_900(100), being the most performing sample in pure CO_2. N-lacking sample S_900(100) again shows the lowest performance in terms of CO_2 adsorption and selectivity.
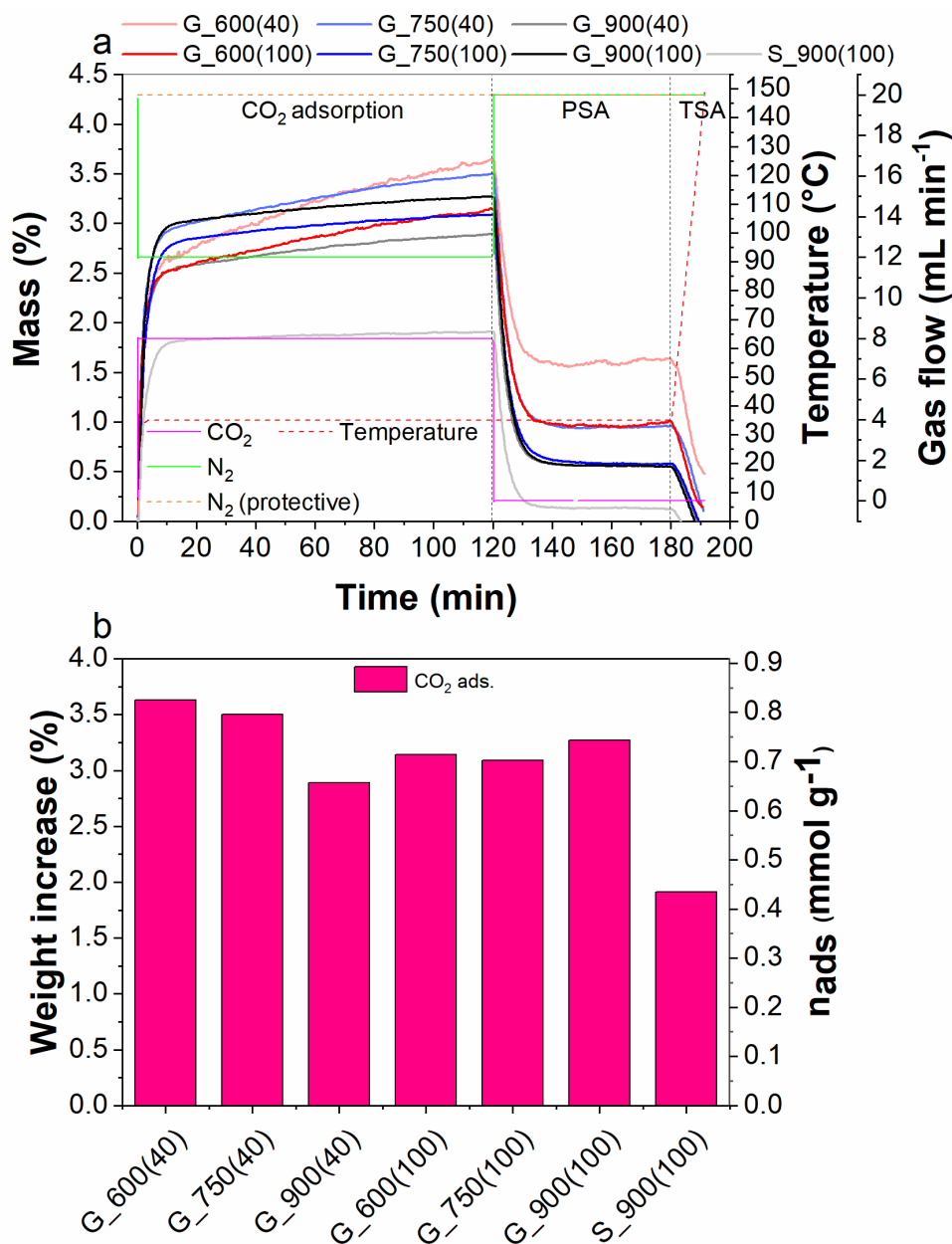
Figure 5.13: (a) Adsorption and desorption steps for CO_2/N_2 adsorption measurements of NOMCs under study, and (b) weight increase due to CO_2 adsorption in a gas mixture of 20 vol. % CO_2 and 80 vol. % of N_2 at 35 °C. Details on setup for CO_2/N_2 selectivity tests by TGA in Appendix A2, Figure A.2.15.

The adsorbed amounts and the percentage of released CO_2 in pressure swing adsorption (PSA) conditions are listed in Table 5.7. The adsorption capacity and selectivity results are consistent with the calculated K_H values (see Table 5.5). It is

interesting to observe that almost all the adsorbed CO_2 is released in PSA (Figure 5.13a), i.e., only exposing the sample to a flow of N_2, without heating. The percentage of CO_2 released under PSA conditions appears to be inversely related to N content. Then, heating was applied to remove CO_2 adsorbed in the most energetic sites. At temperatures < 150 °C, most of the adsorbed CO_2 is released.

Table 5.7: Adsorption and desorption analysis of mixed CO_2/N_2 adsorption tests by TGA.

Samples	Mass change %	CO_2 ads mmol g^{-1}	Released CO_2 in PSA %
G_600(40)	3.6	0.82	55.6
G_750(40)	3.5	0.80	72.6
G_900(40)	2.9	0.66	80.3
G_600(100)	3.1	0.71	67.8
G_750(100)	3.1	0.70	81.2
G_900(100)	3.3	0.74	82.9
S_900(100)	1.9	0.43	93.7

To properly compare our work with other literature reports, the CO_2/N_2 selectivity on the most selective sample (viz., G_600(40)) was also evaluated according to the widely used ideal adsorption solution theory (IAST). Single component adsorption isotherms of CO_2 and N_2 were performed in the same condition (at 30 °C, from 0 to 90 kPa) (see Figure 5.14a). As can be observed from the isotherms in Figure 5.14a, the amount of adsorbed N_2 is much lower compared to the amount of adsorbed CO_2 in the whole pressure range (0.20 and 1.18 mmol g^{-1} at 90 kPa, respectively); this confirms the high CO_2/N_2 selectivity of the G-series of samples. S_{IAST} calculated on the G_600(40) sample lays in the range 37 −24 (for a gas mixture composed of CO_2/N_2=20:80, see Figure 5.14b) or 52−34 (for a gas mixture composed of CO_2/N_2=15:85, see Figure 5.14c) in the tested pressure range (0-90 kPa).
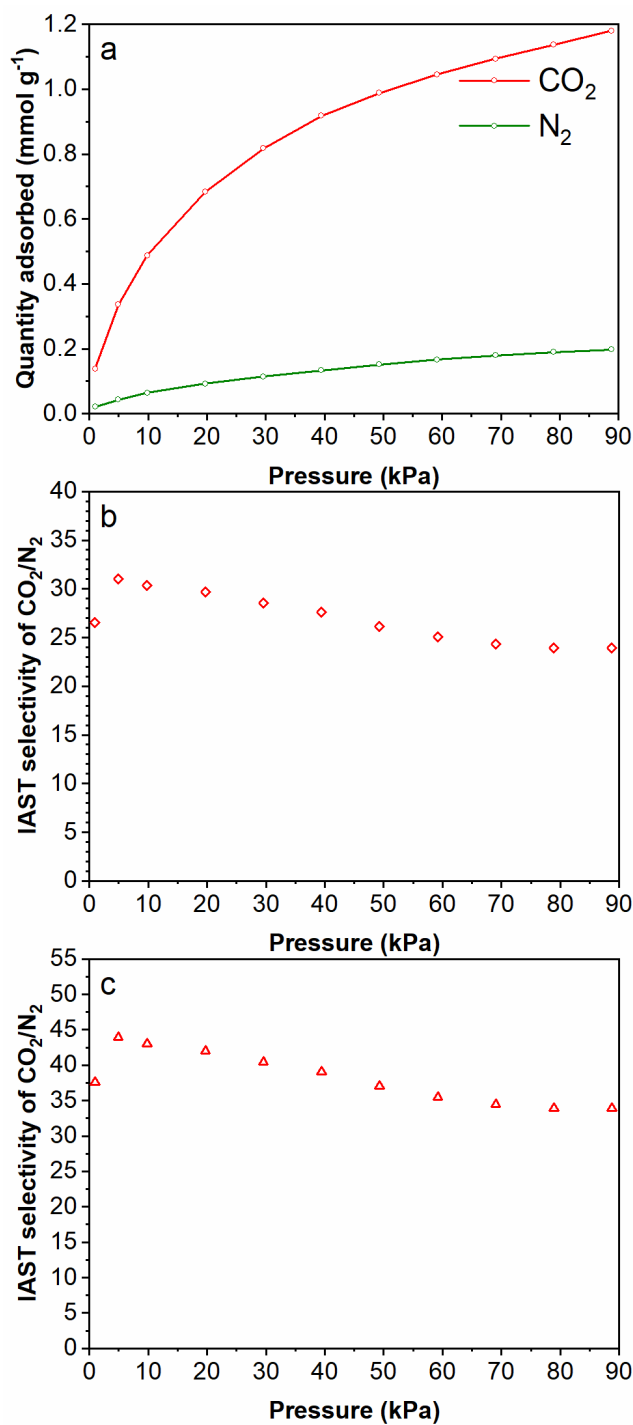
Figure 5.14: (a) CO_2 and N_2 adsorption isotherms at 30 °C and IAST-predicted selectivity for a gas mixture composed by (b) 20 vol. % CO_2 and 80 vol. % of N_2 and (c) by 15 vol. % CO_2 and 85 vol. % of N_2 for the sample G_600(40). Details on S_{IAST} calculation in Appendix A2, Paragraph A2.2.2.2.

5.2.4.4.   Reusability

Reusability of the sorbents was assessed by means of pure CO_2 adsorption measurements at 30 °C and at 20 kPa (0.2 bar), regenerating the sorbents under temperature swing adsorption (TSA) conditions, by heating up to 150 °C between two consecutive cycles (Figure 5.15a).
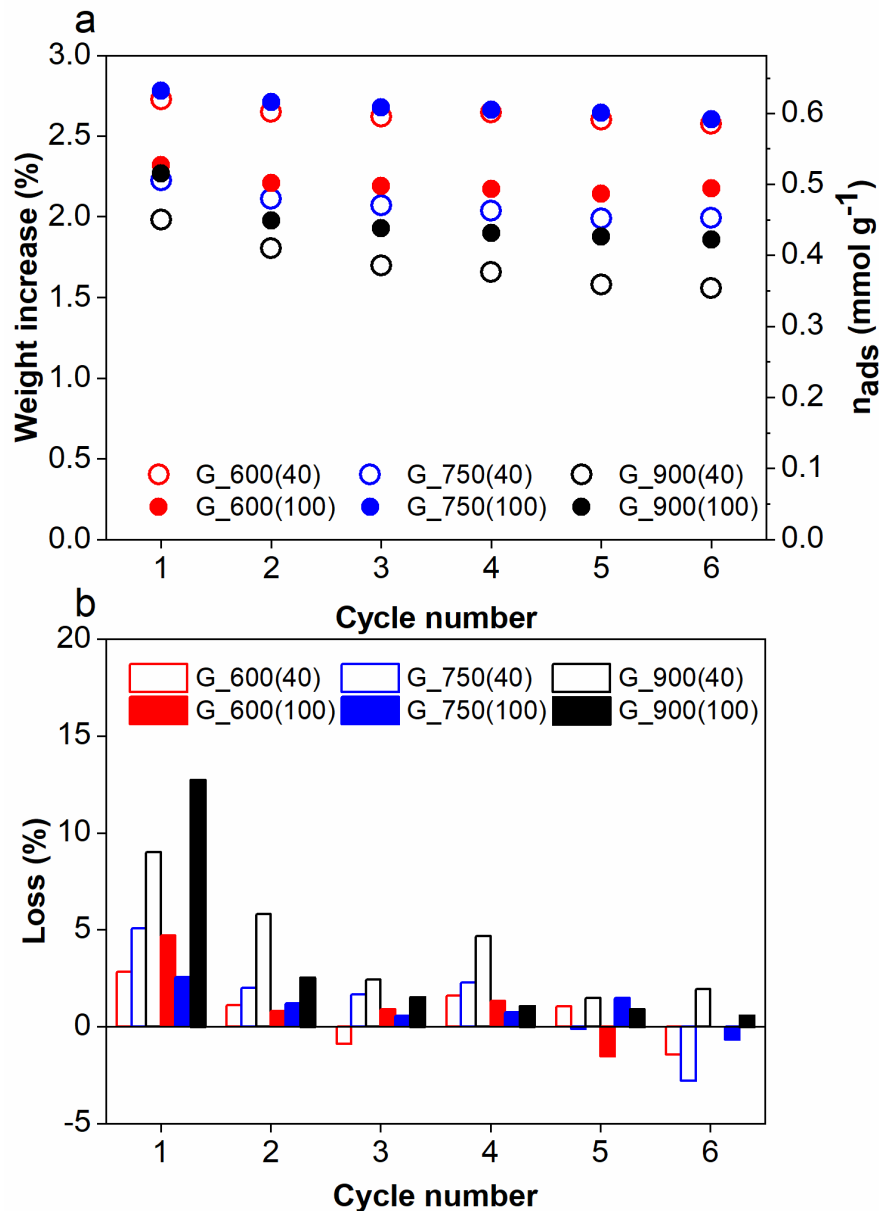
Figure 5.15: Reusability tests of G-series of NOMCs under repetitive adsorption (30 °C) - desorption (150 °C) cycles at 0.2 bar: (a) amount of CO_2 adsorbed and (b) regeneration efficiency over cycling.

Generally, the highest loss in adsorption performances (see Figure 5.15b) occurs between the first and the second cycle, thus a certain amount of CO_2 cannot be desorbed at 150 °C, likely because strongly bonded or remained trapped inside the narrowest micropores. After the second cycle, the adsorbed amount is almost unvaried, proving that the sorbents can be reused without losing their performances and, in addition, be sufficiently regenerated under mild conditions.

5.2.5. Comparison with other literature reports

To enlighten even more the quality and positive characteristics of the glucosamine-derived NOMCs prepared and characterized in this Thesis work, their performances are here compared with the most significant literature reports. These are detailed in Table 5.8 and were selected because similar in terms of overall physico-chemical features and comparable chiefly in terms of selective CO_2 adsorption in CO_2/N_2 gas mixtures. The first three entries of Table 5.8 refer to the presently developed OMCs/NOMCs described above, namely the undoped carbon sample S_900(100), and the most performing NOMCs in terms of pure CO_2 adsorption or CO_2/N_2 separation, viz. G_900(100) or G_600(40), respectively. It is worth noticing that, due to the heterogeneity of the testing conditions, a direct comparison among all the literature reports was hardly carried out. Actually, although a reliable evaluation of separation ability should be realized via gas mixture measurements [96], most of the research articles determine selectivity using single-components adsorption isotherms, by Henry's constant ratio, initial slopes (IS) of the adsorption isotherms (see references [91,92]) or the Ideal Adsorption Solution Theory (IAST) (see references [90,264,266,267]).

In terms of testing conditions, a complete comparison can be performed only with the work of García-Díez et al.[97]: both the NOMC samples developed here demonstrate slightly enhanced selectivity in CO_2/N_2 mixtures (20/80 v/v) [97]. Remarkably, adsorption is also performed at a higher temperature (35 °C vs. 25 °C in the literature counterpart), and no post-treatments for porosity modification are carried out. However, in order to allow a wider comparison with the majority of the literature works, S_{IAST} was calculated for the sample G_600(40) in a gas mixture composed of 15% of CO_2 and 85% of N_2 (see Figure S16 in SI). The most selective sample here synthesized (viz. G_600(40)) reports S_{IAST} within the range of 52-34 (0-90 kPa), perfectly in agreement with the works of Vorokhta et al. [90], Wan et al. [265] and Liu et al. [264] included in the comparison. In terms of pure CO_2 adsorption, even if this condition does not represent the key purpose of the present study, G_900(100) shows comparable CO_2 adsorbed amounts under similar adsorption conditions compared to the sample a-N-OMC reported by Chang et al.

[263]. Anyway, in the latter literature report [263], nitrogen groups were introduced via ammonia heat treatment and amine refluxing, while here no post-treatments are carried out. Samples OMC-20-80-24-700 [92], NOMC-L-0.5 [266], CN-0.45 [91], 0.52@PEI-AOMC [267], CMK-3 [90] and N-OMC-750 [264] seem to outperform the presently synthesized OMCs/NOMCs in terms of pure CO_2 adsorption. However, as a general drawback, the previously cited studies employed toxic carbon sources and/or additional activation steps for the adjustment of microporosity. On the contrary, here it has been shown that adsorbents with abundant and tailored porosity can be readily prepared by the nanocasting procedure, without requiring any further activation steps. Moreover, glucosamine hydrochloride, acting concurrently as both the carbon and the nitrogen source, allows the direct incorporation in a single step of the crucial N functionalities, bypassing time/energy consuming ammonia post-treatments or amine refluxing processes.

   Glucosamine hydrochloride itself is a non-toxic and potential natural occurring source of carbon, hence it shows highly promising prospects as a suitable raw material for biomass valorization in a circular economy loop. Finally, it is fair to underline that here the activation step before CO_2 adsorption measurements is performed at a higher temperature compared to the studies listed in Table 5.8. Therefore, regeneration conditions can be considered as a margin for improvement in this research, in order to make sorbents reuse more feasible from the energy consumption point of view.

Table 5.8: Comparison of the performance in terms of CO_2/N_2 separation of OMCs/NOMCs developed in this work with the most significant literature reports

Samples REF	Synthe-sis	Precursors	N %	CO_2 mmol·g^{-1}	CO_2:N_2	T_{ads}^n °C	P_{ads}^o bar	T_{act}^p °C
S_900(100)	H.T.^{f}	Sucrose	-	0.43 CO_2:N_2=20:80	-	35	1	300
				0.97 100% CO_2	-	30	0.9	
G_900(100)	H.T.^{f}	Glucosamine hydrochlor.	7.2^a	0.74 CO_2:N_2=20:80	-	35	1	300
				1.47 100% CO_2	-	30	0.9	
G_600(40)	H.T.^{f}	Glucosamine hydrochlor.	12.4^a	0.82 CO_2:N_2=20:80	-	35	1	300
				1.18 100% CO_2	52:1 – 34:1^c	30	0.9	

					CO_2:N_2= 15:85			
OMCreo CA 4:1 850[97]	H.T.[f] + C.A.[g]	Creosote	0.37[b]	~ 0.7 CO_2:N_2=20:80	-	25	1	120
OMCreo Pat 48%[97]	H.T.[f] + P.A.[h]		2.39[b]	~ 0.6 CO_2:N_2=20:80	-			
CMK-3[90]	H.T.[f]	Furfuryl alcohol	-	1.7 100% CO_2	-	20	1	200
				-	35.2:1 – 38:1[c] CO_2:N_2= 15:85	20-50		
OMC-20-80-24-700[92]	self-assembly	Resorcinol, HMT[j], urea, ammonia	0.78[a]	2.78 100% CO_2	29:1[d]	25	1	200
NOMC-L-0.5[266]	S.T.[i]	resorcinol, 3-aminophenol, L-lysine	2.5[a]	2.50 100% CO_2	43:1[c] CO_2:N_2= 15:85	25	1	120
a-N-OMC[263]	S.T.[i]	sucrose, ammonia, TEPA[k]	2.56[b]	1.41 100% CO_2	m.i.[e] CO_2:N_2= 10:90	35	1	120
CN-0.45[91]	S.T.[i]	resorcinol, HMT[j], ED[l]	2.97[b]	2.71 100% CO_2	28:1[d]	25	0.95	150
0.52@PEI-AOMC[267]	S.T.[i]	phloroglucinol formaldehyde resol, PEI[m]	21.58[b]	2.58 100% CO_2	64:1[c] CO_2:N_2= 10:90	30	1	180
N-OMC-750[264]	S.T.[i]	Terephthal-aldehyde, *m*-aminophenol, F127, urea	6.53[b]	1.64 100% CO_2	54.0:1[c] CO_2:N_2= 15:85	25	0.15	150

[a] determined by XPS (at. %); [b] determined by elemental analysis (wt. %); [c] determined by Ideal Adsorption Solution Theory (IAST) method; [d] determined by initial slope (IS) method; [e] m.i. denotes missing information; [f] H.T. is for hard template; [g] C.A. is for chemical activation; [h] P.A. is for physical activation; [i] S.T. is for soft templating; [j] HMT is for hexamethylenetetramine; [k] TEPA is for tetraethylenepentamine; [l] EDA is for ethylenediamine; [m] PEI is for poly(ethyleneimine); [n] adsorption temperature; [o] adsorption pressure; [p] activation temperature.

5.3.   Conclusions

D-glucosamine hydrochloride was successfully explored for the first time as a sustainable C/N precursor for the synthesis of nitrogen-containing ordered mesoporous carbons (NOMCs) obtained through the nanocasting technique and specifically conceived for selective CO_2 adsorption. The applied method enabled the accurate design of the pore characteristics through the convenient choice of the KIT-6 silica hard templates and the adjustment of the carbonization process. The effect of the pyrolysis temperature on the development of microporosity and of the different types of nitrogen inclusions was also accurately investigated. XPS analysis was used to identify the nitrogen species (pyridinic, pyrrolic and graphitic nitrogen-based structures), which were formed during the thermal treatment; their respective contribution on CO_2 adsorption and selectivity in CO_2/N_2 mixtures (20/80 v/v) was investigated.

The obtained results revealed that an enhanced micropore content, related to the higher pyrolysis temperature (900 °C), was effective in enhancing adsorption capacity in pure CO_2 flow. On the contrary, the lower pyrolysis temperature (600 °C) allowed for the retention of a higher amount of N inclusions in the carbon framework, mainly in the form of pyrrolic-N and pyridinic-N, the latter being particularly beneficial for improving the selective adsorption of CO_2. Specifically, a maximum CO_2 adsorption capacity of 1.47 mmol g^{-1} was achieved by the sample G_900(100) at 30 °C / 0.9 bar / pure CO_2, while a CO_2 uptake of 0.82 mmol g^{-1} was obtained by the sample G_600(40) at 35 °C / 1 bar / 20 % CO_2. In addition, reusability tests remarkably showed good capacity retention upon reversible and repetitive adsorption-desorption cycles. The maximum adsorption loss was registered between the first and the second cycle, which was ascribed to an insufficient regeneration temperature (150 °C) rather than an efficiency loss by the adsorbents.

In summary, the use of glucosamine hydrochloride as an environmentally friendly carbon/nitrogen source enabled the preparation of selective and high performing ordered mesoporous CO_2 adsorbents, with remarkable features of sustainability and regenerability. The newly developed NOMCs outperformed the undoped analogs obtained from sucrose, also standing amongst the most significant literature reports, chiefly in terms of selective CO_2 adsorption. The obtained results demonstrate that proper combination of the suitable C/N precursors, the synthesis conditions and the pore architecture are highly effective in obtaining high performing, sustainable and reusable CO_2 sorbents, without any need for time/energy consuming activation steps or N-doping post-treatments.

Chapter 6

6. CMK-3-type NOMCs investigated for CO$_2$ adsorption from moist flue gases

6.1.   Introduction

The current chapter details the results of the evaluation of the CMK-3-type N-containing ordered mesoporous carbonaceous sorbents, synthesized in the course of this Ph.D thesis, in terms of specific selectivity towards CO$_2$ capture in a simulated post-combustion flue gas mixture, thus including also N$_2$ and water vapour. The excess of N$_2$ due to the combustion of the fuel in air and the not-negligible impurities of H$_2$O vapor demand sorbents with high selectivity for CO$_2$ capture and the resistance in humid environments [311]. Therefore, after the standard characterizations under pure CO$_2$ and CO$_2$/N$_2$ gas mixtures, already adopted for the CMK-8- type sorbents described in Chapter 5, a special focus was devoted to the evaluation of the CO$_2$ uptake under moist conditions. Indeed, the incorporation of heteroatoms, such as O and N, provide some hydrophilic character to the bare-carbon frameworks, making the hypothesis of competitive CO$_2$/H$_2$O adsorption not negligible. Therefore, it was decided to proceed further with a more accurate analysis on H$_2$O adsorption and CO$_2$ capture from moist mixtures. This analysis was performed on the N-CMK-3 series of samples because the fundamental textural characterization and the preliminary study on CO$_2$ adsorption and CO$_2$/N$_2$ selectivity revealed slightly improved characteristics in comparison to the previously described CMK-8 materials.

Many recent literature reports addressed the problem of the preservation of good CO$_2$ adsorption performances from wet flue gases by water sensitive sorbents, like MOFs [312–318] and zeolites [319,320]. On the contrary, the problem of water contamination in post-combustion flue gases is usually considered less crucial for carbon-based materials, due to their intrinsic hydrophobic nature and their

remarkable tolerance towards moisture [85]. However, the absence of polar groups in hydrophobic carbons limits the efficiency for the selective CO_2 removal in real flue gas mixtures [321]. Hence, O and N, which are often introduced into the bare-carbon frameworks with the aim of enhancing the affinity for CO_2, increase at the same time the polarization and provide some hydrophilic character to the carbon surface [322]. For this reason, it is considered interesting and even unavoidable, the study of the influence of water contaminations on the selective CO_2 capture from simulated post-combustion flue gases by the here prepared N-containing carbonaceous adsorbents.

Similarly to the CMK-8 carbons, the here described N-containing CMK-3-type ordered mesoporous carbonaceous sorbents with high affinity towards CO_2 are prepared through a sustainable and scalable route that avoids post-synthesis functionalization methods. The nanocasting synthesis procedure, which involves SBA-15 ordered mesoporous silica as a hard template and D-glucosamine hydrochloride as a concurrent nitrogen/carbon source, is described in Paragraph A1.4, Appendix A1. The methodology used for the thorough characterization of the sorbents is included in Appendix A2. Precisely, the evaluation of the sorption properties under pure CO_2 and CO_2/N_2 gas mixtures is described in Appendix A2, Paragraphs A2.2.1 and A2.2.2, respectively. As mentioned above, the adsorption performances by the category of sorbents described in this Chapter are examined more in depth, by additionally focusing firstly on the evaluation of single component H_2O adsorption, and subsequently, on the selective CO_2 capture from wet simulated flue gas mixtures (CO_2/H_2O, relative humidity ranging from 0 to 75%), according to the methodology illustrated in Paragraph A2.3, Appendix A2. Finally, the reusability of the sorbents is also evaluated, both under repetitive adsorption-desorption cycles in pure CO_2, and by the comparison of the CO_2 adsorption capacity obtained by a fresh as-synthesized sample and on the same sample previously exposed to H_2O. This articulated analysis aims to provide a thorough evaluation of the potential applicability of the synthetized materials in industrial applications under real operation conditions.

6.2.   Experimental section

6.2.1. Materials and methods

The synthesis procedure for the preparation of the SBA-15 ordered mesoporous silica hard template and, subsequently, of the CMK-3-type N-containing ordered mesoporous carbons, namely N-CMK-3, is described in Appendix A1, Paragraphs

A1.2 and A1.4., respectively. The synthesis procedure aimed to tune the pore architecture and to achieve the right proportion of micropores and N content, by using D-glucosamine hydrochloride as concurrent C/N source and properly setting the pyrolysis treatment (the temperature of pyrolysis, T_p, was varied @ 600, 750 or 900 °C). The list of N-CMK-3 samples under study is summarized in Table 6.1.

Table 6.1: List of N-CMK-3 samples synthesized in this work.

Sample name	Carbon source	Pyrolysis temperature, T_p °C
N-CMK-3_600	Glucosamine hydrochloride	600
N-CMK-3_750	Glucosamine hydrochloride	750
N-CMK-3_900	Glucosamine hydrochloride	900

The methodology adopted for the physico-chemical characterization of the synthesized materials and the CO_2 adsorption testing is illustrated in Appendix A2, precisely the former in Paragraphs A2.1, the latter in Paragraphs A2.2 and A2.3. The schemes in Figure 6.1 illustrate the used technique, with a reference to the relative Paragraph in the Appendix A2 in which they are discussed.
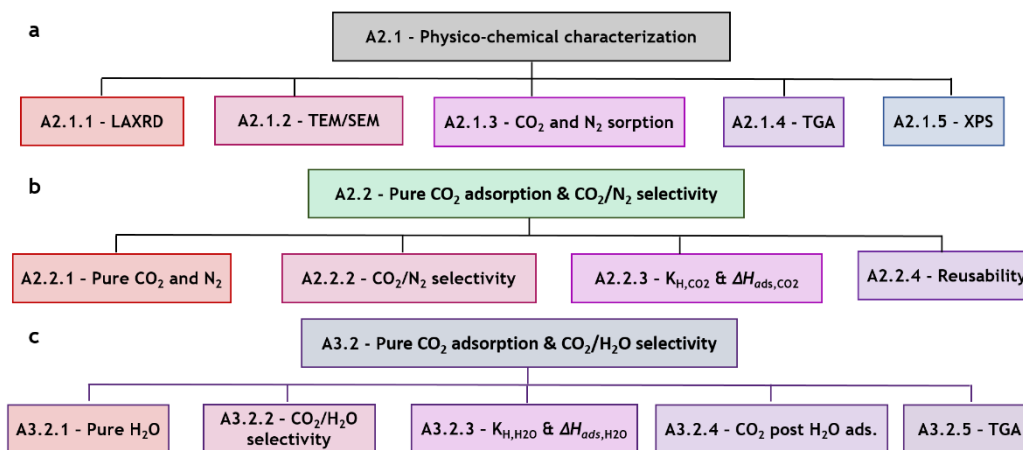
Figure 6.1: Scheme of the investigative methodology: a) physico-chemical characterization, and the evaluation of the performances in b) pure CO_2 adsorption and CO_2/N_2 selectivity, and c) pure H_2O adsorption, CO_2/H_2O selectivity and reusability after H_2O adsorption of the examined N-containing CMK-3 carbons.

6.2.2. Structural-morphological characterization

The textural properties of the N-CMK-3_X materials were investigated by LAXRD, TEM and N_2-physisorption. Figure 6.3b shows the LAXRD patterns of the N-CMK-3_X carbon replicas, that seem to possess analogous arrangement of the pores (*p6mm* hexagonal symmetry [217]) of the parent SBA-15 silica template (Figure 6.2a). The parent silica shows the typical three well-resolved peaks indexed as (100), (110) and (200) planes, while the N-CMK-3_X replicas only display the (100) reflection. The increase of the T_p above 750 °C improved the organization of the pores. The XRD unit cell size a_{100} was calculated from the (100) reflection using the expression $a_{100} = \frac{2}{\sqrt{3}} \cdot d_{100}$ [243], where the interplanar spacing d_{100} was calculated using the Bragg's law. The high-temperature treatment causes the shrinkage of the mesostructure in a higher magnitude as long as T_p increases [323,324], as observed by the reduction of the interplanar d-spacing and, consequently, of the unit cell size (Table 6.2).
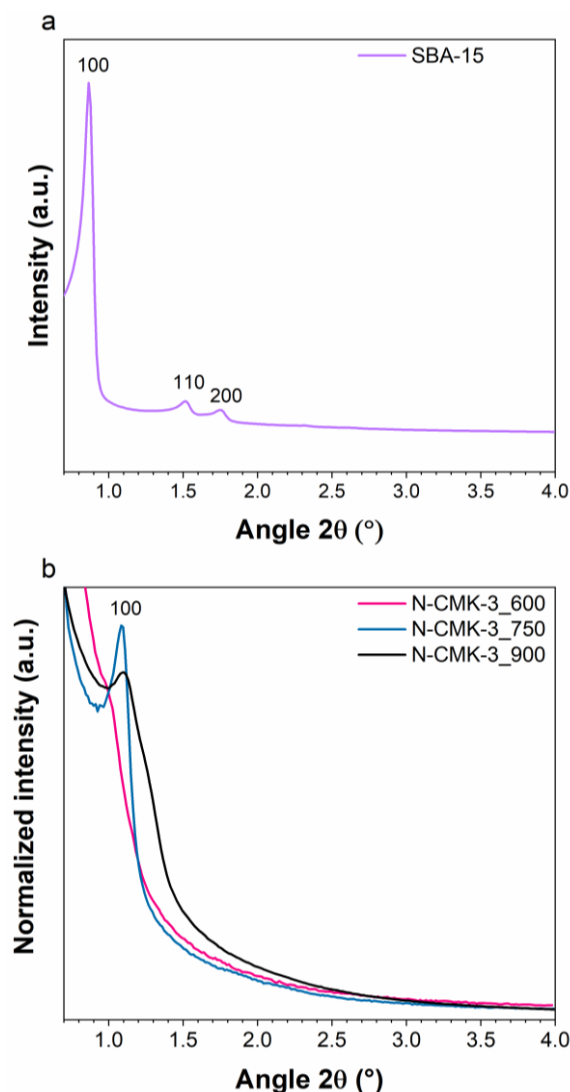
Figure 6.2: LAXRD diffraction patterns of a) SBA-15 OMS hard template, and b) N-CMK-3 samples obtained from the pyrolysis of the glucosamine-based precursor solution at different temperatures, namely N-CMK-3_600, N-CMK-3_750, N-CMK-3_900 (pink, cyan, and black, respectively). The intensity of the diffraction signal from N-CMK-3 samples is normalized in respect to the most intense peak.

The periodic alignment of the pores according to the typical arrangement of CMK-3-type materials is evident also from the TEM/STEM images shown in Figure 6.3, obtained using different objective apertures in order to optimize the image contrast.
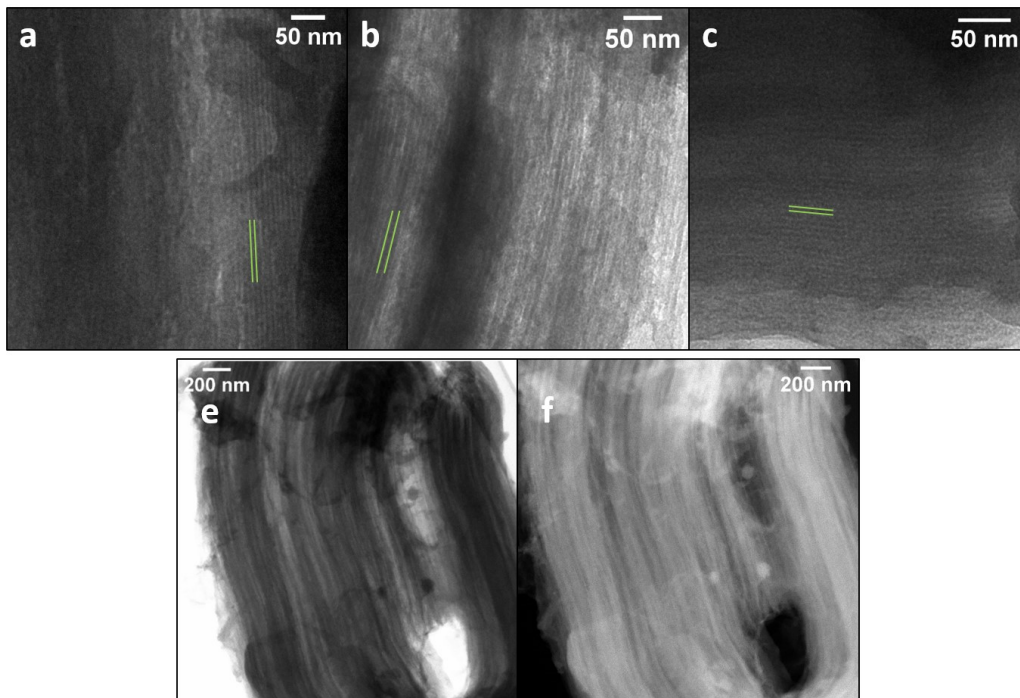
Figure 6.3 : TEM micrographs of a) N-CMK-3_600, b) N-CMK-3_750, c) N-CMK-3_900, and STEM images of N-CMK-750 sample obtained with d) BR and e) HAADF detectors, respectively.

N_2 adsorption-desorption isotherms at -196 °C show type IVa isotherms (Figure 6.4a and Figure 6.5a) for all CMK-3 and SBA-15 samples, which are typically observed on ordered mesoporous materials, with some character of type I [288]. The QSDFT model was selected to calculate the specific surface area and the mesopore size distribution of the N-CMK-3_X samples, as it fits remarkably well the experimental data (see Figure A.2.1). The values of specific surface area calculated by the BET model (S_{BET}) differ from the one calculated by the QSDFT model (S_{DFT}). Indeed, it is known that the BET method can be unreliable for highly microporous materials, owing to the impracticability of separating monolayer-multilayer adsorption and micropore filling [288,289]. Although the Rouquerol criteria partially helped in overcoming the complexity of determining the linear range of relative pressure where BET is applicable, BET area calculated on isotherms obtained on microporous materials does not represent the real probe accessible surface, but only an apparent surface area [289]. On the contrary, in the present case, the surface area and porosity parameters calculated with the QSDFT method are considered more reliable, by taking into account not only the geometry of the pores, but also the solid-fluid interaction and surface roughness [289,325].
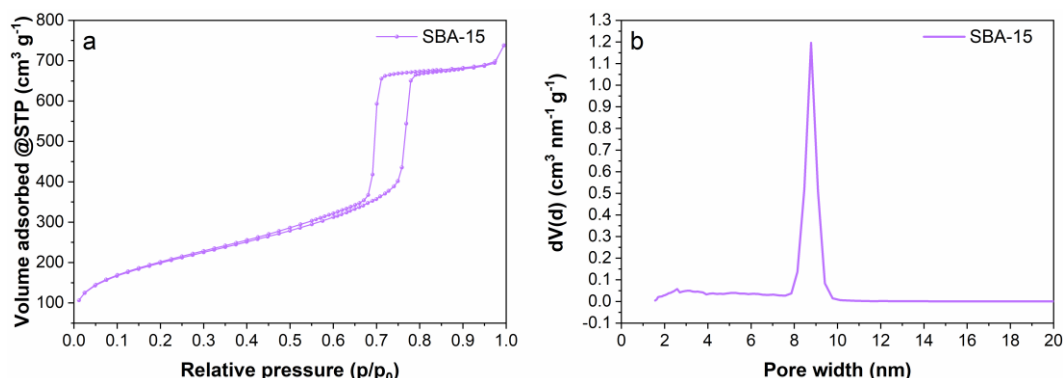
Figure 6.4: a) N$_2$ adsorption-desorption isotherm at −196 °C, b) NLDFT pore size distribution relative to the SBA-15 OMS hard template.

The mesopore size distribution (PSD) is narrow and centred approximately at 4.5 nm (Figure 6.5a) for the samples N-CMK-3_750 and N-CMK-3_900. Conversely, the sample N-CMK-3_600 shows lower specific surface area and pore volume and a less narrow pore size distribution in comparison to the other samples of the series.
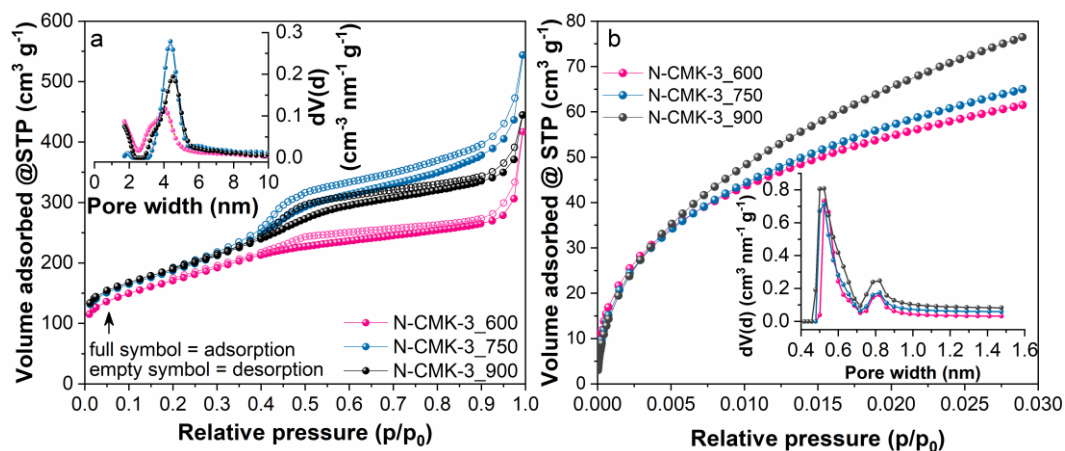
Figure 6.5: a) N$_2$ adsorption-desorption isotherms at −196 °C and, in the inset, the QSDFT pore size distribution in the mesoporous range of NOMC samples, i.e., N-CMK-3_600, N-CMK-3_750, and N-CMK-3_900 (pink, cyan, and black dots, respectively); b) CO$_2$ adsorption-desorption isotherms at 0 °C and, in the inset the, NLDFT pore size distribution in the microporous range of NOMC samples, i.e., N-CMK-3_600, N-CMK-3_750, and N-CMK-3_900 (pink, cyan, and black dots lines respectively).

The micro- and ultramicroporosity of N-CMK-3 samples was specifically analysed via CO_2 adsorption isotherms at 0 °C, taking advantage of the smaller kinetic diameter of CO_2 and the higher absolute temperature and pressure of analysis in comparison to N_2 sorption at cryogenic temperature, for concurrently increasing the adsorptive diffusion and its accessibility in very small pores (D_p < 0.4 nm),), as supported by relevant studies focused on the examination of the proper adsorptive for surface area and pore structural analysis [288,326,327]. From the observation of Figure 6.5b, it is possible to clearly see the presence of microporosity in N-CMK-3 samples, consisting in two populations of micro- and ultramicro-pores, with the maximum of the populations found at 0.8 and 0.5 nm, respectively. The quantities derived from N_2 and CO_2 sorption analysis are summarized in Table 6.2.

Table 6.2. Physicochemical properties of the ordered mesoporous materials prepared and under study in this work.

	a_{100}[a]	S_{BET}	S_{DFT}[b]	V_p[b]	D_p[b]	V_{ump}[c]	V_{mp}[c]	D_{mp}[c]
	nm	$m^2\,g^{-1}$		$cm^3\,g^{-1}$	nm	$cm^3\,g^{-1}$		nm
SBA-15	11.9	719	598	1.0	8.8	-	-	-
N-CMK-3_600	10.2	605	672	0.4	4.1	0.12	0.16	0.5; 0.8
N-CMK-3_750	9.2	656	921	0.6	4.4	0.12	0.19	0.5; 0.8
N-CMK-3_900	9.2	667	818	0.5	4.5	0.14	0.23	0.5; 0.8

[a]unit cell size (a_{100}) calculated using the expression $a_{100} = \frac{2}{\sqrt{3}} \cdot d_{100}$
[b]specific surface area (S_{DFT}), pore volume (V_p) and pore width (D_p) in the mesoporous range, calculated by NLDFT and QSDFT methods for silica and carbons, respectively, applied to N_2 isotherms at −196 °C
[c]ultramicropore volume (V_{ump}), micropore volume (V_{mp}) and pore width (D_{mp}) of N-CMK-3 samples in the microporous range, calculated by NLDFT method, applied to CO_2 isotherms at 0 °C.

6.2.3. Physico-chemical characterization

The CMK-3-type NOMCs samples are mainly constituted by the following elements: C (78.9, 79.1 and 83.4 at.%), O (8.4, 8.9 and 9.4 at.%) and N (11.3, 8.3 and 4.4 at. %), for N-CMK-3_600, N-CMK-3_750 and N-CMK-3_900, respectively, as derived from the XPS survey spectra shown in Figure A.2.8. The increment of T_p lead to the increase of the surface C relative amount as a consequence of the loss of heteroatoms [295]. Therefore, the highest surface atomic concentration of N was found in the sample N-CMK-3_600. Residual amounts of Na (< 2 at.%), S (< 0.5 at.%) and Si (< 0.7 at.%) were observed in all samples. Both Na and S are derived from the synthesis procedures, while the latter is likely related

to the remaining silica hard template. The presence of silica is, however, negligible, confirming the successful removal of the template. The contaminations of S might contribute positively to CO_2 capture [296–299]. However, here it was assumed that the sulfur-containing species are too low in amount for playing a relevant role in respect to the more abundant and properly modulated incorporation of N-species, as illustrated in Paragraph 5.2.3. Regarding the possible effect of S inclusions on the affinity of the carbon surface to water, Seredych et al. [328,329] reported that thiophenic compounds increase the surface hydrophobicity. Conversely, Li and coworkers [330] showed that the presence of water slightly affected the CO_2 capture by sulphur and nitrogen co-doped graphene sorbents. Therefore, based on these assumptions, the contribution of the S functionalities was considered negligible on the examined properties of the N-CMK-3 materials. Similarly, the residual Na from the silica etching procedure, besides being not irrelevant, is randomly distributed in the series of samples and likely does not affect the selectivity of CO_2 capture, since no obvious effects are described in the literature for similar systems. Hence, high-resolution (HR) acquisitions were performed in C1s, N1s and O1s regions to investigate the chemical bonding state of the most relevant elements. From C1s core level peaks three different carbon species were observed (see Figure A.2.9a, Figure A.2.10a and Figure A.2.11a in Appendix A2) assigned to C–C sp^2 (284.3 – 284.8 eV), C–O/C–N (285.9 – 286.5 eV), and C=O/C=N (286.5 – 287.6 eV) [292,293]. Oxygen signals (see Figure A.2.9c, Figure A.2.10c and Figure A.2.11c in Appendix A2) were fitted by using three components assigned to C=O ($\sim$531 eV), C–O ($\sim$533 eV), and COOH ($\sim$534 eV) [293], while the deconvolution of the N1s peak of NOMCs revealed three components assigned to pyridinic (C=N–C, N-6, 397.7 – 398.9 eV), pyrrolic (C–NH–C, N-5, 399.9 – 400.7 eV), and graphitic (C–NH–C, N-Q, 401.0 – 401.8 eV) nitrogen-based structures [292] (see Figure A.2.9b, Figure A.2.10b and Figure A.2.11b in Appendix A2). The relative percentages of each component were calculated from the fitted peak areas quantified by the deconvolution of the HR-XPS signals in the C1s, N1s and O1s regions.

The summary of the quantities derived from XPS analysis is reported in Table 6.3. It is possible to observe that the graphitization degree of the N-CMK-3_X samples increases with the rise of the temperature, observed by the increase of the C−C sp^2 and C=X relative contents. The evolution of nitrogen-containing moieties is related to their different thermal stability. The fraction of N-6 and N-5 decreases with the increase of T_p from 600 to 900 °C, because they are both transformed into N-Q in the pyrolysis temperature range of 600−800°C [294]. Accordingly, N-Q is detected in a higher concentration in the sample pyrolyzed at 900 °C. The O-functionalities are less sensitive to the thermal treatment, indeed their relative

percentage was found to be approximately unchanged in all the N-CMK-3 samples under study.

Table 6.3: Summary of the XPS analysis on the survey and high-resolution spectra of the C1s, N1s and O1s region for the N-CMK-3 samples.

	Peak	Amount[a]	Binding energy	Assignment	Fitted peak area	Fitted peak area[a]
		at.%	eV		counts s^{-1}	%
N-CMK-3_600	C1s	78.9	284.7	C–C	2835.0 $\pm$ 9.3	69.83
			285.8	C–O/C–N	939.2 $\pm$ 10.1	23.13
			287.1	C=O/C=N	285.6 $\pm$ 10.7	7.04
	N1s	11.3	398.4	C=N–C	442.9 $\pm$ 5.6	46.12
			400.4	C–NH–	454.4 $\pm$ 8.2	47.30
			401.3	C–NC–C	63.2 $\pm$ 8.3	6.58
	O1s	8.4	530. 9	C=O	698.3 $\pm$ 33.3	48.70
			532.5	C–O	560.4 $\pm$ 22.0	39.08
			533.5	COOH	175.2 $\pm$ 13.1	12.22
N-CMK-3_750	C1s	79.1	284.8	C–C	4813.3 $\pm$ 14.0	71.67
			285.9	C–O/C–N	1156.9$\pm$ 16.6	17.23
			286.6	C=O/C=N	745.7 $\pm$ 17.9	11.10
	N1s	8.3	398.4	C=N–C	477.3 $\pm$ 8.7	39.00
			400.3	C–NH–C	335.8 $\pm$ 19.1	27.44
			401.1	C–NC–C	410.8 $\pm$14.6	33.56
	O1s	8.9	530. 9	C=O	794.9 $\pm$ 8.8	48.70
			532.5	C–O	586.4 $\pm$ 11.6	39.08
			533.5	COOH	264. 3 $\pm$ 12.7	12.22
N-CMK-3_900	C1s	83.4	284.8	C–C	4860.8 $\pm$ 11.0	70.68
			286.2	C–O/C–N	1202.8 $\pm$ 11.9	17.49
			287.6	C=O/C=N	813.1 $\pm$ 16.0	11.83
	N1s	4.4	398.5	C=N–C	248.5 $\pm$ 6.5	35.94
			399.9	C–NH–C	115.2 $\pm$ 8.6	16.66
			401.1	C–NC–C	327.7 $\pm$ 28.6	47.40
	O1s	9.4	530.9	C=O	616.2 $\pm$ 7.9	46.72
			532.5	C–O	527.1 $\pm$ 12.4	39.98
			533.5	COOH	175.4 $\pm$ 11.4	13.30

[a]derived from the XPS survey scan
[b]the percent fitted peak area is here considered as an indication of the relative amount of each species in the sample.

6.2.4. Pure CO_2 adsorption measurements

The isosteric enthalpy of CO_2 adsorption $\Delta H_{ads,CO2}$ as a function of the surface coverage (CO_2 adsorbed amount, mmol g^{-1}) calculated for N-CMK-3-type samples is shown in Figure 6.6. The main contribution to $\Delta H_{ads,CO2}$ at low coverage is given by the occupation of the adsorption sites associated to a stronger affinity for CO_2 [301]. Successively, at higher loadings, $\Delta H_{ads,CO2}$ decreases as a function of surface coverage and stabilizes approximately to the heat of liquefaction of CO_2, i.e., approximately 17 kJ mol^{-1} in the considered temperature range, because at this point the system is approaching to the pore filling regime, where adsorbate-adsorbate interactions govern the mechanism of adsorption [331]. The values of $\Delta H_{ads,CO2}$ calculated for the N-CMK-3 samples synthesized in this work lay in the range of 30−38 kJ mol^{-1}, which is attributable to a physisorption mechanism (-25 to -50 kJ mol^{-1}) [21]. The values of $\Delta H_{ads,CO2}$ stay within an optimal energetic range (30–50 kJ mol^{-1}) for achieving concurrently efficient adsorption and easy regeneration [49,78].
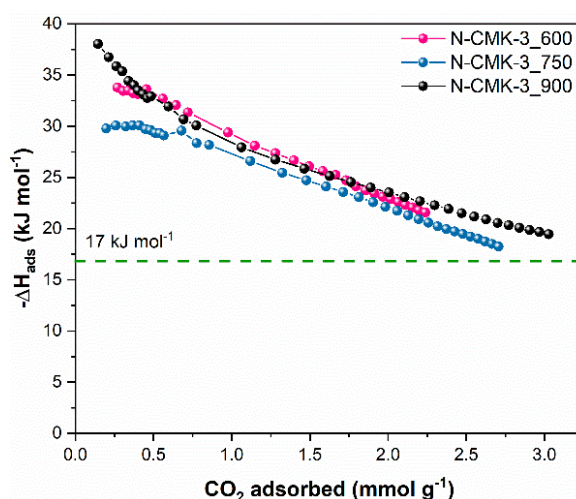
Figure 6.6: Isosteric enthalpy of CO_2 adsorption plotted against the amount of CO_2 adsorbed for N-CMK-3-type samples under study i.e., N-CMK-3_600, N-CMK-3_750, and N-CMK-3_900 (pink, cyan, and dark grey dots, respectively). The green dashed line describes the heat of liquefaction of CO_2 in the temperature range considered.

Henry's constant (K_H) and the virial coefficients C_1 e C_2 were also calculated from the CO_2 isotherms at 0 °C (Figure A.2.17) and listed in Table 6.4. K_H values follow the inverse trend of the pyrolysis temperature as a consequence of the loss

of heteroatoms during the high temperature heat treatment, as it was already observed for the CMK-8 samples described in Chapter 5.

Table 6.4: Henry's constants (K_H) and virial coefficients (C_1 and C_2) of CMK-3-type samples calculated from CO_2 isotherms at 0 °C

Samples	K_H mmol g^{-1} kPa^{-1}	C_1 g mmol^{-1}	C_2 (g mmol^{-1})^2
N-CMK-3_600	0.826 ± 0.032	1.730 ± 0.034	-0.177 ± 0.007
N-CMK-3_750	0.555 ± 0.016	1.442 ± 0.025	-0.146 ± 0.005
N-CMK-3_900	0.340 ± 0.013	0.991 ± 0.027	-0.093 ± 0.005

The evolution of pure CO_2 uptake in respect to the analysed temperature (from −10 to 30 °C) was associated to the most relevant features of the samples. Precisely, the amounts of CO_2 adsorbed by the samples at each temperature (reported in Table 6.5) are correlated to K_H values in the graph in Figure 6.7a.
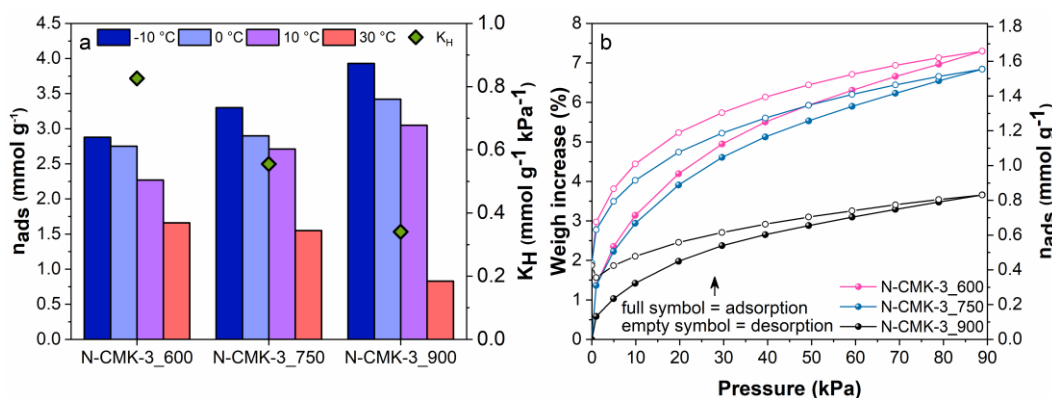
Figure 6.7: (a) Pure CO_2 uptake obtained at −10, 0 and 10 °C with a volumetric sorption analyser and at 30 °C using a gravimetric sorption analyser (column bars) and Henry's law constants (K_H) (green diamonds); (b) CO_2 adsorption-desorption isotherms measured at 30 °C up to 90 kPa with a gravimetric sorption analyser.

The N-CMK-3_900 sample shows the highest CO_2 adsorption capacity at low temperature (up to 10 °C) because, in this condition, the uptake is strongly influenced by micro- and ultra-micropore content. Generally speaking, all the sample experienced a sensitive drop in the capture ability due to the increase of the measurement temperature, which is nevertheless an intrinsic phenomenon of physisorption processes that causes a severe reduction of the uptake when T

approaches to more relevant values for a real application (e.g., 30 °C). This drop in adsorption capacity is more evident for the N-CMK-3_900 sample that shows a huge decrease in the adsorption capacity, $\sim$ 25% (at 30 °C) of the adsorption capacity measured at -10 °C. This difference is less pronounced in the samples pyrolyzed at lower temperatures. This behaviour further confirms that N species play a beneficial role in CO_2 uptake, especially at temperatures close to room temperature (RT) [303]. Indeed, N-CMK-3_600 material shows the highest values for both the K_H and CO_2 adsorption capacity (precisely 7.3 %, i.e., 1.55 mmol g^{-1} of adsorbed CO_2) recorded at 30 °C (Figure 6.7b and Table 6.5), that can be associated to the higher amount of N species present in this sample.

Table 6.5: Pure CO_2 adsorption at -10, 0 and 10 °C in a volumetric sorption analyzer [a] and at 30 °C in a gravimetric sorption analyzer[b]

Sample name	$CO_{2,ads}$[a] @ -10 °C mmol g^{-1}	$CO_{2,ads}$[a] @ 0 °C mmol g^{-1}	$CO_{2,ads}$[a] @ 10 °C mmol g^{-1}	$CO_{2,ads}$[b] @ 30 °C mmol g^{-1}
N_CMK-3_600	2.88	2.75	2.27	1.66
N_CMK-3_750	3.30	2.90	2.71	1.55
N_CMK-3_900	3.93	3.42	3.05	0.83

Pure CO_2 sorption analysis using [a] a volumetric sorption analyzer (p = 1 bar); [b] a gravimetric sorption analyzer (p = 0.89 bar).

6.2.5. Reusability assessment by multiple CO_2 adsorption-desorption cycles

Ten cycles of adsorption-desorption were performed on N-CMK-3 samples, accordingly to the procedure described in Paragraph A2.2.4, Appendix A2 in order to assess the reusability of the sorbents (Figure 6.8). The samples under study showed good reproducibility upon repetitive use under pure CO_2 adsorption measurements at 30 °C and at 20 kPa (0.2 bar). The regeneration of the sorbents was carried out by heating up to 150 °C between consecutive cycles (TSA process). The highest efficiency loss (up to ca. 10 and 16% for N-CMK-3_600 and N-CMK-3_900 samples, respectively) occurred between the first and the second cycle. For both samples, a certain amount of CO_2 cannot be desorbed during the regeneration steps at 150 °C, likely because the adsorbate is strongly bonded to the high energy N-sites or trapped inside the micropores, and thus a higher temperature is required for the complete desorption, as later explained in Paragraph 6.2.9 by TGA-FTIR

and N_2 sorption analysis performed after the adsorption tests. After the second cycle, all the N-CMK-3 studied samples proved to be stable and the adsorbed amount is almost unvaried. This evidence demonstrated that the sorbents can be reused in multiple adsorption/desorption cycles from dry flue gases without losing their performances and, in addition, be satisfactorily regenerated under mild conditions.
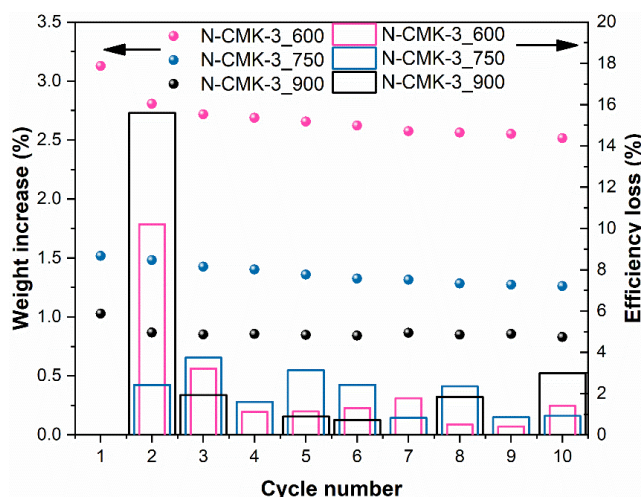
Figure 6.8: Reusability tests of the studied N-CMK-3 samples under repetitive adsorption (30 °C) - desorption (150 °C) cycles at 0.2 bar. The efficiency loss is calculated in respect to the previous cycle.

6.2.6. CO_2/N_2 adsorption measurements

TGA measurements were performed at 35 °C and 1 bar exposing the samples to a mixture, which simulates a typical exhaust gas [26] (20 vol.% CO_2 and 80 vol.% of N_2), in order to evaluate the competitive adsorption of these two gases. The experimental methodology is schematically sketched in Figure A.2.15, Appendix A1 and the recorded mass change profile is shown in Figure 6.9a. N-CMK-3_600 sample, benefitting of the higher surface N content and, particularly, of the superior concentration of pyridinic-N inclusions, achieved an improved selectivity in CO_2/N_2 mixture, which allowed a 4.52 wt.% weight increase (1.03 mmol g^{-1}), as shown in Figure 6.9b and Table 6.6. Similarly to what was observed for the pure CO_2 adsorption measurement, the increase of the pyrolysis temperature promotes a decrease in the selectivity towards CO_2 in the N_2/ CO_2 separation process, which can be associated with the lower quantity of N-6 species in the materials pyrolyzed at higher temperature (*cf.* XPS quantification inTable 6.3). Indeed, pyridinic-N inclusions are considered to provide the stronger contribution to CO_2 adsorption

among the other types of N-containing functional groups. This is likely related to the strong basicity, derived from the lone pair electron of the N atom, which establishes a Lewis acid-base interaction with the electron-deficient carbon atom of the CO_2 molecule [99,171,302]. Moreover, the work of Lin et al. [306] also demonstrated the highest difference between CO_2 and N_2 adsorption energies for the pyridinic group in respect to several analysed N-functionalities, pyrrolic and quaternary N included, thus resulting in improved CO_2/N_2 selectivity [306].
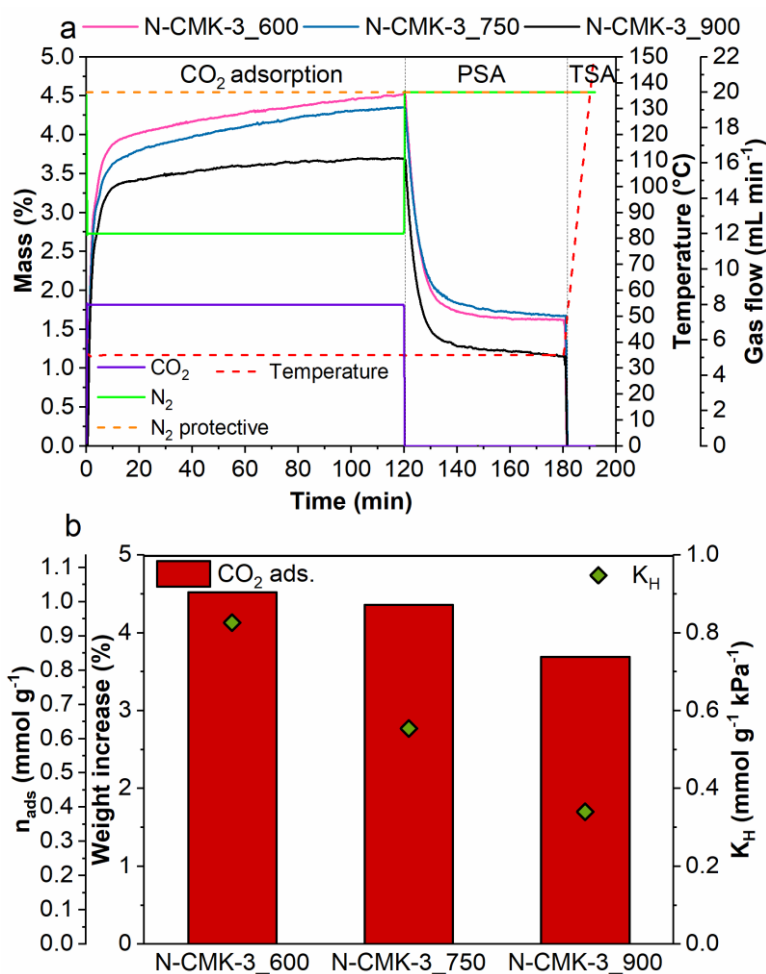
Figure 6.9: (a) Adsorption and desorption steps for CO_2/N_2 adsorption measurements of the N-CMK-3 samples under study, and (b) weight increase due to the CO_2 adsorption in a gas mixture of 20 vol. % CO_2 and 80 vol. % of N_2 at 35 °C. Details on setup for CO_2/N_2 selectivity tests by TGA in Figure A.2.15, Appendix A2.

The regenerability of the sorbents was also considered by the quantification of the percentage of released CO_2 in PSA conditions (third column in Table 6.6). The promotion of the desorption of CO_2 by simply applying a flow of N_2 as in this case is more convenient from an energetic point of view than in the TSA condition effectively applied in Paragraph 6.2.5. It is interesting to observe that almost the overall amount of the adsorbed CO_2 is released in PSA conditions (Figure 6.9a). Then, heating was applied to remove the strongly bonded CO_2. At T < 150 °C, most of the adsorbed CO_2 is released. In addition, under these conditions, the adsorption capacity and selectivity results are consistent with the trend of the calculated K_H values (see Table 6.4).

Table 6.6: Adsorption and desorption analysis of mixed CO_2/N_2 (20/80, v/v) adsorption tests by TGA.

Samples	Mass change wt.%	CO_2 ads mmol g^{-1}	Released CO_2 in PSA wt.%
N-CMK-3_600	4.52	1.03	− 2.90
N-CMK-3_750	4.36	0.99	− 2.68
N-CMK-3_900	3.69	0.84	− 2.55

6.2.7. H_2O adsorption measurements

Single component H_2O adsorption isotherms were performed at four different temperatures, i.e., 30, 40, 50 and 60 °C (Figure 6.10). It is worth taking in consideration that owing to the relatively unstable H_2O adsorption observed by the as-synthesized samples, that revealed their poor hydrophilic character, the isotherms shown in Figure 6.11 are obtained after previous H_2O adsorption measurements at 30 °C. As a result, the carbon-based adsorbents gain increased hydrophilicity after a previous adsorption of water, as shown in Figure 6.11, in agreement with the mechanism of adsorption governed by cluster formation hypothesized by Horikawa et al. [332]. In details, the H_2O adsorption-desorption curves in Figure 6.11 present a sort of type IV isotherm (IUPAC denomination [288]), characterized by Type I character at very low partial pressure [322], indicative of an onset of water adsorption at very low pressure. A change in the concavity of the adsorption/desorption branches describes a two stage-adsorption mechanism, which involves firstly the filling of micropores in the low relative pressure regime and, subsequently, of mesopores at higher pressure. In the present

case, the growing trend of total adsorbed water while increasing the analysis temperature is ascribable to the higher water vapour saturation pressure ($p_{H2Osat,T}$), which allows at conducting the analysis at increased absolute pressure values.
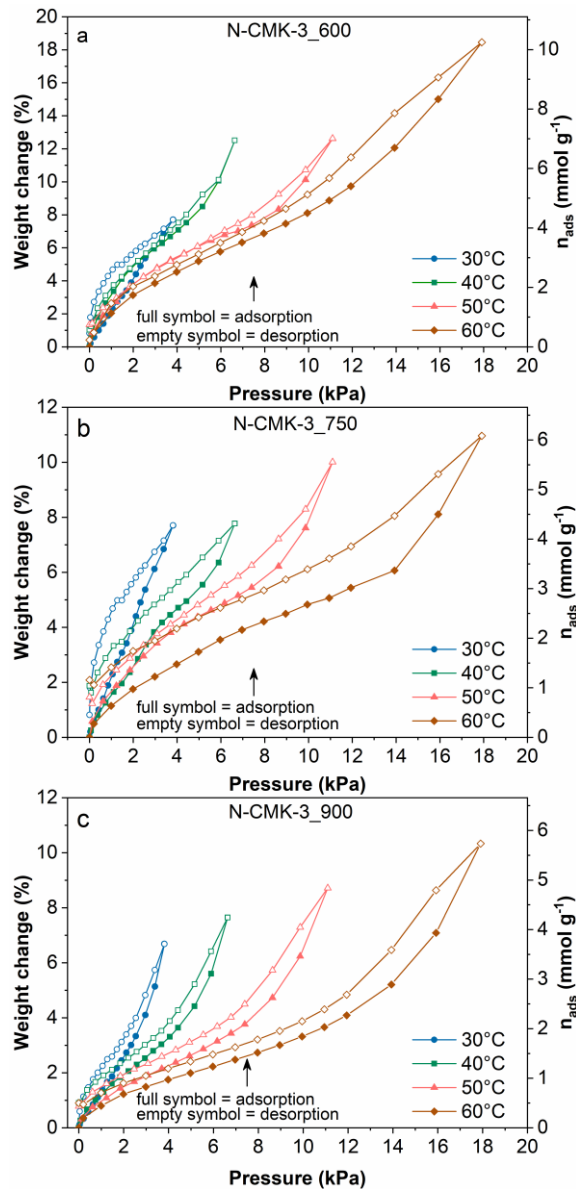
Figure 6.10: Pure H_2O isotherms measured at 30, 40, 50 and 60 °C with a gravimetric sorption analyzer. The weight change was plotted against the relative pressure (p/p_0): N-CMK-3_600 sample (a,), N-CMK-3_750 sample (b), N-CMK-3_900 (c).

Indeed, in the relatively low-pressure regime, the amount of adsorbed H_2O is higher for the isotherms obtained at lower analysis temperature. For the sake of clarity, the

amount of H_2O adsorbed by the N-CMK-3-type samples under study at the respective temperature of analysis is summarized in Table 6.7.
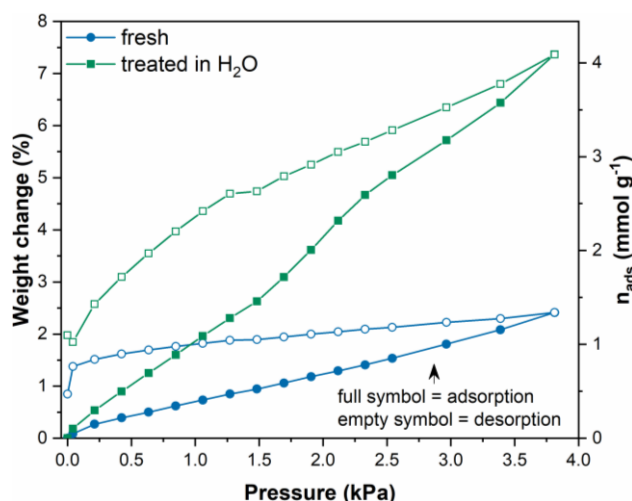
Figure 6.11: H_2O adsorption on N-CMK-3_750 sample: comparison between the fresh untreated sample and the same sample already exposed to water.

From the reported data, it is possible to observe that H_2O adsorption is higher in the N-CMK-3_600 sample than for N-CMK-3_750 and N-CMK-3_900 ones. This evidence is consistent to the predictions, since the more abundant incorporation of heteroatoms (namely, O and N) in the carbon framework obtained at the lowest T_p provides a stronger hydrophilic character. Indeed, N and O species are considered to promote water adsorption especially in the low and intermediate pressure region [332,333], and according to the study of Kumar et al. [334], water vapour adsorption is more influenced by the local density of N species than on the type of N species.

Table 6.7: Pure H_2O adsorption at 30, 40, 50 and 60 °C in a gravimetric sorption analyzer.

Sample name	H_2O_{ads}[a] @ 30°C mmol g^{-1}	H_2O_{ads}[b] @ 40 °C mmol g^{-1}	H_2O_{ads}[c] @ 50 °C mmol g^{-1}	H_2O_{ads}[d] @ 60 °C mmol g^{-1}
N-CMK-3_600	4.28	6.94	7.00	10.25
N-CMK-3_750	4.09	4.31	5.55	6.08
N-CMK-3_900	3.71	4.24	4.39	5.73

Absolute pressure: [a] p = 0.04 bar; [b] p = 0.07 bar; [c] p = 0.11 bar; [d] p = 0.18 bar.

Despite an increased affinity for H_2O given by heteroatoms incorporation inside the pristine carbon surface, the N-CMK-3-type samples under study exhibited a relatively poor hydrophilic character if compared to other highly hydrophilic N-doped carbons, which achieved 4−5 orders of magnitude higher H_2O uptake in the low relative pressure range [322]. This conclusion is particularly encouraging in the perspective of their application of as selective CO_2 sorbents from moisture flue gases.

Analogous observations are also derived from the quantification of the isosteric enthalpy of water adsorption ($-\Delta H_{ads,H2O}$). In the considered loading range, the $\Delta H_{ads,H2O}$ values of all the N-CMK-3 samples (see Figure 6.12) attain below the enthalpy of condensation of water, which lays approximately in the range 42−44 kJ mol^{-1} in the analysed temperature range (30−60 °C) [335]. This indication confirms the hydrophobic nature of the NOMCs samples. However, despite the average behavior, the samples locally present some specific sites, such as micropores or O- or N- sites, where $-\Delta H_{ads,H2O}$ approaches the enthalpy of condensation of water. Precisely, the adsorbate-adsorbent interactions govern water adsorption at low coverage [336]. Hence, the initial modest values of $-\Delta H_{ads,H2O}$ for the N-CMK-3_750 sample likely derive from the lower N content, which causes a weaker affinity for the H_2O, in respect to the N-CMK-3_600 sample. In the case of the N-CMK-3_900 sample, the high content of micropores likely compensates the low concentration of N-species. As the adsorption progresses, the energy involved in the water cluster formation becomes dominant and mostly influences $\Delta H_{ads,H2O}$ values.
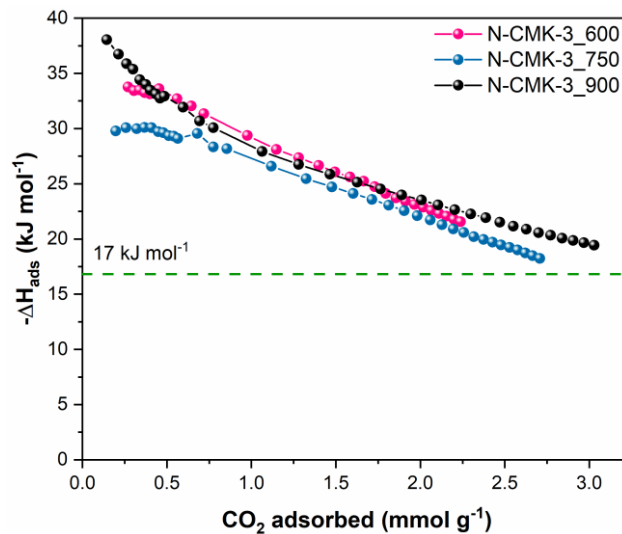
Figure 6.12: Isosteric enthalpy of H_2O adsorption plotted against the amount of H_2O adsorbed calculated in the temperature range 40−60 °C for N-CMK-3_600 (pink), N-CMK-3_750 (cyan) and N-CMK-3_900 (dark grey) samples. The patterned green area describes the range of values for the water heat of condensation in the temperature range considered.

6.2.8. CO₂ adsorption under humid conditions

Three consecutive adsorption-desorption cycles were performed, accordingly to the methodology described in Paragraph A2.3.2, Appendix A2, on the two most promising samples (N-CMK-3_600 and N-CMK-3_750). Different ratios of CO_2 and H_2O at 30 °C were used to study the ability of the samples to capture CO_2 under humid condition. Figure 6.13 shows the weight change of the samples resulting from the exposition to different mixtures of H_2O and CO_2. During the 1st cycle (Figure 6.13 and Figure 6.13b), RH was kept constant at 25%, while CO_2 partial pressure (p_{CO2}) was varied from 0 to 65 %. An increment of p_{CO2} at constant RH corresponds to an increase in the weight of the samples, which is attributable to CO_2 adsorption. The same evidence is observed during the 2nd cycle (Figure 6.13c and Figure 6.13d), when RH was kept constant at 50% and p_{CO2} gradually increases from 0 to 40%. It is worth noticing that a certain amount of the adsorbed species did not desorb during the 1st cycle, thus occupying part of the available pore volume and, in turn, hindering the utilization of the maximum capacity of the sorbents during the subsequent cycles. The same adsorption behaviour is observed during the 2nd cycle (Figure 6.13c and Figure 6.13d), when RH was kept constant at 50% and p_{CO2} gradually increases from 0 to 40%. However, it is encouraging to observe

that the samples are able to capture CO_2 even if water is previously adsorbed in the porosity of the samples and this increment of the sample weight is directly proportional to p_{CO2}. During the 3rd cycle, RH was gradually increased and stabilized at 75% (Figure 6.13e and Figure 6.13f). Subsequently, 15% of p_{CO2} was added.
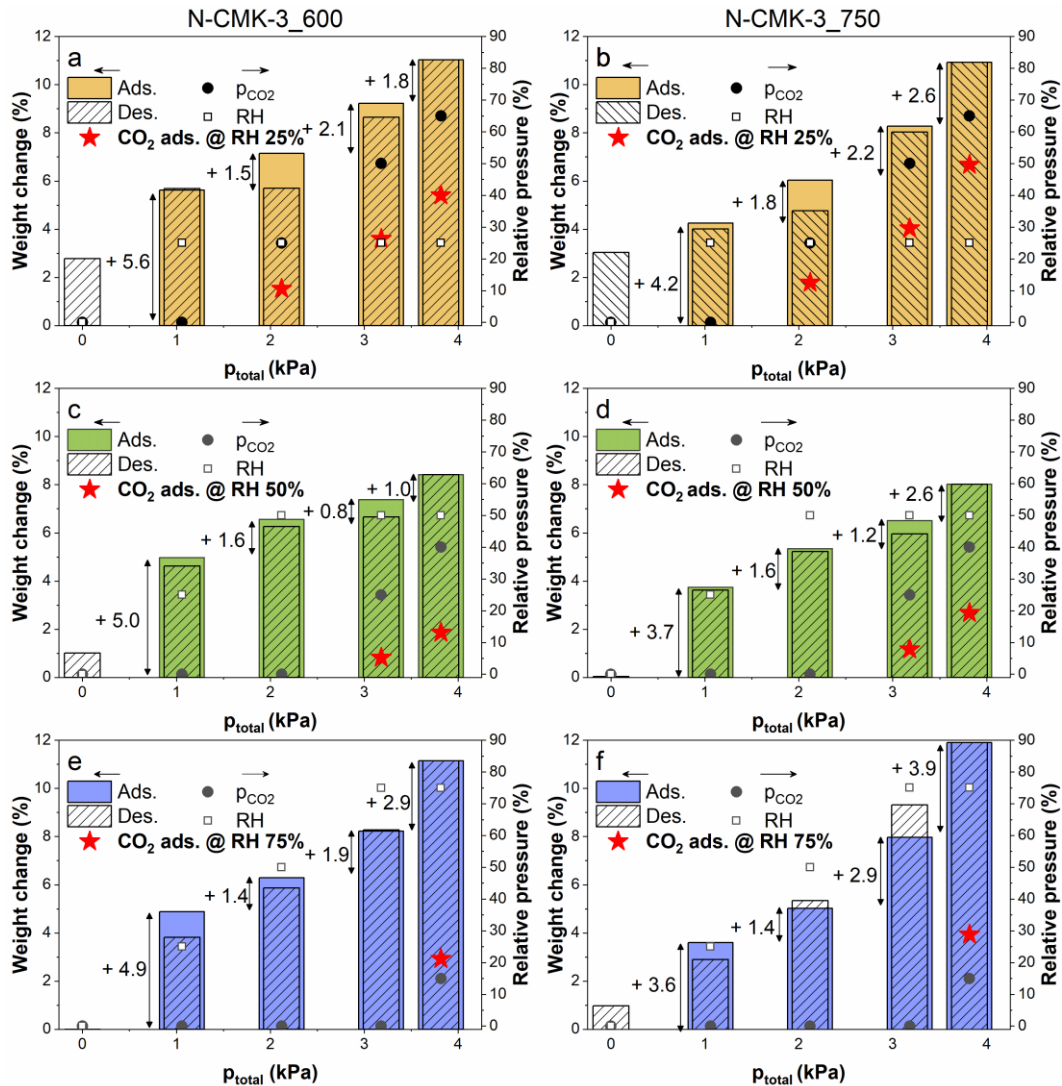
Figure 6.13: Weight increase *vs* total pressure derived from cyclic CO_2/H_2O adsorption-desorption tests performed at 30 °C at different relative pressure of H_2O and CO_2 according to the scheme in Figure A.2.20, Appendix A2. The data refer to the sample N-CMK-3_600 (a, c and e are for 1st, 2nd and 3rd adsorption/desorption cycle, respectively) and to the sample N-CMK-3_750 (b, d and f are for 1st, 2nd and 3rd adsorption/desorption cycle). The arrows indicate weight increase between two

consecutive adsorption cycles and the star symbol indicates the weight increase due to CO_2 adsorption at a certain RH.

The introduction of CO_2 caused a remarkable increment of the weight correspondent to 2.9 and 3.9 % for N-CMK-3_600 and N-CMK-3_750 samples, respectively. Generally, sample N-CMK-3_750 adsorbs a lower amount of H_2O, as observed also in single component isotherms (see Figure 6.10 and Table 6.7), and a higher amount of CO_2 in comparison to the sample N-CMK-3_600 under humid conditions. In Table 6.8 the amounts of CO_2 adsorbed under different conditions of humidity are reported. The maximum amount of adsorbed CO_2 in presence of water (RH = 25%) is comparable to the one under pure CO_2 (see Figure 6.7), which means that the presence of moisture does not affect the ability of the adsorbents to capture CO_2, especially for the N-CMK-3_750 sample. However, by rising the RH up to 75%, the amount of CO_2 adsorbed was significantly reduced. Nonetheless, this behavior is not linear. For instance, the quantity of the CO_2 adsorbed decreases after the increase of RH from 25% to 50%, but on the contrary, the adsorbed CO_2 amount increased from RH 50% to 75 %. A similar behaviour has already been reported in the literature [337–339], demonstrating that the effect of H_2O on CO_2 adsorption is a balance between the competition towards the occupation of the adsorption sites and the promotion of side reactions at the N-species that increase CO_2 consumption. Considering the two examined samples, the lowest affinity for H_2O shown by the N-CMK-3_750 allowed a higher retention of satisfying CO_2 capture capabilities in presence of water. This result makes it the most suitable sorbent among the studied ones for CO_2 capture under humid conditions. It is fair mentioning that no activation process was applied between consecutive cycles (see Paragraph A2.3.2 in Appendix A2), so the CO_2 uptake recorded at 50% and 75% RH might be improved by applying heating before any measurement.

Table 6.8: CO_2 adsorption at 30 °C under different humidity percentage for the N-CMK-3-type samples under study.

Sample name	$CO_{2,ads}$[a] @ RH 0 % mmol g^{-1}	$CO_{2,ads}$[b] @ RH 25% mmol g^{-1}	$CO_{2,ads}$[c] @ RH 50% mmol g^{-1}	$CO_{2,ads}$[d] @ RH 75% mmol g^{-1}
N-CMK-3_600	1.66	1.23	0.42	0.66
N-CMK-3_750	1.55	1.52	0.61	0.89

[a] p_{CO2} = 89 kPa, [b] p_{CO2} = 2.8 kPa, [c] p_{CO2} = 1.7 kPa, [d] p_{CO2} = 0.6 kPa.

6.2.9. Assessment of sorbents reusability after H_2O adsorption

The adsorption in pure CO_2 at 30 °C was repeated after the tests under humid gas mixtures (as described in Paragraph A2.3.3), observing a considerable reduction in the CO_2 uptake after the exposition to water (− 45% for N-CMK-3_600 and − 65% for N-CMK-3_750). This might be related either to the incomplete desorption of the adsorbates from the previous tests, even upon reactivation at 300 °C under vacuum, or to a structural collapse during the reactivation, promoted by the same trapped gases. Indeed, some irreversibility between adsorption and desorption was observed during the CO_2/H_2O adsorption tests in Figure 6.13). As a matter of fact, at the end of the desorption branch of the 1st cycle, the final weight of the sample was around the 3% of the initial weight (see Figure 6.13a and Figure 6.13b). The amount of the gas that is unable to be desorbed during the 1st cycle, occupies the porosity, thus hindering the utilization of the maximum capacity of the sorbents during the subsequent cycles.
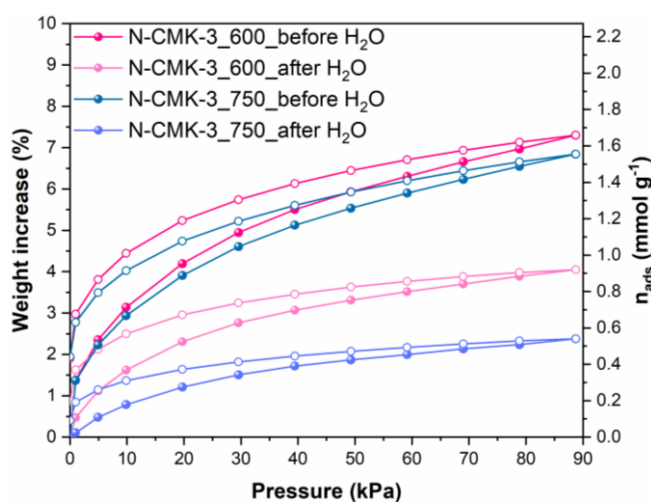
Figure 6.14: a) Pure CO_2 isotherms at 30 °C up to 90 kPa performed before and after H_2O adsorption by the N-CMK-3-type samples under study.

In order to confirm or confute the more convincing hypothesis of unsuccessful regeneration as the main cause of the decrease of CO_2 uptake, even after the usual activation process at 300 °C preceding each measurement, a further analysis of the textural features before and after the exposition to H_2O on N-CMK-3_600 sample was performed by N_2 adsorption-desorption isotherms at −196 °C, according to the procedure described in Paragraph A2.3.3, Appendix A2. This sample was chosen

among others of the N-CMK-3 series for its more marked hydrophilic character, derived from the higher content of N-species. The samples were activated at 300 °C under vacuum for 1 h before the analysis, in conformity with the procedure used for the measurements under CO_2/H_2O atmosphere. A further attempt was considered by extending the activation treatment up to 12 h, with the aim of evaluating the potential beneficial effect of a longer treatment in improving the evacuation of the adsorbed species. The isotherms obtained in Figure 6.15a of the fresh sample and to the same sample treated in H_2O and subsequently activated for 1 h or 12 h are characterized by the same combination of type I plus type IV typology, confirming the retention of the peculiar CMK-3 mesostructure. Similarly, the dimensional distributions of the pores in Figure 6.15b are all roughly comparable, thus unequivocally supporting the hypothesis of pore occlusion by the H_2O molecules, rather than the structure collapse during water adsorption tests and/or the reactivation treatment. Nevertheless, the sample treated in H_2O shows a sizeable reduction of the BET surface area, total pore volume and micropore volume, even after the activation procedure, with a stronger deterioration, as predictable, in the case of the shortest duration of 1 h. Precisely a reductions of − 60.6 % of S_{BET}, −47.1 % of V_p, and −89.6 % of V_{mp} were recorded in the case of the activation at 300 °C for 1 h. The longer treatment carried out at 12 h only slightly helped in restoring the initial textural features. The dramatic decrease of the micropore volume is the most remarkable information deduced from this analysis since this element is important for CO_2 adsorption. Therefore, it is reasonable that the considerable reduction of the number of these preferential sites of adsorption is the cause of the inability to restore the initial uptake capability by the considered sample. Indeed, the disappearance of the population of pores < 1 nm and of certain populations in the mesopores range within 2−5 nm is clearly observed after H_2O adsorption in respect to the fresh sample, while other populations appear completely unaffected.
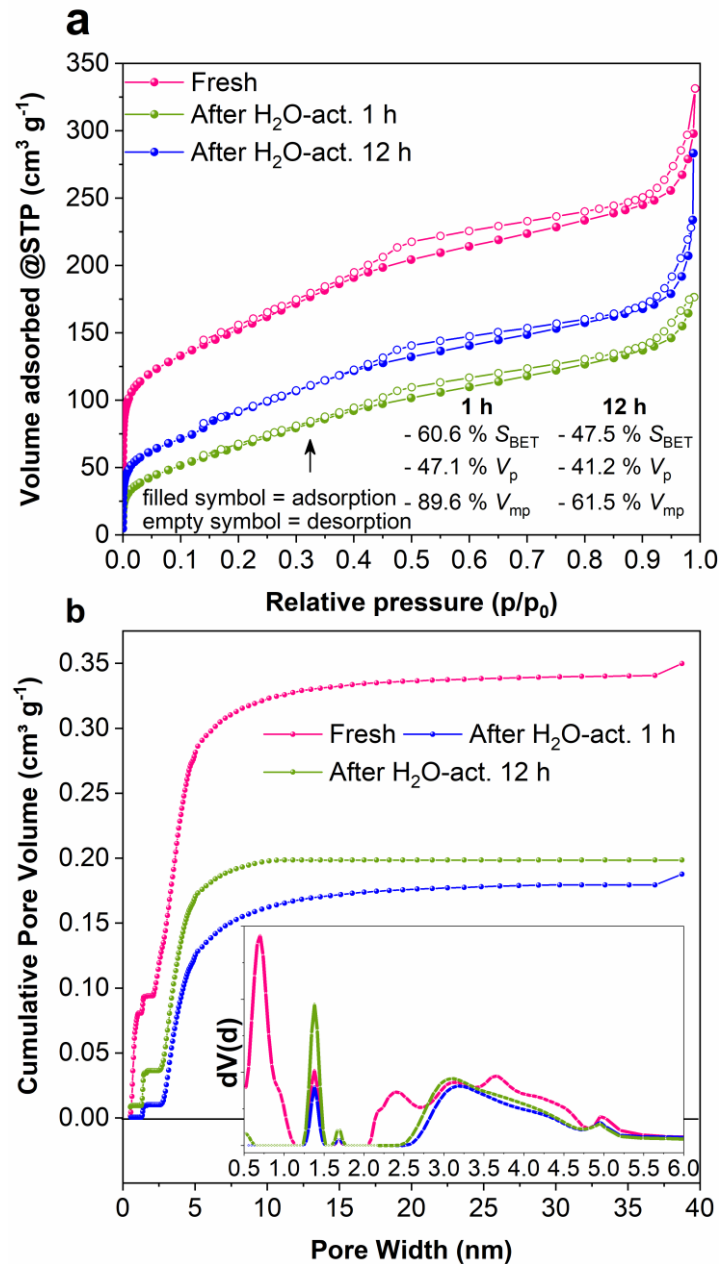
Figure 6.15: Investigation of the change in the porosity features on the N-CMK-3_600 sample before and after H2O adsorption: a) N2 adsorption-desorption isotherms at −196 °C and, b) DFT pore size distribution in the micro- and mesoporous range.

To further investigate this phenomenon, a thermogravimetric analysis coupled with Fourier transform infrared spectroscopy (methodology in Appendix A2, Paragraph A2.3.3) on the N-CMK-3_600 sample was performed (see Figure 6.16a)

after H_2O adsorption and compared with the fresh sample. The TGA profile of the fresh sample shows a first degradation peak at 70 °C, corresponding to a weight loss of about 8 wt.%, then a constant limited loss of 6 wt.% for temperatures varying from 100 to 600 °C and a final step of weight loss equal to ca. 10 wt.% from 600 to 800 °C. The evolved gases are composed mainly by H_2O, CO_2, CO, NH_3 and HCN; their relative intensities change during the test as shown in Figure 6.17a. During the first step (Figure 6.16b), the fresh sample mainly released H_2O that was adsorbed from the atmosphere; in the second step (Figure 6.16c), the main component of the evolved gas mixture is CO_2, while from temperatures higher than 600 °C, the weight loss slowly increases as expected from a carbonaceous material prepared at 600 °C. Indeed, in this phase (see Figure 6.16d), the fresh carbon sample slowly evolves producing HCN and NH_3, thus reducing the quantity of nitrogen incorporated in the carbon framework, as expected on the basis of the XPS analysis, and producing CO and CO_2 from material graphitization. The TGA analysis on the sample tested in H_2O adsorption, here labelled as "treated", shows several differences in comparison to the fresh sample.

Firstly, the thermodegradation test exhibits a new step with a maximum at around 235 °C and a weight loss of ca. 20 wt.% (Figure 12e). In this range of temperatures, the IR spectra (see Figure 6.16f,g and Figure 6.17b) clearly show the presence of paraffin and carbonyl groups typical of ketones, carboxylic acids, etc. It can be assumed that the presence of paraffin derives from the vacuum system of the apparatus used for the gas adsorption tests, which is linked to a vacuum oil pump. Hence, small quantities of oil at very low vapour pressure might be adsorbed from the sample during the activation and weight stabilization stages preceding gas adsorption; usually, the above-mentioned oil can be released by simply heating. In addition, it is worth noticing that, differently form the fresh sample, at temperatures higher than 300 °C, the IR spectra of the treated sample evidences the release of H_2O (see Figure 6.16h), with a continuous increment of the intensity of the signal as long as the temperature increases (Figure 6.17b).
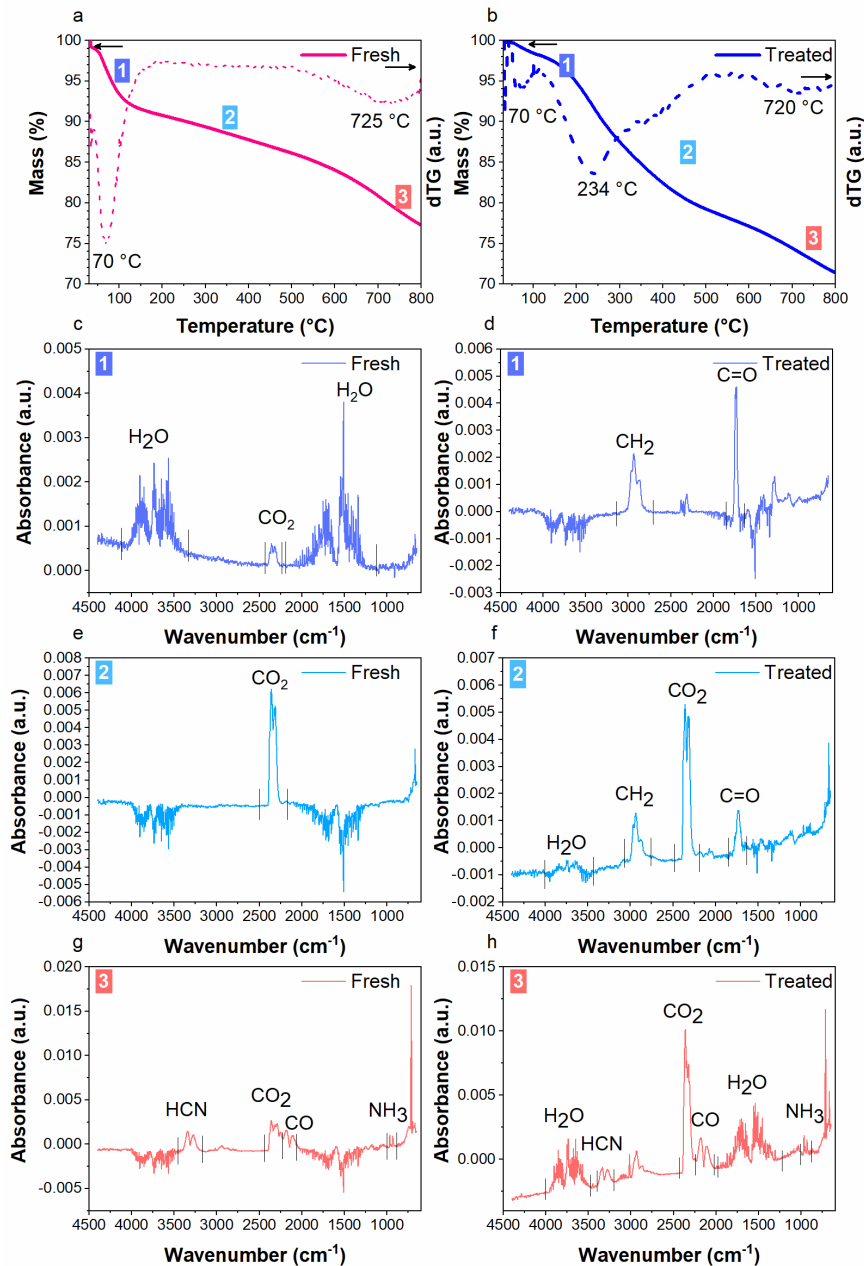
Figure 6.16: TGA-FTIR analysis of fresh N-CMK-3_600 sample: a) mass change vs. temperature (wt.% vs. °C) and differential weight (dTG) vs. temperature (d%wt. d°C^{-1} vs. °C); b) FTIR of gases developed at 77 °C; c) FTIR of gases developed at 354 °C; d) FTIR of gases developed at 800 °C. TGA-FTIR analysis of N-CMK-3_600 sample after H_2O adsorption: e) mass change vs. temperature (wt.% vs. °C) and differential weight (dTG) vs. temperature (d%wt./d°C vs. °C); f) FTIR of gases developed at 197 °C; g) FTIR of gasses developed at 385 °C; h) FTIR of gases developed at 798 °C (spectra reference [340–345]).

Summarizing, the volumetric and TGA-IR analysis considerably helped in extrapolating useful information regarding the optimal regeneration condition for the studied sorbents after their exposition to moist environments. In details, the usual activation process carried out at 300 °C revealed to be not completely successful in evacuating the previously adsorbed species during H_2O or H_2O/CO_2 adsorption tests. The attempt of maintaining the same temperature (i.e., 300 °C) while prolonging the activation time was also not totally decisive in gaining appreciable advantages in the restauration of the initial features of the sorbents, thus justifying the increment of the duration of a collateral step of the capture process. On the contrary, the increment of the activation temperature, as suggested from the thermogravimetric analysis, could be more effective in totally restoring the initial adsorption capacity, but the feasibility of the process is still questionable in terms of energy consumption for a real application.
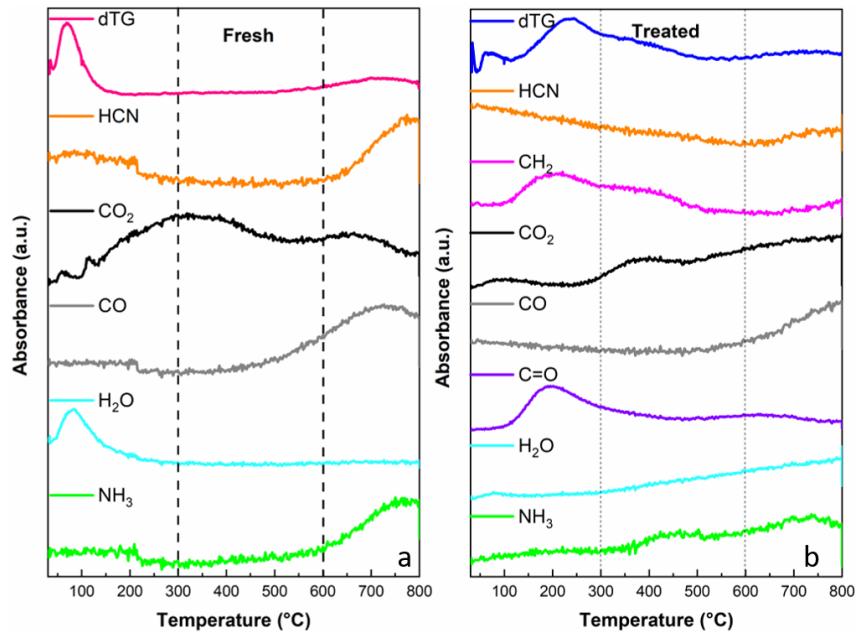
Figure 6.17: a) Intensity vs. temperature of differential weight change and peaks relative to NH_3 at 965 cm^{-1}, H_2O at 1505 cm^{-1}, CO at 2179 cm^{-1}, CO_2 at 2349 cm^{-1}, HCN at 3735 cm^{-1} for fresh N-CMK-3_600 sample. b) Intensity vs. temperature of differential weight change and peaks relative to NH_3 at 965 cm^{-1}, H_2O at 1505 cm^{-1}, CO at 2179 cm^{-1}, CO_2 at 2349 cm^{-1}, HCN at 3735 cm^{-1}, paraffin oil by $–CH_2$ stretching at 2925 cm^{-1}, oxidized paraffin by $–C=O$ stretching at 1715 cm^{-1} (spectra reference [340–345]).

6.2.10.   Comparison with other literature reports

The samples described in this work were compared to the most widely studied families of materials in terms of pure CO_2 adsorption capacity, cyclability in pure CO_2, selectivity in CO_2/N_2, and CO_2/H_2O binary mixtures (see Table 6.9) [98,315,337,346–348]. Interestingly, althought the heterogeneity of the testing conditions hinders an accurate comparison among the selected literature works, it is possible to claim that the adsorption features of the NOMCs materials analysed in this study are consistent and promising in respect to the most relevant reports in the field.

Table 6.9: Comparison of the performance in terms of CO_2/N_2 separation in dry and moist flue gases of OMCs/NOMCs developed in this work with the most significant literature reports.

Materials [REF]	Samples [REF]	CO_2 capacity mmol g^{-1}	T_{ads} [a] °C	P_{ads} [b] bar	T_{act} [c] °C
NOMC [d this work]	N-CMK-3_600	1.03 (CO_2:N_2=20:80)	35	1	
		0.66 (RH 75%)	30	0.04	300
		1.66 (100% CO_2)	30	0.9	
NOMC [d this work]	N-CMK-3_750	0.99 (CO_2:N_2=20:80)	35	1	
		0.89 (RH 75%)	30	0.04	300
		1.55 (100% CO_2)	30	0.9	
MOF [e]	MIL-101(Cr)-4F(1%) [315]	0.097 (RH 5%)	25	0.05	180
		~ 1.3 (100% CO_2)	25	1	
	Mg-MOF-74 [346]	5.77 (CO_2:N_2:H_2O=15:82:3, RH=86%)	27	1	267
		~ 6 (CO_2:N_2=15:85)			
PEI [f] impregnated silica [337]	PEI-SS_50%	1.79 (CO_2:N_2=10:80)	75	1	120
	PEI-SS_30%	1.024 (RH 70%)			
	CNT-SD_DETASi	0.43 (CO_2:N_2=20:80)	35	1	120

DETASi [g] modified-MWCNT [h] [98]		~ 0.45 (RH 75%)	30	0.04	
		0.48 (100% CO_2)	30	0.9	
Zeolite	13X [346]	2.27 (CO_2:N_2:H_2O=15:82:3, RH=86%)	27	1	267
		~ 2.27 (CO_2:N_2=15:85)			
	13X (monolith) [347]	1.8 (CO_2:N_2=10:90, in H_2O)	25	1	350
		2.2 (CO_2:N_2=10:90)			
	ZSM-5 [348]	0.44 (CO_2:N_2 =15:85, RH=100%)	40	1	400
	Silicalite ZSM-5 [348]	0.52 (CO_2:N_2 =15:85, RH=100%)			

6.3.   Conclusions

The CO_2 capture ability in simulated post-combustion flue gases by N-containing carbonaceous adsorbents was investigated and described in this chapter. N_2 and H_2O, together with CO_2, are the main components of the flue gases from coal- or natural gas- fired power plants, therefore the specific selectivity of the sorbents for the target gas is a fundamental requirement. Particularly, the effect of the presence of water contaminations in simulated exhausted gas was the main purpose of this study, since this aspect has not been widely investigated so far in the literature for this kind of materials. Indeed, since the incorporation of heteroatoms (particularly, O and N) in bare-carbon frameworks provide some hydrophilic character, the accidental competitive H_2O adsorption cannot be neglected in the evaluation of the CO_2 capture from wet flue gases. Therefore, this section reported the evaluation of the selectivity of N-containing ordered mesoporous carbons of the CMK-3-type, synthesized through the nanocasting procedure from a SBA-15 ordered mesoporous silica hard template.

Firstly, single component pure CO_2 and H_2O adsorption tests were performed, then also CO_2 capture in CO_2/N_2 and CO_2/H_2O mixtures was investigated. N content, varied in the different samples by tuning the pyrolysis temperature, was found to be crucial in the adsorption performances at RT and in binary CO_2/N_2 mixtures. A higher N content improved the adsorption at temperature close to RT (30 °C) and the selectivity in CO_2/N_2 mixtures. However, N species improved also the affinity for H_2O; indeed the N-CMK-3_600 sample experienced a higher reduction in CO_2/H_2O selectivity in comparison to the sample N-CMK-3_750, which contains less amount of nitrogen (11.3 and 8.3 at.% of N in N-CMK-3_600

and N-CMK-3_750, respectively). Generally speaking, despite an unavoidable reduction in CO_2 uptake in humid gas mixtures due to the competitive adsorption between CO_2 and H_2O, the samples under study still retain good CO_2 capture capability. Specifically, amaximum CO_2 adsorption capacities of 1.66 mmol g^{-1} at 30 °C / 0.9 bar / pure CO_2, and of 1.03 mmol g^{-1} at 35 °C / 1 bar / 20 % CO_2 have been obtained by the N-CMK-3_600 sample. As mentioned above, N-CMK-3_750 better preserved the selectivity for CO_2 uptake in wet gas compositions with a CO_2 uptake of 1.52, 0.61 and 0.89 mmol g^{-1} at 30 °C / 0.6 bar at RH 25, 50 and 75%, respectively. However, the repetition of the CO_2 adsorption tests after H_2O adsorption revealed a considerable reduction in the uptake, due to the incomplete desorption of water from narrow micropores during previous tests, which makes the binding sites unavailable for the subsequent capture of CO_2. Conversely, the retention of the CO_2 capture properties under repetitive sorption-desorption cycles from dry flue gas compositions was assessed by reusability tests in pure CO_2. The performances of the N-containing N-CMK-3-type samples remained almost unvaried after 10 pure CO_2 adsorption/desorption cycles. An appreciable efficiency loss was registered between the first and the second cycle for the sample N-CMK-3_600, but it is ascribable to irreversible sorption of CO_2 molecules which remained bonded at the most energetic sites after the regeneration step at 150 °C. The hypothesis of the degradation of the samples is excluded because after the second cycle, the adsorption kept reproducible and unvaried upon multiple cycles.

In summary, the samples described in this section are prepared from a sustainable and renewable nitrogen-rich carbon source and display good characteristics of selectivity in CO_2/N_2 and CO_2/H_2O binary mixtures and regenerability in pure CO_2. However, the appreciable loss of the initial performances after H_2O adsorption still constitutes a limit in the applicability of the samples. Despite the regenerability of the sorbents after the exposition to wet flue gases still need to be fully unravelled, this study satisfies the tentative to shed light on water adsorption in N-doped carbons, with a particular interest on the evaluation of the competitive effect in CO_2 capture from simulated post-combustion flue gas mixtures.

Chapter 7

7. Other applications of NOMCs: anode materials in secondary batteries

7.1.   Introduction

The peculiar characteristics of ordered mesoporous carbons, described in Chapter 4, find wide applicability in different research/application fields besides gas adsorption and separation, as dealt during this dissertation. One of these consists in their application as negative electrodes (anodes) in energy storage devices, such as Li- or Na-ion secondary batteries (abbreviated as LIBs and NIBs, respectively). In this context, the high surface area, pore ordering and connectivity typical of OMCs might be beneficial for increasing and improving the active contact area at the interface with the electrolyte, thus facilitating the charge transfer reactions and ion transport by providing favourable diffusion pathways [277,278]. Moreover, porous materials are also known for being advantageous as electrode materials, thanks to their structural features and related ability of accommodating the volume changes occurring during cycling [280]. Moreover, in addition to the previously mentioned positive characteristics, the NOMCs studied in the course of this thesis work offer another possible advantage, as provided by the inclusion of N species into the ordered porous carbon framework surface. Indeed, N functionalities as heteroatoms incorporated in the carbon framework increase the electronic conductivity, owing to the stronger electronegativity of N than C, and the hybridization of the N lone pair electrons with the π electrons in carbon [277,278,281]. Hence the incorporation of N-species not only creates favourable binding sites for Li/Na storage, but also enhances the interlayer spacing, which might generate a facilitated pathway for ion storage, especially in the case of Na-ions, which have a larger ionic radius (0.102 nm) than Li-ions (0.076 nm) [272]. These positive characteristics help in coping the shortcoming due to the insufficient

interlayer distance of usual graphite-based anodes, particularly in the case of reversible Na storage [272,281].

In this chapter, the preliminary results of the electrochemical testing of N-rich CMK-8 ordered mesoporous carbons are described, with the aim at expanding the panorama of possible applications for this category of materials. Briefly, here NOMC materials, applied as anodic electrodes in Li- and Na-ion batteries were prepared by impregnating D-glucosamine into the pores of the KIT-6 ordered mesoporous silica hard-template aged at 140 °C, followed by pyrolysis at 900 °C and the final silica removal steps. The CMK-8 mesostructure was considered more suitable than the CMK-3 one for this application, owing to the interpenetrating bicontinuous pore channels network of the former, which allows an easier access and diffusion of alkali metal ions, as demonstrated by Saikia et al. [349]. In addition, the large pores in the carbon framework achieved by the proper choice of the silica template allowed the more homogeneous and complete impregnation of the C/N precursor solution in the porous network; it resulted in the formation of thick pore walls in the carbon replica, which in turn improved the structural stability to better tolerate volume changes during intercalation/de-intercalation processes.

7.2.   Experimental section

7.2.1. Materials and methods

The synthesis of the CMK-8-type NOMC sample investigated as anode material in LIBs or NIBs was performed using KIT-6 silica aged at 140 °C (named as KIT-6_140) as the hard template, the porosity of which was impregnated with the G-based solution, as for the samples described in the previous chapters. The sample under study was named as N-CMK-8_900(140), in order to explicitly identify the pyrolysis and ageing temperature of the KIT-6 silica hard template (i.e., 900 and 140 °C, respectively).

Details of the synthesis procedure are thoroughly described in Appendix A1, whereas the methodology adopted for the physico-chemical characterization of the studied sample is illustrated in Appendix A2, precisely in Paragraph A2.1 (as illustrated in the scheme in Figure 7.1). The electrode preparation, cell assembly and electrochemical characterization are described in Appendix A3.
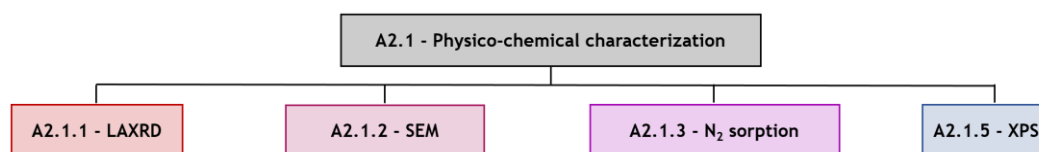
Figure 7.1: Physico-chemical characterization on N-containing CMK-8 carbons applied as anode in laboratory-scale Li- and Na-based batteries.

7.2.2. Structural-morphological characterization

Low-angle X-ray diffraction analysis, FESEM imaging and N_2 sorption at -196 °C were used as accurate methods for assessing the good quality of the replication process occurred during nanocasting. The LAXRD diffraction pattern of KIT-6_140 hard template, characteristic of cubic $Ia\overline{3}d$ pore symmetry, was retained by the N-CMK-8_900(140) sample, even though the definition of the diffraction peaks is slightly reduced in the carbon replica sample (see Figure 7.2a and b) [218]. The FESEM image in Figure 7.2c shows the highly porous characteristics of the material, which is combined to smooth surface regions.

The investigation of the porosity features by N_2 adsorption-desorption measurements at -196 °C confirmed the previous results obtained for KIT-6 and CMK-8 materials, namely type IVa isotherms characteristic of mesoporous materials (see Figure 7.3 and Figure 7.4). Precisely, KIT-6 silica aged at higher temperatures (i.e., 140 °C) shows very large mesopores of 10.5 nm width.
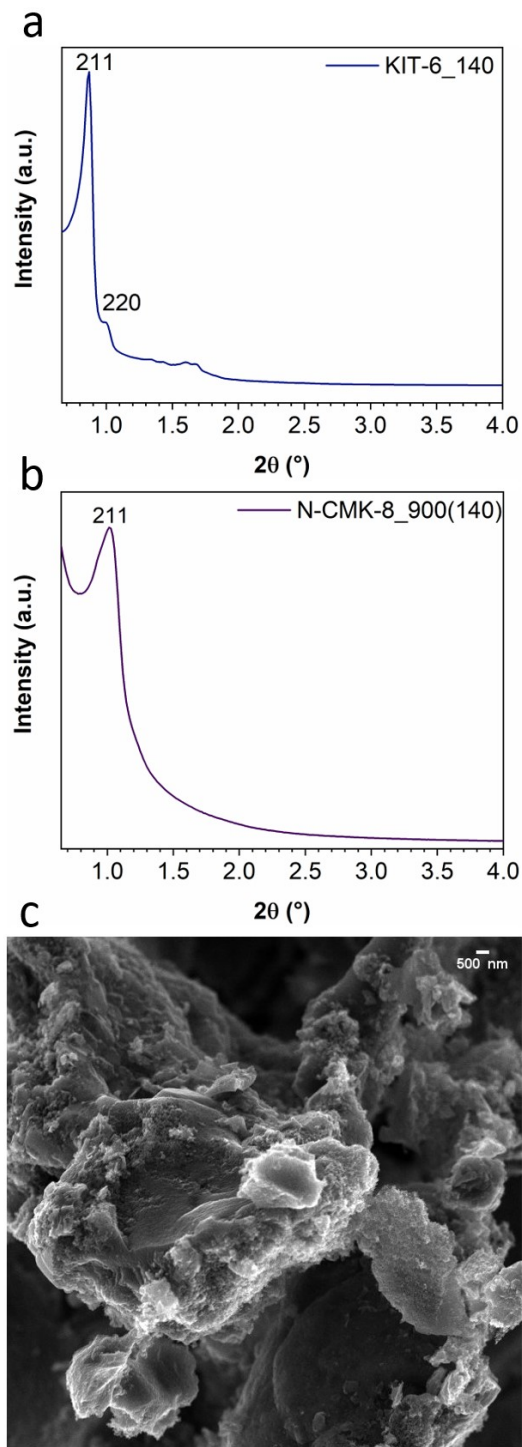
Figure 7.2: a) LAXRD pattern of KIT-6_140 hard template and b) LAXRD pattern and c) FESEM image of the N-CMK-8_900(140) carbon replica.
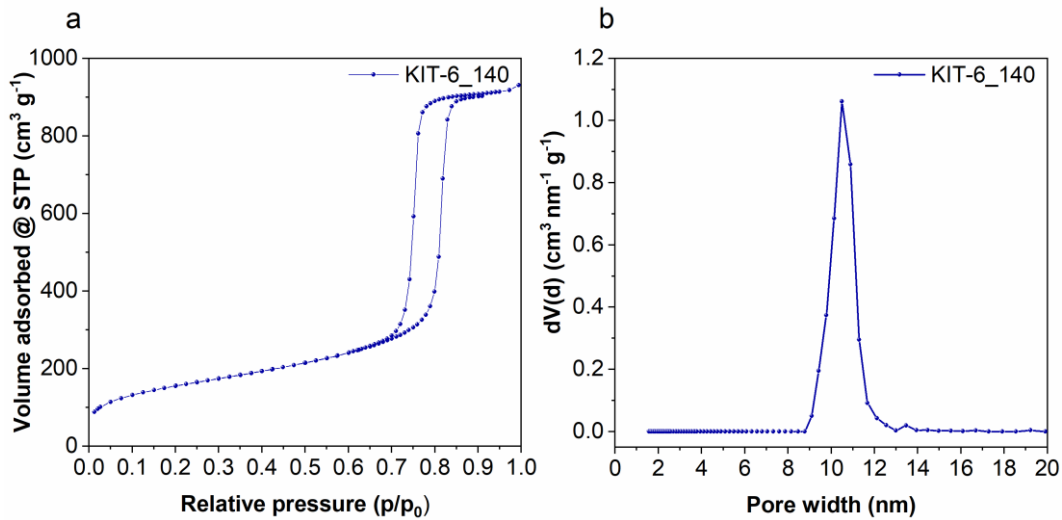
Figure 7.3: a) N$_2$ adsorption-desorption isotherm at −196 °C, b) NLDFT pore size distribution of the KIT-6_140 OMS hard template.

The larger pore size facilitated the impregnation of the C/N precursor solution in the porous network and determined the formation of thick pore walls in the carbon replica, which result in a more robust framework. In principle, this has to be considered a positive feature, which should allow the material to accommodate more efficiently the intercalation/de-intercalation processes during reversible cell cycling.
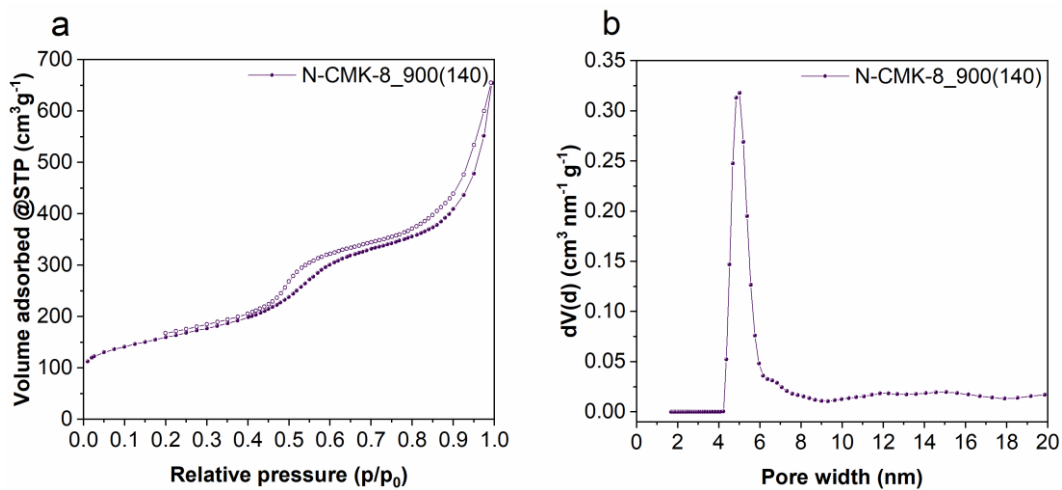
Figure 7.4: a) N$_2$ adsorption-desorption isotherm at −196 °C, b) QSDFT pore size distribution of the CMK-8_900(140) sample.

The textural properties collected from LAXRD and N_2 sorption analysis are summarized in Table 7.1.

Table 7.1: Physicochemical properties of the OMCs under study.

| Samples | a_{211} [a] | b [b] | S_{BET} | S_{DFT} | $V_{p,DFT}$ | D_p [c] |
	nm	nm	$m^2\,g^{-1}$	$m^2\,g^{-1}$	$cm^3\,g^{-1}$	nm
KIT-6_140	24.8	1.9	553	526	1.4	10.5
N-CMK-8_900(140)	21.3	5.7	561	808	0.8	5.0

[a] unit cell size (a_{211}) calculated using the expression $a_{211} = \sqrt{6} \cdot d_{211}$
[b] wall thickness (b) calculated by geometrical model, $b = {a_{211}}/{2} - D_{p,DFT}$ [229]
[c] pore width (D_p) in the mesoporous range, calculated by NLDFT and QSDFT methods for silica and carbons, respectively, applied to N_2 isotherms at $-196\ °C$

7.2.3. Physico-chemical characterization

The XPS analysis aimed to investigate the overall surface-chemical properties of the NOMC sample under study, and particularly, the quantification of the N amount and the identification of its bonding state. This information represents a crucial aspect also for electrochemical application, due to the relevant role of N functionalities in influencing the electronic and structural features of the material and, in turn, the ability to store alkali metal ions (see Paragraph 7.1). The surface atomic content of C, N, and O atoms was determined by the XPS survey scan (Figure A.2.12) and the respective XPS regions were selected for high-resolution (HR) acquisitions (Figure A.2.13). Precisely, carbon signal was fitted by using three components (see Figure A.2.13a in Paragraph A2.1.5, Appendix A2) assigned to C–C sp^2 (284.8 eV), C–O/C–N (285.8 eV), and C=O/C=N (286.8 eV) [292,293]. Oxygen signal (see Figure A.2.13c in Paragraph A2.1.5, Appendix A2) was fitted by using three components assigned to C=O (530.9 eV), C–O (532.4 eV), and COOH (533.5 eV) [293]. The N1s signals of NOMCs were fitted by using three components assigned to pyridinic (C=N–C, N-6, 398.4 eV), pyrrolic (C–NH–C, N-5, 399.9 eV), and graphitic (C–NC–C, N-Q, 401.1 eV) nitrogen-based structures [292] (Figure A.2.13b in Paragraph A2.1.5, Appendix A2). On the basis of the percent quantification of the different N-based species from the calculation based on the fitted peak area, the concentration of N-6 is around the 38% in respect to N-5 and N-Q, which is a relevant result, since according to Ma et al., pyridinic nitrogen is more suitable for Li storage than pyrrolic and graphitic nitrogen [350]. Table 7.2 describes all the data derived from XPS investigation, included the percentage of each C, N and O species on the surface of N-CMK-8_900(140) sample.

Table 7.2: Summary of the XPS analysis on the survey and high-resolution spectra of the C1s, N1s and O1s region for the N-CMK-8_900(140) sample.

	Peak	Amount[a]	Binding energy	Assignment	Fitted peak area	Fitted peak area[a]
		at.%	eV		counts s^{-1}	%
N-CMK-8_900(140)	C1s	84.3	284.8	C–C	3234.13 ± 13.91	70.9
			285.8	C–O/C–N	1121.48 ± 16.78	4.5
			286.8	C=O/C=N	206.48 ± 15.66	24.6
	N1s	6.4	398.4	C=N–C	214.41 ± 6.02	37.9
			399.9	C–NH–C	60.69 ± 7.97	10.7
			401.1	C–NC–C	291.28 ± 10.73	51.4
	O1s	7.6	530.9	C=O	385.32 ± 8.60	33.0
			532.4	C–O	459.97 ± 10.67	39.3
			533.5	COOH	323.76 ± 11.45	27.7

[a]derived from the XPS survey scan; [b]indication of the relative amount of each species in the sample.

7.2.4. Electrochemical characterization

The electrochemical behaviour of the studied NOMC sample as anode in LIBs or NIBs was tested in half-cells countered with metallic Li or Na. Details of the fundamental definitions of the electrochemical quantities and brief description of the here used electrochemical characterization techniques, electrode preparation, and cell assembly are present in Appendix A3. The CV profiles of the Li-half cell prepared with the NOMC-based anode are typical of carbon anodes, with a cathodic peak at 0−1 V, which is more pronounced during the 1st cycle and becomes less intense during the following cycles. Hence, it is ascribed to irreversible charge consumption due to solid electrolyte interphase (SEI) formation and irreversible storage of Li$^+$ ions in specific sites (see Figure 7.5a) occurring during the initial "activation" cycle [272]. These irreversible processes cause an appreciable difference between the discharge capacity (1643 mA h g^{-1}, 0.1 A g^{-1}) and the charge capacity (605 mA h g^{-1}, 0.1 A g^{-1}) during the 1st cycle (Figure 7.5b), resulting in a low initial Coulombic efficiency of 37 %. Such a low initial efficiency is readily ascribed to the very high surface area of the material; clearly, the higher the surface area and the more extended the passivation effect at the interface. On the other hand, the SEI layer participates also positively as a passivation layer by preventing further electrolyte decomposition during the following cycles, thus allowing a reversible capacity of 655 mA h g^{-1} after the 2nd cycle and the retention of stable charge/discharge capacity values in the following cycles, reaching Coulombic efficiencies higher than 95% already after the 5th cycle. The NOMC-based electrode

showed also remarkable rate capability, by tolerating high currents (reversible capacity of 148 mA h g^{-1} at 2 A g^{-1}). In addition, the material is very stable upon prolonged cycling and does not undergo structural degradation, as indicated by the fact that the initial reversible capacity is recovered when the C-rate is reversed back to 0.1 A g^{-1} after 90 cycles and the Coulombic efficiency approached 100 %.
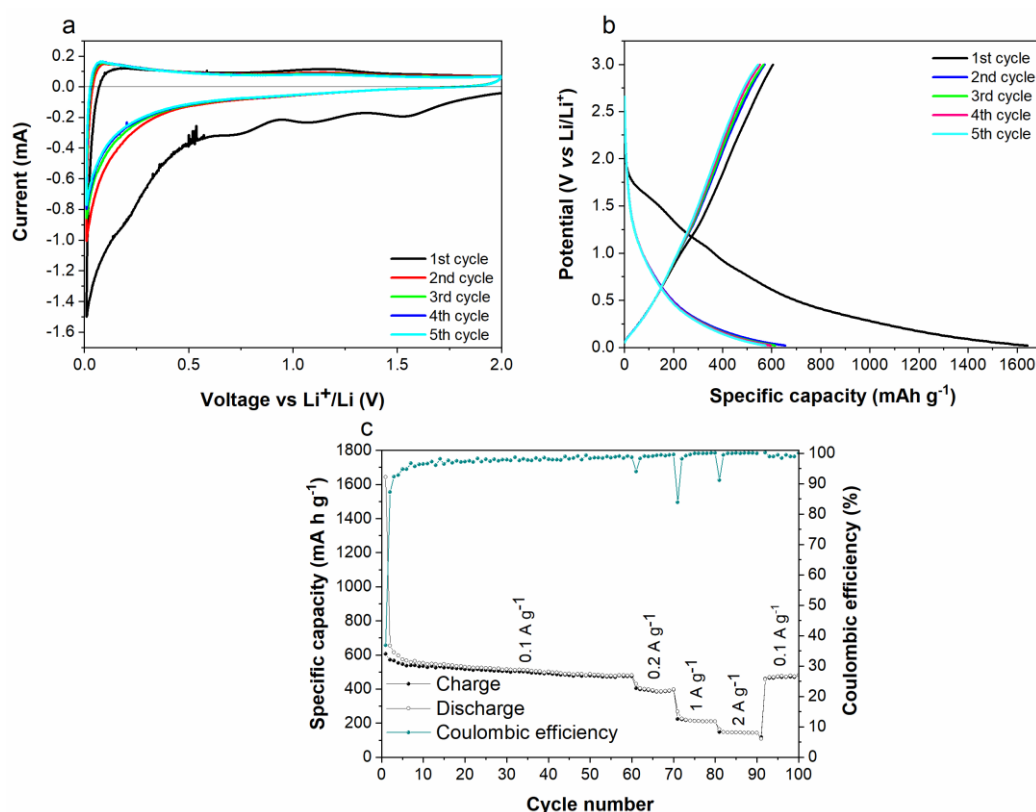
Figure 7.5: Electrochemical response in lab-scale Li-metal cell of the N-CMK-8_900(140) anode: a) cyclic voltammetric (CV) profiles (initial five cycles at 0.1 mV s^{-1}), b) potential *vs.* specific capacity profiles (at 0.1 A g^{-1}), and c) galvanostatic charge/discharge cycling at different current regimes (from 0.1 to 2 A g^{-1}, viz. from C/10 to 2C rate).

The electrochemical response of the NOMC-based electrodes in lab-scale Na-metal cell is shown in Figure 7.6. The material shows a similar behavior than in LIBs. Irreversible processes (SEI formation and irreversible Na storage) are responsible for the considerable difference between the discharge and charge capacities during the 1st cycle (694 and 132 mA h g^{-1} at 0.1 A g^{-1}, respectively), which determines a low Coulombic efficiency of 19 %. However, during the subsequent cycles, the charge/discharge processes became highly reversible

(Coulombic efficiency higher than 95%, reversible capacity of 135 mA h g^{-1} after 15 cycles, in respect to the reversible capacity calculated at the 2nd cycle, namely 175 mA h g^{-1}). The NOMC-based electrodes showed also good rate capability, with a very low reduction of the specific capacity by doubling the applied current and also stable performances at relatively high currents, with a reversible capacity of 45 mA h g^{-1} at 1 A g^{-1}. Of course, the specific capacity is lower than the corresponding LIBs, but this is in line with the results for NIBs. Again, the initial capacity was also restored when the current is reversed back to 0.1 Ag^{-1}, after 80 cycles at currents up to 1 A g^{-1}, accounting for the great stability of the materials also in Na-based cells.
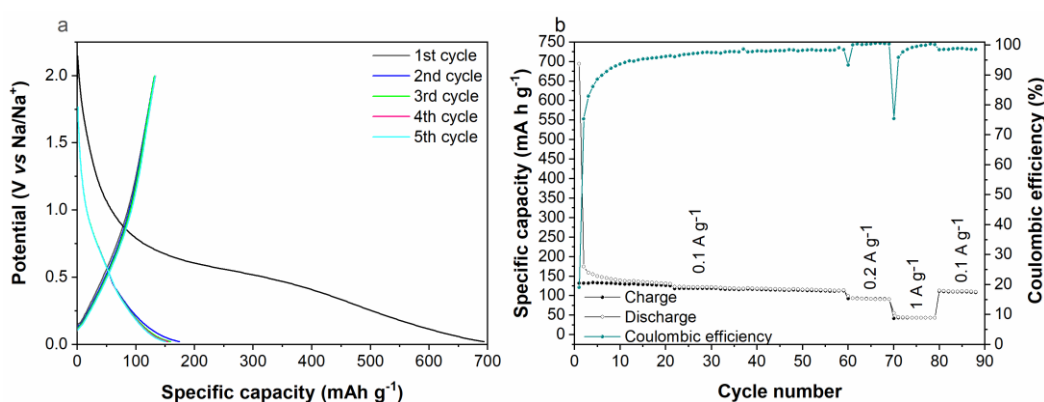
Figure 7.6: Electrochemical response of the N-CMK-8_900(140) anode in lab-scale Na half-cell: a) potential *vs.* specific capacity profiles (at 0.1 A g^{-1}), and b) galvanostatic charge/discharge cycling at different current regimes (from 0.1 to 1 A g^{-1}, viz. from C/10 to 1C rate).

7.3.   Conclusions

As additional peculiar and interesting features of the NOMCs synthesised by the nanocasting synthetic route and characterised during this PhD Thesis, they were exploited in terms of their electrochemical behaviour as anodes in laboratory-scale Li- and Na-based cells. Indeed, the here reported preliminary investigations and "proof-of-concept" cell results aimed to validate the positive influence derived from the high surface area, pore volume, along with the opportunely tuned ordered porous network and incorporation of N species to the improvement of the electrochemical response of the NOMC materials as battery electrodes. After thorough evaluation and cell testing of the different synthesized samples, the N-CMK-8-type carbon obtained from KIT-6 silica aged at 140 °C showed the best electrochemical features and was here presented.

In particular, the tree-dimensional pore network of the CMK-8 mesostructure is believed to facilitate electrolyte and ion diffusion and the thicker pore walls, achieved by the choice of large mesopore silica hard template, to provide enhanced structural resistance, which is beneficial for accommodating mechanical stresses originated during cycling. It is worth noticing that these are preliminary results and more efforts should be focused on unravelling the full electrochemical potential of these materials. Thus, the future perspective of this analysis will take in consideration a deeper investigation of the irreversible processes occurring during the initial cycling stages, particularly the SEI formation, and the examination of other electrolyte formulations. Notwithstanding this, the "proof-of-concept" Li- and Na-metal cells assembled in this thesis demonstrated stable cycling at different current regimes, which accounts for the promising prospects of the synthesized materials also in energy storage and conversion devices.

8. Concluding remarks

The design of innovative technologies to replace fossil fuel-based energy production through electrification or pollutant sequestration from GHG sources through efficient sorption systems is the breakthrough target of our modern society. Focusing on carbon dioxide (CO_2), being the most abundant among GHGs and impactful to global warming, several strategies have been examined up to now for its capture before its release in the atmosphere after combustion processes, chiefly from large point sources. The challenging target in designing an efficient CO_2 sorbent deals with the fulfilment of several requirements, including, first of all, a sizeable and selective capture ability in respect to the other components of the flue gas mixture. Likewise, an efficient reusability, intended as a complete and low-energy regeneration, as well as thermal and chemical stability under adsorption/desorption conditions are radically important. Finally, the sorbent manufacturing process must be sustainable, environmentally friendly and cheap, thus assuring the feasibility of the whole entire production and utilization chain on a large scale.

Starting from these assumptions, during this Thesis work, N-rich ordered mesoporous carbons were synthesised, thoroughly characterised with the physico-chemical viewpoint and investigated mainly as efficient CO_2 sorbents. In addition, in an attempt to demonstrate the versatility of the newly synthesised materials in other energy-related fields, their promising features as electrode active materials in lithium/sodium ion batteries were accounted by assembly preliminary "proof-of-concept" lab-scale cells, which provided stable cycling at relatively high capacity in a standard configuration.

Indeed, the main aim was exploiting the peculiar regular porous network for improving gas diffusion and the accessibility of the specific adsorption sites. First, the nanocasting synthesis procedure enabled the desired design of the pore characteristics through the convenient choice of the ordered mesoporous silica hard template. Concurrently, the fine-tuning of the pyrolysis (performed at 600, 750 and 900 °C) of the D-glucosamine hydrochloride-based solution, *viz.* the environmentally friendly C/N source, enabled the successful development of the favourable microporosity and the introduction of basic N-species, which both proved to foster the specific interaction with the acidic CO_2 molecule. D-glucosamine hydrochloride-derived samples were not only enriched of N-species, but also showed a larger content of micropores, thus revealing better adsorption

features in respect to an undoped comparative sample obtained from sucrose. Hence, the innovative choice of the precursor and the synthetic route demonstrated to improve the adsorption features, while overcoming common post-synthesis modification procedures for microporosity introduction and basic N-sites incorporation. In details, the higher pyrolysis temperature (i.e., 900 °C) determined the increment of the micropore volume, but conversely caused the reduction of N content. XPS analysis was used to identify the influence of the thermal treatment in respect to the bonding configuration of the produced nitrogen species (pyridinic, pyrrolic and graphitic nitrogen-based structures). This investigation was effective in unraveling the respective role of the different types of nitrogen inclusions, among which pyridinic-N contributes the most in CO_2 capture enhancement. Thus, the best performances in CO_2 capture at temperatures close to RT and in CO_2/N_2 mixtures were achieved by means of the low-temperature treatment, which allows the retention of a higher amount of N, in large part of the pyridinic type. Precisely, the N-CMK-3_600 sample was the most promising under the above-mentioned testing conditions, by achieving the maximum CO_2 adsorption values of 1.66 and 1.03 mmol g^{-1} in pure CO_2 at 30 °C and in CO_2/N_2 mixtures (20/80, v/v) at 35 °C, respectively.

The incorporation of N atoms provides some hydrophilic character in bare-carbon frameworks. Accordingly, N species improved not only the interaction of the bare carbon surface with CO_2, but also the affinity for H_2O. Hence, the accidental competitive H_2O adsorption cannot be neglected in the evaluation of the CO_2 capture from wet flue gases. In details, N-CMK-3_600, which proved to be the most promising sample in pure CO_2 and CO_2/N_2 gas mixtures, conversely experienced a high reduction in CO_2 when H_2O was also present in the gas mixture. On the other hand, the homologous sample pyrolysed at the intermediate temperature of 750 °C, namely N-CMK-3_750, better preserved the selectivity for CO_2 uptake in moist gas compositions at 30 °C, recording CO_2 uptake values of 1.55, 1.52, 0.61 and 0.89 mmol g^{-1} at RH 0, 25, 50 and 75%, respectively.

The reusability of the sorbents was evaluated both in terms of multiple adsorption-desorption cycles from dry flue gas compositions and as the repetition of pure CO_2 capture after H_2O adsorption. In the former case, the performances of the NOMCs samples remained almost unvaried after 10 pure CO_2 adsorption/desorption cycles, with a regeneration step between two consecutive cycles under mild temperature conditions (i.e., 150 °C). Conversely, the repetition of the tests after H_2O adsorption revealed a considerable reduction in the CO_2 uptake. It was ascribed to the incomplete desorption of water from narrow

micropores during previous tests, which makes a part of the preferential binding sites unavailable for the subsequent capture of CO_2.

In conclusion, the newly designed NOMC sorbents under study showed valuable advantages in terms of sustainable preparation procedure and capture and selectivity characteristics under pure CO_2 and CO_2/N_2 gas mixtures. However, for designing an efficient and marketable sorbent, the characteristics of selectivity in CO_2/H_2O binary mixtures and regenerability after working in moist flue gases require a focused improvement. As a matter of fact, the study on the competitive CO_2/H_2O adsorption carried out in this work aims to shed light on water adsorption in N-doped carbons, in order to pave the way to future efforts towards the optimization of these crucial aspects for a future large-scale industrial application of these nanostructured materials.

Appendix A1

A1.   Description of the synthesis procedures for ordered mesoporous materials

A1.1.   Chemicals

Poly(ethylene glycol)-block-poly(propylene glycol)-block-poly(ethylene glycol) ($EO_{20}PO_{70}EO_{20}$, P123, Mn~5800), tetraethyl orthosilicate ($Si(OC_2H_5)_4$, TEOS, 98%), sucrose ($C_{12}H_{22}O_{11}$, ≥ 99.0%, namely S in this work) were purchased from Sigma-Aldrich. Ethanol (C_2H_6O, EtOH, 96%) was purchased from Brenntag. 1-butanol (BuOH, 99%), sodium hydroxide (NaOH, 98%, flakes) and D-glucosamine hydrochloride ($C_6H_{13}NO_5 \cdot HCl$, > 98%, namely G in this work) were bought from Alfa Aesar, and hydrochloric acid (HCl, 37%) and sulfuric acid (H_2SO_4, 95%) were obtained from VWR. All chemicals were used as received without further purification steps. Particularly, P123 was used as structure directing agent and TEOS as the silica source, for SBA-15 and KIT-6 silica syntheses; in addition, butanol acted as co-solvent and co-template during KIT-6 silica synthesis. On the other hand, regarding the OMCs/NOMCs synthesis, S is the carbon sources in OMCs synthesis, whereas D-glucosamine hydrochloride the simultaneous carbon/nitrogen precursor in NOMCs synthesis. Sulphuric acid is the polymerization catalyst when using both sucrose and D-glucosamine hydrochloride as carbon sources.

A1.2.   Synthesis of SBA-15

The SBA-15 silica hard template was synthesized following the procedure described by Nicolas et al. [351]. Precisely, 8.0072 g of P123 were dissolved at 35 °C in ca. 150 mL of 0.3 M HCl aqueous solution in a 250 mL polypropylene bottle. When P123 was completely dissolved and a clear solution is obtained, 13.0071 g of TEOS was added to the mixture (P123:TEOS = 1:45 in mole ratio) and let for

stirring at the same constant temperature of 35 °C. After 24 h, the mixture was hydrothermally treated at 100 °C for 48 h in an oven under static condition (Binder, Thermo Fisher Scientific). The hot solution was filtered and dried in oven firstly at 100 °C for 2h, then at the final temperature of 140 °C for 12 h. After the hydrothermal treatment, P123 was removed by solvent extraction in EtOH-HCl solution and, subsequently, by calcination at 550 °C for 3h, with a previous step at 120 °C for 2 h in a muffle furnace (Nabertherm). The details of the synthesis procedure and the amounts of each respective chemical are shown in Figure A.1.1 and summarized in Table A.1, respectively.

Table A.1: List of chemicals for SBA-15 silica synthesis and their respective amounts used.

Chemical	Mass
	g
P123	8.0072
H_2O	146.25
HCl 37%	4.4625
TEOS	13.0071
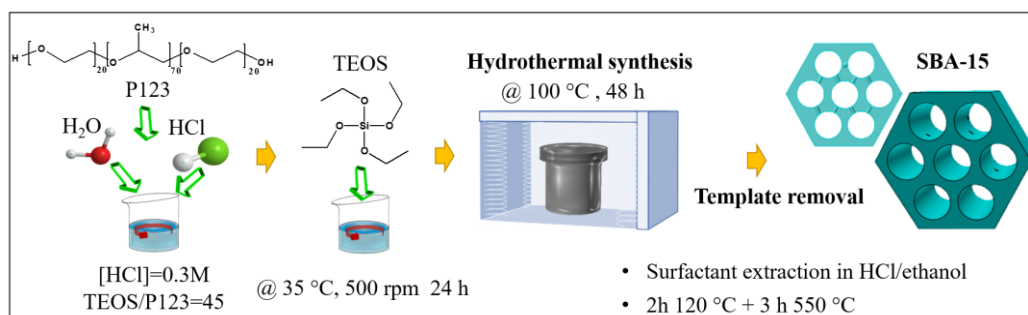
Figure A.1.1: Schematic representation of the hydrothermal synthesis of SBA-15-type ordered mesoporous silica.

A1.3.   Synthesis of KIT-6

For the synthesis of KIT-6 ordered mesoporous silica, 5.1290 g of P123 and the same amount of BuOH (BuOH = 1:1, wt%) were dissolved in a 0.5M HCl aqueous solution in a 250 mL polypropylene bottle at a controlled constant temperature of 35 °C for 24 h. After the complete dissolution of P123, so that the

solution is clear, generally achieved by stirring the mixture overnight, 11.0274 g of TEOS are added to the mixture (=P123:TEOS = 1:60, in mole ratio) and stirred at 35°C for 24 h. Once this time has elapsed, the mixture was transferred to the oven and hydrothermally treated under static condition at a constant temperature of 40 °C for 72 h in the case of silica named as KIT-6_40, whereas at 100 °C for 48 h, in the case of silica denominated KIT-6_100. The procedure was similar for the sample named KIT-6_140, but in this case the hydrothermal treatment was conducted in autoclave, at 140 °C for 48 h. After the hydrothermal treatment, the solid product was filtered under vacuum, without washing with any solvent. After filtration, the powders were collected from the filter and transferred inside a crucible and dried in the muffle furnace at 100 °C for 2 h and at 140 °C for 12 h. The surfactant is firstly removed by extraction in ethanol-HCl solution at room temperature (RT), subsequently by calcination at 550 °C for 3h, with a previous step at 120 °C for 2 h. The details of the synthesis procedure and the amounts of each respective chemical are shown in Figure A.1.2 and in Table A.2, respectively.

Table A.2: List of chemicals used for KIT-6 silica synthesis and their respective amounts.

Chemical	Mass g
P123	5.1290
H_2O	185.3285
HCl 37%	9.9332
BuOH	5.1290
TEOS	11.0274
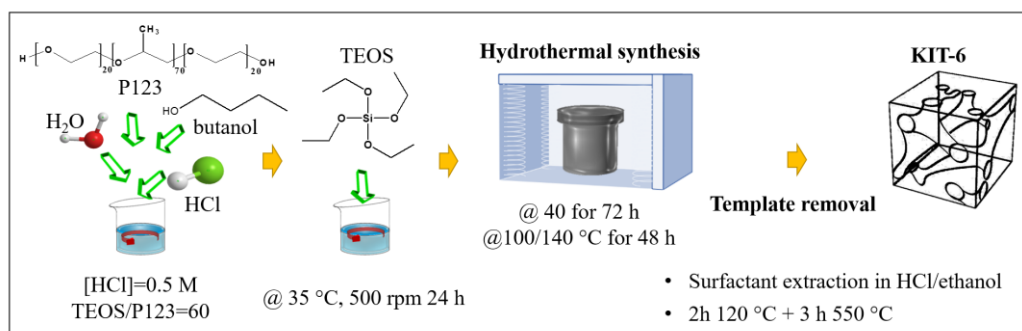
Figure A.1.2: Schematic representation of the hydrothermal synthesis of KIT-6-type ordered mesoporous silica.

A1.4.   Synthesis of CMK-3

The nanocasting synthesis of N-containing CMK-3 carbons consists in the impregnation of the SBA-15 template (degassed overnight at 150 °C under vacuum), in two steps with D-glucosamine hydrochloride dissolved in a sulfuric acid aqueous solution. The relative amounts of glucosamine hydrochloride, water and sulfuric acid were estimated from adjustments of a frequently used standard procedure for the impregnation with sucrose as the carbon source [227,246]. Precisely, 1.58 g of D-glucosamine hydrochloride, 0.097 mL of H_2SO_4, and 6 g of deionized water for each gram of SBA-15 were used in the first impregnation step, while in the second one the amounts were reduced to the 61% (0.96 g of D-glucosamine hydrochloride, 0.06 mL of H_2SO_4 and 3.66 g of H_2O). The slurry was stirred for 1 h at room temperature until a homogeneous gel-like consistency was obtained and, then, thermally treated in a calcination furnace at 100 °C for 6h, 140 °C for 2h and 160 °C for 6h (heating rate 150 °C min^{-1}) during the first impregnation, and at 100 °C for 6 h and 140 °C for 2h during the second impregnation step. The obtained powders were moved and pyrolized in a controlled atmosphere inside a quartz reactor with a capillary cap and pyrolyzed at 600, 750 or 900 °C (heating rate 3 °C min^{-1}) for 4h in a calcination furnace in air under atmospheric pressure [249]. The two intermediate steps at 200 °C for 6 h and at 655 °C for 4h (except for the sample pyrolized at 600 °C) were introduced before reaching the final pyrolysis temperature (T_p).

The silica dissolution stage was carried out with three rounds of dissolution at room temperature (RT) overnight in a 2M sodium hydroxide (NaOH, 98%, flakes) H_2O/EtOH solution (H_2O: EtOH = 1:1, v/v). The samples underwent several repetitive washing steps in water and ethanol and were finally dried overnight at 70 °C. The samples were denominated N-CMK-3_X, where X is the pyrolysis temperature (i.e., 600, 750 or 900 °C); details of the synthesis procedure and the amounts of each respective chemical are shown in Figure A.1.3 and Table A.3, respectively.

Table A.3: List of chemicals used for CMK-3-type carbon synthesis and their amounts for each gram of silica template.

Chemical	1st impregnation	2nd impregnation
Glucosamine hydrochloride, G (g)	1.58	0.96
H$_2$SO$_4$ (mL)	0.097	0.06
H$_2$O (g)	6.00	3.66
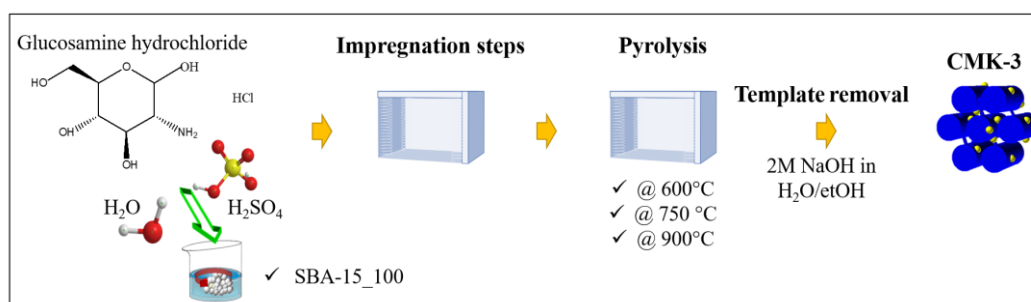
Figure A.1.3: Schematic representation of the hard templated synthesis of N-containing CMK-3 ordered mesoporous carbons.

A1.5.   Synthesis of CMK-8

N-containing CMK-8 samples were prepared by using a two-step impregnation procedure. The silica template was previously degassed overnight at 150 °C under vacuum; its pore volume value was used to determine the amount of the carbon source necessary to fulfill the porous template [246]. The relative amounts of G, H$_2$0 and H$_2$SO$_4$ were estimated from adjustments of a frequently used standard procedure for the impregnation with sucrose as the carbon source [227,246]. Precisely, for the first impregnation step, 1.0 g of G, 0.062 mL of H$_2$SO$_4$, and 4.0 g of doubly deionized water or 2.0 g of G, 0.123 mL of H$_2$SO$_4$, and 8.0 g of deionized water were used for each gram of KIT-6_40 or KIT-6_100/KIT-6_140, respectively. Glucosamine was previously dissolved in the sulfuric acid aqueous solution and added dropwise to the silica powders. The mixture was stirred for 1 h at RT until a homogenous gel-like consistency was obtained. Then, the slurry was thermally treated using three-step heating in a muffle furnace at 100 °C for 6 h, 140 °C for 2 h, and 160 °C for 6 h. The same procedure was repeated for the second impregnation step, reducing the initial amounts of reagents to 0.61 g of G, 0.038 mL of H$_2$SO$_4$, and 2.44 g of doubly deionized water or 1.22 g of G, 0.075 mL of

H_2SO_4, and 4.88 g of doubly deionized water for KIT-6_40 or KIT-6_100 KIT-6_140 templates, respectively. The mixture was again treated at 100 °C for 6 h and 140 °C for 2 h in a muffle furnace. Then, each family of CMK-8 samples was pyrolyzed at three different temperatures: 600, 750, and 900 °C, for 4 h. The pyrolysis was carried out in a muffle furnace, in a controlled atmosphere using a quartz reactor with a capillary cap under laboratory pressure [249]. The samples were heated from RT to the target T_p (heating rate = 3 °C min^{-1}), with two intermediate steps at 200 °C for 6 h and at 655 °C for 4 h (the latter was absent on the samples pyrolyzed at 600 °C). Finally, the silica template was dissolved by stirring the carbonized powders overnight at RT in a 2M NaOH water/ethanol solution (H_2O:EtOH = 1:1 v/v). A complete silica removal was accomplished by repeating this procedure three times (verified by the negligible amount of residual sample after thermogravimetric analysis under air). After that, the samples were washed several times in water and ethanol and dried overnight at 70 °C. For comparison purpose, another material was prepared with the same procedure, but using S as the carbon source and KIT-6_100 as the hard template. The details of NOMCs and OMCs synthesis and the amounts of each respective chemical are summarized in Table A.4 and Table A.5, respectively. The schematic representation of the synthesis procedure is shown in Figure A.1.4.

Table A.4: List of chemicals and their amounts for each gram of silica template used for N-containing CMK-8-type carbon synthesis.

Chemical	1st impregnation	2nd impregnation
G (g)	1.00[a]; 2.00[b]	0.61[a]; 1.22[b]
H_2SO_4 (mL)	0.062[a]; 0.123[b]	0.038[a]; 0.075[b]
H_2O (g)	4.00[a]; 8.00[b]	2.44[a]; 4.88[b]

Amount of chemicals calculated for [a] KIT-6_40 or [b] KIT-6_100/KIT-6_140 silica hard template.

Table A.5: List of chemicals and their amounts for each gram of silica template used for undoped CMK-8-type carbon synthesis.

Chemical	Amount
S (g)	2.00
H_2SO_4 (mL)	0.123
H_2O (g)	8.00
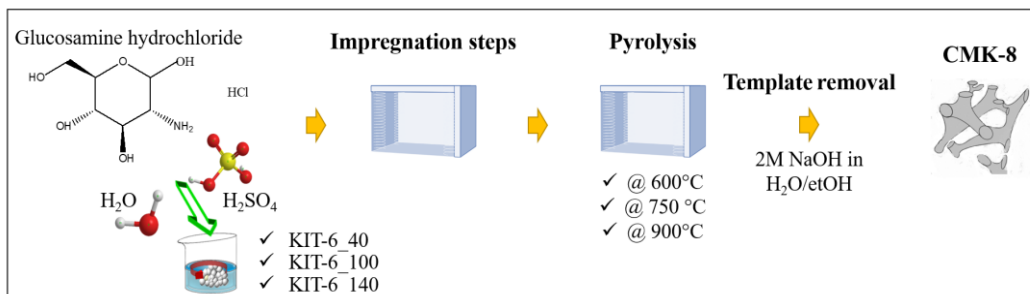
Figure A.1.4: Schematic representation of the hard templated synthesis of N-containing CMK-8 ordered mesoporous carbons.

Appendix 2

A2.   Description   of   the methodologies   and   the characterization techniques

A2.1.   Physico-chemical characterization

A2.1.1.   Low-angle X-ray diffraction (LAXRD)

Generally speaking, ordered mesoporous materials usually do not possess long-range order at the atomic scale, so conventional X-ray diffraction analysis is not an useful tool for their structural characterization [352]. However, their nanoscale mesoporous ordering allows the observation of distinct reflection peaks in the low-angle diffraction region, making this technique suitable for their structural investigation [352]. A PANalytical EMPYREAN powder diffractometer equipped with the PIXcel^{3D} detector (Malvern PANalytical, United Kingdom) was used for the low-angle X-ray diffraction (LAXRD) analysis. The LAXRD patterns were collected in transmission mode (using focusing mirror geometry) using a Cu K$\alpha_{1/2}$ radiation, at an operating voltage of 45.0 kV and a tube current of 40.0 mA. The measurements were carried out in continuous mode with a step size of $2\theta = 0.0131°$ and a data time per step of 50 s.

A2.1.2.   Transmission (TEM) and scanning (SEM) electron microscopy

The morphology and the periodic arrangement of the pores was confirmed by electron microscopy analyses. High-resolution transmission electron microscopy (HR-TEM) images of CMK-8-samples were taken at the University of Vienna with a Philips CM20 transmission electron microscope at an accelerating voltage of 200 keV in brightfield mode. For HR-TEM analysis, the samples were dispersed in ethanol via gentle sonication and a droplet of the resulting mixture was deposited

onto an aluminum TEM grid and dried at RT. Regarding sample preparation for TEM characterization, the dry powders were dispersed in high purity ethanol, sonicated for 15 minutes with the aim to achieve a good dispersion and subsequently drop-casted onto lacey-carbon Cu TEM grids.

The morphology of the CMK-8 materials was also studied by Field Emission Scanning Electron Microscopy (FESEM) using a Zeiss Supra 40 microscope (Zeiss, Milano, Italy). The images were taken with magnifications from 1000 to 250000 times at 5 kV. The samples for SEM were prepared using the following procedure: the carbon powder was dispersed in EtOH, sonicated gently and a droplet was deposited on a double-sided sticky carbon tape fixed to a flat sample holder and dried at RT. The morphology and structure of CMK-3 carbon-based materials was investigated at the IIT center in Torino with a FEI Tecnai G2 F20 S-twin microscope operated at 200 kV acceleration voltage. To enhance image contrast from the carbon-based material, different objective apertures were used to achieve bright-field imaging. Scanning transmission electron microscopy (STEM) images were acquired with two different detectors: Bright-field (BF) and High-Angle Annular Dark Field (HAADF).

A2.1.3. N_2 and CO_2 sorption for specific surface area and porosity investigation

Specific surface area and porosity evaluation in the mesoporous range were carried out by N_2 adsorption-desorption measurements at 77 K (i.e., -196 °C), while microporosity was studied performing adsorption at 0 °C and using CO_2 as a gas probe. Adsorption-desorption of N_2 (at -196 °C) and CO_2 (at -10, 0 and 10 °C) were performed in an Anton Paar Quantatech Inc. IQ2 instrument (Boynton Beach, FL, USA). Before sorption analysis, silica and carbon samples were outgassed at 150 and 300 °C, respectively, for 12 h under vacuum. The calculations were carried out using the AsiQwin 5.2 software provided by Anton Paar Quantatech Inc. The specific surface area (S_{DFT}), pore size distribution (PSD), pore width (D_p) and pore volume ($V_{p,DFT}$) in the mesoporous range of silica samples were calculated using the non-local density functional theory (NLDFT) method, applied on the equilibrium branch of N_2 isotherms at -196 °C, considering an amorphous silica surface and a cylindrical pore model. The quench solid density functional theory (QSDFT) was used as preferential method for the estimation of S_{DFT}, PSD, D_p and $V_{p,DFT}$ of carbon samples. QSDFT method was applied at the adsorption branch of N_2 isotherms at -196 °C, considering the model for carbons and cylindrical pores as adsorbent and pore shape, respectively. QSDFT method was chosen as the most accurate for this analysis because, in respect to NLDFT, it

includes a roughness parameter, which takes into account the surface heterogeneity of some carbon materials [353]. Indeed, a good fit of the QSDFT model with the experimental data was observed, as shown in Figure A.2.1.

Brunauer-Emmett-Teller (BET) surface area (S_{BET}) was also calculated adjusting opportunely the relative pressure of data point selection in the range 0.05 < p/p$_0$ < 0.2. Micropore size distribution, pore width (D_{mp}) in the microporous range, micropore (V_{mp}, < 2 nm) and ultramicropore volume (V_{ump}, < 0.7 nm) were calculated from the adsorption branch of the CO_2 isotherms at 0 °C, using a NLDFT method specific for carbon surfaces.
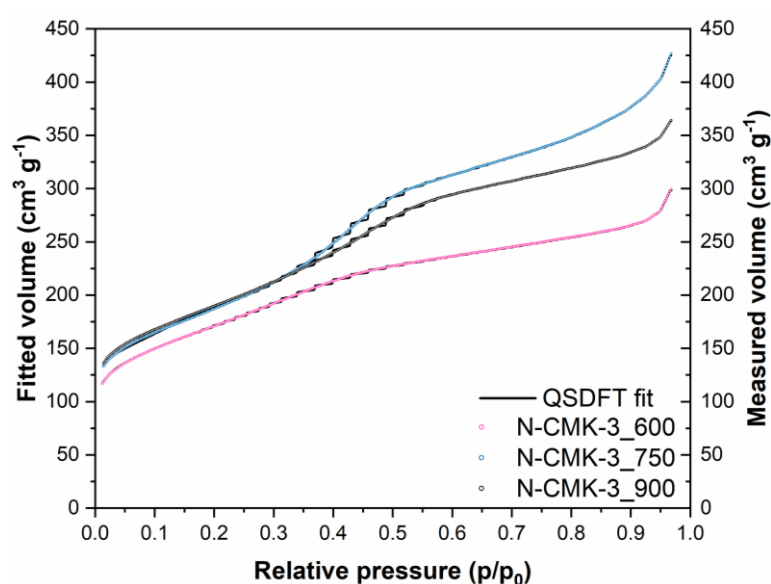
Figure A.2.1: QSDFT fit (solid black line) of N_2 adsorption-desorption isotherm measured at −196 °C for the CMK-3_600, CMK-3_750 and CMK-3_900 samples (red, black and blue dots, respectively).

A2.1.4.   Thermo-gravimetric analysis (TGA)

A2.1.4.1.   Thermal degradation study under air

Thermal degradation analysis on CMK-8 samples (Figure A.2.2) was performed in a thermogravimetric analyzer NETZSCH TG 209 F3 Tarsus®. An amount of 5-7 mg of sample was burned in an alumina pan under air flow (20 mL min^{-1}) with N_2 as a protective gas (20 mL min^{-1}) in the temperature range of 30 – 800 °C (heating rate 10 °C min^{-1}).
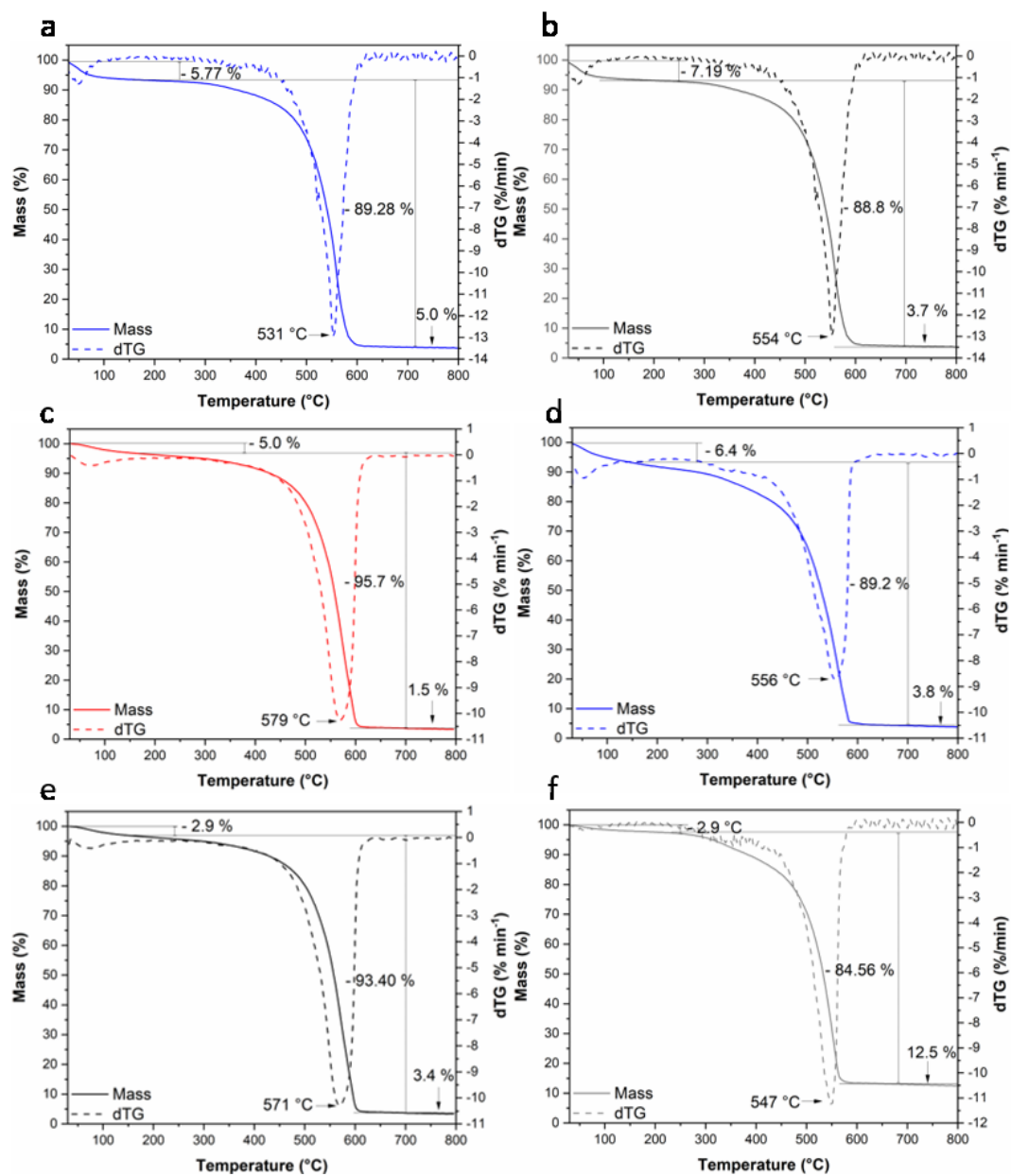
Figure A.2.2: Thermal stability under air up to 800 °C for the samples (a) G_750(40), (b) G_900(40), (c) G_600(100), (d) G_750(100), (e) G_900(100), and (f) S_900(100).

A2.1.4.2. Thermo-gravimetric analysis under inert atmosphere

The thermo-gravimetric analysis on N-CMK-3 samples was conducted at the University of Turin with a TA Instruments Q600 programmed with a heating rate

of 1 °C min^{-1} from RT to 800 °C in N$_2$ atmosphere (100 mL min^{-1} flows), on about 3 mg of each sample in an alumina crucible.

A2.1.5.   X-ray photoelectron spectroscopy (XPS)

X-ray photoelectron spectroscopy on CMK-8 samples was performed at the University of Vienna with a XPS, Nexsa, Thermo-Scientific, Massachusetts, USA equipment, using Al Kα radiation source operating at 72 W and an integrated flood gun. A pass energy of 200 eV, "Standard Lens Mode", CAE Analyzer Mode and an energy step size of 1 eV for the survey spectrum was used. The diameter of the X-ray beam was 400 µm. Prior to analysis the surface was cleaned by sputtering with Ar-clusters (1000 atoms, 6000 eV, 1 mm raster size) for 60 s. High-resolution spectra were acquired with 50 passes at a pass energy of 50 eV and an energy step size of 0.1 eV. XPS survey spectra of the CMK-8 samples under study is shown in Figure A.2.3.
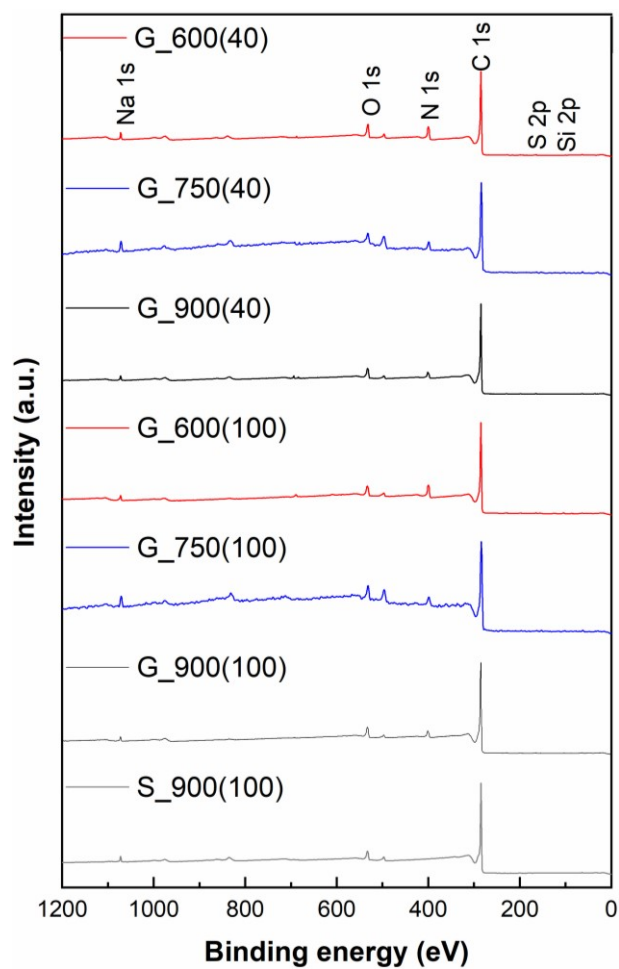
Figure A.2.3: XPS survey spectra of the CMK-8 samples under study.
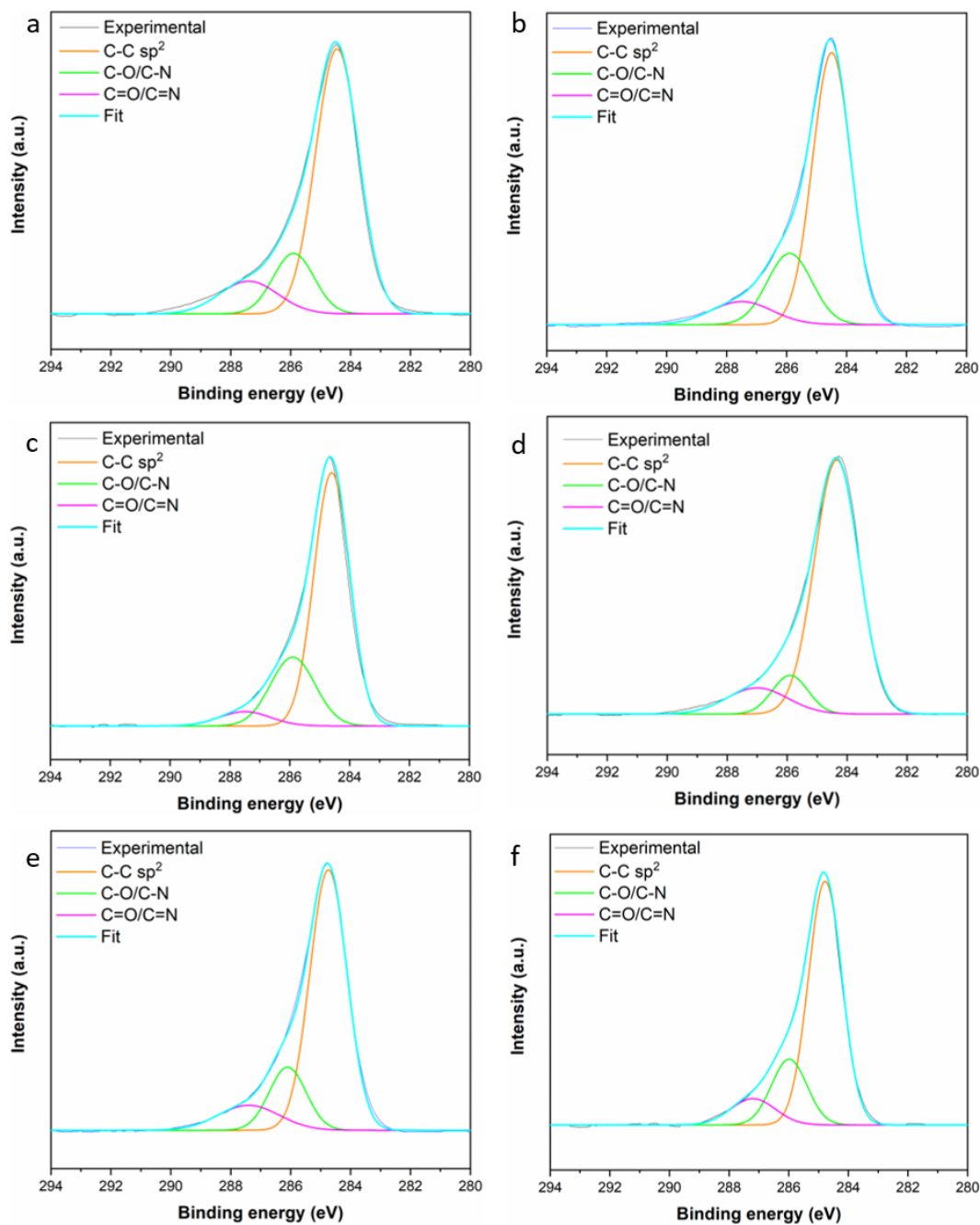
Figure A.2.4: XPS high-resolution spectra of the C1s region for all the samples, with the corresponding deconvolution: (a) G_600(40), (b) G_750(40), (c) G_900(40), (d) G_600(100), (e) G_750(100), and (f) G_900(100).
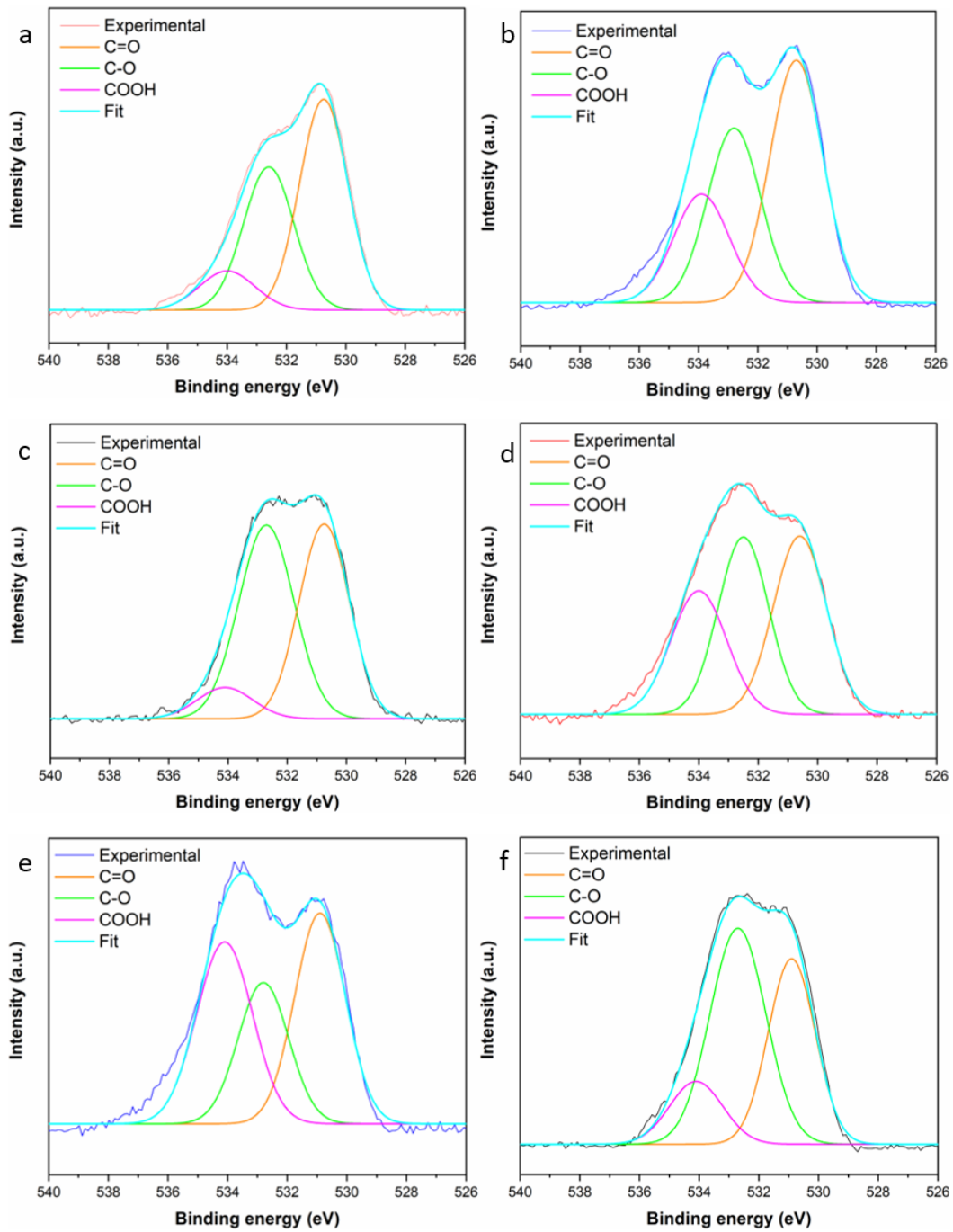
Figure A.2.5: XPS high-resolution spectra of the O1s region for all the samples, with the corresponding deconvolution: (a) G_600(40), (b) G_750(40), (c) G_900(40), (d) G_600(100), (e) G_750(100), and (f) G_900(100).
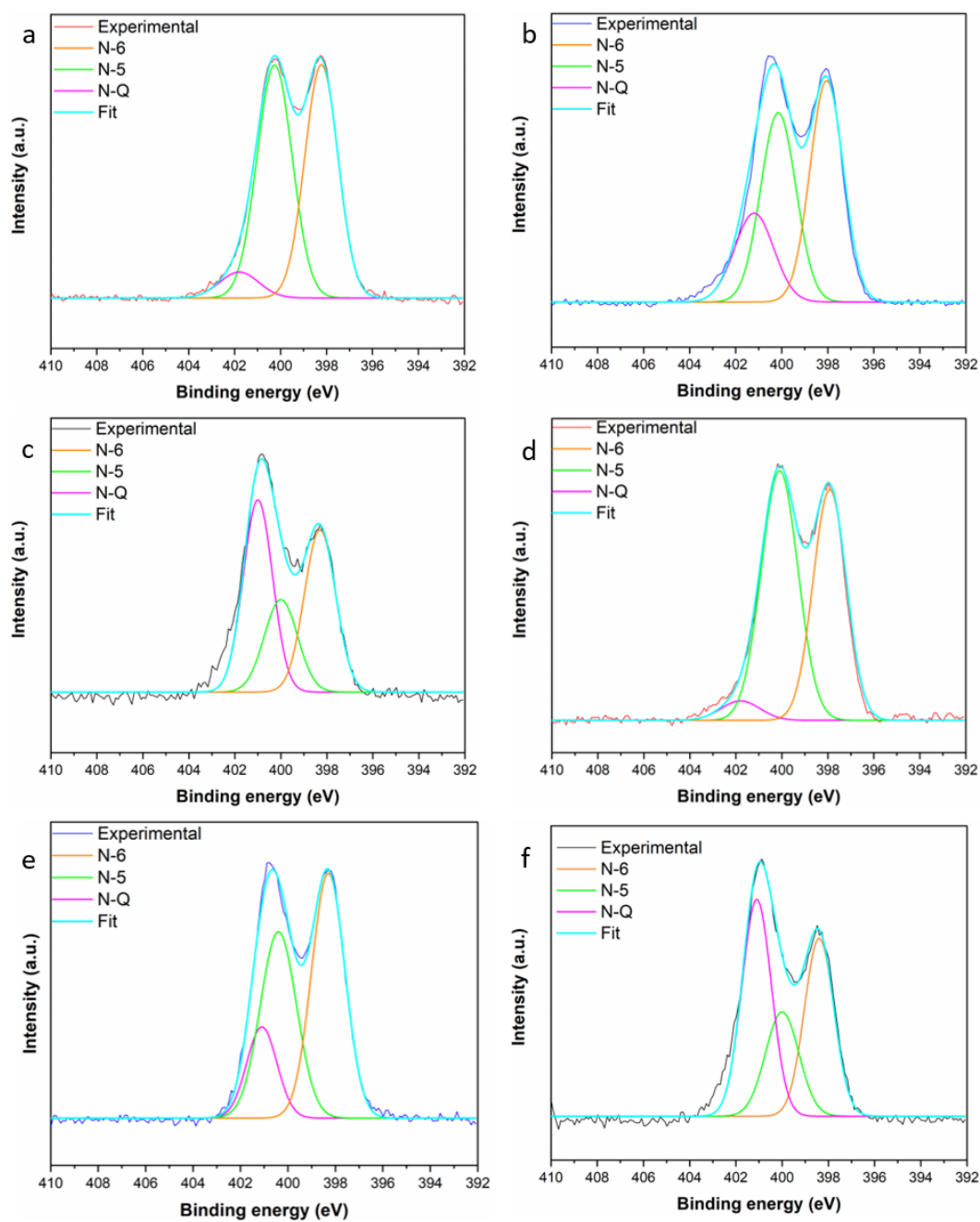
Figure A.2.6: XPS high-resolution spectra of the N1s region for all the samples, with the corresponding deconvolution: (a) G_600(40), (b) G_750(40), (c) G_900(40), (d) G_600(100), (e) G_750(100), and (f) G_900(100).
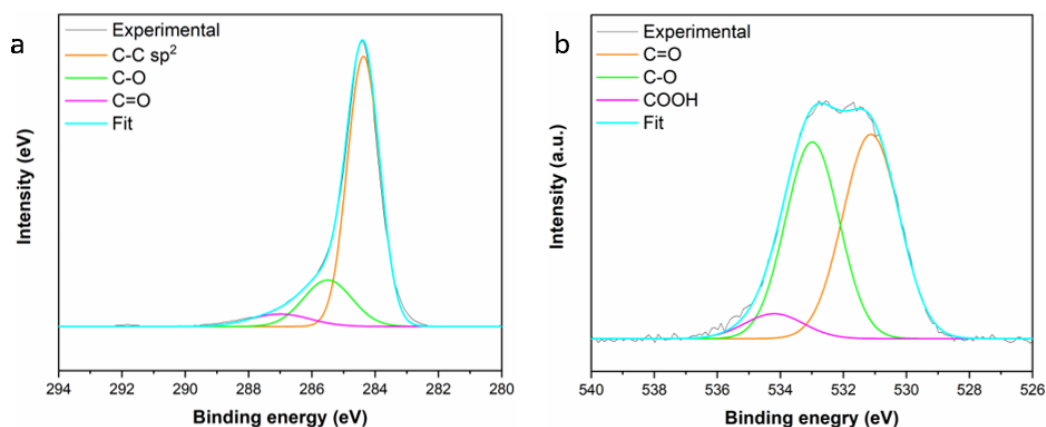
Figure A.2.7: C1s (a) and O1s (b) high resolution XPS spectra of S_900(100).

X-Ray photoelectron spectroscopy on N-CMK-3 samples (PHI 5000 VersaProbe, Physical Electronics) was performed at Politecnico di Torino using Al Kα radiation source operating at an energy of 1486.6 eV. A pass energy of 187.75 eV and of 23.5 eV were used for the survey spectrum and the HR spectra, respectively. The diameter of the X-ray beam was 100 μm. Charge compensation during measurements was obtained with a combination of electron beam and low-energy Ar beam system. High resolution XPS spectra were fitted with Gaussian functions and a spline for the background subtraction using the software OriginPro 2020. High resolution XPS spectra of both CMK-8 and CMK-3 samples were fitted with Gaussian functions and a spline for the background subtraction using the software OriginPro 2020.
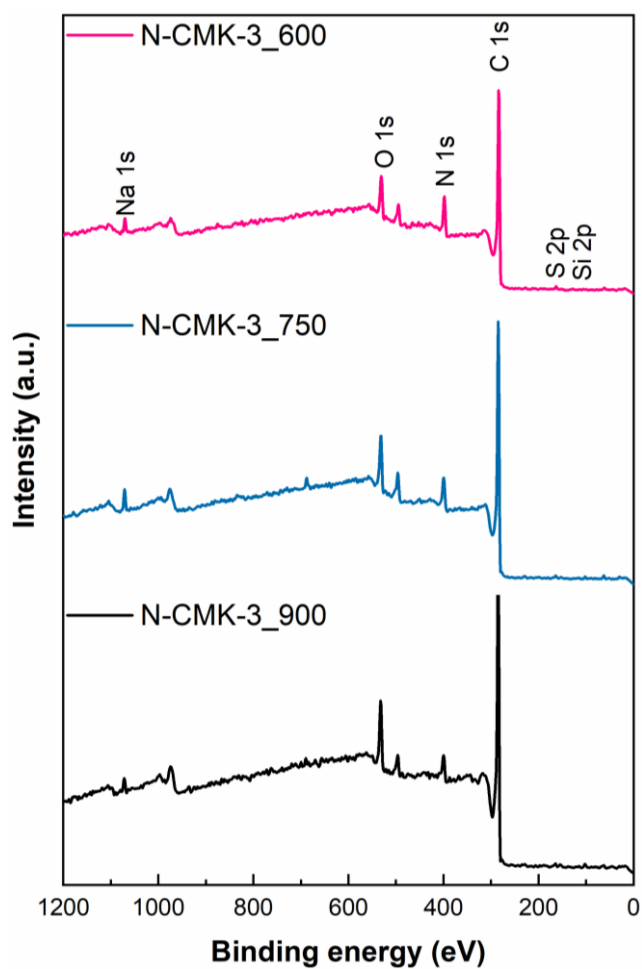
Figure A.2.8: XPS survey spectra of the N-CMK-3 samples under study.
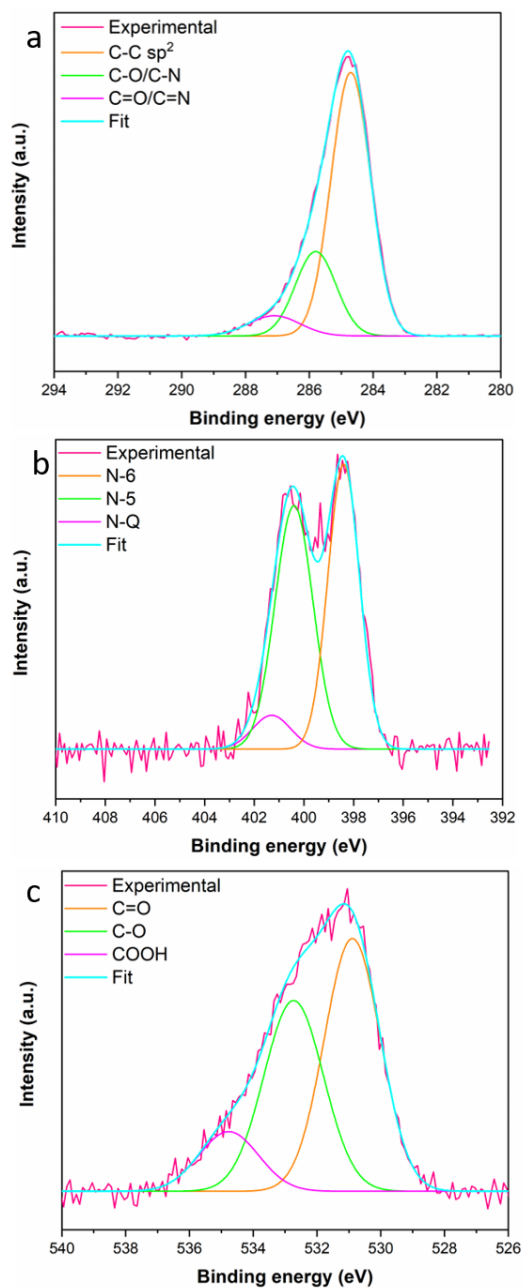
Figure A.2.9: XPS high-resolution spectra of the C1s (a), N1s (b) and O1s (c) region for the sample N-CMK-3_600.
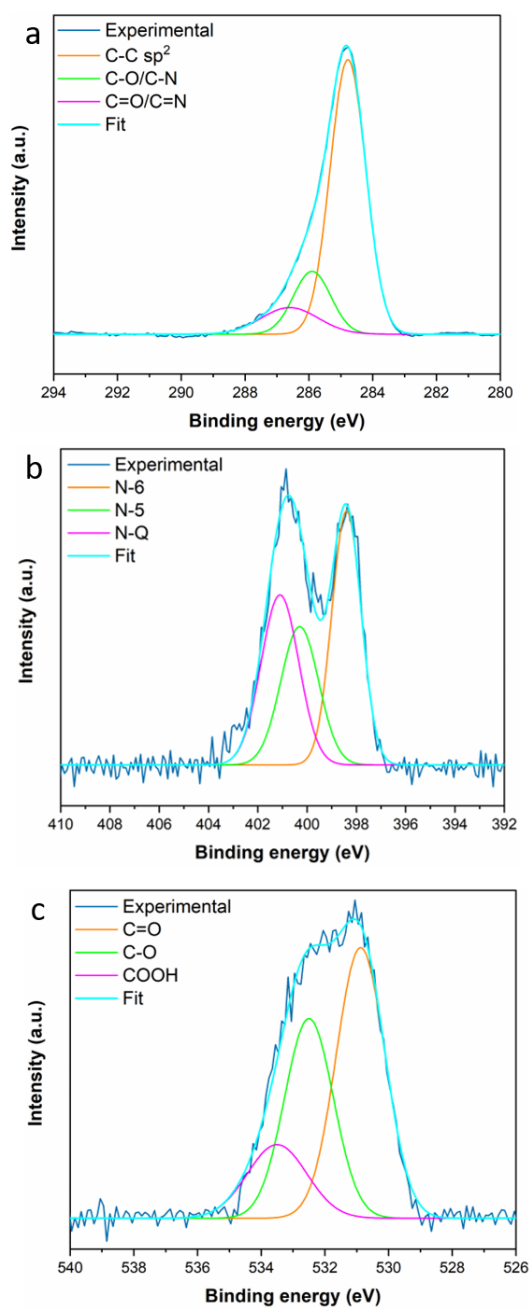
Figure A.2.10: High-resolution XPS spectra of the C 1s (a), N 1s (b) and O 1s (c) region for the sample N-CMK-3_750.
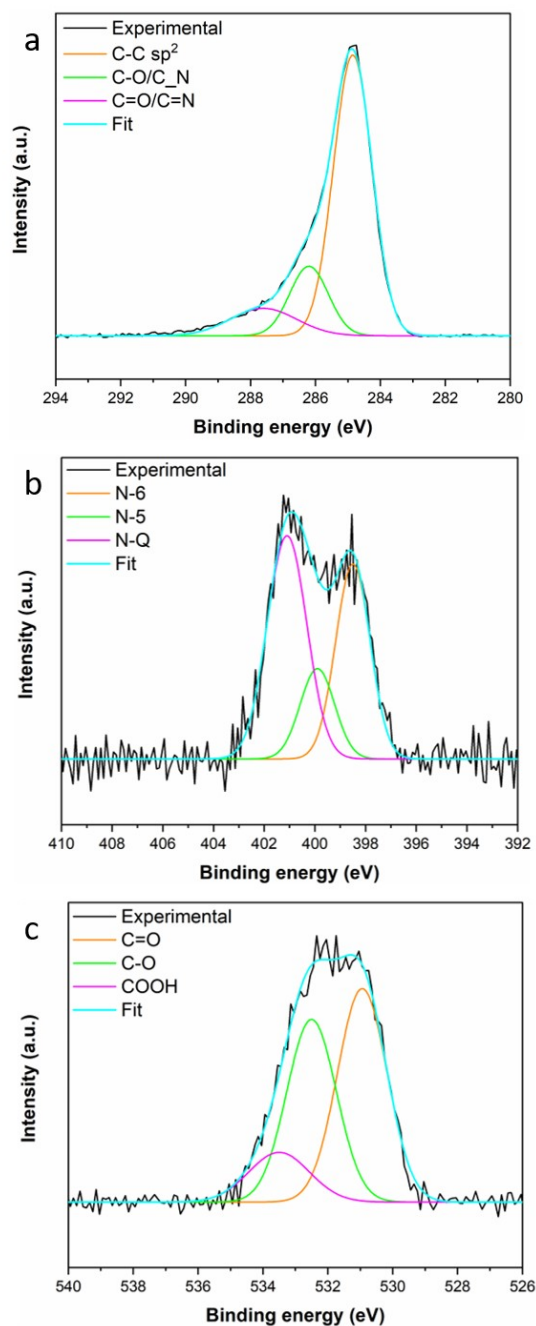
Figure A.2.11: High-resolution XPS spectra of the C 1s (a), N 1s (b) and O 1s (c) region for the sample N-CMK-3_900.
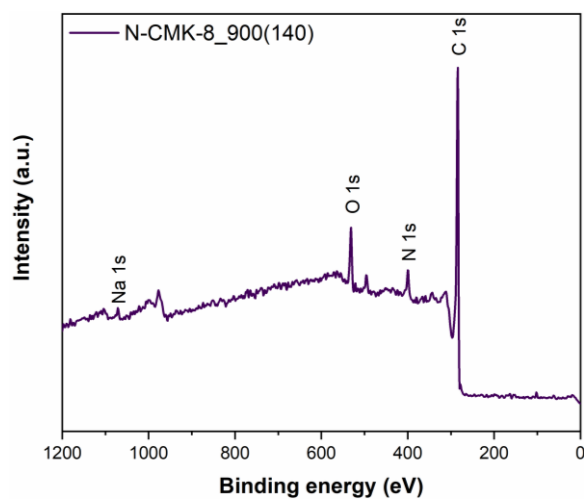
Figure A.2.12: XPS survey spectra of the N-CMK-8_900(140) samples under study.
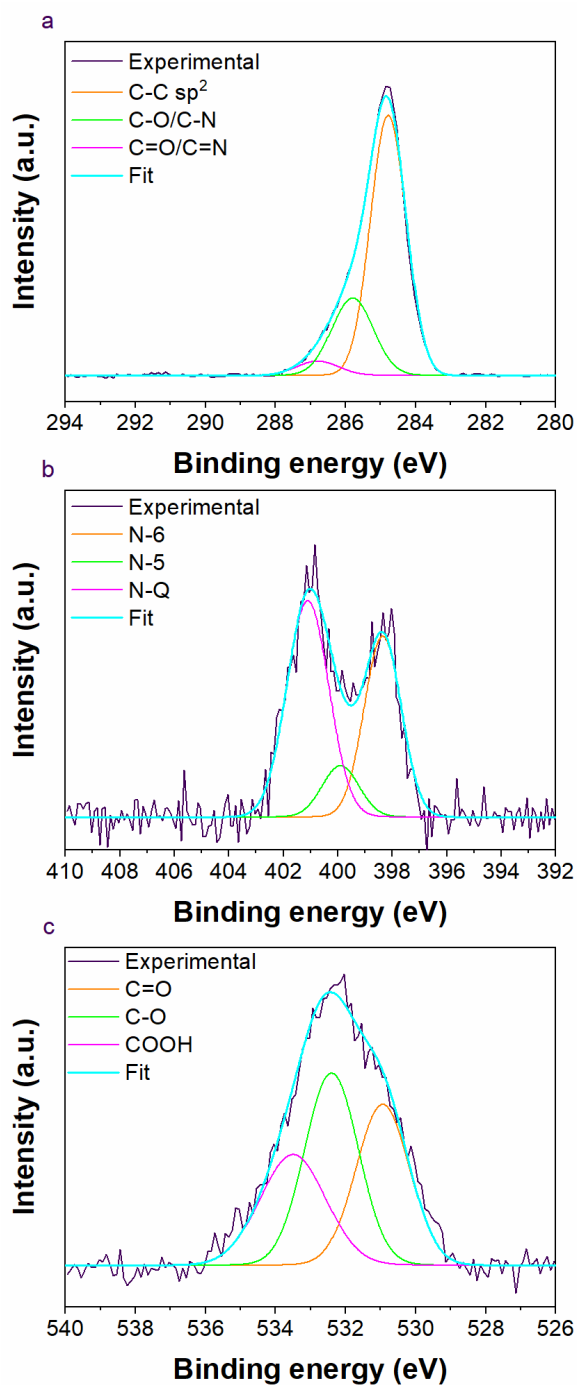
Figure A.2.13: High-resolution XPS spectra of the C 1s (a), N 1s (b) and O 1s (c) region for the N-CMK-8_900(140).

A2.2.   Pure CO₂ adsorption and CO₂/N₂ selectivity evaluation

A2.2.1.   Pure CO₂ and N₂ adsorption

Pure CO_2 and N_2 adsorption isotherms and cyclic CO_2 adsorption-desorption measurements were performed using a Surface Measurement System, Dynamic Vapor Sorption (DVS) instrument (Figure A.2.14). The samples were activated under vacuum at 300 °C for 30 min before each analysis. The pure CO_2 and N_2 isotherms were carried out at a constant temperature of 30 °C while increasing the pressure up to 0.9 bar (10% of p/p_0 increase at each step). The equilibrium criterion condition for each step was chosen as $dm/dt = 0.002$ % min^{-1}.
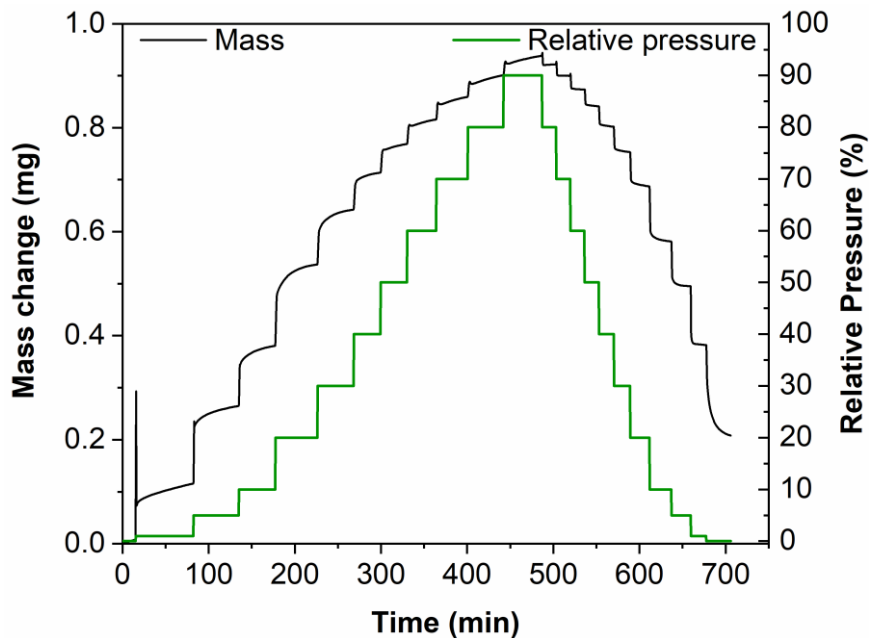
Figure A.2.14: Experimental setup for isothermal CO_2 performed in DVS apparatus.

A2.2.2. CO$_2$/N$_2$ selectivity evaluation under multicomponent and single component conditions

A2.2.2.1. CO$_2$/N$_2$ selectivity from multicomponent gas mixture

The selectivity for CO$_2$ adsorption in a mixture with N$_2$ was evaluated by thermogravimetric analysis (TGA) on a NETZSCH TG 209 F1 Libra at 35 °C and ambient laboratory pressure (~1 bar). A schematic representation of the setup is shown in Figure A.2.15. Before each test, in order to remove contaminants (mainly adsorbed gases or water), which can occlude the porosity, the samples were activated as follows: approximately 20 mg of sample was activated with one cycle of vacuum and, successively, heating up to 500 °C for 15 min (heating rate 10 °C min^{-1}) under N$_2$ flow. While cooling down the temperature to 35 °C (cooling rate 40 °C min^{-1}), the sample was exposed to pure N$_2$ for 15 min, for stabilizing the weight. After that, a simulated flue gas [354] made up of 20 vol. % of CO$_2$ and 80 vol. % of N$_2$ (8 mL min^{-1} of CO$_2$ in a total flow of 40 mL min^{-1}) replaced N$_2$; the weight increase observed after the CO$_2$/N$_2$ gas mixture exposition for 120 min corresponds to the amount of CO$_2$ adsorbed by the sample. The desorption procedure was carried out in two stages: first at the same temperature of 35 °C by sweeping the gas mixture for a pure N$_2$ flow for 1 h, to remove adsorbed CO$_2$; then, by heating the sample to 500 °C for 15 min (10 °C min^{-1}) for desorbing CO$_2$ adsorbed at the more energetic sites.
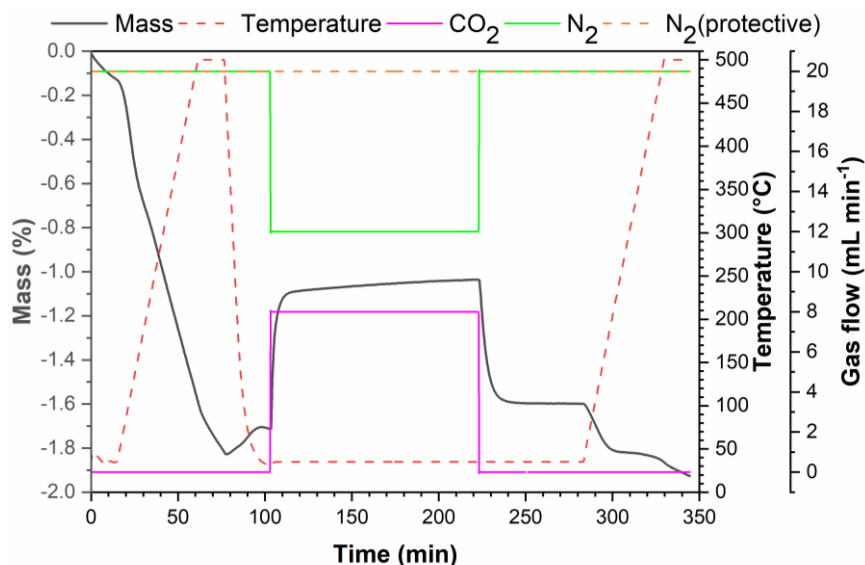
Figure A.2.15: Experimental setup for CO$_2$/N$_2$ selectivity tests by TGA.

A2.2.2.2.   CO₂/N₂ selectivity by IAST method

Ideal adsorption solution theory (IAST) was applied on single component adsorption isotherms of CO_2 and N_2 at 30 °C, from 0 to 90 kPa. Precisely, IAST selectivity (S_{IAST}) was calculated according to the Equation 3.3 [90]. The molar fraction of the gas phase (y_{CO2} and y_{N2}) was chosen as 20% of CO_2 and 80% of N_2 for the gas mixture measurements in TGA, or as 15% of CO_2 and 85% of N_2 for more precise comparison with the majority of the literature reports. In details, the molar fraction of adsorbed CO_2 (x_{CO2}) and N_2 (y_{CO2}) in a single component adsorption isothermal measurement simulating a CO_2/N_2 mixture for the chosen composition were calculated according to the Equation A.1 and A.2, respectively:

$$x_{CO2} = \frac{n_{CO2}(p)}{(n_{CO2}(p) + n_{N2}(p))} \qquad \text{(Eq. A. 1)}$$

$$x_{N2} = \frac{n_{N2}(p)}{\left(n_{CO2}(p) + n_{N2}(p)\right)} \qquad \text{(Eq. A. 2)}$$

where $n_{CO2}(p)$ and $n_{N2}(p)$ correspond to the adsorbed amounts of CO_2 and N_2 (mmol g^{-1}), respectively, at a certain pressure p.

A2.2.3.   Henry's law constant and isosteric enthalpy of CO₂ adsorption

The affinity of CO_2 for the adsorbent surface was estimated by the Henry's law constant (K_H). K_H (mmol g^{-1} kPa^{-1}) was calculated from pure CO_2 adsorption isotherms obtained at 0 °C (see Figure A.2.16 and Figure A.2.17) in the limit of zero coverage using the virial isotherm model (Equation 3.2).
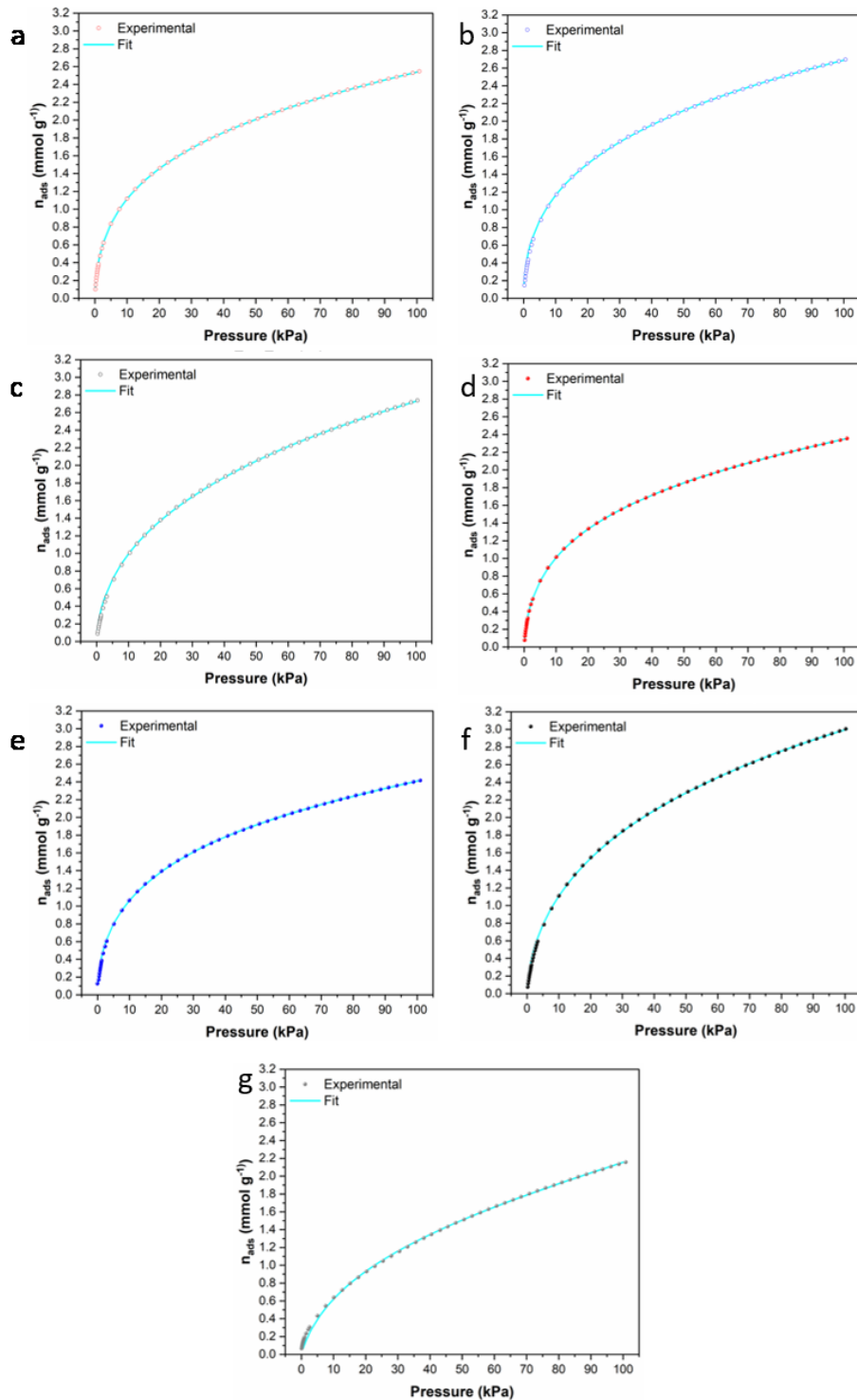
Figure A.2.16: Adsorption equilibrium isotherms of pure CO_2 at 0 °C fitted with the virial isotherm model of the samples: a) G_600(40), b) G_750(40), c) G_900(40), d) G_600(100), e) G_750(100), f) G_900(100), and g) S_900(100).
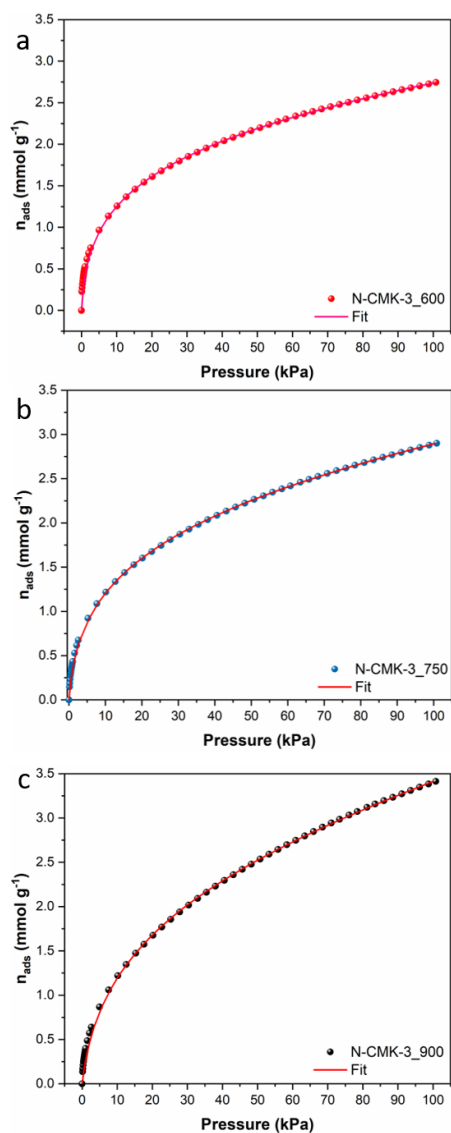
Figure A.2.17: Adsorption equilibrium isotherms of pure CO_2 at 0 °C fitted with the virial isotherm model of the samples: a) N-CMK-3_600, b) N-CMK-3_750 and c) N-CMK-3_900.

The isosteric enthalpy of adsorption (ΔH_{ads}) was calculated from the CO_2 adsorption branches of the isotherms obtained at three different temperatures, i.e. -10, 0 and 10 °C, ($\Delta T = 10$ °C) and analyzed by the Clausius-Clapeyron approach using the software AsiQwin 5.2. The ΔH_{ads} values are derived from the slope of the Arrhenius plot ($\ln p$ vs. $1/T$), where p is the value of pressure at equal coverage and T is the respective absolute temperature. The software calculation is based on the Clausius-Clapeyron equation (Equation 3.1) [87], where $\Delta H_{ads}(n_{ads,i})$ values are

derived from the slope of the Arrhenius plot ($\ln p$ *vs.* $1/T$ plot), constructed in the loading range within the nearly linear region of $\ln p$ *vs.* n_{ads} plot; p are couples of pressure values correspondent to the same loading n_{ads} (isosteric condition). R = 8.314 J mol^{-1} K^{-1} is the universal gas constant.

A2.2.4.   Reusability tests: multiple CO$_2$ adsorption-desorption cycles

The reusability of the sorbents was tested by means of multiple consecutive adsorption-desorption cycles. Cyclic CO$_2$ adsorption-desorption measurements were performed using a DVS instrument (Figure A.2.14). The samples were activated under vacuum at 300 °C for 30 min before each analysis. Each adsorption step was performed at 20% of CO$_2$ vapour pressure ($\sim$ 19.7 kPa) and 30 °C (equilibrium criterion dm/dt = 0.01 % min^{-1}). The desorption/regeneration step was carried out at 150 °C. The schematic representation of the measurement is shown in Figure A.2.18.
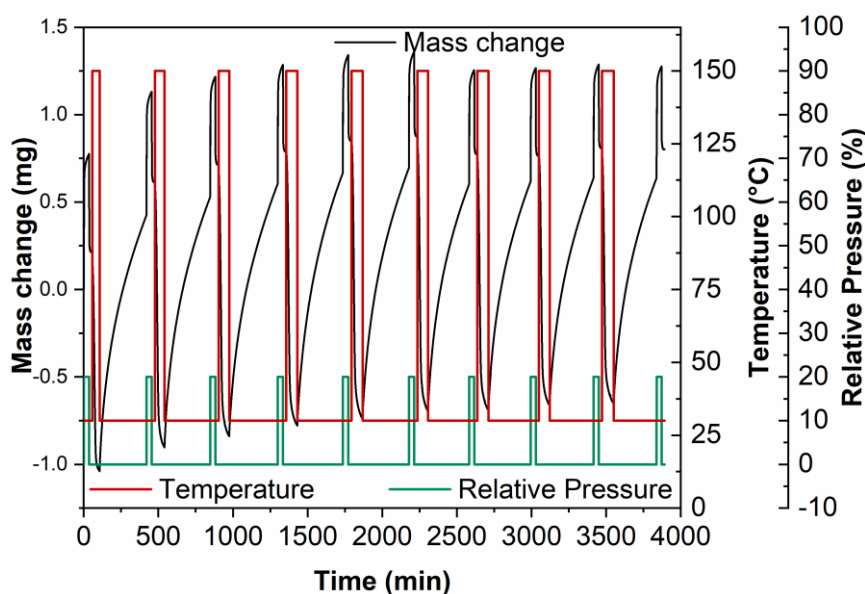
Figure A.2.18: Experimental setup for isothermal cyclic CO$_2$ adsorption-desorption tests performed in DVS apparatus.

A2.3. Pure H₂O adsorption, CO₂/H₂O selectivity and reusability

Pure H_2O and CO_2/H_2O isotherms and were performed using a DVS instrument. Approximately, 20 mg of sample were activated under vacuum at 300 °C for 30 min before each analysis.

A2.3.1. Pure H₂O adsorption

The pure H_2O isotherms (see Figure A.2.19) were performed at 30, 40, 50 and 60 °C, varying the relative humidity (RH, %) from 0 up to 75% ($RH = \frac{p_{H2O}\,(kPa)}{p_{H2Osat,T}\,(kPa)} \times 100$), where $p_{\text{H2Osat,T}}$ is the water vapour saturation pressure at the analysis temperature (i.e., 4.2, 7.4, 12.3 and 19.9 kPa, for 30, 40, 50 and 60 °C, respectively). From the observation that H_2O adsorption was unstable on samples never exposed to water before the measurement, it was decided to consider H_2O adsorption isotherms obtained on samples already exposed to water, in order to have comparable isotherms obtained subsequently at different temperatures.
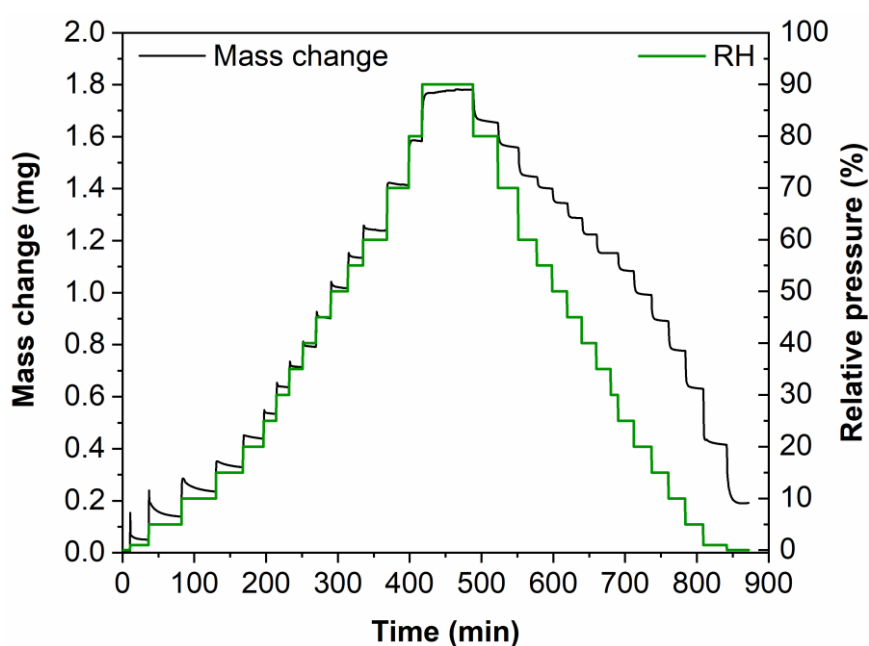
Figure A.2.19: Experimental setup for isothermal H_2O adsorption-desorption tests performed in DVS apparatus.

A2.3.2.   CO₂/H₂O   selectivity   evaluation   under multicomponent gas mixtures

CO_2/H_2O adsorption tests were performed at 30 °C, varying the total pressure from 0 to 90% of the H_2O vapour pressure at 30 °C, i.e., 4.2 kPa. Three adsorption-desorption cycles were performed; during each cycle, H_2O and CO_2 were mixed in different ratios according to the scheme in Figure A.2.20. The regeneration of the sorbents between consecutive cycles was performed in PSA condition, simply reducing the pressure, therefore without applying heating. The equilibrium criterion condition for each step was chosen as $dm/dt = 0.002$ % min^{-1}.
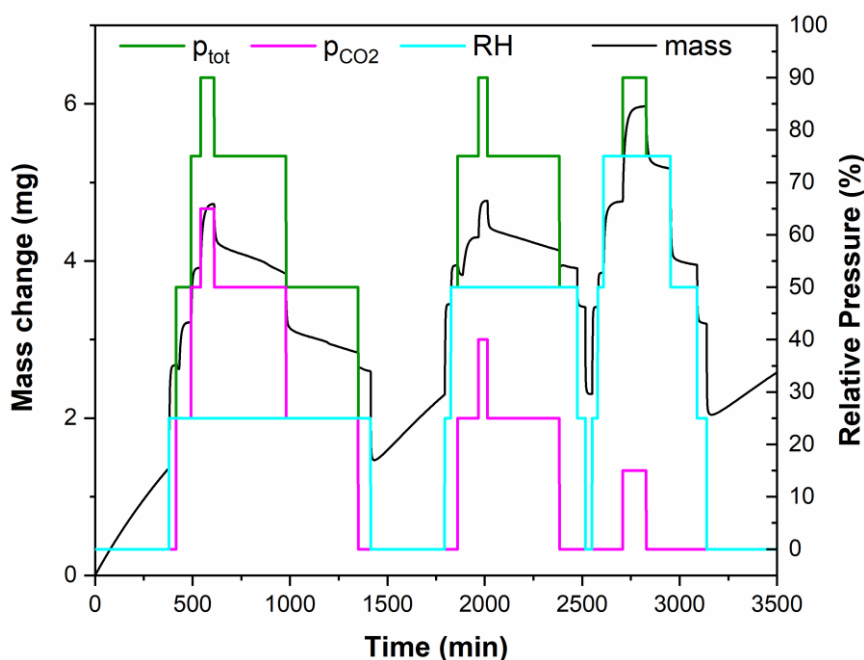
Figure A.2.20: Experimental setup for isothermal CO_2/H_2O adsorption-desorption tests performed in DVS apparatus.

A2.3.3.   Assessment of sorbents reusability after H₂O adsorption

Pure CO_2 adsorption at 30 °C was repeated after the measurements under moist gas mixtures in order to investigate the reusability of the sorbents after the exposition to water. The pure CO_2 adsorption measurements, preceded by an activation step at 300 °C under vacuum) were performed using a DVS instrument as described in Paragraph A2.2.1. Specific surface area and porosity measurements

by N_2 adsorption-desorption measurements at 77K (i.e., -196 °C) (3Flex, Micromeritics Instrument Corporation) were also carried out at the University of Turin on both fresh samples and the same sample exposed to H_2O, in order to investigate the eventual reduction in pore volume and specific surface area due to incomplete H_2O desorption during the activation step preceding the CO_2 adsorption measurements. Before N_2 sorption analysis, carbon samples were outgassed at 300 °C for 1 h or 12 h under vacuum, in order to simulate the activation step preceding the CO_2 adsorption measurement in the gravimetric DVS apparatus. The calculations were carried out using the DFT method, considering a cylindrical pore geometry. BET area was calculated in the pressure range $0.02 < p/p_0 < 0.2$, according to Rouquerol theoretical requirements.

Sorbents' reactivation treatment after H_2O adsorption at higher temperatures was considered and monitored by thermogravimetric analysis coupled with Fourier transform infrared spectroscopy (TGA-FTIR). The TGA-FTIR was carried out on about 2 mg of each sample using a TG 209 F1 Libra® (NETZSCH GmbH), at 20 °C min^{-1} heating rate, from 25 °C to 800 °C under N_2 flow (40 cm^3 min^{-1}). Experimental error was estimated to be typically lower than 0.05 mg (approximately $\pm$ 2.5%). Gas transmittance spectra of the evolved gases were collected on a Bruker Tensor II equipped with IR gas cell (TGA–FTIR) heated at 200 °C to avoid condensation of degraded products. The instruments were coupled by Netzsch FT-IR Coupling Systems transfer line heated at 230 °C. In order to have a stable infrared (IR) background, the line was cleaned using vacuum during three cycles of vacuum/refill with N_2. IR spectra of the evolved gases were sampled at 3 °C (ca. 10 s) intervals. The FTIR analysis is collected in the absorbance mode in the range $650 - 4400$ cm^{-1}. The gas development kinetics were followed at the maximum of absorption for the different molecules: ammonia (NH_3) 965 cm^{-1} [340]; water (H_2O) 1505 cm^{-1} [341]; carbon monoxide (CO) 2179 cm^{-1} [342]; carbon dioxide (CO_2) 2349 cm^{-1} [343]; hydrogen cyanide (HCN) 3735 cm^{-1} [344]; paraffin oil by -CH_2- stretching at 2925 cm^{-1} [345] and oxidised paraffin oil from carbonyl stretching at 1715 cm^{-1} G[345].

Appendix A3

A3. Laboratory-scale Li and Na metal cell assembly and electrochemical characterization

A3.1. Electrode preparation

The electrodes for the electrochemical testing were prepared by spreading a slurry obtained by using the here-synthesized N-rich CMK-8-type ordered mesoporous carbons as the active material, carbon black (C-NERGY™ Super C45, Imerys) as the electrically conductive additive, and polyvinylidene fluoride (PVDF, Solvay Solef 2010) as the binder. The weight ratio among active material, conductive additive and binder was chosen as 70:20:10. The procedure of the slurry preparation consists in mixing/grinding the active material and carbon black in an agate mortar, and the subsequent addition of the powders to a solution of PVDF dissolved in N-methylpirrolidone (NMP, Merk). The mixture was kept under stirring for ca. 4 h, and after having acquired a homogeneous dense consistency, it was casted on a copper foil using a doctor-blade. The deposited slurry was left drying under a fume hood for removing NMP solvent by spontaneous evaporation at ambient laboratory temperature. Afterwards, the electrodes were punched out with a suitable diameter (between 10 and 18 mm, according to the dimension of the electrode support in the assembled cell) and dried overnight in vacuum at 120 °C, immediately before cell-assembly.

A3.2. Cell assembly

The cell assembly procedure occurred in a dry and controlled atmosphere by using a GP Dry-Glove Box Workstation by Jacomex filled with Ar. Li- or Na-metal foils worked as the counter electrode (and also as the reference electrode in the case of cyclic voltammetry) in both T-cells or ECC-Ref test cell (El-Cell GmbH, Germany), whereas a Whatman glass wool disc, used as the separator between the

working and the counter electrode, was drenched with 200 µL of electrolyte. The liquid electrolyte used for Li-metal cells was 1M solution of lithium hexafluorophosphate ($LiPF_6$) in a mixture of ethylene carbonate (EC) and dimethyl carbonate (DMC) (1:1 vol.%) with 3 wt.% of fluoroethylene carbonate (FEC) (Solvionic). The liquid electrolyte used for Na-metal cells was 1M sodium perchlorate ($NaClO_4$) in ethylene carbonate (EC) and propylene carbonate (PC) (1:1 % vol.%).

A3.3. Characterization techniques and quantities defining the operational functioning of batteries

For the courtesy of the readers, a brief glossary of the main characterization techniques and the resulting quantities used to define the operational functioning of batteries are listed hereafter [271]:

⬧ *Cyclic voltammetry (CV)*: a potentio-dynamic technique, which consists in the application of a linear scan of potential, relative to a reference electrode, to the working electrode, while the current flowing between working and counter electrode is recorded. CV is able to evidence the electrochemical processes occurring in a certain range of potential by qualitatively identifying the position of the respective peaks.

⬧ *Galvanostatic cycling*: a technique, which consists in the application of a direct and constant current, while the voltage is monitored as a function of time in order to identify the potentials of the oxidation/reduction processes of the active materials and the total amount of charge passed per unit mass of electrode material (i.e., the specific capacity, see below) during each cycle of complete charge/discharge.

⬧ *Specific capacity*: total amount of electric charge supplied by the electrode materials defined per unit mass (Ah g^{-1}).

⬧ *Theoretical capacity:* maximum amount of charge that can be extracted from a battery with respect to the amount of the active material.

- *C-rate:* parameter that defines the applied current required to fully charge/discharge a battery as a function of the period of time necessary to complete the process. It is expressed as C/n, where *n* corresponds to the time unit. For instance, a C-rate of 1C (n=1) corresponds to the current required for fully charging/discharging a battery in 1h, 2C in half an hour (n=0.5), 0.5C in 2 h (n=2).

- *Coulombic efficiency (CE):* parameter that provides an indication of the reversibility of the discharge/charge process, and it is obtained as the ratio between the charge capacity and the previous discharge capacity (for anodes, *viceversa* for cathodes).

A3.4. Electrochemical testing

The electrochemical properties of the materials were investigated by cyclic voltammetry (CV) with a VMP3 electrochemical workstation by BioLogic Science Intruments (potential scan range of 0.01–2.0 V vs. Li^+/Li, scan rate 0.100 mV s^{-1}, Li-metal working as both counter and reference electrode) in order to evaluate the occurring electrochemical processes and, consequently, to identify the working potential range of the system. Subsequently, information on the specific capacity, CE, stability and duration of the cell operational life was deduced by galvanostatic charge/discharge cycling at different C-rates (Li cells cut-off potentials: 0.02 – 3 V vs. Li^+/Li; Na cells cut-off potentials: 0.02 – 2 V vs. Na^+/Na), with an Arbin BT-2000 battery tester. The active mass is calculated subtracting the weight of the copper current collector disc and weighting the resultant mass on the percentage of active material in the slurry composition (i.e., 70 wt.%).

References

[1]   A.A. Lacis, J.E. Hansen, G.L. Russell, V. Oinas, J. Jonas, The role of long-lived greenhouse gases as principal LW control knob that governs the global surface temperature for past and future climate change, Tellus, Ser. B Chem. Phys. Meteorol. 65 (2013). https://doi.org/10.3402/tellusb.v65i0.19734.

[2]   J. Houghton, Global Warming: The Complete briefing, Cambridge University Press, 2004.

[3]   D. Kweku, O. Bismark, A. Maxwell, K. Desmond, K. Danso, E. Oti-Mensah, A. Quachie, B. Adormaa, Greenhouse Effect: Greenhouse Gases and Their Impact on Global Warming, J. Sci. Res. Reports. 17 (2018) 1–9. https://doi.org/10.9734/jsrr/2017/39630.

[4]   S.R. Shewchuk, A. Mukherjee, A.K. Dalai, Selective carbon-based adsorbents for carbon dioxide capture from mixed gas streams and catalytic hydrogenation of CO2 into renewable energy source: A review, Chem. Eng. Sci. 243 (2021) 116735. https://doi.org/10.1016/j.ces.2021.116735.

[5]   D. Ehhalt, M. Prather, Atmospheric Chemistry and Greenhouse Gases, Clim. Chang. 2001 Sci. Basis. (2001) 239–287. http://scholar.google.com/scholar?hl=en&btnG=Search&q=intitle:Agriculture.+In+Climate+Change+2007:+Mitigation.+Contribution+of+Working+Group+III+to+the+Fourth+Assessment+Report+of+the+Intergovernmental+Panel+on+Climate+Change+[B.#0.

[6]   A.A.. Lacis, A. Schmidt, D.. Rind, R.A.. Ruedy, Atmospheric CO2: Principal Control Knob Governing Earth's Temperature, Science (80-.). (2011) 356–360.

[7]   N.M. Allen, M.R., O.P. Dube, W. Solecki, F. Aragón-Durand, W. Cramer, S. Humphreys, M. Kainuma, J. Kala, and K.Z. Y. Mulugetta, R. Perez, M. Wairiu, Global Warming of 1.5°C. An IPCC Special Report on the impacts of global warming of 1.5°C above pre-industrial levels and related global greenhouse gas emission pathways, in the context of strengthening the global response to the threat of climate change, 2018.

[8]   IPCC, Climate Change 2021: The Physical Science Basis. Contribution of Working Group I to the Sixth Assessment Report of the Intergovernmental Panel on Climate Change [Masson-Delmotte, V., P. Zhai, A. Pirani, S. L. Connors, C. Péan, S. Berger, N. Caud, Y. Chen, Cambridge Univ. Press.

(2021)   3949.
https://www.ipcc.ch/report/ar6/wg1/downloads/report/IPCC_AR6_WGI_F
ull_Report.pdf.

[9]   J.T. Houghton, Y. Ding, D.J. Griggs, M. Noguer, P.J. van der Linden, X.
        Dai, K. Maskell, C.A. Johnson, CLIMATE CHANGE 2001: THE
        SCIENTIFIC BASIS, in: Intergov. Panel Clim. Chang., CAMBRIDGE
        UNIVERSITY PRESS, 2001: p. 95. http://www.metoffice.gov.uk.

[10]   P. Friedlingstein, M. O'Sullivan, M. Jones, R. Andrew, J. Hauck, A. Olsen,
        G. Peters, W. Peters, J. Pongratz, S. Sitch, C. Le Quéré, J. Canadell, P. Ciais,
        R. Jackson, S. Alin, L. Aragão, A. Arneth, V. Arora, N. Bates, M. Becker,
        A. Benoit-Cattin, H. Bittig, L. Bopp, S. Bultan, N. Chandra, F. Chevallier,
        L. Chini, W. Evans, L. Florentie, P. Forster, T. Gasser, M. Gehlen, D.
        Gilfillan, T. Gkritzalis, L. Gregor, N. Gruber, I. Harris, K. Hartung, V.
        Haverd, R. Houghton, T. Ilyina, A. Jain, E. Joetzjer, K. Kadono, E. Kato, V.
        Kitidis, J.I. Korsbakken, P. Landschützer, N. Lefèvre, A. Lenton, S. Lienert,
        Z. Liu, D. Lombardozzi, G. Marland, N. Metzl, D. Munro, J. Nabel, S.-I.
        Nakaoka, Y. Niwa, K. O'Brien, T. Ono, P. Palmer, D. Pierrot, B. Poulter, L.
        Resplandy, E. Robertson, C. Rödenbeck, J. Schwinger, R. Séférian, I.
        Skjelvan, A. Smith, A. Sutton, T. Tanhua, P. Tans, H. Tian, B. Tilbrook, G.
        van der Werf, N. Vuichard, A. Walker, R. Wanninkhof, A. Watson, D.
        Willis, A. Wiltshire, W. Yuan, X. Yue, S. Zaehle, Global Carbon Budget
        2020,   Earth   Syst.   Sci.   Data   Discuss.   (2020)   1–3.
        https://doi.org/10.5194/essd-2020-286.

[11]   O. Edenhofer, R. Pichs-Madruga, Y. Sokona, J.C. Minx, E. Farhani, S.
        Kadner, K. Seyboth, A. Adler, I. Baum, S. Brunner, P. Eickemeier, B.
        Kriemann, J. Savolainen, S. Schlomer, C. von Stechow, T. Zwickel,
        CLIMATE CHANGE 2014 Mitigation of Climate Change, Cambridge
        University Press, 2015.

[12]   T.F. Stocker, D. Qin, G.-K. Plattner, M. Tignor, S.K. Allen, J. Boschung, A.
        Nauels, Y. Xia, V. Bex, P.M. Midgley, Climate Change 2013 The Physical
        Science Basis, Clim. Chang. 2013 Phys. Sci. Basis. Contrib. Work. Gr. I to
        Fifth Assess. Rep. Intergov. Panel Clim. Chang. (2013) 203.

[13]   P. Forster, P. Artaxo, Changes in Atmospheric Constituents and in Radiative
        Forcing, Notes. 18 (2005).

[14]   B. Ki-moon, Kyoto Protocol Reference Manual, United Nations Framew.
        Conv. Clim. Chang. (2008) 130. https://doi.org/10.5213/jkcs.1998.2.2.62.

[15]   J. Delbeke, A. Runge-Metzger, Y. Slingenberg, J. Werksman, The paris
        agreement, Towar. a Clim. Eur. Curbing Trend. (2019) 24–45.
        https://doi.org/10.4324/9789276082569-2.

[16]   COP26, COP26 Explained, UN Clim. Chang. Conf. UK 2021. (2021). https://ukcop26.org/.

[17]   A. Sabherwal, M.T. Ballew, S. van der Linden, A. Gustafson, M.H. Goldberg, E.W. Maibach, J.E. Kotcher, J.K. Swim, S.A. Rosenthal, A. Leiserowitz, The Greta Thunberg Effect: Familiarity with Greta Thunberg predicts intentions to engage in climate activism in the United States, J. Appl. Soc. Psychol. 51 (2021) 321–333. https://doi.org/10.1111/jasp.12737.

[18]   M. Borasio, S. Moret, Deep decarbonisation of regional energy systems: A novel modelling approach and its application to the Italian energy transition, Renew. Sustain. Energy Rev. 153 (2022) 111730. https://doi.org/10.1016/j.rser.2021.111730.

[19]   H. Liao, W. Chang, Integrated assessment of air quality and climate change for policy-making: Highlights of IPCC AR5 and research challenges, Natl. Sci. Rev. 1 (2014) 176–179. https://doi.org/10.1093/nsr/nwu005.

[20]   J. Gibbins, H. Chalmers, Carbon capture and storage, Energy Policy. 36 (2008) 4317–4322. https://doi.org/10.1016/j.enpol.2008.09.058.

[21]   A. Samanta, A. Zhao, G.K.H. Shimizu, P. Sarkar, R. Gupta, Post-combustion CO_2 capture using solid sorbents: A review, Ind. Eng. Chem. Res. 51 (2012) 1438–1463. https://doi.org/10.1021/ie200686q.

[22]   A. Mukherjee, J.A. Okolie, A. Abdelrasoul, C. Niu, A.K. Dalai, Review of post-combustion carbon dioxide capture technologies using activated carbon, J. Environ. Sci. (China). 83 (2019) 46–63. https://doi.org/10.1016/j.jes.2019.03.014.

[23]   K. Jordal, M. Anheden, J. Yan, L. Stromberg, OXYFUEL COMBUSTION FOR COAL-FIRED POWER GENERATION WITH CO2 CAPTURE-OPPORTUNITIES AND CHALLENGES, Greenh. Gas Control Technol. I (2005) 10.

[24]   K. Sumida, D.L. Rogow, J.A. Mason, T.M. McDonald, E.D. Bloch, Z.R. Herm, T.H. Bae, J.R. Long, Carbon dioxide capture by metal organic frameworks, Chem. Rev. 112 (2012) 724–781. https://doi.org/dx.doi.org/10.1021/cr2003272.

[25]   C. Song, W. Pan, S.T. Srimat, J. Zheng, Y. Li, Y. Wang, B. Xu, Q. Zhu, Tri-reforming of Methane over Ni Catalysts for CO2 Conversion to Syngas With Desired H2/CO Ratios Using Flue Gas of Power Plants Without CO2 Separation, Stud. Surf. Sci. Catal. 153 (2004) 315–322.

[26]   S.D. Kenarsari, D. Yang, G. Jiang, S. Zhang, J. Wang, A.G. Russell, Q. Wei, M. Fan, Review of recent advances in carbon dioxide separation and capture,

RSC Adv. 3 (2013) 22739–22773. https://doi.org/10.1039/c3ra43965h.

[27] T.A. Adams, L. Hoseinzade, P.B. Madabhushi, I.J. Okeke, Comparison of CO_2 capture approaches for fossil-based power generation: Review and meta-study, Processes. 5 (2017). https://doi.org/10.3390/pr5030044.

[28] F. Hussin, M.K. Aroua, Recent trends in the development of adsorption technologies for carbon dioxide capture: A brief literature and patent reviews (2014–2018), J. Clean. Prod. 253 (2020) 119707. https://doi.org/10.1016/j.jclepro.2019.119707.

[29] Y. Yuan, H. You, L. Ricardez-Sandoval, Recent advances on first-principles modeling for the design of materials in CO_2 capture technologies, Chinese J. Chem. Eng. 27 (2019) 1554–1565. https://doi.org/10.1016/j.cjche.2018.10.017.

[30] R. Ben-Mansour, M.A. Habib, O.E. Bamidele, M. Basha, N.A.A. Qasem, A. Peedikakkal, T. Laoui, M. Ali, Carbon capture by physical adsorption: Materials, experimental investigations and numerical modeling and simulations - A review, Appl. Energy. 161 (2016) 225–255. https://doi.org/10.1016/j.apenergy.2015.10.011.

[31] A. Modak, S. Jana, Advancement in porous adsorbents for post-combustion CO_2 capture, Microporous Mesoporous Mater. 276 (2019) 107–132. https://doi.org/10.1016/j.micromeso.2018.09.018.

[32] M. Zaman, J.H. Lee, Carbon capture from stationary power generation sources: A review of the current status of the technologies, Korean J. Chem. Eng. 30 (2013) 1497–1526. https://doi.org/10.1007/s11814-013-0127-3.

[33] N. Khallaghi, D.P. Hanak, V. Manovic, Techno-economic evaluation of near-zero CO_2 emission gas-fired power generation technologies: A review, J. Nat. Gas Sci. Eng. 74 (2020) 103095. https://doi.org/10.1016/j.jngse.2019.103095.

[34] T. N.Borhani, M. Wang, Role of solvents in CO_2 capture processes: The review of selection and design methods, Renew. Sustain. Energy Rev. 114 (2019) 109299. https://doi.org/10.1016/j.rser.2019.109299.

[35] D. Aaron, C. Tsouris, Separation of CO_2 from flue gas: A review, Sep. Sci. Technol. 40 (2005) 321–348. https://doi.org/10.1081/SS-200042244.

[36] M.T. Ravanchi, S. Sahebdelfar, F.T. Zangeneh, Carbon dioxide sequestration in petrochemical industries with the aim of reduction in greenhouse gas emissions, Front. Chem. Eng. China. 5 (2011) 173–178. https://doi.org/10.1007/s11705-010-0562-1.

[37] D. Bonalumi, S. Lillia, G. Valenti, Rate-based simulation and techno-economic analysis of coal-fired power plants with aqueous ammonia carbon capture, Energy Convers. Manag. 199 (2019) 111966. https://doi.org/10.1016/j.enconman.2019.111966.

[38] C. Yu, C. Huang, C. Tan, A Review of CO_2 Capture by Absorption and Adsorption, (2012) 745–769. https://doi.org/10.4209/aaqr.2012.05.0132.

[39] E. Davarpanah, S. Hernández, G. Latini, C.F. Pirri, S. Bocchini, Enhanced CO_2 Absorption in Organic Solutions of Biobased Ionic Liquids, Adv. Sustain. Syst. 4 (2020) 1–8. https://doi.org/10.1002/adsu.201900067.

[40] S. Zeng, X. Zhang, L. Bai, X. Zhang, H. Wang, J. Wang, D. Bao, M. Li, X. Liu, S. Zhang, Ionic-Liquid-Based CO_2 Capture Systems: Structure, Interaction and Process, Chem. Rev. 117 (2017) 9625–9673. https://doi.org/10.1021/acs.chemrev.7b00072.

[41] S. Sarmad, J.-P. Mikkola, X. Ji, Carbon Dioxide Capture with Ionic Liquids and Deep Eutectic Solvents_ A New Generation of Sorbents, ChemSusChem. 10 (2017) 324–352. https://doi.org/doi.org/10.1002/cssc.201600987.

[42] N. Hedin, L. Andersson, L. Bergström, J. Yan, Adsorbents for the post-combustion capture of CO_2 using rapid temperature swing or vacuum swing adsorption, Appl. Energy. 104 (2013) 418–433. https://doi.org/10.1016/j.apenergy.2012.11.034.

[43] C.T. Chiou, Fundamentals of the Adsorption Theory, Partit. Adsorpt. Org. Contam. Environ. Syst. (2003) 39–52. https://doi.org/10.1002/0471264326.ch4.

[44] A.M. Varghese, G.N. Karanikolos, CO_2 capture adsorbents functionalized by amine – bearing polymers: A review, Int. J. Greenh. Gas Control. 96 (2020) 103005. https://doi.org/10.1016/j.ijggc.2020.103005.

[45] S. Choi, J.H. Drese, C.W. Jones, Adsorbent materials for carbon dioxide capture from large anthropogenic point sources, ChemSusChem. 2 (2009) 796–854. https://doi.org/10.1002/cssc.200900036.

[46] L. Nie, Y. Mu, J. Jin, J. Chen, J. Mi, Recent developments and consideration issues in solid adsorbents for CO_2 capture from flue gas, Chinese J. Chem. Eng. 26 (2018) 2303–2317. https://doi.org/10.1016/j.cjche.2018.07.012.

[47] K.S.W. Sing, R.T. Williams, Physisorption hysteresis loops and the characterization of nanoporous materials, Adsorpt. Sci. Technol. 22 (2004) 773–782. https://doi.org/10.1260/0263617053499032.

[48]   O. Cheung, N. Hedin, Zeolites and related sorbents with narrow pores for CO2 separation from flue gas, RSC Adv. 4 (2014) 14480–14494. https://doi.org/10.1039/c3ra48052f.

[49]   Y. Zhao, X. Liu, Y. Han, Microporous carbonaceous adsorbents for CO2 separation via selective adsorption, RSC Adv. 5 (2015) 30310–30330. https://doi.org/10.1039/c5ra00569h.

[50]   A.E. Creamer, B. Gao, Carbon-based adsorbents for postcombustion CO2 capture: A critical review, Environ. Sci. Technol. 50 (2016) 7276–7289. https://doi.org/10.1021/acs.est.6b00627.

[51]   N. Kundu, S. Sarkar, Journal of Environmental Chemical Engineering Porous organic frameworks for carbon dioxide capture and storage, J. Environ. Chem. Eng. 9 (2021) 105090. https://doi.org/10.1016/j.jece.2021.105090.

[52]   Y. Zeng, R. Zou, Y. Zhao, Covalent Organic Frameworks for CO2 Capture, (2016) 2855–2873. https://doi.org/10.1002/adma.201505004.

[53]   S.A. Salaudeen, B. Acharya, A. Dutta, CaO-based CO 2 sorbents : A review on screening , enhancement , cyclic stability , regeneration and kinetics modelling, J. CO2 Util. 23 (2018) 179–199. https://doi.org/10.1016/j.jcou.2017.11.012.

[54]   M.T. Dunstan, F. Donat, A.H. Bork, C.P. Grey, C.R. Mu, CO 2 Capture at Medium to High Temperature Using Solid Oxide- Based Sorbents : Fundamental Aspects , Mechanistic Insights , and Recent Advances, (2021). https://doi.org/10.1021/acs.chemrev.1c00100.

[55]   X. Zhao, Q. Cui, B. Wang, X. Yan, S. Singh, F. Zhang, X. Gao, Y. Li, Recent progress of amine modified sorbents for capturing CO2 from flue gas, Chinese J. Chem. Eng. 26 (2018) 2292–2302. https://doi.org/10.1016/j.cjche.2018.04.009.

[56]   T. Gelles, S. Lawson, A.A. Rownaghi, F. Rezaei, Recent advances in development of amine functionalized adsorbents for CO2 capture, Adsorption. 26 (2020) 5–50. https://doi.org/10.1007/s10450-019-00151-0.

[57]   M. Li, X. Jiang, G. He, Application of membrane separation technology in postcombustion carbon dioxide capture process, Front. Chem. Sci. Eng. 8 (2014) 233–239. https://doi.org/10.1007/s11705-014-1408-z.

[58]   R. Khalilpour, K. Mumford, H. Zhai, A. Abbas, G. Stevens, E.S. Rubin, Membrane-based carbon capture from flue gas: A review, J. Clean. Prod. 103 (2015) 286–300. https://doi.org/10.1016/j.jclepro.2014.10.050.

[59] K.K. Wong, Z.A. Jawad, A review and future prospect of polymer blend mixed matrix membrane for CO2 separation, J. Polym. Res. 26 (2019). https://doi.org/10.1007/s10965-019-1978-z.

[60] Y. Han, W.S.W. Ho, Recent advances in polymeric membranes for CO2 capture, Chinese J. Chem. Eng. 26 (2018) 2238–2254. https://doi.org/10.1016/j.cjche.2018.07.010.

[61] P. Luis, T. Van Gerven, B. Van Der Bruggen, Recent developments in membrane-based technologies for CO 2 capture, Prog. Energy Combust. Sci. 38 (2012) 419–448. https://doi.org/10.1016/j.pecs.2012.01.004.

[62] X. He, A review of material development in the field of carbon capture and the application of membrane-based processes in power plants and energy-intensive industries, Energy. Sustain. Soc. 8 (2018). https://doi.org/10.1186/s13705-018-0177-9.

[63] H.A. Alalwan, A.H. Alminshid, Science of the Total Environment CO 2 capturing methods : Chemical looping combustion (CLC) as a promising technique, 788 (2021). https://doi.org/10.1016/j.scitotenv.2021.147850.

[64] H. Lu, X. Ma, K. Huang, L. Fu, M. Azimi, Carbon dioxide transport via pipelines: A systematic review, J. Clean. Prod. 266 (2020) 121994. https://doi.org/10.1016/j.jclepro.2020.121994.

[65] M.N. Anwar, A. Fayyaz, N.F. Sohail, M.F. Khokhar, M. Baqar, W.D. Khan, K. Rasool, M. Rehan, A.S. Nizami, CO2 capture and storage: A way forward for sustainable environment, J. Environ. Manage. 226 (2018) 131–144. https://doi.org/10.1016/j.jenvman.2018.08.009.

[66] D.Y.C. Leung, G. Caramanna, M.M. Maroto-Valer, An overview of current status of carbon dioxide capture and storage technologies, Renew. Sustain. Energy Rev. 39 (2014) 426–443. https://doi.org/10.1016/j.rser.2014.07.093.

[67] T. Wilberforce, A.G. Olabi, E.T. Sayed, K. Elsaid, M.A. Abdelkareem, Progress in carbon capture technologies, Sci. Total Environ. 761 (2021) 143203. https://doi.org/10.1016/j.scitotenv.2020.143203.

[68] K. Johnsen, K. Helle, S. Røneid, H. Holt, DNV recommended practice: Design and operation of CO2 pipelines, Energy Procedia. 4 (2011) 3032–3039. https://doi.org/10.1016/j.egypro.2011.02.214.

[69] A.N. Rehman, C.B. Bavoh, R. Pendyala, B. Lal, Research Advances, Maturation, and Challenges of Hydrate-Based CO2Sequestration in Porous Media, ACS Sustain. Chem. Eng. 9 (2021) 15075–15108. https://doi.org/10.1021/acssuschemeng.1c05423.

[70]   NDA (Nuclear Decommissioning Authority), Guide to Technology Readiness Levels for the NDA Estate and its Supply Chain, EDRMS No. 22515717.   (2014)   1–27. https://assets.publishing.service.gov.uk/government/uploads/system/upload s/attachment_data/file/457514/Guide-to-Technology-Readiness-Levels-for-the-NDA-Estate-and-its-Supply-Chain.pdf.

[71]   US Department of Energy, Technology Readiness Assessment Guide, SpringerReference.   (2011)   73. https://assets.publishing.service.gov.uk/government/uploads/system/upload s/attachment_data/file/457514/Guide-to-Technology-Readiness-Levels-for-the-NDA-Estate-and-its-Supply-Chain.pdf.

[72]   M. Bui, C.S. Adjiman, A. Bardow, E.J. Anthony, A. Boston, S. Brown, P.S. Fennell, S. Fuss, A. Galindo, L.A. Hackett, J.P. Hallett, H.J. Herzog, G. Jackson, J. Kemper, S. Krevor, G.C. Maitland, M. Matuszewski, I.S. Metcalfe, C. Petit, G. Puxty, J. Reimer, D.M. Reiner, E.S. Rubin, S.A. Scott, N. Shah, B. Smit, J.P.M. Trusler, P. Webley, J. Wilcox, N. Mac Dowell, Carbon capture and storage (CCS): The way forward, Energy Environ. Sci. 11 (2018) 1062–1176. https://doi.org/10.1039/c7ee02342a.

[73]   S.G. Subraveti, S. Roussanaly, R. Anantharaman, L. Riboldi, A. Rajendran, How much can novel solid sorbents reduce the cost of post-combustion CO_2 capture? A techno-economic investigation on the cost limits of pressure–vacuum swing adsorption, Appl. Energy. 306 (2022) 117955. https://doi.org/10.1016/j.apenergy.2021.117955.

[74]   N. Harun, T. Nittaya, P.L. Douglas, E. Croiset, L.A. Ricardez-Sandoval, Dynamic simulation of MEA absorption process for CO_2 capture from power plants, Int. J. Greenh. Gas Control. 10 (2012) 295–309. https://doi.org/10.1016/j.ijggc.2012.06.017.

[75]   C.H. Yu, C.H. Huang, C.S. Tan, A review of CO_2 capture by absorption and adsorption,   Aerosol   Air   Qual.   Res.   12   (2012)   745–769. https://doi.org/10.4209/aaqr.2012.05.0132.

[76]   A.B. Rao, E.S. Rubin, A technical, economic, and environmental assessment of amine-based CO_2 capture technology for power plant greenhouse gas control,   Environ.   Sci.   Technol.   36   (2002)   4467–4475. https://doi.org/10.1021/es0158861.

[77]   M. Khraisheh, S. Mukherjee, A. Kumar, F. Al Momani, G. Walker, M.J. Zaworotko, An overview on trace CO_2 removal by advanced physisorbent materials,   J.   Environ.   Manage.   255   (2020)   109874. https://doi.org/10.1016/j.jenvman.2019.109874.

[78]   M. Oschatz, M. Antonietti, A search for selectivity to enable CO2 capture with porous adsorbents, Energy Environ. Sci. 11 (2018) 57–70. https://doi.org/10.1039/c7ee02110k.

[79]   J. Wang, Q. Pu, P. Ning, S. Lu, Activated carbon-based composites for capturing CO2: a review, Greenh. Gases Sci. Technol. 11 (2021) 377–393. https://doi.org/10.1002/ghg.2051.

[80]   Y. Shi, Q. Liu, Y. He, CO2 Capture Using Solid Sorbents, 2015. https://doi.org/10.1007/978-1-4614-6431-0.

[81]   S. Wang, Z. Su, X. Lu, Energy-consumption analysis of carbon-based material for CO2 capture process, Fluid Phase Equilib. 510 (2020) 112504. https://doi.org/10.1016/j.fluid.2020.112504.

[82]   Y.S. Bae, R.Q. Snurr, Development and evaluation of porous materials for carbon dioxide separation and capture, Angew. Chemie - Int. Ed. 50 (2011) 11586–11596. https://doi.org/10.1002/anie.201101891.

[83]   G. Sethia, A. Sayari, Comprehensive study of ultra-microporous nitrogen-doped activated carbon for CO2 capture, Carbon N. Y. 93 (2015) 68–80. https://doi.org/10.1016/j.carbon.2015.05.017.

[84]   V. Presser, J. McDonough, S.H. Yeon, Y. Gogotsi, Effect of pore size on carbon dioxide sorption by carbide derived carbon, Energy Environ. Sci. 4 (2011) 3059–3066. https://doi.org/10.1039/c1ee01176f.

[85]   J. Zhou, X. Wang, W. Xing, Carbon-based CO2 Adsorbents, The Royal Society of Chemistry, 2019.

[86]   J.R. Li, R.J. Kuppler, H.C. Zhou, Selective gas adsorption and separation in metal-organic frameworks, Chem. Soc. Rev. 38 (2009) 1477–1504. https://doi.org/10.1039/b802426j.

[87]   A. Nuhnen, C. Janiak, A practical guide to calculate the isosteric heat/enthalpy of adsorption: Via adsorption isotherms in metal-organic frameworks, MOFs, Dalt. Trans. 49 (2020) 10295–10307. https://doi.org/10.1039/d0dt01784a.

[88]   Quanthachrome Instruments, GAS SORPTION SYSTEM OPERATING MANUAL, (2014) 1–415.

[89]   J. Pires, V.K. Saini, M.L. Pinto, Studies on selective adsorption of biogas components on pillared clays: Approach for biogas improvement, Environ. Sci. Technol. 42 (2008) 8727–8732. https://doi.org/10.1021/es8014666.

[90]   M. Vorokhta, J. Morávková, M. Dopita, A. Zhigunov, M. Šlouf, R. Pilař, P.

Sazama, Effect of micropores on CO2 capture in ordered mesoporous CMK-3 carbon at atmospheric pressure, Adsorption. (2021). https://doi.org/10.1007/s10450-021-00322-y.

[91] J.H. Yu, J.H. So, Synthesis and characterization of nitrogen-containing hydrothermal carbon with ordered mesostructure, Chem. Phys. Lett. 716 (2019) 237–246. https://doi.org/10.1016/j.cplett.2018.12.014.

[92] Z. Zhang, N. Sun, W. Wei, Facile and controllable synthesis of ordered mesoporous carbons with tunable single-crystal morphology for CO2 capture, Carbon N. Y. 161 (2020) 629–638. https://doi.org/10.1016/j.carbon.2020.02.009.

[93] S.K. Das, P. Bhanja, S.K. Kundu, S. Mondal, A. Bhaumik, Role of Surface Phenolic-OH Groups in N-Rich Porous Organic Polymers for Enhancing the CO2 Uptake and CO2/N2 Selectivity: Experimental and Computational Studies, ACS Appl. Mater. Interfaces. 10 (2018) 23813–23824. https://doi.org/10.1021/acsami.8b05849.

[94] H. Cong, M. Zhang, Y. Chen, K. Chen, Y. Hao, Y. Zhao, L. Feng, Highly selective CO2 capture by nitrogen enriched porous carbons, Carbon N. Y. 92 (2015) 297–304. https://doi.org/10.1016/j.carbon.2015.04.052.

[95] A.K. Sekizkardes, S. Altarawneh, Z. Kahveci, I. Timur, H.M. El-kaderi, Highly Selective CO 2 Capture by Triazine-Based Benzimidazole- Linked Polymers ˙lamog l, (2014).

[96] P. Serra-Crespo, E. V. Ramos-Fernandez, J. Gascon, F. Kapteijn, Synthesis and characterization of an amino functionalized MIL-101(Al): Separation and catalytic properties, Chem. Mater. 23 (2011) 2565–2572. https://doi.org/10.1021/cm103644b.

[97] E. García-Díez, A. Castro-Muñiz, J.I. Paredes, M.M. Maroto-Valer, F. Suárez-García, S. García, CO2 capture by novel hierarchical activated ordered micro-mesoporous carbons derived from low value coal tar products, Microporous Mesoporous Mater. 318 (2021). https://doi.org/10.1016/j.micromeso.2021.110986.

[98] M.A.O. Lourenço, M. Fontana, P. Jagdale, C.F. Pirri, S. Bocchini, Improved CO2 adsorption properties through amine functionalization of multi-walled carbon nanotubes, Chem. Eng. J. 414 (2021) 128763. https://doi.org/10.1016/j.cej.2021.128763.

[99] E. Maruccia, M.A.O. Lourenço, T. Priamushko, M. Bartoli, S. Bocchini, F.C. Pirri, G. Saracco, F. Kleitz, C. Gerbaldi, Nanocast nitrogen-containing ordered mesoporous carbons from glucosamine for selective CO2 capture, Mater. Today Sustain. 17 (2022) 100089.

https://doi.org/10.1016/j.mtsust.2021.100089.

[100] C. Colella, A.F. Gualtieri, Cronstedt's zeolite, Microporous Mesoporous Mater. 105 (2007) 213–221. https://doi.org/10.1016/j.micromeso.2007.04.056.

[101] Y. Li, J. Yu, New Stories of Zeolite Structures : Their Descriptions , Determinations , Predictions , and Evaluations, (2014).

[102] E.M. Flanigen, R.W. Broach, S.T. Wilson, Introduction, in: Zeolites Ind. Sep. Catal., 2010: pp. 1–26. https://doi.org/10.1002/9783527629565.ch1.

[103] A. Salmankhani, S. Soroush, M. Khadem, F. Seidi, A. Hamed, Adsorption onto zeolites : molecular perspective, Chem. Pap. 75 (2021) 6217–6239. https://doi.org/10.1007/s11696-021-01817-2.

[104] M. Moliner, C. Martínez, A. Corma, Synthesis strategies for preparing useful small pore zeolites and zeotypes for gas separations and catalysis, Chem. Mater. 26 (2014) 246–258. https://doi.org/10.1021/cm4015095.

[105] M.P. Singh, G.S. Baghel, S.J.J. Titinchi, H.S. Abbo, Zeolites: Smart Materials for Novel, Efficient, and Versatile Catalysis, Adv. Catal. Mater. 3 (2015) 385–410. https://doi.org/10.1002/9781118998939.ch11.

[106] M.M. Zagho, M.K. Hassan, M. Khraisheh, M.A.A. Al-Maadeed, S. Nazarenko, A review on recent advances in CO2 separation using zeolite and zeolite-like materials as adsorbents and fillers in mixed matrix membranes (MMMs), Chem. Eng. J. Adv. 6 (2021) 100091. https://doi.org/10.1016/j.ceja.2021.100091.

[107] J. Yang, Q. Zhao, H. Xu, L. Li, J. Dong, J. Li, Adsorption of CO2, CH4, and N2 on gas diameter grade ion-exchange small pore zeolites, J. Chem. Eng. Data. 57 (2012) 3701–3709. https://doi.org/10.1021/je300940m.

[108] G.K. Li, J. Shang, Q. Gu, R. V. Awati, N. Jensen, A. Grant, X. Zhang, D.S. Sholl, J.Z. Liu, P.A. Webley, E.F. May, Temperature-regulated guest admission and release in microporous materials, Nat. Commun. 8 (2017) 1–9. https://doi.org/10.1038/ncomms15777.

[109] J. Shang, G. Li, R. Singh, Q. Gu, K.M. Nairn, T.J. Bastow, N. Medhekar, C.M. Doherty, A.J. Hill, J.Z. Liu, P.A. Webley, Discriminative separation of gases by a "molecular trapdoor" mechanism in chabazite zeolites, J. Am. Chem. Soc. 134 (2012) 19246–19253. https://doi.org/10.1021/ja309274y.

[110] J. Shang, G. Li, R. Singh, P. Xiao, J.Z. Liu, P.A. Webley, Potassium chabazite: A potential nanocontainer for gas encapsulation, J. Phys. Chem. C. 114 (2010) 22025–22031. https://doi.org/10.1021/jp107456w.

[111] J. Shang, G. Li, Q. Gu, R. Singh, P. Xiao, J.Z. Liu, P.A. Webley, Temperature controlled invertible selectivity for adsorption of N 2 and CH4 by molecular trapdoor chabazites, Chem. Commun. 50 (2014) 4544–4546. https://doi.org/10.1039/c4cc00269e.

[112] J. Shang, G. Li, P.A. Webley, J.Z. Liu, A density functional theory study for the adsorption of various gases on a caesium-exchanged trapdoor chabazite, Comput. Mater. Sci. 122 (2016) 307–313. https://doi.org/10.1016/j.commatsci.2016.05.040.

[113] T. Du, X. Fang, L. Liu, J. Shang, B. Zhang, Y. Wei, H. Gong, S. Rahman, E.F. May, P.A. Webley, G. Li, An optimal trapdoor zeolite for exclusive admission of CO2 at industrial carbon capture operating temperatures, Chem. Commun. 54 (2018) 3134–3137. https://doi.org/10.1039/c8cc00634b.

[114] Z. Song, Q. Dong, W.L. Xu, F. Zhou, X. Liang, M. Yu, Molecular Layer Deposition-Modified 5A Zeolite for Highly Efficient CO2 Capture, ACS Appl. Mater. Interfaces. 10 (2018) 769–775. https://doi.org/10.1021/acsami.7b16574.

[115] E. Khoramzadeh, M. Mofarahi, C.H. Lee, Equilibrium Adsorption Study of CO2 and N2 on Synthesized Zeolites 13X, 4A, 5A, and Beta, J. Chem. Eng. Data. 64 (2019) 5648–5664. https://doi.org/10.1021/acs.jced.9b00690.

[116] T. Frising, P. Leflaive, Extraframework cation distributions in X and Y faujasite zeolites: A review, Microporous Mesoporous Mater. 114 (2008) 27–63. https://doi.org/10.1016/j.micromeso.2007.12.024.

[117] O. Cheung, Z. Bacsik, N. Fil, P. Krokidas, D. Wardecki, N. Hedin, Selective Adsorption of CO2on Zeolites NaK-ZK-4 with Si/Al of 1.8-2.8, ACS Omega. 5 (2020) 25371–25380. https://doi.org/10.1021/acsomega.0c03749.

[118] A.P. Beltrao-Nunes, R. Sennour, V.A. Arus, S. Anoma, M. Pires, N. Bouazizi, R. Roy, A. Azzouz, CO2 capture by coal ash-derived zeolites-roles of the intrinsic basicity and hydrophilic character, J. Alloys Compd. 778 (2019) 866–877. https://doi.org/10.1016/j.jallcom.2018.11.133.

[119] M. Signorile, J.G. Vitillo, M. D'Amore, V. Crocellà, G. Ricchiardi, S. Bordiga, Characterization and Modeling of Reversible CO2 Capture from Wet Streams by a MgO/Zeolite y Nanocomposite, J. Phys. Chem. C. 123 (2019) 17214–17224. https://doi.org/10.1021/acs.jpcc.9b01399.

[120] S. Kumar, R. Srivastava, J. Koh, Utilization of zeolites as CO2capturing agents: Advances and future perspectives, J. CO2 Util. 41 (2020) 101251. https://doi.org/10.1016/j.jcou.2020.101251.

[121] S. Chatterjee, S. Jeevanandham, M. Mukherjee, D.V.N. Vo, V. Mishra, Significance of re-engineered zeolites in climate mitigation – A review for carbon capture and separation, J. Environ. Chem. Eng. 9 (2021) 105957. https://doi.org/10.1016/j.jece.2021.105957.

[122] T.H. Bae, M.R. Hudson, J.A. Mason, W.L. Queen, J.J. Dutton, K. Sumida, K.J. Micklash, S.S. Kaye, C.M. Brown, J.R. Long, Evaluation of cation-exchanged zeolite adsorbents for post-combustion carbon dioxide capture, Energy Environ. Sci. 6 (2013) 128–138. https://doi.org/10.1039/c2ee23337a.

[123] X. Qian, G. Bai, P. He, Z. Fei, Q. Liu, Z. Zhang, X. Chen, J. Tang, M. Cui, X. Qiao, Rapid CO 2 Adsorption over Hierarchical ZSM-5 with Controlled Mesoporosity, Ind. Eng. Chem. Res. 57 (2018) 16875–16883. https://doi.org/10.1021/acs.iecr.8b03325.

[124] Z. Qiang, R. Li, Z. Yang, M. Guo, F. Cheng, M. Zhang, Zeolite X Adsorbent with High Stability Synthesized from Bauxite Tailings for Cyclic Adsorption of CO2, Energy and Fuels. 33 (2019) 6641–6649. https://doi.org/10.1021/acs.energyfuels.9b01268.

[125] A.A. Dabbawala, I. Ismail, B. V. Vaithilingam, K. Polychronopoulou, G. Singaravel, S. Morin, M. Berthod, Y. Al Wahedi, Synthesis of hierarchical porous Zeolite-Y for enhanced CO2 capture, Microporous Mesoporous Mater. 303 (2020) 110261. https://doi.org/10.1016/j.micromeso.2020.110261.

[126] Y. Kamimura, M. Shimomura, A. Endo, CO2 adsorption-desorption properties of zeolite beta prepared from OSDA-free synthesis, Microporous Mesoporous Mater. 219 (2016) 125–133. https://doi.org/10.1016/j.micromeso.2015.07.033.

[127] J.R. Li, J. Sculley, H.C. Zhou, Metal-organic frameworks for separations, Chem. Rev. 112 (2012) 869–932. https://doi.org/10.1021/cr200190s.

[128] R.B. Lin, S. Xiang, W. Zhou, B. Chen, Microporous Metal-Organic Framework Materials for Gas Separation, Chem. 6 (2020) 337–363. https://doi.org/10.1016/j.chempr.2019.10.012.

[129] L. Jiao, J.Y.R. Seow, W.S. Skinner, Z.U. Wang, H.L. Jiang, Metal–organic frameworks: Structures and functional applications, Mater. Today. 27 (2019) 43–68. https://doi.org/10.1016/j.mattod.2018.10.038.

[130] O.K. Farha, I. Eryazici, N.C. Jeong, B.G. Hauser, C.E. Wilmer, A.A. Sarjeant, R.Q. Snurr, S.T. Nguyen, A.Ö. Yazaydin, J.T. Hupp, Metal-organic framework materials with ultrahigh surface areas: Is the sky the limit?, J. Am. Chem. Soc. 134 (2012) 15016–15021. https://doi.org/10.1021/ja3055639.

[131] C.A. Trickett, A. Helal, B.A. Al-Maythalony, Z.H. Yamani, K.E. Cordova, O.M. Yaghi, The chemistry of metal-organic frameworks for CO2 capture, regeneration and conversion, Nat. Rev. Mater. 2 (2017) 1–16. https://doi.org/10.1038/natrevmats.2017.45.

[132] T. Ghanbari, F. Abnisa, W.M.A. Wan Daud, A review on production of metal organic frameworks (MOF) for CO2 adsorption, Sci. Total Environ. 707 (2020). https://doi.org/10.1016/j.scitotenv.2019.135090.

[133] X. Coudert, Responsive Metal − Organic Frameworks and Framework Materials: Under Pressure, Taking the Heat, in the Spotlight, with Friends †, (2015). https://doi.org/10.1021/acs.chemmater.5b00046.

[134] T. Ghanbari, F. Abnisa, W.M.A. Wan Daud, A review on production of metal organic frameworks (MOF) for CO2 adsorption, Sci. Total Environ. 707 (2020) 135090. https://doi.org/10.1016/j.scitotenv.2019.135090.

[135] R.A. Schneemann, A., Bon, V., Schwedler, I., Senkovska, I., Kaskel, S., Fisher, Flexible metal-organic frameworks, Chem. Soc. Rev. 43 (2014) 6062–6096. https://doi.org/10.1039/c4cs00101j.

[136] A. Schneemann, Y. Takahashi, R. Rudolf, S.I. Noro, R.A. Fischer, Influence of Co-adsorbates on CO2 induced phase transition in functionalized pillared-layered metal-organic frameworks, J. Mater. Chem. A. 4 (2016) 12963–12972. https://doi.org/10.1039/c6ta03266d.

[137] I. Schwedler, S. Henke, M.T. Wharmby, S.R. Bajpe, A.K. Cheetham, R.A. Fischer, Mixed-linker solid solutions of functionalized pillared-layer MOFs - Adjusting structural flexibility, gas sorption, and thermal responsiveness, Dalt. Trans. 45 (2016) 4230–4241. https://doi.org/10.1039/c5dt03825a.

[138] 2018_Kim_Selective CO2 sorption by a new breathing three-dimensional Zn-MOF with Lewis basic N-rich channels.pdf, (n.d.).

[139] Y. Tang, A. Kourtellaris, A.J. Tasiopoulos, S.J. Teat, D. Dubbeldam, G. Rothenberg, S. Tanase, Selective CO2 adsorption in water-stable alkaline-earth based metal-organic frameworks, Inorg. Chem. Front. 5 (2018) 541–549. https://doi.org/10.1039/c7qi00734e.

[140] M. Sin, N. Kavoosi, M. Rauche, J. Pallmann, S. Paasch, I. Senkovska, S. Kaskel, E. Brunner, In Situ 13 C NMR Spectroscopy Study of CO 2 /CH 4 Mixture Adsorption by Metal-Organic Frameworks: Does Flexibility Influence Selectivity?, Langmuir. 35 (2019) 3162–3170. https://doi.org/10.1021/acs.langmuir.8b03554.

[141] S. Wang, N. Xhaferaj, M. Wahiduzzaman, K. Oyekan, X. Li, K. Wei, B. Zheng, A. Tissot, J. Marrot, W. Shepard, C. Martineau-Corcos, Y. Filinchuk,

K. Tan, G. Maurin, C. Serre, Engineering Structural Dynamics of Zirconium Metal-Organic Frameworks Based on Natural C4 Linkers, J. Am. Chem. Soc. 141 (2019) 17207–17216. https://doi.org/10.1021/jacs.9b07816.

[142] P. Zhao, H. Fang, S. Mukhopadhyay, A. Li, S. Rudić, I.J. McPherson, C.C. Tang, D. Fairen-Jimenez, S.C.E. Tsang, S.A.T. Redfern, Structural dynamics of a metal–organic framework induced by CO 2 migration in its non-uniform porous structure, Nat. Commun. 10 (2019) 1–8. https://doi.org/10.1038/s41467-019-08939-y.

[143] N. Chanut, A. Ghoufi, M.V. Coulet, S. Bourrelly, B. Kuchta, G. Maurin, P.L. Llewellyn, Tailoring the separation properties of flexible metal-organic frameworks using mechanical pressure, Nat. Commun. 11 (2020) 1–7. https://doi.org/10.1038/s41467-020-15036-y.

[144] L. Yang, X. Cui, Y. Zhang, Q. Wang, Z. Zhang, X. Suo, H. Xing, Anion Pillared Metal-Organic Framework Embedded with Molecular Rotors for Size-Selective Capture of CO 2 from CH 4 and N 2, ACS Sustain. Chem. Eng. 7 (2019) 3138–3144. https://doi.org/10.1021/acssuschemeng.8b04916.

[145] V. Giullerm, D. Kim, F. Eubank, Jarrod, R. Luebke, X. Liu, K. Adil, S. Lah, M. Eddaoudi, A supermolecular building approach metal – organic frameworks, Chem. Soc. Rev. 43 (2014) 6141–6172. https://doi.org/10.1039/c4cs00135d.

[146] J.J.I. Perry, J.A. Perman, M.J. Zaworotko, Metal – organic frameworks issue polyhedra as supermolecular building blocks w, Chem. Soc. Rev. 38 (2009) 1400–1417. https://doi.org/10.1039/b807086p.

[147] Y. Liu, Two Analogous Polyhedron-Based MOFs with High Density of Lewis Basic Sites and Open Metal Sites: Signi fi cant CO 2 Capture and Gas Selectivity Performance, (2017) 2–10. https://doi.org/10.1021/acsami.7b10795.

[148] X. Song, M. Zhang, C. Chen, J. Duan, W. Zhang, Y. Pan, J. Bai, Pure-Supramolecular-Linker Approach to Highly Connected Metal-Organic Frameworks for CO2 Capture, J. Am. Chem. Soc. 141 (2019) 14539–14543. https://doi.org/10.1021/jacs.9b07422.

[149] H.M. Wen, C. Liao, L. Li, A. Alsalme, Z. Alothman, R. Krishna, H. Wu, W. Zhou, J. Hu, B. Chen, A metal-organic framework with suitable pore size and dual functionalities for highly efficient post-combustion CO 2 capture, J. Mater. Chem. A. 7 (2019) 3128–3134. https://doi.org/10.1039/c8ta11596f.

[150] H. Li, K. Wang, Z. Hu, Y.P. Chen, W. Verdegaal, D. Zhao, H.C. Zhou, Harnessing solvent effects to integrate alkylamine into metal-organic frameworks for exceptionally high CO2 uptake, J. Mater. Chem. A. 7 (2019)

7867–7874. https://doi.org/10.1039/c8ta11300a.

[151] P.G. Boyd, A. Chidambaram, E. García-Díez, C.P. Ireland, T.D. Daff, R. Bounds, A. Gładysiak, P. Schouwink, S.M. Moosavi, M.M. Maroto-Valer, J.A. Reimer, J.A.R. Navarro, T.K. Woo, S. Garcia, K.C. Stylianou, B. Smit, Data-driven design of metal–organic frameworks for wet flue gas CO2 capture, Nature. 576 (2019) 253–256. https://doi.org/10.1038/s41586-019-1798-7.

[152] M. Kang, J.E. Kim, D.W. Kang, H.Y. Lee, D. Moon, C.S. Hong, A diamine-grafted metal-organic framework with outstanding CO2 capture properties and a facile coating approach for imparting exceptional moisture stability, J. Mater. Chem. A. 7 (2019) 8177–8183. https://doi.org/10.1039/c8ta07965j.

[153] I. Erucar, S. Keskin, Unlocking the Effect of H2O on CO2 Separation Performance of Promising MOFs Using Atomically Detailed Simulations, Ind. Eng. Chem. Res. 59 (2020) 3141–3152. https://doi.org/10.1021/acs.iecr.9b05487.

[154] Z. Shi, Y. Tao, J. Wu, C. Zhang, H. He, L. Long, Y. Lee, T. Li, Y.B. Zhang, Robust Metal-Triazolate Frameworks for CO2 Capture from Flue Gas, J. Am. Chem. Soc. 142 (2020) 2750–2754. https://doi.org/10.1021/jacs.9b12879.

[155] A. Masala, J.G. Vitillo, G. Mondino, C.A. Grande, R. Blom, M. Manzoli, M. Marshall, S. Bordiga, CO2 capture in dry and wet conditions in UTSA-16 metal-organic framework, ACS Appl. Mater. Interfaces. 9 (2017) 455–463. https://doi.org/10.1021/acsami.6b13216.

[156] Y. Ban, M. Zhao, W. Yang, Metal-organic framework-based CO2 capture: From precise material design to high-efficiency membranes, Front. Chem. Sci. Eng. 14 (2020) 188–215. https://doi.org/10.1007/s11705-019-1872-6.

[157] L. Lai, J.R. Potts, D. Zhan, L. Wang, C.K. Poh, C. Tang, H. Gong, Z. Shen, J. Lin, R.S. Ruoff, Exploration of the active center structure of nitrogen-doped graphene-based catalysts for oxygen reduction reaction, Energy Environ. Sci. 5 (2012) 7936–7942. https://doi.org/10.1039/c2ee21802j.

[158] S. Kazemi, V. Safarifard, Carbon dioxide capture in MOFs: The effect of ligand functionalization, Polyhedron. 154 (2018) 236–251. https://doi.org/10.1016/j.poly.2018.07.042.

[159] N. Kundu, S. Sarkar, Porous organic frameworks for carbon dioxide capture and storage, J. Environ. Chem. Eng. 9 (2021). https://doi.org/10.1016/j.jece.2021.105090.

[160] A.P. Côté, A.I. Benin, N.W. Ockwig, M. O'Keeffe, A.J. Matzger, O.M.

Yaghi, Chemistry: Porous, crystalline, covalent organic frameworks, Science (80-.). 310 (2005) 1166–1170. https://doi.org/10.1126/science.1120411.

[161] A.A. Olajire, Recent advances in the synthesis of covalent organic frameworks for CO2 capture, J. CO2 Util. 17 (2017) 137–161. https://doi.org/10.1016/j.jcou.2016.12.003.

[162] H.R. Abuzeid, A.F.M. EL-Mahdy, S.-W. Kuo, Covalent organic frameworks: Design principles, synthetic strategies, and diverse applications, Giant. 6 (2021) 100054. https://doi.org/10.1016/j.giant.2021.100054.

[163] Y. Ge, H. Zhou, Y. Ji, L. Ding, Y. Cheng, R. Wang, S. Yang, Y. Liu, X. Wu, Y. Li, Understanding Water Adsorption and the Impact on CO2 Capture in Chemically Stable Covalent Organic Frameworks, J. Phys. Chem. C. 122 (2018) 27495–27506. https://doi.org/10.1021/acs.jpcc.8b09033.

[164] Y. Zhao, K.X. Yao, B. Teng, T. Zhang, Y. Han, A perfluorinated covalent triazine-based framework for highly selective and water-tolerant CO2 capture, Energy Environ. Sci. 6 (2013) 3684–3692. https://doi.org/10.1039/c3ee42548g.

[165] U. Kamran, S.J. Park, Chemically modified carbonaceous adsorbents for enhanced CO2 capture: A review, J. Clean. Prod. 290 (2021) 125776. https://doi.org/10.1016/j.jclepro.2020.125776.

[166] M. Bermeo, L.F. Vega, M.R.M. Abu-Zahra, M. Khaleel, Critical assessment of the performance of next-generation carbon-based adsorbents for CO2 capture focused on their structural properties, Sci. Total Environ. 810 (2022) 151720. https://doi.org/10.1016/j.scitotenv.2021.151720.

[167] H. Zhao, X. Luo, H. Zhang, N. Sun, W. Wei, Y. Sun, Carbon-based adsorbents for post-combustion capture: a review, Greenh. Gases Sci. Technol. 8 (2018) 11–36. https://doi.org/10.1002/ghg.1758.

[168] Z. Zhang, Z.P. Cano, D. Luo, H. Dou, A. Yu, Z. Chen, Rational design of tailored porous carbon-based materials for CO2 capture, J. Mater. Chem. A. 7 (2019) 20985–21003. https://doi.org/10.1039/c9ta07297g.

[169] R.S. Liu, X.D. Shi, C.T. Wang, Y.Z. Gao, S. Xu, G.P. Hao, S. Chen, A.H. Lu, Advances in Post-Combustion CO2 Capture by Physical Adsorption: From Materials Innovation to Separation Practice, ChemSusChem. 14 (2021) 1428–1471. https://doi.org/10.1002/cssc.202002677.

[170] D. Saha, M.J. Kienbaum, Role of oxygen, nitrogen and sulfur functionalities on the surface of nanoporous carbons in CO2 adsorption: A critical review,

Microporous   Mesoporous   Mater.   287   (2019)   29–55.
https://doi.org/10.1016/j.micromeso.2019.05.051.

[171] B. Petrovic, M. Gorbounov, S. Masoudi Soltani, Influence of surface
modification on selective CO2 adsorption: A technical review on
mechanisms and methods, Microporous Mesoporous Mater. 312 (2021)
110751. https://doi.org/10.1016/j.micromeso.2020.110751.

[172] R. Ahmed, G. Liu, B. Yousaf, Q. Abbas, H. Ullah, M.U. Ali, Recent
advances in carbon-based renewable adsorbent for selective carbon dioxide
capture and separation-A review, J. Clean. Prod. 242 (2020) 118409.
https://doi.org/10.1016/j.jclepro.2019.118409.

[173] N. Abuelnoor, A. AlHajaj, M. Khaleel, L.F. Vega, M.R.M. Abu-Zahra,
Activated carbons from biomass-based sources for CO2 capture
applications,   Chemosphere.   282   (2021)   131111.
https://doi.org/10.1016/j.chemosphere.2021.131111.

[174] W. Li, W. Tu, J. Cheng, F. Yang, X. Wang, L. Li, D. Shang, X. Zhou, C. Yu,
A. Yuan, J. Pan, Tuning N-doping thermal-process enables biomass-carbon
surface modification for potential separation effect of CO2/CH4/N2, Sep.
Purif.   Technol.   282   (2022)   120001.
https://doi.org/10.1016/j.seppur.2021.120001.

[175] A. Mukherjee, V.B. Borugadda, J.J. Dynes, C. Niu, A.K. Dalai, Carbon
dioxide capture from flue gas in biochar produced from spent coffee grounds:
Effect of surface chemistry and porous structure, J. Environ. Chem. Eng. 9
(2021) 106049. https://doi.org/10.1016/j.jece.2021.106049.

[176] W. Shi, Q. Zhang, S. Liu, S. Su, B. Chang, B. Yang, Copper ions-assisted
inorganic dynamic porogen of graphene-like multiscale microporous carbon
nanosheets for effective carbon dioxide capture, J. Colloid Interface Sci. 600
(2021) 670–680. https://doi.org/10.1016/j.jcis.2021.04.146.

[177] G. Zainab, A.A. Babar, N. Ali, A.A. Aboalhassan, X. Wang, J. Yu, B. Ding,
Electrospun carbon nanofibers with multi-aperture/opening porous
hierarchical structure for efficient CO2 adsorption, J. Colloid Interface Sci.
561 (2020) 659–667. https://doi.org/10.1016/j.jcis.2019.11.041.

[178] A.Z. Peng, S.C. Qi, X. Liu, D.M. Xue, S.S. Peng, G.X. Yu, X.Q. Liu, L.B.
Sun, N-doped porous carbons derived from a polymer precursor with a
record-high N content: Efficient adsorbents for CO2 capture, Chem. Eng. J.
372 (2019) 656–664. https://doi.org/10.1016/j.cej.2019.04.190.

[179] M. Pardakhti, T. Jafari, Z. Tobin, B. Dutta, E. Moharreri, N.S. Shemshaki,
S. Suib, R. Srivastava, Trends in Solid Adsorbent Materials Development for
CO2 Capture, ACS Appl. Mater. Interfaces. 11 (2019) 34533–34559.

https://doi.org/10.1021/acsami.9b08487.

[180] P. Thomas, C.W. Lai, M.R. Bin Johan, Recent developments in biomass-derived carbon as a potential sustainable material for super-capacitor-based energy storage and environmental applications, J. Anal. Appl. Pyrolysis. 140 (2019) 54–85. https://doi.org/10.1016/j.jaap.2019.03.021.

[181] G. Singh, K.S. Lakhi, S. Sil, S. V. Bhosale, I.Y. Kim, K. Albahily, A. Vinu, Biomass derived porous carbon for CO 2 capture, Carbon N. Y. 148 (2019) 164–186. https://doi.org/10.1016/j.carbon.2019.03.050.

[182] M.M. Sabzehmeidani, S. Mahnaee, M. Ghaedi, H. Heidari, V.A.L. Roy, Carbon based materials: a review of adsorbents for inorganic and organic compounds, Mater. Adv. 2 (2021) 598–627. https://doi.org/10.1039/d0ma00087f.

[183] S. Joseph, G. Saianand, M.R. Benzigar, K. Ramadass, G. Singh, A.I. Gopalan, J.H. Yang, T. Mori, A.H. Al-Muhtaseb, J. Yi, A. Vinu, Recent Advances in Functionalized Nanoporous Carbons Derived from Waste Resources and Their Applications in Energy and Environment, Adv. Sustain. Syst. 5 (2021) 1–30. https://doi.org/10.1002/adsu.202000169.

[184] A.A. Abd, S.Z. Naji, A.S. Hashim, M.R. Othman, Carbon dioxide removal through physical adsorption using carbonaceous and non-carbonaceous adsorbents: A review, J. Environ. Chem. Eng. 8 (2020) 104142. https://doi.org/10.1016/j.jece.2020.104142.

[185] M.R. Benzigar, S.N. Talapaneni, S. Joseph, K. Ramadass, G. Singh, J. Scaranto, U. Ravon, K. Al-Bahily, A. Vinu, Recent advances in functionalized micro and mesoporous carbon materials: Synthesis and applications, Chem. Soc. Rev. 47 (2018) 2680–2721. https://doi.org/10.1039/c7cs00787f.

[186] E.J. Jelmy, N. Thomas, D.T. Mathew, J. Louis, N.T. Padmanabhan, V. Kumaravel, H. John, S.C. Pillai, Impact of structure, doping and defect-engineering in 2D materials on CO2capture and conversion, React. Chem. Eng. 6 (2021) 1701–1738. https://doi.org/10.1039/d1re00214g.

[187] R. Balasubramanian, S. Chowdhury, Recent advances and progress in the development of graphene-based adsorbents for CO2 capture, J. Mater. Chem. A. 3 (2015) 21968–21989. https://doi.org/10.1039/c5ta04822b.

[188] T. Khandaker, M.S. Hossain, P.K. Dhar, S. Rahman, A. Hossain, M.B. Ahmed, Efficacies of Carbon-Based Adsorbents for Carbon Dioxide Capture, Processes. 8 (2020) 654. https://doi.org/10.3390/pr8060654.

[189] B. Szczęśniak, J. Choma, M. Jaroniec, Gas adsorption properties of

graphene-based materials, Adv. Colloid Interface Sci. 243 (2017) 46–59. https://doi.org/10.1016/j.cis.2017.03.007.

[190] L. Li, X.F. Wang, J.J. Zhong, X. Qian, S.L. Song, Y.G. Zhang, D.H. Li, Nitrogen-enriched porous polyacrylonitrile-based carbon fibers for CO2 Capture, Ind. Eng. Chem. Res. 57 (2018) 11608–11616. https://doi.org/10.1021/acs.iecr.8b01836.

[191] G. Zainab, A.A. Babar, N. Ali, A.A. Aboalhassan, X. Wang, J. Yu, B. Ding, Electrospun carbon nanofibers with multi-aperture/opening porous hierarchical structure for efficient CO2 adsorption, J. Colloid Interface Sci. 561 (2020) 659–667. https://doi.org/10.1016/j.jcis.2019.11.041.

[192] S.M. Hong, S.H. Kim, B.G. Jeong, S.M. Jo, K.B. Lee, Development of porous carbon nanofibers from electrospun polyvinylidene fluoride for CO2 capture, RSC Adv. 4 (2014) 58956–58963. https://doi.org/10.1039/c4ra11290c.

[193] F.E.C. Othman, N. Yusof, S. Samitsu, N. Abdullah, M.F. Hamid, K. Nagai, M.N.Z. Abidin, M.A. Azali, A.F. Ismail, J. Jaafar, F. Aziz, W.N.W. Salleh, Activated carbon nanofibers incorporated metal oxides for CO2adsorption: Effects of different type of metal oxides, J. CO2 Util. 45 (2021) 101434. https://doi.org/10.1016/j.jcou.2021.101434.

[194] S. Ma, Y. Wang, Z. Liu, M. Huang, H. Yang, Z. liang Xu, Preparation of carbon nanofiber with multilevel gradient porous structure for supercapacitor and CO2 adsorption, Chem. Eng. Sci. 205 (2019) 181–189. https://doi.org/10.1016/j.ces.2019.05.001.

[195] J. Choma, L. Osuchowski, M. Marszewski, A. Dziura, M. Jaroniec, Developing microporosity in Kevlar®-derived carbon fibers by CO2 activation for CO2 adsorption, J. CO2 Util. 16 (2016) 17–22. https://doi.org/10.1016/j.jcou.2016.05.004.

[196] H. Gao, Q. Li, S. Ren, Progress on CO2 capture by porous organic polymers, Curr. Opin. Green Sustain. Chem. 16 (2019) 33–38. https://doi.org/10.1016/j.cogsc.2018.11.015.

[197] L. Zou, Y. Sun, S. Che, X. Yang, X. Wang, M. Bosch, Q. Wang, H. Li, M. Smith, S. Yuan, Z. Perry, H.C. Zhou, Porous Organic Polymers for Post-Combustion Carbon Capture, Adv. Mater. 29 (2017) 1–35. https://doi.org/10.1002/adma.201700229.

[198] M. Sai Bhargava Reddy, D. Ponnamma, K.K. Sadasivuni, B. Kumar, A.M. Abdullah, Carbon dioxide adsorption based on porous materials, RSC Adv. 11 (2021) 12658–12681. https://doi.org/10.1039/d0ra10902a.

[199] D.S. Ahmed, G.A. El-Hiti, E. Yousif, A.A. Ali, A.S. Hameed, Design and synthesis of porous polymeric materials and their applications in gas capture and storage: A review, J. Polym. Res. 25 (2018) 1–21. https://doi.org/10.1007/s10965-018-1474-x.

[200] G. Kupgan, L.J. Abbott, K.E. Hart, C.M. Colina, Modeling Amorphous Microporous Polymers for CO2 Capture and Separations, Chem. Rev. 118 (2018) 5488–5538. https://doi.org/10.1021/acs.chemrev.7b00691.

[201] W. Wang, M. Zhou, D. Yuan, Carbon dioxide capture in amorphous porous organic polymers, J. Mater. Chem. A. 5 (2017) 1334–1347. https://doi.org/10.1039/c6ta09234a.

[202] A. Sattari, A. Ramazani, H. Aghahosseini, M.K. Aroua, The application of polymer containing materials in CO2capturing via absorption and adsorption methods, J. CO2 Util. 48 (2021) 101526. https://doi.org/10.1016/j.jcou.2021.101526.

[203] M. Hartmann, Hierarchical zeolites: A proven strategy to combine shape selectivity with efficient mass transport, Angew. Chemie - Int. Ed. 43 (2004) 5880–5882. https://doi.org/10.1002/anie.200460644.

[204] R.B. Vieira, P.A.S. Moura, E. Vilarrasa-García, D.C.S. Azevedo, H.O. Pastore, Polyamine-Grafted Magadiite: High CO2 Selectivity at Capture from CO2/N2 and CO2/CH4 Mixtures, J. CO2 Util. 23 (2018) 29–41. https://doi.org/10.1016/j.jcou.2017.11.004.

[205] M. Inagaki, M. Toyoda, Y. Soneda, S. Tsujimura, T. Morishita, Templated mesoporous carbons: Synthesis and applications, Carbon N. Y. 107 (2016) 448–473. https://doi.org/10.1016/j.carbon.2016.06.003.

[206] N. Díez, M. Sevilla, A.B. Fuertes, Synthesis strategies of templated porous carbons beyond the silica nanocasting technique, Carbon N. Y. 178 (2021) 451–476. https://doi.org/10.1016/j.carbon.2021.03.029.

[207] M. Enterría, J.L. Figueiredo, Nanostructured mesoporous carbons: Tuning texture and surface chemistry, Carbon N. Y. 108 (2016) 79–102. https://doi.org/10.1016/j.carbon.2016.06.108.

[208] Y. Wan, D. Zhao, On the controllable soft-templating approach to mesoporous silicates, Chem. Rev. 107 (2007) 2821–2860. https://doi.org/10.1021/cr068020s.

[209] D. Gu, F. Schüth, Synthesis of non-siliceous mesoporous oxides, Chem. Soc. Rev. 43 (2014) 313–344. https://doi.org/10.1039/c3cs60155b.

[210] H. Nishihara, T. Kyotani, Zeolite-templated carbons-three-dimensional

microporous graphene frameworks, Chem. Commun. 54 (2018) 5648–5673. https://doi.org/10.1039/c8cc01932k.

[211] B. Kaur, M.T. Gilbert, J.H. Knox, Porous Glassy Carbon , A New Columns Packing Material for Gas Chromatography and High-Performance Liquid Chromatography, Chromatographia. 16 (1982).

[212] T. Kyotani, N. Sonobe, A. Tomita, ChemInform Abstract: Formation of Highly Oriented Graphite from Polyacrylonitrile by Using a Two-Dimensional Space between Montmorillonite Lamellae., ChemInform. 19 (1988) 3–5. https://doi.org/10.1002/chin.198822027.

[213] D. Zhao, Q. Huo, J. Feng, B.F. Chmelka, G.D. Stucky, Nonionic triblock and star diblock copolymer and oligomeric sufactant syntheses of highly ordered, hydrothermally stable, mesoporous silica structures, J. Am. Chem. Soc. 120 (1998) 6024–6036. https://doi.org/10.1021/ja974025i.

[214] C.T. Kresge, M.E. Leonowicz, W.J. Roth, J.C. Vartuli, J.S. Beck, Ordered mesoporous molecular sieves synthesized by a liquid-crystal template mechanism, Nature. 359 (1992) 710–712. https://doi.org/10.1038/359710a0.

[215] J.S. Beck, J.C. Vartuli, W.J. Roth, M.E. Leonowicz, C.T. Kresge, K.D. Schmitt, C.T.W. Chu, D.H. Olson, E.W. Sheppard, S.B. McCullen, J.B. Higgins, J.L. Schlenker, A New Family of Mesoporous Molecular Sieves Prepared with Liquid Crystal Templates, J. Am. Chem. Soc. 114 (1992) 10834–10843. https://doi.org/10.1021/ja00053a020.

[216] J.A.S. Costa, R.A. De Jesus, D.O. Santos, J.B. Neris, R.T. Figueiredo, C.M. Paranhos, Synthesis, functionalization, and environmental application of silica-based mesoporous materials of the M41S and SBA-n families: A review, J. Environ. Chem. Eng. 9 (2021). https://doi.org/10.1016/j.jece.2021.105259.

[217] D. Zhao, J. Feng, Q. Huo, N. Melosh, G.H. Fredrickson, B.F. Chmelka, G.D. Stucky, Triblock copolymer syntheses of mesoporous silica with periodic 50 to 300 angstrom pores, Science (80-.). 279 (1998) 548–552. https://doi.org/10.1126/science.279.5350.548.

[218] F. Kleitz, S.H. Choi, R. Ryoo, Cubic Ia3d large mesoporous silica: Synthesis and replication to platinum nanowires, carbon nanorods and carbon nanotubes, Chem. Commun. 3 (2003) 2136–2137. https://doi.org/10.1039/b306504a.

[219] C.G. Göltner, A.J.C. Weißenberger, Mesoporous organic polymers obtained by "twostep nanocasting," Acta Polym. 49 (1998) 704–709. https://doi.org/10.1002/(SICI)1521-4044(199812)49:12<704::AID-APOL704>3.0.CO;2-X.

[220] B. Sakintuna, Y. Yürüm, Templated porous carbons: A review article, Ind. Eng. Chem. Res. 44 (2005) 2893–2902. https://doi.org/10.1021/ie049080w.

[221] M. Enterría, J.L. Figueiredo, Nanostructured mesoporous carbons: Tuning texture and surface chemistry, Carbon N. Y. 108 (2016) 79–102. https://doi.org/10.1016/j.carbon.2016.06.108.

[222] T. Kyotani, L. Tsai, A. Tomita, Formation of Ultrafine Carbon Tubes by Using an Anodic Aluminum Oxide Film as a Template, 7 (1995) 1427–1428.

[223] T. Kyotani, T. Nagai, S. Inoue, A. Tomita, Formation of New Type of Porous Carbon by Carbonization in Zeolite Nanochannels, Chem. Mater. 9 (1997) 609–615. https://doi.org/10.1021/cm960430h.

[224] R. Ryoo, S.H. Joo, S. Jun, Synthesis of highly ordered carbon molecular sieves via template-mediated structural transformation, J. File///C/Users/Emaruccia/OneDrive - Fond. Ist. Ital. Tecnol. EM/Mesoporous Carbons/Literature/Ryoo/2004_Ryoo_Nanostractured Carbons.PdfPhysical Chem. B. 103 (1999) 7743–7746. https://doi.org/10.1021/jp991673a.

[225] R. Ryoo, S.H. Joo, Nanostructured carbon materials synthesized from mesoporous silica crystals by replication, Stud. Surf. Sci. Catal. 148 (2004) 241–260. https://doi.org/10.1016/s0167-2991(04)80200-3.

[226] L.A. Solovyov, V.I. Zaikovskii, A.N. Shmakov, O. V. Belousov, R. Ryoo, Framework characterization of mesostructured carbon CMK-1 by X-ray powder diffraction and electron microscopy, J. Phys. Chem. B. 106 (2002) 12198–12202. https://doi.org/10.1021/jp0257653.

[227] S. Jun, Sang Hoon Joo, R. Ryoo, M. Kruk, M. Jaroniec, Z. Liu, T. Ohsuna, O. Terasaki, Synthesis of new, nanoporous carbon with hexagonally ordered mesostructure [5], J. Am. Chem. Soc. 122 (2000) 10712–10713. https://doi.org/10.1021/ja002261e.

[228] Y. Xia, Z. Yang, R. Mokaya, Templated nanoscale porous carbons, Nanoscale. 2 (2010) 639–659. https://doi.org/10.1039/b9nr00207c.

[229] T.W. Kim, F. Kleitz, B. Paul, R. Ryoo, MCM-48-like large mesoporous silicas with tailored pore structure: Facile synthesis domain in a ternary triblock copolymer-butanol-water system, J. Am. Chem. Soc. 127 (2005) 7601–7610. https://doi.org/10.1021/ja042601m.

[230] H.Y. Hsueh, C.T. Yao, R.M. Ho, Well-ordered nanohybrids and nanoporous materials from gyroid block copolymer templates, Chem. Soc. Rev. 44 (2015) 1974–2018. https://doi.org/10.1039/c4cs00424h.

[231] W. Libbrecht, A. Verberckmoes, J.W. Thybaut, P. Van Der Voort, J. De Clercq, Soft templated mesoporous carbons: Tuning the porosity for the adsorption of large organic pollutants, Carbon N. Y. 116 (2017) 528–546. https://doi.org/10.1016/j.carbon.2017.02.016.

[232] R. Ryoo, S.H. Joo, S. Jun, Synthesis of highly ordered carbon molecular sieves via template-mediated structural transformation, J. Phys. Chem. B. 103 (1999) 7743–7746. https://doi.org/10.1021/jp991673a.

[233] R. Ryoo, S.H. Joo, M. Kruk, M. Jaroniec, Ordered mesoporous carbons, Adv. Mater. 13 (2001) 677–681. https://doi.org/10.1002/1521-4095(200105)13:9<677::AID-ADMA677>3.0.CO;2-C.

[234] M. Kaneda, T. Tsubakiyama, A. Carlsson, Y. Sakamoto, T. Ohsuna, O. Terasaki, S.H. Joo, R. Ryoo, Structural study of mesoporous MCM-48 and carbon networks synthesized in the spaces of MCM-48 by electron crystallography, J. Phys. Chem. B. 106 (2002) 1256–1266. https://doi.org/10.1021/jp0131875.

[235] M. Kruk, M. Jaroniec, S.H. Joo, R. Ryoo, Characterization of regular and plugged SBA-15 silicas by using adsorption and inverse carbon replication and explanation of the plug formation mechanism, J. Phys. Chem. B. 107 (2003) 2205–2213. https://doi.org/10.1021/jp0271514.

[236] T.W. Kim, R. Ryoo, K.P. Gierszal, M. Jaroniec, L.A. Solovyov, Y. Sakamoto, O. Terasaki, Characterization of mesoporous carbons synthesized with SBA-16 silica template, J. Mater. Chem. 15 (2005) 1560–1571. https://doi.org/10.1039/b417804a.

[237] Huo, D.I. Margolese*, T.E.G.U.C. Pingyun Feng*, P.M.P.P.S. Rosa Leont, F.S.& G.D. Stucky, Generalized synthesis of periodic surfactant/inorganic composite materials, Nature. 368 (1994) 317–321.

[238] T. Kimura, Surfactant-templated mesoporous aluminophosphate-based materials and the recent progress, Microporous Mesoporous Mater. 77 (2005) 97–107. https://doi.org/10.1016/j.micromeso.2004.08.023.

[239] A. Berggren, A.E.C. Palmqvist, K. Holmberg, Surfactant-templated mesostructured materials from inorganic silica, Soft Matter. 1 (2005) 219–226. https://doi.org/10.1039/b507551n.

[240] J.L. Blin, M. Impéror-Clerc, Mechanism of self-assembly in the synthesis of silica mesoporous materials: In situ studies by X-ray and neutron scattering, Chem. Soc. Rev. 42 (2013) 4071–4082. https://doi.org/10.1039/c2cs35362h.

[241] S. Manet, J. Schmitt, M. Impéror-Clerc, V. Zholobenko, D. Durand, C.L.P. Oliveira, J.S. Pedersen, C. Gervais, N. Baccile, F. Babonneau, I. Grillo, F.

Meneau, C. Rochas, Kinetics of the formation of 2D-hexagonal silica nanostructured materials by nonionic block copolymer templating in solution, J. Phys. Chem. B. 115 (2011) 11330–11344. https://doi.org/10.1021/jp200213k.

[242] A. Galarneau, H. Cambon, F. Di Renzo, R. Ryoo, M. Choi, F. Fajula, Microporosity and connections between pores in SBA-15 mesostructured silicas as a function of the temperature of synthesis, New J. Chem. 27 (2003) 73–79. https://doi.org/10.1039/b207378c.

[243] S.H. Joo, R. Ryoo, M. Kruk, M. Jaroniec, Evidence for general nature of pore interconnectivity in 2-dimensional hexagonal mesoporous silicas prepared using block copolymer templates, J. Phys. Chem. B. 106 (2002) 4640–4646. https://doi.org/10.1021/jp013583n.

[244] M. Imperor-Clerc, P. Davidson, A. Davidson, Existence of a microporous corona around the mesopores of silica-based SBA-15 materials templated by triblock copolymers, J. Am. Chem. Soc. 122 (2000) 11925–11933. https://doi.org/10.1021/ja002245h.

[245] R. Ryoo, C.H. Ko, M. Kruk, V. Antochshuk, M. Jaroniec, Block-copolymer-templated ordered mesoporous silica: Array of uniform mesopores or mesopore-micropore network?, J. Phys. Chem. B. 104 (2000) 11465–11471. https://doi.org/10.1021/jp002597a.

[246] S.H. Joo, S. Jun, R. Ryoo, Synthesis of ordered mesoporous carbon molecular sieves CMK-1, Microporous Mesoporous Mater. 44–45 (2001) 153–158. https://doi.org/10.1016/S1387-1811(01)00179-2.

[247] M. V. Zakharova, N. Masoumifard, Y. Hu, J. Han, F. Kleitz, F.G. Fontaine, Designed Synthesis of Mesoporous Solid-Supported Lewis Acid-Base Pairs and Their CO2 Adsorption Behaviors, ACS Appl. Mater. Interfaces. 10 (2018) 13199–13210. https://doi.org/10.1021/acsami.8b00640.

[248] K.P. Gierszal, T.W. Kim, R. Ryoo, M. Jaroniec, Adsorption and structural properties of ordered mesoporous carbons synthesized by using various carbon precursors and ordered siliceous P6mm and Ia3̄d mesostructures as templates, J. Phys. Chem. B. 109 (2005) 23263–23268. https://doi.org/10.1021/jp054562m.

[249] L.L. Perreault, S. Giret, M. Gagnon, J. Florek, D. Larivière, F. Kleitz, Functionalization of Mesoporous Carbon Materials for Selective Separation of Lanthanides under Acidic Conditions, ACS Appl. Mater. Interfaces. 9 (2017) 12003–12012. https://doi.org/10.1021/acsami.6b16650.

[250] J.S. Lee, S.H. Joo, R. Ryoo, Synthesis of Mesoporous Silicas of Controlled Pore Wall Thickness and Their Replication to Ordered Nanoporous Carbons

with Various Pore Diameters, J. AM. CHEM. SOC. 124 (2002) 2002.

[251] M. Anbia, Z. Parvin, M. Sepehrian, Application of modified nanoporous materials in ascorbic acid adsorption, Part. Sci. Technol. 37 (2019) 750–756. https://doi.org/10.1080/02726351.2018.1438546.

[252] V.C. Almeida, R. Silva, M. Acerce, O.P. Junior, A.L. Cazetta, A.C. Martins, X. Huang, M. Chhowalla, T. Asefa, N-doped ordered mesoporous carbons with improved charge storage capacity by tailoring N-dopant density with solvent-assisted synthesis, J. Mater. Chem. A. 2 (2014) 15181–15190. https://doi.org/10.1039/c4ta02236j.

[253] R. Silva, D. Voiry, M. Chhowalla, T. Asefa, Efficient Metal-Free Electrocatalysts for Oxygen Reduction: Polyaniline-Derived N- and O - Doped Mesoporous Carbons, (2013) 8–11.

[254] Z. Xue, F. Zhang, D. Qin, Y. Wang, J. Zhang, J. Liu, Y. Feng, X. Lu, One-pot synthesis of silver nanoparticle catalysts supported on N-doped ordered mesoporous carbon and application in the detection of nitrobenzene, Carbon N. Y. 69 (2014) 481–489. https://doi.org/10.1016/j.carbon.2013.12.051.

[255] X. Sheng, N. Daems, B. Geboes, M. Kurttepeli, S. Bals, T. Breugelmans, A. Hubin, I.F.J. Vankelecom, P.P. Pescarmona, N-doped ordered mesoporous carbons prepared by a two-step nanocasting strategy as highly active and selective electrocatalysts for the reduction of O2 to H2O2, Appl. Catal. B Environ.   176–177   (2015)   212–224. https://doi.org/10.1016/j.apcatb.2015.03.049.

[256] M. Chen, H. Xuan, X. Zheng, J. Liu, X. Dong, F. Xi, N-doped mesoporous carbon by a hard-template strategy associated with chemical activation and its enhanced supercapacitance performance, Electrochim. Acta. 238 (2017) 269–277. https://doi.org/10.1016/j.electacta.2017.04.034.

[257] D. Zhang, Y. Hao, L. Zheng, Y. Ma, H. Feng, H. Luo, Nitrogen and sulfur co-doped ordered mesoporous carbon with enhanced electrochemical capacitance performance, J. Mater. Chem. A. 1 (2013) 7584–7591. https://doi.org/10.1039/c3ta11208j.

[258] D.S. Yang, D. Bhattacharjya, S. Inamdar, J. Park, J.S. Yu, Phosphorus-doped ordered mesoporous carbons with different lengths as efficient metal-free electrocatalysts for oxygen reduction reaction in alkaline media, J. Am. Chem. Soc. 134 (2012) 16127–16130. https://doi.org/10.1021/ja306376s.

[259] J. Gao, X. Wang, Y. Zhang, J. Liu, Q. Lu, M. Liu, Boron-doped ordered mesoporous carbons for the application of supercapacitors, Electrochim. Acta. 207 (2016) 266–274. https://doi.org/10.1016/j.electacta.2016.05.013.

[260] H. Wang, J. Ding, J. Zhang, C. Wang, W. Yang, H. Ren, A. Kong, Fluorine and nitrogen co-doped ordered mesoporous carbon as a metal-free electrocatalyst for oxygen reduction reaction, RSC Adv. 6 (2016) 79928–79933. https://doi.org/10.1039/c6ra14748h.

[261] J. Kim, M. Choi, R. Ryoo, Synthesis of mesoporous carbons with controllable N-content and their supercapacitor properties, Bull. Korean Chem. Soc. 29 (2008) 413–416. https://doi.org/10.5012/bkcs.2008.29.2.413.

[262] J. Ye, H. Zhao, W. Song, N. Wang, M. Kang, Z. Li, Enhanced electronic conductivity and sodium-ion adsorption in N/S co-doped ordered mesoporous carbon for high-performance sodium-ion battery anode, J. Power Sources. 412 (2019) 606–614. https://doi.org/10.1016/j.jpowsour.2018.12.002.

[263] R.W. Chang, C.J. Lin, S.Y.H. Liou, M.A. Bañares, M.O. Guerrero-Pérez, R.M. Martín Aranda, Enhanced cyclic CO2/N2 separation performance stability on chemically modified N-doped ordered mesoporous carbon, Catal. Today. 356 (2020) 88–94. https://doi.org/10.1016/j.cattod.2019.08.004.

[264] X. Liu, Y. Zhou, C.L. Wang, Y. Liu, D.J. Tao, Solvent-free self-assembly synthesis of N-doped ordered mesoporous carbons as effective and bifunctional materials for CO2 capture and oxygen reduction reaction, Chem. Eng. J. 427 (2022) 130878. https://doi.org/10.1016/j.cej.2021.130878.

[265] X. Wan, Y. Li, H. Xiao, Y. Pan, J. Liu, Hydrothermal synthesis of nitrogen-doped ordered mesoporous carbon: Via lysine-assisted self-assembly for efficient CO2 capture, RSC Adv. 10 (2020) 2932–2941. https://doi.org/10.1039/c9ra09983b.

[266] X. Wan, Y. Li, H. Xiao, Y. Pan, J. Liu, Hydrothermal synthesis of nitrogen-doped ordered mesoporous carbon: Via lysine-assisted self-assembly for efficient CO2 capture, RSC Adv. 10 (2020) 2932–2941. https://doi.org/10.1039/c9ra09983b.

[267] W. Kong, J. Liu, Ordered mesoporous carbon with enhanced porosity to support organic amines: efficient nanocomposites for the selective capture of CO2, New J. Chem. 43 (2019) 6040–6047. https://doi.org/10.1039/c9nj00617f.

[268] M.D. Slater, D. Kim, E. Lee, C.S. Johnson, Sodium-Ion Batteries, Adv. Funct. Mater. 23 (2013) 947–958. https://doi.org/10.1002/adfm.201200691.

[269] A. Manthiram, An Outlook on Lithium Ion Battery Technology, ACS Cent. Sci. 3 (2017) 1063–1069. https://doi.org/10.1021/acscentsci.7b00288.

[270] A. Mauger, C.M. Julien, State-of-the-Art Electrode Materials for Sodium-Ion Batteries, Materials (Basel). 13 (2020) 3453.

[271] C. Gerbaldi, Mesoporous Materials and Nanostructured LiFePO4 as Cathodes for Secondary Li-ion Batteries: Synthesis and Characterization, Politecnico di Torino, 2005.

[272] Y. Zhang, L. Chen, Y. Meng, J. Xie, Y. Guo, D. Xiao, Lithium and sodium storage in highly ordered mesoporous nitrogen-doped carbons derived from honey, J. Power Sources. 335 (2016) 20–30. https://doi.org/10.1016/j.jpowsour.2016.08.096.

[273] M.H. Sun, S.Z. Huang, L.H. Chen, Y. Li, X.Y. Yang, Z.Y. Yuan, B.L. Su, Applications of hierarchically structured porous materials from energy storage and conversion, catalysis, photocatalysis, adsorption, separation, and sensing to biomedicine, Chem. Soc. Rev. 45 (2016) 3479–3563. https://doi.org/10.1039/c6cs00135a.

[274] J. Asenbauer, T. Eisenmann, M. Kuenzel, A. Kazzazi, Z. Chen, D. Bresser, The success story of graphite as a lithium-ion anode material – fundamentals, remaining challenges, and recent developments including silicon (oxide) composites, Sustain. Energy Fuels. 4 (2020). https://doi.org/10.1039/d0se00175a.

[275] Z. Li, Y. Cao, G. Li, L. Chen, W. Xu, M. Zhou, B. He, W. Wang, Z. Hou, High rate capability of S-doped ordered mesoporous carbon materials with directional arrangement of carbon layers and large d-spacing for sodium-ion battery, Electrochim. Acta. 366 (2021) 137466. https://doi.org/10.1016/j.electacta.2020.137466.

[276] Z. Jiang, C. Zhang, X. Qu, B. Xing, G. Huang, Humic acid resin-based amorphous porous carbon as high rate and cycle performance anode for sodium-ion batteries, Electrochim. Acta. 372 (2021) 137850. https://doi.org/10.1016/j.electacta.2021.137850.

[277] Y. Zhang, Y. Meng, L. Chen, Y. Guo, D. Xiao, High lithium and sodium anodic performance of nitrogen-rich ordered mesoporous carbon derived from alfalfa leaves by a ball-milling assisted template method, J. Mater. Chem. A. 4 (2016) 17491–17502. https://doi.org/10.1039/c6ta08485k.

[278] Z. Wang, Y. Li, X.J. Lv, N-doped ordered mesoporous carbon as a high performance anode material in sodium ion batteries at room temperature, RSC Adv. 4 (2014) 62673–62677. https://doi.org/10.1039/c4ra09084e.

[279] L. Wang, W. Ding, Y. Sun, The preparation and application of mesoporous materials for energy storage, Mater. Res. Bull. 83 (2016) 230–249. https://doi.org/10.1016/j.materresbull.2016.06.008.

[280] M.H. Sun, S.Z. Huang, L.H. Chen, Y. Li, X.Y. Yang, Z.Y. Yuan, B.L. Su, Applications of hierarchically structured porous materials from energy storage and conversion, catalysis, photocatalysis, adsorption, separation, and sensing to biomedicine, Chem. Soc. Rev. 45 (2016) 3479–3563. https://doi.org/10.1039/c6cs00135a.

[281] Y. Qu, M. Guo, X. Wang, C. Yuan, Novel nitrogen-doped ordered mesoporous carbon as high-performance anode material for sodium-ion batteries, J. Alloys Compd. 791 (2019) 874–882. https://doi.org/10.1016/j.jallcom.2019.03.370.

[282] Y. Ishii, Y. Nishiwaki, A. Al-zubaidi, S. Kawasaki, Pore Size Determination in Ordered Mesoporous Materials Using Powder X - ray Di ff raction, (2013).

[283] B. Schwind, J. Smått, M. Tiemann, C. Weinberger, Microporous and Mesoporous Materials Modeling of gyroidal mesoporous CMK-8 and CMK-9 carbon nanostructures and their X-Ray diffraction patterns, Microporous Mesoporous Mater. 310 (2021) 110330. https://doi.org/10.1016/j.micromeso.2020.110330.

[284] Y.J. Sa, K. Kwon, J.Y. Cheon, F. Kleitz, S.H. Joo, Ordered mesoporous Co_3O_4 spinels as stable, bifunctional, noble metal-free oxygen electrocatalysts, J. Mater. Chem. A. 1 (2013) 9992–10001. https://doi.org/10.1039/c3ta11917c.

[285] M. Kruk, M. Jaroniec, R. Ryoo, S.H. Joo, Characterization of ordered mesoporous carbons synthesized using MCM-48 silicas as templates, J. Phys. Chem. B. 104 (2000) 7960–7968. https://doi.org/10.1021/jp000861u.

[286] F. Jiao, A.H. Hill, A. Harrison, A. Berko, A. V. Chadwick, P.G. Bruce, Synthesis of ordered mesoporous NiO with crystalline walls and a bimodal pore size distribution, J. Am. Chem. Soc. 130 (2008) 5262–5266. https://doi.org/10.1021/ja710849r.

[287] T. Grewe, X. Deng, H. Tüysüz, A study on the growth of Cr_2O_3 in ordered mesoporous silica and its replication, Chem. - A Eur. J. 20 (2014) 7692–7697. https://doi.org/10.1002/chem.201402301.

[288] M. Thommes, K. Kaneko, A. V. Neimark, J.P. Olivier, F. Rodriguez-Reinoso, J. Rouquerol, K.S.W. Sing, Physisorption of gases, with special reference to the evaluation of surface area and pore size distribution (IUPAC Technical Report), Pure Appl. Chem. 87 (2015) 1051–1069. https://doi.org/10.1515/pac-2014-1117.

[289] M. Thommes, K.A. Cychosz, Physical adsorption characterization of nanoporous materials: Progress and challenges, Adsorption. 20 (2014) 233–

250. https://doi.org/10.1007/s10450-014-9606-z.

[290] R. Konnola, T.S. Anirudhan, Efficient carbon dioxide capture by nitrogen and sulfur dual-doped mesoporous carbon spheres from polybenzoxazines synthesized by a simple strategy, J. Environ. Chem. Eng. 8 (2020) 103614. https://doi.org/10.1016/j.jece.2019.103614.

[291] Y. Meng, D. Gu, F. Zhang, Y. Shi, L. Cheng, D. Feng, Z. Wu, Z. Chen, Y. Wan, A. Stein, D. Zhao, A family of highly ordered mesoporous polymer resin and carbon structures from organic-organic self-assembly, Chem. Mater. 18 (2006) 4447–4464. https://doi.org/10.1021/cm060921u.

[292] M. Ayiania, M. Smith, A.J.R. Hensley, L. Scudiero, J.S. McEwen, M. Garcia-Perez, Deconvoluting the XPS spectra for nitrogen-doped chars: An analysis from first principles, Carbon N. Y. 162 (2020) 528–544. https://doi.org/10.1016/j.carbon.2020.02.065.

[293] Y. Wang, X. Hu, J. Hao, R. Ma, Q. Guo, H. Gao, H. Bai, Nitrogen and Oxygen Codoped Porous Carbon with Superior CO_2 Adsorption Performance: A Combined Experimental and DFT Calculation Study, Ind. Eng. Chem. Res. 58 (2019) 13390–13400. https://doi.org/10.1021/acs.iecr.9b01454.

[294] K. Stańczyk, R. Dziembaj, Z. Piwowarska, S. Witkowski, Transformation of nitrogen structures in carbonization of model compounds determined by XPS, Carbon N. Y. 33 (1995) 1383–1392. https://doi.org/10.1016/0008-6223(95)00084-Q.

[295] M. Gehring, H. Tempel, A. Merlen, R. Schierholz, R.A. Eichel, H. Kungl, Carbonisation temperature dependence of electrochemical activity of nitrogen-doped carbon fibres from electrospinning as air-cathodes for aqueous-alkaline metal-air batteries, RSC Adv. 9 (2019) 27231–27241. https://doi.org/10.1039/c9ra03805a.

[296] H. Seema, K.C. Kemp, N.H. Le, S. Park, V. Chandra, J.W. Lee, K.S. Kim, Highly selective CO_2 capture by S-doped microporous carbon materials, Carbon N. Y. 66 (2014) 320–326. https://doi.org/10.1016/j.carbon.2013.09.006.

[297] D. Li, W.B. Li, J.S. Shi, F.W. Xin, Influence of doping nitrogen, sulfur, and phosphorus on activated carbons for gas adsorption of H_2, CH_4 and CO_2, RSC Adv. 6 (2016) 50138–50143. https://doi.org/10.1039/C6RA06620H.

[298] Y. Xia, Preparation of sulfur-doped microporous carbons for the storage of hydrogen and carbon dioxide, Carbon N. Y. 50 (2012) 5543–5553. https://doi.org/10.1016/j.carbon.2012.07.044.

[299] Y. Sun, J. Zhao, J. Wang, N. Tang, R. Zhao, D. Zhang, T. Guan, K. Li,
       Sulfur-Doped Millimeter-Sized Microporous Activated Carbon Spheres
       Derived from Sulfonated Poly (styrene − divinylbenzene) for CO 2 Capture,
       (2017). https://doi.org/10.1021/acs.jpcc.7b02195.

[300] Y. Sun, K. Li, J. Zhao, J. Wang, N. Tang, D. Zhang, T. Guan, Z. Jin, Nitrogen
       and sulfur Co-doped microporous activated carbon macro-spheres for CO 2
       capture, J. Colloid Interface Sci. 526 (2018) 174–183.
       https://doi.org/10.1016/j.jcis.2018.04.101.

[301] A. Gonciaruk, M.R. Hall, M.W. Fay, C.D.J. Parmenter, C.H. Vane, A.N.
       Khlobystov, N. Ripepi, Kerogen nanoscale structure and CO2 adsorption in
       shale micropores, Sci. Rep. 11 (2021) 1–13. https://doi.org/10.1038/s41598-
       021-83179-z.

[302] P. Pornaroontham, G. Panomsuwan, S. Chae, N. Saito, N. Thouchprasitchai,
       Y. Phongboonchoo, S. Pongstabodee, Nitriding an oxygen-doped
       nanocarbonaceous sorbent synthesized via solution plasma process for
       improving CO2 adsorption capacity, Nanomaterials. 9 (2019).
       https://doi.org/10.3390/nano9121776.

[303] Á. Sánchez-Sánchez, F. Suárez-García, A. Martínez-Alonso, J.M.D. Tascón,
       Influence of porous texture and surface chemistry on the CO2 adsorption
       capacity of porous carbons: Acidic and basic site interactions, ACS Appl.
       Mater. Interfaces. 6 (2014) 21237–21247.
       https://doi.org/10.1021/am506176e.

[304] H. Yuan, J. Chen, D. Li, H. Chen, Y. Chen, 5 Ultramicropore-rich renewable
       porous carbon from biomass tar with excellent adsorption capacity and
       selectivity for CO2 capture, Chem. Eng. J. 373 (2019) 171–178.
       https://doi.org/10.1016/j.cej.2019.04.206.

[305] J. Li, M. Hou, Y. Chen, W. Cen, Y. Chu, S. Yin, Enhanced CO 2 capture on
       graphene via N, S dual-doping, Appl. Surf. Sci. 399 (2017) 420–425.
       https://doi.org/10.1016/j.apsusc.2016.11.157.

[306] G. Lim, K.B. Lee, H.C. Ham, Effect of N-Containing Functional Groups on
       CO2 Adsorption of Carbonaceous Materials: A Density Functional Theory
       Approach, J. Phys. Chem. C. 120 (2016) 8087–8095.
       https://doi.org/10.1021/acs.jpcc.5b12090.

[307] F. Sun, X. Liu, J. Gao, X. Pi, L. Wang, Z. Qu, Y. Qin, Highlighting the role
       of nitrogen doping in enhancing CO2 uptake onto carbon surfaces: a
       combined experimental and computational analysis, J. Mater. Chem. A. 4
       (2016) 18248–18252. https://doi.org/10.1039/c6ta08262a.

[308] D. Wu, J. Liu, Y. Yang, Y. Zheng, Nitrogen/Oxygen Co-Doped Porous

Carbon Derived from Biomass for Low-Pressure CO2Capture, Ind. Eng. Chem. Res. 59 (2020) 14055–14063. https://doi.org/10.1021/acs.iecr.0c00006.

[309] D. Wu, Y. Yang, J. Liu, Y. Zheng, Plasma-Modified N/O-Doped Porous Carbon for CO2Capture: An Experimental and Theoretical Study, Energy and Fuels. 34 (2020) 6077–6084. https://doi.org/10.1021/acs.energyfuels.0c00415.

[310] E. García-Díez, A. Castro-Muñiz, J.I. Paredes, M.M. Maroto-Valer, F. Suárez-García, S. García, CO2 capture by novel hierarchical activated ordered micro-mesoporous carbons derived from low value coal tar products, Microporous Mesoporous Mater. 318 (2021). https://doi.org/10.1016/j.micromeso.2021.110986.

[311] K.J. Chen, D.G. Madden, T. Pham, K.A. Forrest, A. Kumar, Q.Y. Yang, W. Xue, B. Space, J.J. Perry, J.P. Zhang, X.M. Chen, M.J. Zaworotko, Tuning Pore Size in Square-Lattice Coordination Networks for Size-Selective Sieving of CO2, Angew. Chemie - Int. Ed. 55 (2016) 10268–10272. https://doi.org/10.1002/anie.201603934.

[312] C. Yu, Q. Ding, J. Hu, Q. Wang, X. Cui, H. Xing, Selective capture of carbon dioxide from humid gases over a wide temperature range using a robust metal–organic framework, Chem. Eng. J. 405 (2021) 126937. https://doi.org/10.1016/j.cej.2020.126937.

[313] A. Masala, J.G. Vitillo, G. Mondino, C.A. Grande, R. Blom, M. Manzoli, M. Marshall, S. Bordiga, CO2 capture in dry and wet conditions in UTSA-16 metal-organic framework, ACS Appl. Mater. Interfaces. 9 (2017) 455–463. https://doi.org/10.1021/acsami.6b13216.

[314] J. Rogacka, A. Seremak, A. Luna-Triguero, F. Formalik, I. Matito-Martos, L. Firlej, S. Calero, B. Kuchta, High-throughput screening of metal – Organic frameworks for CO2 and CH4 separation in the presence of water, Chem. Eng. J. 403 (2021). https://doi.org/10.1016/j.cej.2020.126392.

[315] P.A. Sáenz Cavazos, M.L. Díaz-Ramírez, E. Hunter-Sellars, S.R. McIntyre, E. Lima, I.A. Ibarra, D.R. Williams, Fluorinated MIL-101 for carbon capture utilisation and storage: uptake and diffusion studies under relevant industrial conditions, RSC Adv. 11 (2021) 13304–13310. https://doi.org/10.1039/d1ra01118a.

[316] D.G. Madden, A.B. Albadarin, D. O'Nolan, P. Cronin, J.J. Perry, S. Solomon, T. Curtin, M. Khraisheh, M.J. Zaworotko, G.M. Walker, Metal-Organic Material Polymer Coatings for Enhanced Gas Sorption Performance and Hydrolytic Stability under Humid Conditions, ACS Appl. Mater.

Interfaces. 12 (2020) 33759–33764. https://doi.org/10.1021/acsami.0c08078.

[317] B.L. Suh, S. Lee, J. Kim, Size-matching ligand insertion in MOF-74 for enhanced CO2 capture under humid conditions, J. Phys. Chem. C. 121 (2017) 24444–24451. https://doi.org/10.1021/acs.jpcc.7b08239.

[318] R. Ben-Mansour, N.A.A. Qasem, M.A. Antar, Carbon dioxide adsorption separation from dry and humid CO2/N2 mixture, Comput. Chem. Eng. 117 (2018) 221–235. https://doi.org/10.1016/j.compchemeng.2018.06.016.

[319] D. Madden, T. Curtin, Carbon dioxide capture with amino-functionalised zeolite-β: A temperature programmed desorption study under dry and humid conditions, Microporous Mesoporous Mater. 228 (2016) 310–317. https://doi.org/10.1016/j.micromeso.2016.03.041.

[320] D. Kwon, J.C. Kim, H. Lee, W. Lee, C. Jo, Engineering micropore walls of beta zeolites by post-functionalization for CO2 adsorption performance screening under humid conditions, Chem. Eng. J. 427 (2022) 131461. https://doi.org/10.1016/j.cej.2021.131461.

[321] R.L. Siegelman, E.J. Kim, J.R. Long, Porous materials for carbon dioxide separations, Nat. Mater. 20 (2021) 1060–1072. https://doi.org/10.1038/s41563-021-01054-8.

[322] J. Kossmann, R. Rothe, T. Heil, M. Antonietti, N. López-Salas, Ultrahigh water sorption on highly nitrogen doped carbonaceous materials derived from uric acid, J. Colloid Interface Sci. 602 (2021) 880–888. https://doi.org/10.1016/j.jcis.2021.06.012.

[323] L. Gao, A. Chandra, Y. Nabae, T. Hayakawa, Inducing defects in ordered mesoporous carbons via the block copolymerlated higherature carbonization of nitrogen-containing polymeric precursors, Polym. J. 50 (2018) 389–396. https://doi.org/10.1038/s41428-018-0023-0.

[324] Q. Li, J. Yang, D. Feng, Z. Wu, Q. Wu, S.S. Park, C.S. Ha, D. Zhao, Facile synthesis of porous carbon nitride spheres with hierarchical three-dimensional mesostructures for CO2 capture, Nano Res. 3 (2010) 632–642. https://doi.org/10.1007/s12274-010-0023-7.

[325] G.Y. Gor, M. Thommes, K.A. Cychosz, A. V. Neimark, Quenched solid density functional theory method for characterization of mesoporous carbons by nitrogen adsorption, Carbon N. Y. 50 (2012) 1583–1590. https://doi.org/10.1016/J.CARBON.2011.11.037.

[326] K.A. Cychosz, R. Guillet-Nicolas, J. García-Martínez, M. Thommes, Recent advances in the textural characterization of hierarchically structured

nanoporous materials, Chem. Soc. Rev. 46 (2017) 389–414. https://doi.org/10.1039/c6cs00391e.

[327] X. Wu, W. Xing, J. Florek, J. Zhou, G. Wang, S. Zhuo, Q. Xue, Z. Yan, F. Kleitz, On the origin of the high capacitance of carbon derived from seaweed with an apparently low surface area, J. Mater. Chem. A Mater. Energy Sustain. 2 (2014) 18998–19004. https://doi.org/10.1039/C4TA03430A.

[328] M. Seredych, K. Lμszló, T.J. Bandosz, Sulfur-Doped Carbon Aerogel as a Metal-Free Oxygen Reduction Catalyst, ChemCatChem. 7 (2015) 2924–2931. https://doi.org/10.1002/cctc.201500192.

[329] M. Seredych, K. László, E. Rodríguez-castellón, T.J. Bandosz, S-doped carbon aerogels / GO composites as oxygen reduction catalysts, J. Energy Chem. 25 (2016) 236–245. https://doi.org/10.1016/j.jechem.2016.01.005.

[330] X. Li, Q. Xue, D. He, L. Zhu, Y. Du, W. Xing, T. Zhang, Sulfur − Nitrogen Codoped Graphite Slit-Pore for Enhancing Selective Carbon Dioxide Adsorption: Insights from Molecular Simulations, ACS Sustain. Chem. Eng. 5 (2017) 8815–8823. https://doi.org/10.1021/acssuschemeng.7b01612.

[331] A. Nuhnen, C. Janiak, A practical guide to calculate the isosteric heat/enthalpy of adsorption: Via adsorption isotherms in metal-organic frameworks, MOFs, Dalt. Trans. 49 (2020) 10295–10307. https://doi.org/10.1039/d0dt01784a.

[332] T. Horikawa, N. Sakao, D.D. Do, Effects of temperature on water adsorption on controlled microporous and mesoporous carbonaceous solids, Carbon N. Y. 56 (2013) 183–192. https://doi.org/10.1016/j.carbon.2013.01.003.

[333] J. Fujiki, K. Yogo, Water adsorption on nitrogen-doped carbons for adsorption heat pump/desiccant cooling: Experimental and density functional theory calculation studies, Appl. Surf. Sci. 492 (2019) 776–784. https://doi.org/10.1016/j.apsusc.2019.06.267.

[334] K.V. Kumar, K. Preuss, Z.X. Guo, M.M. Titirici, Understanding the Hydrophilicity and Water Adsorption Behavior of Nanoporous Nitrogen-Doped Carbons, J. Phys. Chem. C. 120 (2016) 18167–18179. https://doi.org/10.1021/acs.jpcc.6b06555.

[335] J. Heske, R. Walczak, J.D. Epping, S. Youk, S.K. Sahoo, M. Antonietti, T.D. Kühne, M. Oschatz, When water becomes an integral part of carbon – combining theory and experiment to understand the zeolite-like water adsorption properties of porous C 2 N materials , J. Mater. Chem. A. 9 (2021) 22563–22572. https://doi.org/10.1039/d1ta05122a.

[336] C. Urita, K. Urita, T. Araki, K. Horio, M. Yoshida, I. Moriguchi, New

insights into the heat of adsorption of water, acetonitrile, and n-hexane in porous carbon with oxygen functional groups, J. Colloid Interface Sci. 552 (2019) 412–417. https://doi.org/10.1016/j.jcis.2019.05.090.

[337] J. Wu, X. Zhu, F. Yang, T. Ge, R. Wang, Easily-synthesized and low-cost amine-functionalized silica sol-coated structured adsorbents for CO2 capture, Chem. Eng. J. 425 (2021) 131409. https://doi.org/10.1016/j.cej.2021.131409.

[338] Y. Wang, X. Hu, T. Guo, W. Tian, J. Hao, Q. Guo, The competitive adsorption mechanism of CO2, H2O and O2 on a solid amine adsorbent, Chem. Eng. J. 416 (2021) 129007. https://doi.org/10.1016/j.cej.2021.129007.

[339] F. Su, C. Lu, W. Cnen, H. Bai, J.F. Hwang, Capture of CO2 from flue gas via multiwalled carbon nanotubes, Sci. Total Environ. 407 (2009) 3017–3023. https://doi.org/10.1016/j.scitotenv.2009.01.007.

[340] John Wiley & Sons, Inc. SpectraBase, (n.d.). https://spectrabase.com/spectrum/77SJur7fazW (accessed March 21, 2022).

[341] John Wiley & Sons, Inc. SpectraBase, (n.d.). https://spectrabase.com/spectrum/BnpcCEB1yUv (accessed March 21, 2022).

[342] John Wiley & Sons, Inc. SpectraBase, (n.d.). https://spectrabase.com/spectrum/Big2BLmUPf2 (accessed March 21, 2022).

[343] John Wiley & Sons, Inc. SpectraBase, (n.d.). https://spectrabase.com/spectrum/Big2BLmUPf2 (accessed March 21, 2022).

[344] National Institute of Standards and Technology (NIST) - U.S. Department of Commerce, NIST Standard Reference Database Number 69, (n.d.). https://webbook.nist.gov/cgi/cbook.cgi?Scan=cob10480&Type=IR (accessed March 22, 2022).

[345] G. Socrates, Infrared and Raman Characteristic Group Frequencies, John Wiley & Sons, 2001. https://doi.org/10.1016/0160-9327(81)90159-9.

[346] N.A.A. Qasem, R. Ben-Mansour, Adsorption breakthrough and cycling stability of carbon dioxide separation from CO2/N2/H2O mixture under ambient conditions using 13X and Mg-MOF-74, Appl. Energy. 230 (2018) 1093–1107. https://doi.org/10.1016/j.apenergy.2018.09.069.

[347] Q. Al-Naddaf, S. Lawson, A.A. Rownaghi, F. Rezaei, Analysis of dynamic

CO2 capture over 13X zeolite monoliths in the presence of SOx, NOx and humidity, AIChE J. 66 (2020). https://doi.org/10.1002/aic.16297.

[348] M. Miyamoto, S. Ono, K. Kusukami, Y. Oumi, S. Uemiya, High Water Tolerance of a Core–Shell-Structured Zeolite for CO2 Adsorptive Separation under Wet Conditions, ChemSusChem. 11 (2018) 1756–1760. https://doi.org/10.1002/cssc.201800063.

[349] D. Saikia, T.H. Wang, C.J. Chou, J. Fang, L.D. Tsai, H.M. Kao, A comparative study of ordered mesoporous carbons with different pore structures as anode materials for lithium-ion batteries, RSC Adv. 5 (2015) 42922–42930. https://doi.org/10.1039/c5ra05168a.

[350] C. Ma, X. Shao, D. Cao, Nitrogen-doped graphene nanosheets as anode materials for lithium ion batteries: A first-principles study, J. Mater. Chem. 22 (2012) 8911–8915. https://doi.org/10.1039/c2jm00166g.

[351] R. Nicolas, F. Bérubé, T.W. Kim, M. Thommes, F. Kleitz, Tailoring mesoporosity and intrawall porosity in large pore silicas: synthesis and nitrogen sorption behavior, Elsevier B.V., 2008. https://doi.org/10.1016/S0167-2991(08)80165-6.

[352] L.A. Solovyov, Diffraction analysis of mesostructured mesoporous materials, Chem. Soc. Rev. 42 (2013) 3708–3720. https://doi.org/10.1039/c2cs35248f.

[353] K.A. Cychosz, M. Thommes, Progress in the Physisorption Characterization of Nanoporous Gas Storage Materials, Engineering. 4 (2018) 559–566. https://doi.org/10.1016/j.eng.2018.06.001.

[354] A. Sayari, Y. Belmabkhout, R. Serna-Guerrero, Flue gas treatment via CO2 adsorption, Chem. Eng. J. 171 (2011) 760–774. https://doi.org/10.1016/j.cej.2011.02.007.